University of Strathclyde

Department of Naval Architecture, Ocean & Marine Engineering

Numerical Investigation on Fatigue and Corrosion Behaviour of 3-D Printed Structures

by

Olena Karpenko

A thesis presented in fulfilment of the requirements for the degree of

Doctor of Philosophy

Glasgow, UK

2022

AUTHOR STATEMENT

This thesis is the result of the author's original research. It has been composed by the author and has not been previously submitted for examination which has led to the award of a degree.

The copyright of this thesis belongs to the author under the terms of the United Kingdom Copyright Acts as qualified by University of Strathclyde Regulation 3.50. Due acknowledgement must always be made of the use of any material contained in, or derived from, this thesis.

Signed: Olena Karpenko   Date: 22 January 2022

ACKNOWLEDGEMENTS

ABSTRACT

Structural failure can be a challenging and unpredictable phenomenon to detect, especially under the combination of mechanical loads and environmental conditions. Additive manufacturing has recently gained interest because of its capability of producing complex metal geometries directly from a digital model. However, despite its high potential, the process induced imperfections, like pores, microstructural changes due to the layer-by-layer manufacturing, and residual stresses could significantly reduce the material resistance and impact the crack growth behaviour. Therefore, the combinations of those manufacturing factors add another complexity layer that needs further investigation with advanced and sophisticated numerical techniques.

The numerical techniques commonly used to investigate the structural behaviour are primarily based on classical continuum mechanics with the governing equations in the form of partial differential equations. However, such methods become inadequate in the presence of the field's discontinuities, such as cracks, especially when dealing with additively manufactured materials.

To overcome these limitations, in this dissertation, a new continuum mechanics theory (i.e., Peridynamics) based on integro-differential equations is utilised. Peridynamics already proved its applicability and effectiveness in modelling discontinuities such as crack nucleation and propagation, micro-cracks interaction problems, polycrystalline fracture, stress-corrosion cracking and simulations of fracture phenomena under different loading conditions, accounting for potential failure due to corrosion. Nonetheless, its applicability and accuracy for the investigation of additively manufactured materials still remain to be assessed.

For this reason, this work focused on the application of Peridynamics on fatigue and corrosion fatigue problems in additively manufactured materials utilized in marine environment. The developed methodology showed its capability of evaluating the effects of porosity on fatigue nucleation and propagation process. Additionally, the application of the columnar granularity and residual stresses in the structure proved the anisotropy in the material response and their substantial impact on fatigue crack growth rates. Lastly, a numerical framework for corrosion fatigue problems, which combines the Peridynamics fatigue crack growth model and Peridynamics diffusion model is

proposed in order to couple the mechanical and diffusion fields existing in the material due to the impact of environmental fatigue. The developed numerical corrosion fatigue model showed the capability of the framework to predict the corrosion fatigue crack growth rates by capturing the effects of the loading frequency on the fatigue performance.

The numerical results have been validated against the experimental data available in the literature and verified with the commonly used commercial Finite Element Analysis numerical solutions.

TABLE OF CONTENTS

LIST OF FIGURES

LIST OF TABLES

ABBREVIATIONS

ADR	Adaptive Dynamic Relaxation
ALM	Additive Layer Manufacturing
AM	Additive Manufacturing
BC	Boundary Conditions
BiCG	Stabilised Biconjugate gradients method
CAD	Computer-Aided Design
CCM	Classical Continuum Mechanics
CDD	Concentration-Dependent Damage
CF	Corrosion Fatigue
CFCG	Corrosion Fatigue Crack Growth
COD	Crack Opening Displacement
C(T)	Compact Tension Sample
EBM	Electron Beam Melting
FCG	Fatigue Crack Growth
FCGR	Fatigue Crack Growth Rates
FEM	Finite Element Method
GB	Grain Boundaries
GI	Grain Interior
HCF	High Cycle Fatigue
HE	Hydrogen Embrittlement
H-C(T)	Horizontal Compact Tension sample
LCF	Low Cycle Fatigue
LEFM	Linear Elastic Fracture Mechanics
MDM	Molecular Dynamics Model
MRP	Metal Rapid Prototyping
MSC	Mechanically Small Cracks
PD	Peridynamics
PMMA	Polymethyl Methacrylate
RS	Residual Stresses
SCC	Stress Corrosion Cracking
SIF	Stress Intensity Factor
SLM	Selective Laser Melting
TCF	True Corrosion Fatigue
V-C(T)	Vertical Compact Tension sample
VHCF	Very High Cycle Fatigue
WAAM	Wire+Arc Additive Manufacturing
XFEM	Extended Finite Element Method

NOMENCLATURE

Latin Characters

a	Crack length
a_n	Pre-notch length
a_{PD}, $\quad b_{PD}$, d_{PD}, a_{2PD}	Peridynamic parameters
A, m	Material constants in the PD fatigue model
A_1, m_1	Material constants for Phase I (crack nucleation) in the PD fatigue model
A_2, m_2	Material constants for Phase II (crack propagation) in the PD fatigue model
b	Peridynamic constant for in-plane defermations
$\boldsymbol{b}$	The vector of body loads
b_y	Body force density
$\boldsymbol{B}$	Body load matrix
c_R	Rayleigh wave speed
C_H	Hydrogen concentration
$\dot{C}_H$	Time derivative of hydrogen concentration
d	Diameter of the pins in C(T) sample
d_{bc}	Diffusion bond constant
d_p	Pore diameter
da/dN	Fatigue Crack Growth Rate
D_H	Hydrogen diffusion coefficient
E	Young's modulus
f	Frequency
$\boldsymbol{f}$	Peridynamic pairwise force densities
$\boldsymbol{f_H}$	Hydrogen diffusion response function
ΔF	Cyclic loads with cyclic load extremes F_{max} and F_{min}
G_0	Energy release rate
G_c	Fracture energy
h	Thickness of the sample
H_x	Horizon of the material point with coordinates x

k	Grain coefficient with k_{GI} for grain boundaries and k_{GB} for grain interior
$\boldsymbol{K}$	Global stiffness matrix
K_0	SIF for a plate with only macro-crack
K^*	SIF for a plate with macro-crack and micro-cracks
ΔK	SIF range
K_{IC}	SIF approaches the toughness of the material
ΔK_p	SIF range for pores
ΔK_{SCC}	SIF range for SCC
ΔK_{th}	Threshold of SIF
$\Delta K_{th,p}$	SIF range limit for specified pores
$\Delta K_{th,LC}$	Threshold SIF range for the long crack
L	Length of the sample
M	Total number of the family members
n	Cycle range
N	Number of loading cycles
N_b	Number of broken bonds
N_f	Number of cycles to crack nucleation
$N_{p_{tot}}$	Total number of pores
N_T	Total number of the bonds
P	Porosity ratio
p^0	Critical load for a plate with only single macro-crack
p^*	Critical load for a plate with a macro-crack and distributed micro-cracks
r	Radius of the hole
R	Load ratio
R_f	Fictitious boundary layer
$s_{(i)(j)}$	Stretch between material points i and j
s^{max}, s^{min}	Maximum and minimum bond stretches
s_c	Critical stretch
s_{cf}	Surface correction factor
t	Time
Δt	Time step size

T	Temperature
$\boldsymbol{u}$	Displacement vector
u	Displacement in x-dirextion
$\dot{u}$	Velocity in x-direction
$\ddot{\boldsymbol{u}}_{(i)}$	Acceleration vector of the material point i
$\boldsymbol{U}$	Displacement matrices
v	Displacement in y-direction
$\dot{v}$	Velocity in y-direction
v_c	Volume correction factor
V_c	Velocity of the propagating crack
V	Incremental volume
ΔV_Δ	Volume of the boundary layer
V_p, V_T	Volume of void-space and bulk volume of material
w_p	Pore location
W	Width of the sample
$\boldsymbol{x}$	Vector of coordinates
Δx	Spacing between material points
$\boldsymbol{y}$	Location of the material point after deformation

Greek Characters

α	Coefficient of thermal expansion
α^0	Inclanation angle
δ	Horizon size
ε	Cyclic bond strain
η_x, η_y	Relative displacements between material points in x and y directions
θ	Dilatation
θ_H	Hydrogen coverage
λ	Remaining life of the bond
μ	Shear modulus
ν	Poisson's ratio
$\boldsymbol{\xi}$	Relative position vector
ξ_x, ξ_y	Reference lengths in x and y directions

ρ	Mass density
σ	Characteristic stress
σ_a	Stress amplitude
$\sigma_{max}, \sigma_{min}$	Maximum and the minimum stresses
$\sigma_x^{rs}, \sigma_y^{rs}$	longitudinal and transverse RS
$\Delta\sigma_e$	Intrinsic fatigue limit
φ	Local damage of each material point
χ	Pore coefficient
ψ	State of the bond (intact or broken)

1   INTRODUCTION

1.1   Background and motivation

Additive manufacturing (AM), or known as 3D printing technology, is a subject of undergoing intense research and development studies in the field of Metal Rapid Prototyping (MRP). 3D printed structures are widely used in aerospace, automotive, and biomedical industries [1–4], and, nowadays, its application is extended to the marine industry [5, 6].

The rapid increase of AM in industrial applications provides flexibility in designing and manufacturing complex metal structures involving titanium, stainless steel, nickel and aluminium alloys [7]. Moreover, the AM process of building layer-by-layer metal components, as shown in Figure 1.1, according to the designed 3D model [3] increases production efficiency and product customisation. Titanium alloy Ti6Al4V is recognized as the most popular titanium alloy, which is used in aerospace, energy, marine, automobile, biomedical and chemical industries [8]. Ti6Al4V is produced by traditional manufacturing methods (casting, forging, extrusion) and AM, which increases production efficiency and customizes the product [8]. Due to the particular interest in Ti6Al4V alloy in most fields, presented research on additively manufactured materials will focus on Ti6Al4V alloy. Moreover, the low density, high specific strength, and corrosion resistance of Ti6Al4V alloy is widely investigated by experiments, which are available in the literature, and are beneficial for the numerical models' verifications in the presented research.
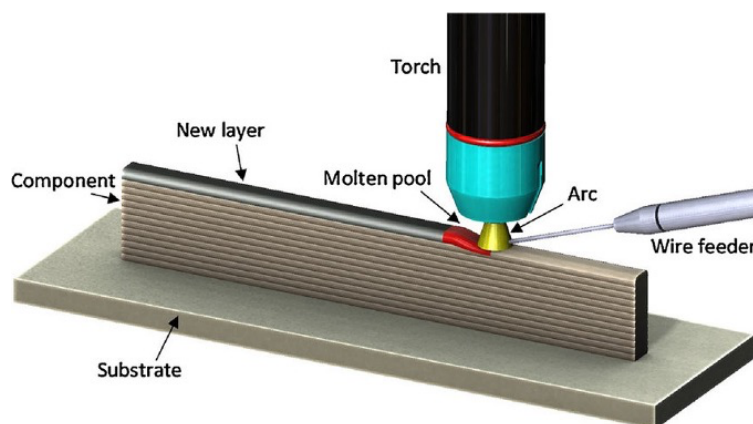
Figure 1.1 AM process (Wire+Arc AM) [9].

Figure 1.2 Process – induced (casting) defects due to layer-by-layer manufacturing [10].
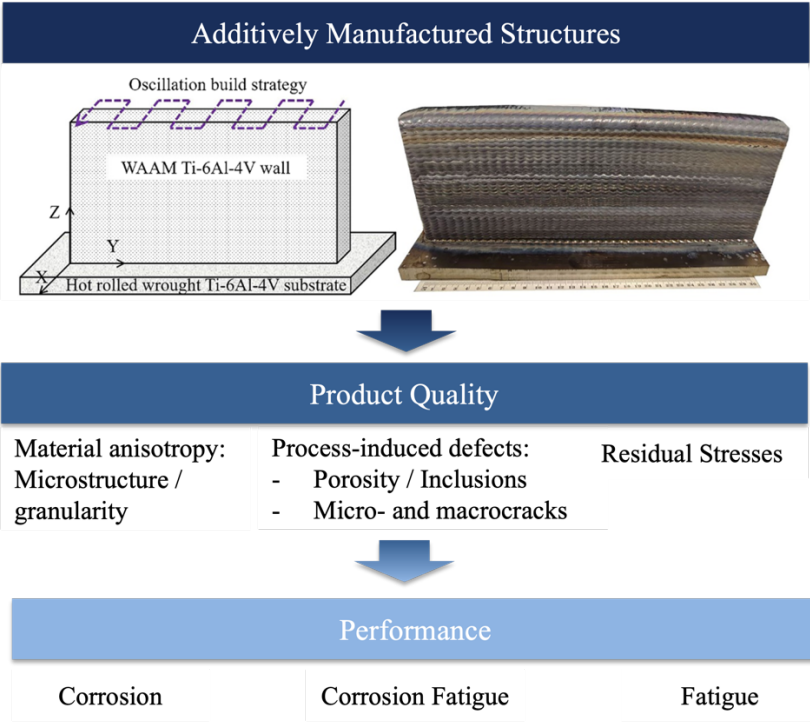
Figure 1.3 Product quality due to layer-by-layer manufacturing. Schematic of WAAM [10].

Looking at additively manufactured components many studies have been carried out, where some experimental studies showed the existence of process-induced defects, as shown in Figure 1.2, and the differences in the product quality of the structures produced by Additive Layer Manufacturing (ALM), which can influence the fatigue performance of the additively manufactured parts [10–13]. Firstly, the variations in the

microstructure and the material properties (layer quality) were reported [14, 15]. Secondly, layer-by-layer manufacturing results in material anisotropy [16], process-induced defects [10, 12, 17, 18] and Residual Stresses (RS) development [19]. All these quantities influence the fatigue performance of the material, as summarized in Figure 1.3.

The common practice to evaluate the performance of newly built additively manufactured structures is to perform the experiments. The experiments provide a good insight into the material microstructure and properties. On the other hand, it is a time-consuming and expensive procedure that limits the broader understanding of the performance and possible cause of failure due to the complexity of the additively manufactured material. On the other hand, numerical modelling is an excellent alternative to material performance predictions. Utilizing the numerical tool, the role of different variables on fatigue performance can be analysed, and the combination of multiple factors, like porosities and granularity can be investigated. Moreover, looking at more complex processes like environmental fatigue (Corrosion Fatigue (CF)) can be an even greater concern among engineers. The corrosion-resistant alloys used in various industries and structures (aircraft, vessels, power plants, bridges etc.) can result in catastrophic failures in corrosive environments, especially marine environments. In combination with the fatigue loading conditions, the Stress Corrosion Cracking (SCC) belongs to the group of the most dangerous environments for metal failure. The primary difference between CF and SCC is that static tensile loading is responsible for SCC, while CF is defined as environmentally induced crack propagation due to cyclic loading. If there is no influence of SCC on Fatigue Crack Growth (FCG), then CF is named as True Corrosion Fatigue (TCF). The combination of TCF and SCC can be schematized by a diagram shown in Figure 1.4. Moreover, metal, subjected to lower frequencies and higher load ratio of fatigue can experience the SCC mechanism [20]. The process and subdivisions of CF and SCC are described in Chapter 2.5. The models for CF predictions in Chapter 2.5 are mainly based on experimental data and parameters identification based on experimental results.
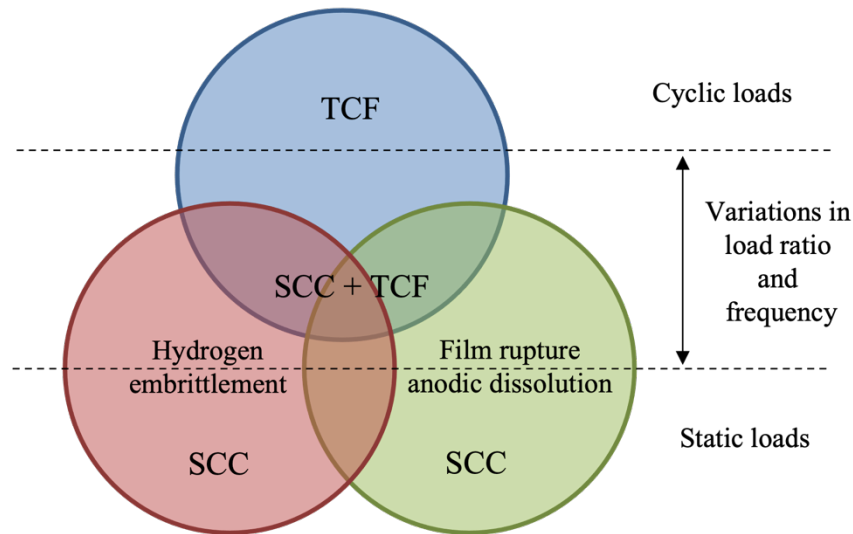
Figure 1.4 Interdependence between CF and SCC (modified from [20]).

Numerical tools are widely used for material behaviour prediction and progressive failure analysis, as will be discussed in Chapter 2. Various techniques are available for failure mode prediction within the framework of classical (local) and nonlocal theories. Finite Element Method (FEM) is a very commonly used tool for failure analysis which is based on the partial differential equations of Classical Continuum Mechanics (CCM). Therefore, FEM faces challenges in the problems involved with cracks and cannot address crack nucleation in a continuous material. Moreover, in the crack propagation problems, FEM suffers from inherent limitations, and re-meshing is required, becoming computationally costly. Additionally, to re-meshing, FEM requires the kinetic relation for the crack growth with the guidance of the crack direction and speed. Considering the shortcomings of FEM, the Cohesive Zone Elements (CZE) method and Extended Finite Elements method (XFEM) was introduced. CZE and XFEM eliminate the need to re-mesh but still require knowledge on the crack path. In the complex analysis of multiple cracks in the system, the methods which are based on the local continuum model, where the material point is influenced by the material points located in its immediate vicinity, are not practical. Instead, in the nonlocal continuum model (Peridynamics theory), the material point is influenced by the other material points located within the region of finite radius. The Peridynamics (PD) is basically the re-formulation of CCM theory but includes the Molecular Dynamics Model (MDM) as when the radius becomes infinitely large, and the nonlocal theory becomes the

continuous version of MDM. Because of the PD theory's nonlocal nature, the failure analysis involving the crack nucleation, crack propagation, and interaction between the multiple cracks is not problematic. Firstly, the concept of damage which is naturally present in PD formulation and will be discussed in Chapter 3, is beneficial in dealing with the process-induced defects due to AM, shown in Figure 1.2. Secondly, PD is a powerful tool for analysing the materials on macro, micro or nano scales, which gives an advantage on dealing with material anisotropy of AM structures. Lastly, the multiple physical fields can be treated within the same PD framework and utilised for a complex phenomena such as corrosion fatigue. In this study, the developed numerical models are based on PD and used to analyse the structural damage in additively manufactured Ti6Al4V alloy (considering microstructure, porosity, and RS) subjected to the fatigue loading conditions and exposure to the corrosive environment.

1.2   Aim and objectives of research

The aim of the research in this thesis is to predict fatigue, and corrosion of the 3D printed structures by exploiting a new computational methodology – Peridynamics.

The research described in this thesis has four main objectives:

- Creation of a numerical model based on PD theory to investigate the dual role of holes and micro-crack arrays on toughening and degradation mechanisms in structures. The study of the macro- and micro-cracks interaction problem is analysed to understand if the cracks suppress or enhance the crack propagation and what is the crack behaviour in the presence of micro- defects or defects as holes. This study is a starting point for developing porosities interaction in the fatigue nucleation and propagation problems, described in Chapter 5 and Chapter 6, respectively. To the best of the author's knowledge, there is currently no study available in the literature concerning the numerical analysis by PD of the crack arrest phenomena and the shielding effects of the various micro-cracks distributions and micro-crack interactions between each other. This goal is achieved in [21] and [22] as a part of the research described in this thesis (Chapter 4).

- Creation of a numerical model based on PD theory to investigate the effects of process-induced defects in additively manufactured structures on fatigue life. To the best of the author's knowledge, it is the first time of the numerical implementation by means of PD the porosities in the samples which are subjected to cycling loading conditions. The study includes an analysis of critical porosities in the structure and the assessments of the effects of the pores interactions on the fatigue life. The results of this study have been published in [23] and presented in Chapter 5.

- Creation of a numerical model based on PD theory to investigate the microstructure, porosity, and RS on the Fatigue Crack Growth Rates (FCGR). All three main factors that decrease the performance of additively manufactured materials are analysed in Chapter 6. To the best of the author's knowledge, it is the first time PD is used for: 1. modelling and fatigue analysis of the columnar polycrystal structure as a result of ALM; 2. combined problem of modelling polycrystals and porosities in the additively manufacturing structures and analysing their effects on the fatigue behaviour, 3. numerical modelling of the RS in the material using the parabolic temperature profile and the investigation of the impact of RS on fatigue crack propagation. The results of these studies have been published in [24] and [25].

- Creation of a numerical model based on PD theory to investigate CF (Chapter 7) for FCG problems. To the best of the author's knowledge, it is the first time PD has been used to develop such complex phenomena. The results of this study have been published in [26].

Each of the described objectives are steps to reach the main aim of the research, where the first focus of numerical PD models are on fracture mechanics problems, then followed by fatigue and after corrosion problems, and finally predicting the complex phenomena – CF. The overview of the steps of each part of the research is visualized in Figure 1.5.
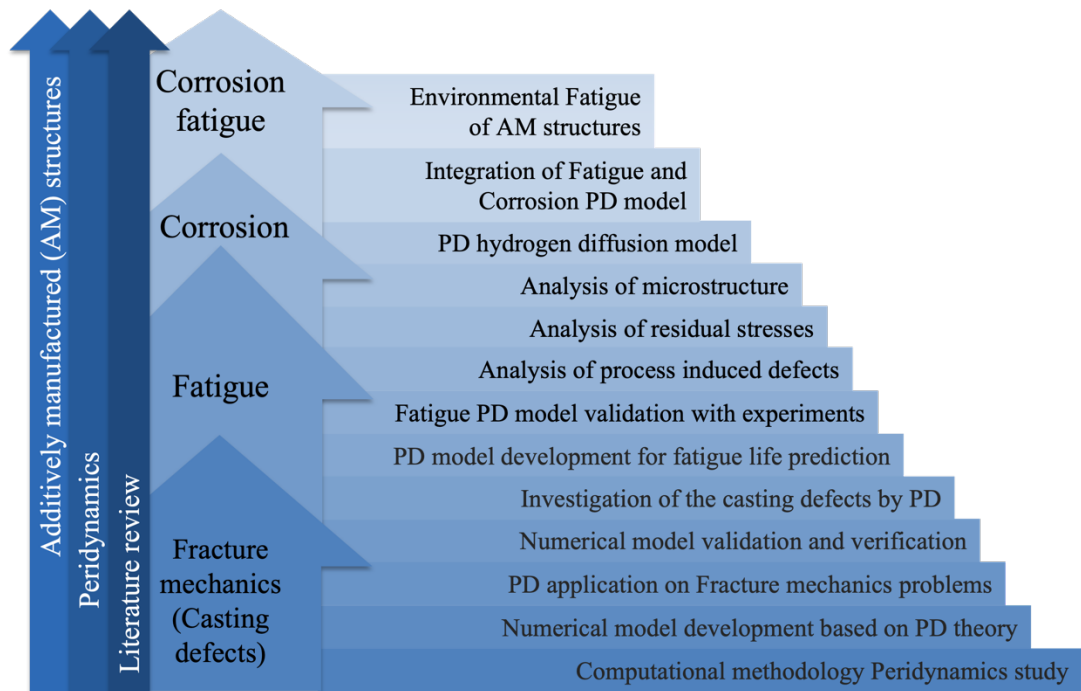
Figure 1.5 Thesis roadmap.

1.3   Thesis structure

The following eight chapters constitute this thesis:

- Chapter 1. This chapter provides a basic overview of the AM, the drawbacks in the material due to the layer-by-layer manufacturing and the response of the structures to the fatigue and the CF environment. In this regard, the objectives of this research and the thesis structure are described.

- Chapter 2. This chapter provides an overview of the most popular techniques for brittle fracture predictions under various loading conditions (static, dynamic, fatigue) and the limitations of these methods. Moreover, an introduction is given to the fatigue and CF failures and the response of the additively manufactured structures to the mechanical and environmental loading conditions. Finally, the major contributors to the fatigue performance of the additively manufactured structures are discussed (granularity, porosity, RS), pointing to the main problems in the 3D printed structures considered in this research.

- Chapter 3. This chapter describes the numerical approach (PD) used for the problems investigated in this research.

- Chapter 4. This chapter presents an in-depth investigation of the stretch based failure criterion in Ordinary State-based PD for both static and dynamic conditions. Also, analysis is performed on the dual role of holes and micro-crack arrays on toughening and degradation mechanisms in brittle structures. For the study of the macro- and micro-cracks interaction problem, various cases of the micro-crack distribution and inclination angles are considered and validated with analytical studies.

- Chapter 5. This chapter focuses on evaluating the effect of the pores in Ti6Al4V dog-bone samples produced by AM. The methodology is proposed to model the PD fatigue model's pores and estimate the fatigue life reduction due to the internal pores. Furthermore, a numerical approach is presented to assess the critical pore characteristics and the influence of the pore location and size on the fatigue life of Ti6Al4V. Finally, the results are discussed and compared with experimental data available in the literature.

- Chapter 6. This chapter evaluates the effect of the process-induced imperfections of AM, like microstructure, pores and RS on the fatigue resistance and crack growth behaviour. A new approach is proposed for RS implementation in the PD, and the crack growth rates are compared with experimental data available in the literature.

- Chapter 7. This chapter describes the PD model of CF and its mathematical formulation. The analysis is performed for wrought and additively manufactured Ti6Al4V alloys, and the numerical prediction of the fatigue performance of the metals in the corrosive environment is compared to the experimental data available in the literature.

- Chapter 8. This chapter summarised the major findings and the contributions of this research, followed by the recommended future work.

2   LITERATURE REVIEW

2.1   Introduction

This chapter summarises the literature review undertaken for the realisation of the research on fatigue and corrosion problems. The discussion in the thesis is about the fracture as the body's response to externally applied loads or the body's response due to the temperature gradients and/or aggressive environments. The fracture process involves the initiation and the propagation processes, which will be discussed in the next Chapters. Overall, the discussion within the chapters will be on the body (plate), which consists of macro- and/or micro-cracks and/or pores. The focus is on the material's resistance to crack nucleation and/or propagation. The typical description of the mechanical state in the deformative body containing a crack includes the geometrical configuration of the body, an empirical relation between the internal stresses and deformations, and the balance law of physics. Irwin [27] introduced the Stress Intensity Factor (SIF), K, which characterises the stress field in the vicinity of the crack tip, as shown on Figure 2.1, and the stresses close to the crack tip can be written in the following form [27]:

$$\sigma_{ij} = \frac{K}{\sqrt{2\pi c}} f_{ij}(\vartheta) \tag{2.1}$$

where c and ϑ are the polar coordinates and functions $f_{ij}(\vartheta)$ are:

$$f_{xx}(\vartheta) = \cos\left(\frac{\vartheta}{2}\right)\left[1 - \sin\left(\frac{\vartheta}{2}\right)\sin\left(3\frac{\vartheta}{2}\right)\right]$$

$$f_{xy}(\vartheta) = \cos\left(\frac{\vartheta}{2}\right)\left[1 + \sin\left(\frac{\vartheta}{2}\right)\cos\left(3\frac{\vartheta}{2}\right)\right] \tag{2.2}$$

$$f_{yy}(\vartheta) = \sin\left(\frac{\vartheta}{2}\right)\cos\left(\frac{\vartheta}{2}\right)\cos\left(3\frac{\vartheta}{2}\right)$$
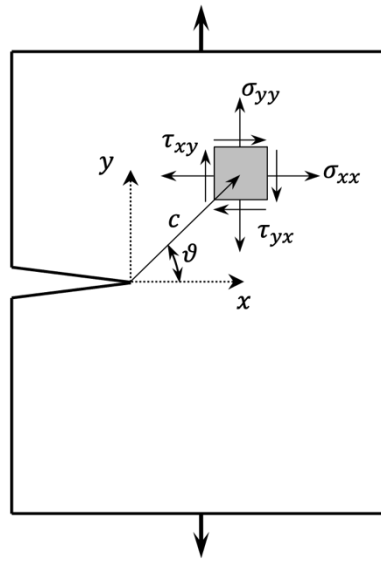
Figure 2.1 Irwin's SIF [27].
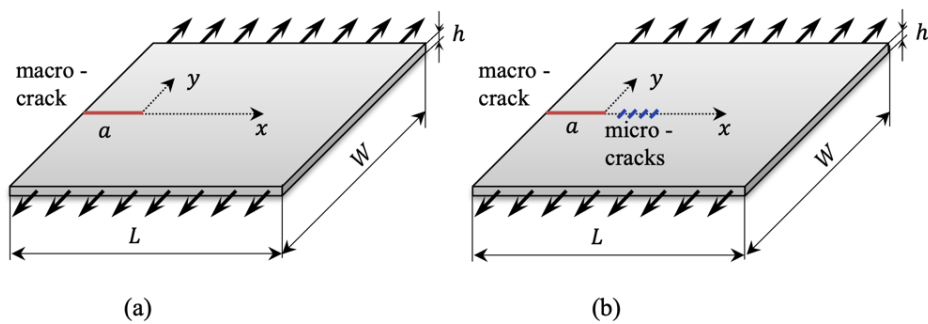
Figure 2.2 Plate under tensile loading with: (a) single macro-crack; (b) macro- and micro-cracks.

SIF depends on the specimen geometry, the applied load and the existence of micro-cracks if any. The general solution of SIF for three modes of loading (Mode I: opening mode; Mode II: in-plane shear load; Mode III: out-of-plane mode, shear load) is given as:

$$K_{(I,II,III)} = \sigma\sqrt{\pi a}f(L,a) \tag{2.3}$$

where σ is the characteristic stress and $f(L,a)$ is a function of the geometry dimension and crack length, as shown on Figure 2.2.

The research on the interaction of macro-crack with micro-cracks is introduced in Section 2.2, where K_0 is the SIF in a plate with a single macro-crack, as shown on

Figure 2.2a, and K_I is the SIF in a plate with a macro- and micro-cracks, as shown on Figure 2.2b. Additionally, Section 2.2 gives an overview of the most popular numerical methods for structural damage predictions. Then, Section 2.3 explains a general introduction to fatigue, the fatigue life and FCG predictions, and the numerical tools for fatigue damage predictions. The additively manufactured structures are discussed in Section 2.4, and the major contributors to the fatigue performance are introduced. Next, the literature review is undertaken on the three main factors (granularity, process-induced defects and RS) that affect the structure's fatigue response. Lastly, the CF models are discussed in Section 2.5, followed by a summary of this chapter.

2.2 Numerical fracture analysis in brittle materials

The problem of damage prediction in the structure has attracted significant interest in the literature. A significant number of studies [28–32] indicated that a slight overload could induce brittle fracture when a crack initiates at the point of maximum stress and then propagates. Quite a lot of focus is on brittle fracture because it can happen very fast and bring massive damage to structures. Instead, ductile fracture occurs over a period of time and at higher stress levels than brittle fracture. Additionally, many metals that are ductile under the effect of temperature can exhibit brittle fracture. For example, titanium alloys change from ductile to brittle fractures at decreasing temperatures of around -40 degrees [33]. The crack development through the structure depends on the loading conditions, and a crack can propagate as a single crack, change its original trajectory, or split into two or multiple branches [28]. Several experimental studies have been performed and reported [2–7] to analyse the fracture behaviour in the literature. Very high crack propagation speeds, approaching the speed of sound in the material, are observed during the experiments [29]. Such behaviour is called fast fracture when a sudden failure occurs in the structure with a rapid crack growth after crack nucleation. Theoretically, the Rayleigh wave speed is the limiting speed for tensile failure. Moreover, the experimental results [30] show that crack instability occurs at speeds lower than Rayleigh wave speed, and micro-branching occurs at critical velocity. Before branching occurs, an increase in fracture surface roughness is observed [31, 32], and after branching, the crack propagation speed reduces by 5 to 10% [29]. Although

experimental fracture analyses are very valuable, experimental tests can be costly, and laboratory experiments have to be carefully controlled to obtain accurate results. A significant number of numerical models, as shown in Figure 2.3, are developed to predict structural damage. The most popular approaches are the FEM and XFEM.

FEM is the most common numerical tool for fracture problems and is based on Linear Elastic Fracture Mechanics (LEFM). However, the applicability of the FEM on fracture mechanics problems showed difficulties in the treatment of singularities in discontinuous stress and strain fields. Furthermore, additional difficulties with FEM are found when modelling propagating cracks. FEM requires external crack growth criteria and prior knowledge of crack propagation direction and speed [34, 35]. Commonly, the crack path is assumed to be a straight line, and as the crack propagates, re-meshing procedures are implemented. This process can be computationally expensive and problematic for elastic-plastic materials, where stress and strain are history-dependent. CZE model can be used in FEM to model the fracture behaviour and to represent the damage zone that develops near the crack tip. CZE model was initially developed for crack formation and growth in concrete [36], but later on was used for Fibre Reinforced Polymers, PMMA, and steels, as discussed in [37]. But one of the drawbacks of the CZE model is the fine mesh which has to be used for the analysis in order to capture the softening ahead of the crack tip. Using the very fine meshes in the models can result in high computational costs [37].

Instead, XFEM was developed to overcome problems, including mesh-dependency [38, 39]. XFEM has been applied to various problems [40–43] and has become a good alternative to the CZE model. However, in XFEM, local mesh refinement is necessary before each propagation step, and the branching point has to be identified from the stresses, which sometimes makes the technique inefficient [42–46].
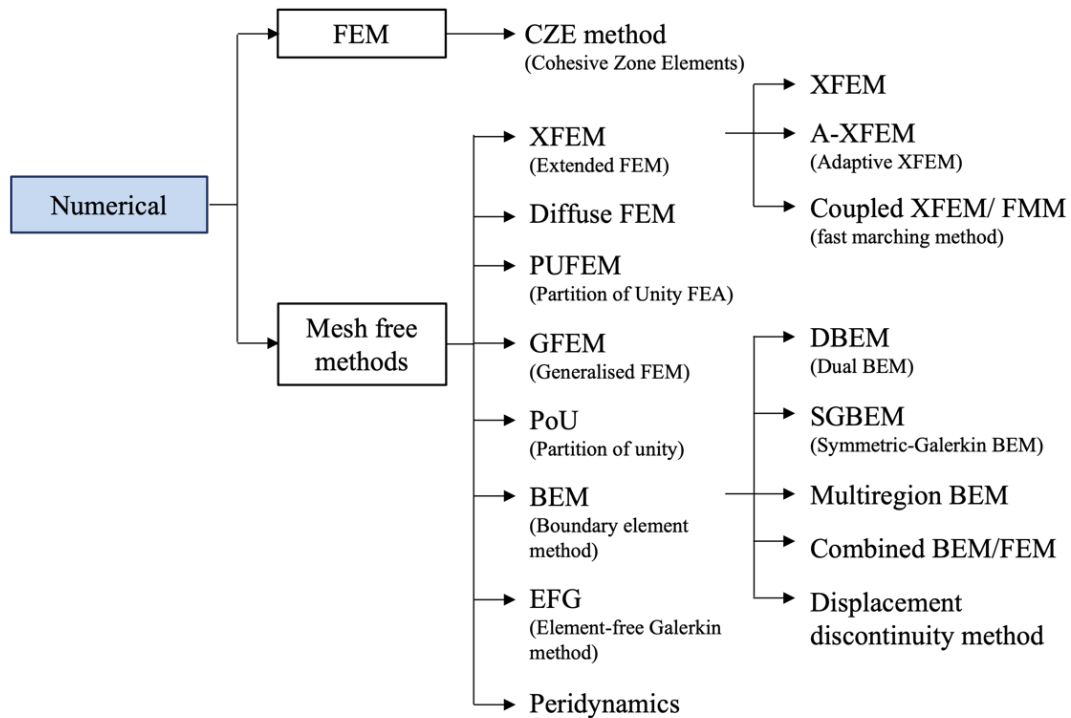
Figure 2.3 Overview of the numerical methods for structural damage predictions.

Additionally, brittle materials, such as concrete, ceramics and rocks, can consist of randomly distributed small-size defects such as voids, micro-cracks and holes [47]. These defects can have significant influence on the propagation behaviour of macro-cracks. Various experimental studies in the literature investigate the interaction between macro-cracks and small-size defects [48–51]. Different studies suggest that the existence of micro-cracks can lead to "micro-crack toughening phenomena" [52–54]. Micro-crack presence can act as the suppressors of the macro-crack propagation and contribute to the increase of the fracture zone [55]. Moreover, depending on the distribution, distances, sizes and inclination angles of micro-cracks, micro-cracks interacting with a macro-crack can lead to stress shielding effects with the decrease of SIF [47, 53]. Multiple analytical studies were performed for problems with a single micro-crack ahead of the main crack [56], the interaction between the main crack with multiple micro-crack arrays [53] and the surrounding micro-cracks [57]. The applied methods analyse the stress fields ahead of the crack tip, characterised by K_0 for the models with a single macro crack, and K_I – SIF for various distributions of micro-cracks, as shown on Figure 2.2, and describe the macro- and micro-crack interaction

by using the parameter K_I/K_0. The parameter K_I/K_0 is helpful to identify if micro-cracks enhance or suppress the macro crack propagation and is very useful for understanding the complex structural behaviour with defects. Besides, when the plate consists of both macro- and micro-cracks, micro-cracks can have influence on the main crack propagation behaviour where the main crack follows the orientation of micro-cracks. The macro- and micro- crack interaction problems will be further discussed and visualised in Section 4.3. The CCM based approaches were used to solve the complex problems of crack interactions, but assumptions were made to simplify the problem. For example, analytical calculations include only the interaction of the main crack with micro-cracks, but the mutual interaction between the micro-cracks is neglected [58, 59].

On the other hand, the studies of the crack-hole interaction (the hole radius is $\leq$ $0.005\ m$) resulted in the momentary crack-arrest phenomena [60, 61]. These studies showed that the fracture in the specimen was momentarily interrupted for several microseconds, then reinitiated usually with the increased crack propagation speed. Such behaviour is noticed in the structure when the hole defects are present ahead of the propagating crack. The location and dimensions of the holes, loading rates have an effect on whether propagation of the crack can be stopped, or it can propagate through the holes. It was investigated that when the hole lies eccentrically at some distance from the axis of the main crack, the propagating crack deflects towards the hole and then recovers its initial trajectory. As concluded by authors in [60], the asymmetry of the stress field in the area of the hole resulted in the curvature of the propagating crack, as will be discussed in Section 4.4 and showed on Figure 4.17, with the crack arrest phenomena. The change of the parameter K_I/K_0 was also discussed in [62] by mentioning that the values of the SIF are increasing during the crack arrest period. An integral equation approach was proposed in [63] to investigate the hole-crack arrangements and stated that the distribution of holes could also lead to toughening phenomena in the structure. Therefore, the sizes and distribution of the holes have a major impact on stress reduction or amplification.

Using the numerical approaches, like FEM and XFEM, on the problems involving microcracks, voids, interactions between micro- and micro-cracks can not always be

viable. The limitations in the mathematical formulation and assumptions that the solid remain continuous as it deforms, the numerical models based on CCM become invalid in the presence of cracks in the system [64].

As an alternative approach, to overcome the limitations of CCM models, PD was introduced by Silling [65] and demonstrated success in modelling dynamic fracture problems. For material failure predictions, integration, rather than differentiation, is used to calculate the total force-density acting on each material point and spatial derivatives are not used in the formulation. PD formulation allows dealing with complex crack interaction problems where multiple cracks of arbitrary shapes can be introduced in the structure. PD model does not require crack tip tracking and specification of the crack behaviour when the crack changes its direction or crack branching occurs. This is the reason why PD is chosen for this work, where crack initiation and propagation with discontinuous concentration fields are expected. A more detailed overview of the PD method can be found in Chapter 3.

2.3 Fatigue behaviour

Fatigue failures can be a severe problem, and multiple studies, as summarized in [66], provide convincing evidence that mechanical failure of the structures occurred due to fatigue. The phenomenon known as fatigue is the failure of the material due to the repeated application of loads. The discovery that the fatigue damage depends on the amplitude of the cyclic stress was discovered by Wöhler [67]. Wöhler was the first to understand the importance of the stress amplitude and the mean stress on the fatigue resistance of the material. When the tests or analysis is performed on the material's life, the specimen is subjected to a sinusoidal load and cycling between two extremes of stresses σ_{max} and σ_{min}, as shown in Figure 2.4. The parameters to identify the cyclic loading are specified by stress amplitude σ_a and mean stress σ_m in the following way:

$$\sigma_a = \frac{\sigma_{max} - \sigma_{min}}{2} \tag{2.4}$$

$$\sigma_m = \frac{\sigma_{max} + \sigma_{min}}{2} \tag{2.5}$$
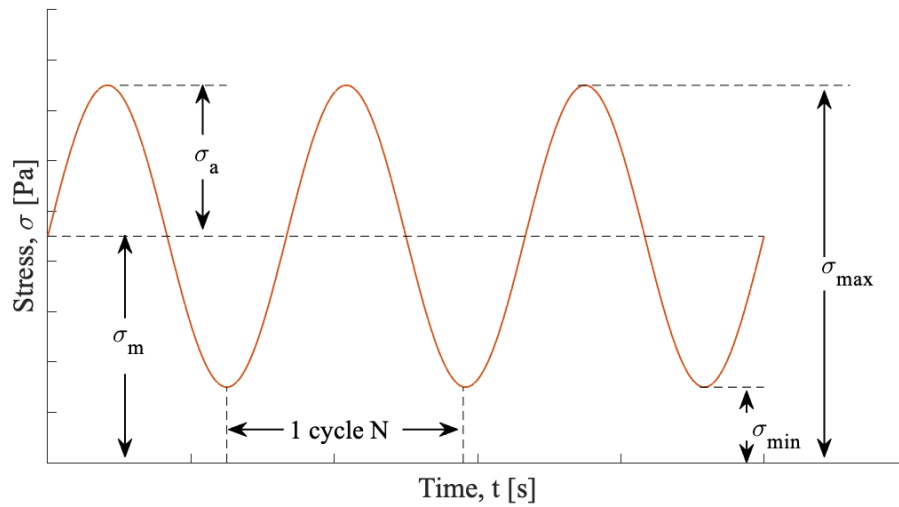
Figure 2.4 Fatigue loading curve.

Moreover, the stress ratio R is used to indicate the variations in stresses:

$$R = \frac{\sigma_{min}}{\sigma_{max}} \tag{2.6}$$

For example, if $R = 0$, this means that pulsating tensile stress is applied and $\sigma_a = \sigma_m$, or if $R = -1$ the test is performed with $\sigma_m = 0$.

The purpose of finding out the fatigue life is to appropriately select the material to meet the specific end-use requirements. The fatigue mechanism is usually split into three stages: crack initiation, propagation (growth), and final failure. There is a differentiation of each of the stages due to the conditions (e.g. surface effects, environmental conditions, material bulk properties) that can affect one of the stages but can be neglected on another one. Moreover, each of the stages represents the particular behaviour of the material, as shown in Figure 2.5 (Phases of material response) under the cyclic loading. During the initiation phase, the damage nucleation with activation of plastic slips occurs with further formation of Mechanically Small Cracks (MSC). After the FCG process starts with the growth of MSC into macrocracks until the final failure. The MSC or microcracks can be described with dimensions of $3\mu m < microcrack < 300\mu m$, as defined by researchers [20]. More detailed summary of the processes occurring in the material due to fatigue can be found in [20].
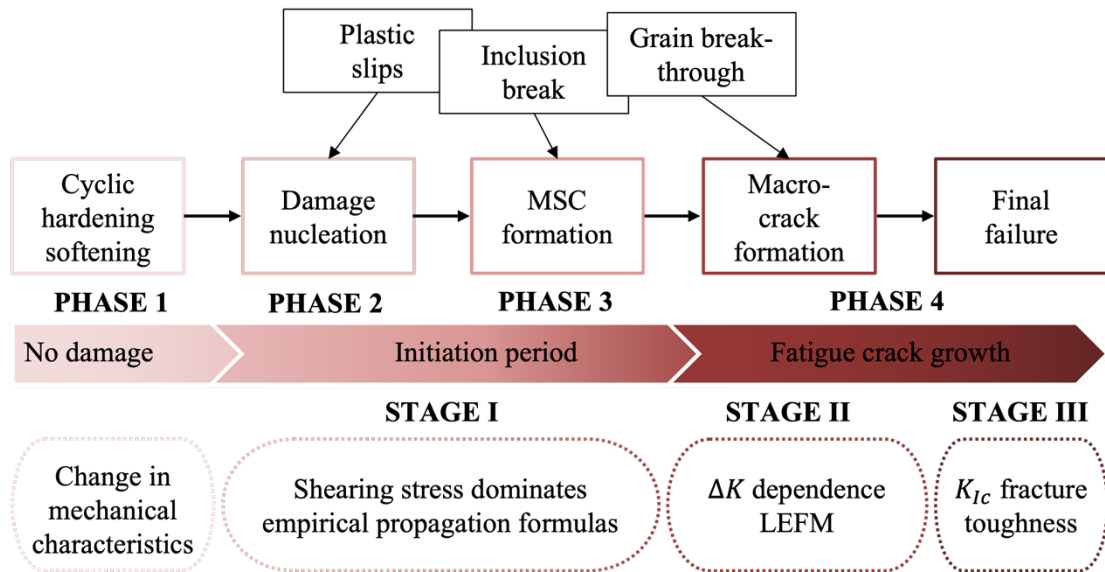
Figure 2.5 Stages and Phases of fatigue that characterise fatigue crack initiation and growth periods [20].

2.3.1 Stress-Life (S-N) curve assessment

Wohler [67], in 1870, after multiple studies on fatigue damage, concluded the dependency of the material failure on the amplitude of cyclic stress, as discussed in Section 2.3. During his work, Wohler understood the role of the stress amplitude on the fatigue resistance of the material and came up with the idea of presenting those dependencies in Wohler`s diagram or S-N curves. S-N curve is a graph of the magnitude of cyclic stress amplitude, σ_a, against the cycles to failure, N (in logarithmic scale), as shown in Figure 2.6. The number of tests have to be performed with different loading amplitude and identical stress ratios to build one S-N curve. Each test is a scatter point at the S-N curve plotted as a stress amplitude versus the number of cycles to failure.

Each scatter point is the fatigue life which is expressed by the number of stress cycles required for crack initiation, propagation and final failure of the samples. During the tests, when material is subjected to cyclic loading conditions, the fatigue limit or endurance limit can be identified. The aim is to find out the fatigue endurance limit, σ_e, or fatigue limit of the material, which is the value of the stress below which the material can withstand the unlimited number of stress cycles (infinite life). Fatigue endurance limit is identified for the material which can operate for a defined number

of cycles. Instead, fatigue limit can also be defined during the tests, which is the identified load limit below which the material has infinite life. Depending on the structural applications of the titanium alloy and what type of fatigue loading the material is exposed to, the material production process, chemical composition, post-processing, and the response to fatigue loads have to be taken into account [20]. For example, from the microstructure perspective, crystallographic texture, grain size, phase dimensions, and age hardening conditions affect fatigue life [68–70]. The Ti6Al4V fabrication process can result in different crystallographic textures [68], and fabrication by thermomechanical powder consolidation and subsequent heat treatment resulted in an endurance limit of around $530\ MPa$ [69], compared to the pressed and vacuum as-sintered Ti6Al4V alloy with an endurance limit of $430\ MPa$ [71], which are tested at $R = 0.1$. Therefore, it is important to specify the loading ratio R, as the samples tested at $R = 0.5$ has higher endurance limit compared to the samples tested $R = 0.1$ [68]. This means that load type, also load frequency, and type of the test (e.g., tension-tension, tension-compression, bending, rotational bending) have an effect on the fatigue limit of the material [20]. Another important parameter is the surface treatment, where the mechanical surface treatments (short peening, laser or ultrasonic shock peening, deep rolling) increase the High Cycle Fatigue (HCF), strength of Ti6Al4V by at least 10% relative to the Ti6Al4V without treatment [72]. The researchers in [72] indicated that combined laser shock and glass shot peening treatment of the Ti6Al4V samples resulted in the best fatigue outcome with increased fatigue performance by 17.2%.

Additionally, the S-N curve can be split into three characteristic regions: Low Cycle Fatigue (LCF), HCF, and the region of infinite life. The fatigue response of the material is cyclic load-dependent and the phases, shown in Figure 2.5, occur in different regions of the S-N curve. The S-N curve in Figure 2.6 is the characteristic curve for titanium and steel in benign environmental conditions. Instead, aluminium, copper alloys, and magnesium do not have well defined endurance limits, and the S-N curve is continuously decreasing. For example, in the LCF region, the material softens or hardens, with the dependency of the process on dislocation motion of crystallographic plates, where the entire section of a specimen is exposed to plastic deformations. On

the other hand, at the HCF, the shear stresses of the specimen can also be the cause of plastic slips with damage initiation at the grains, and the damage can develop at the surface of the specimen.
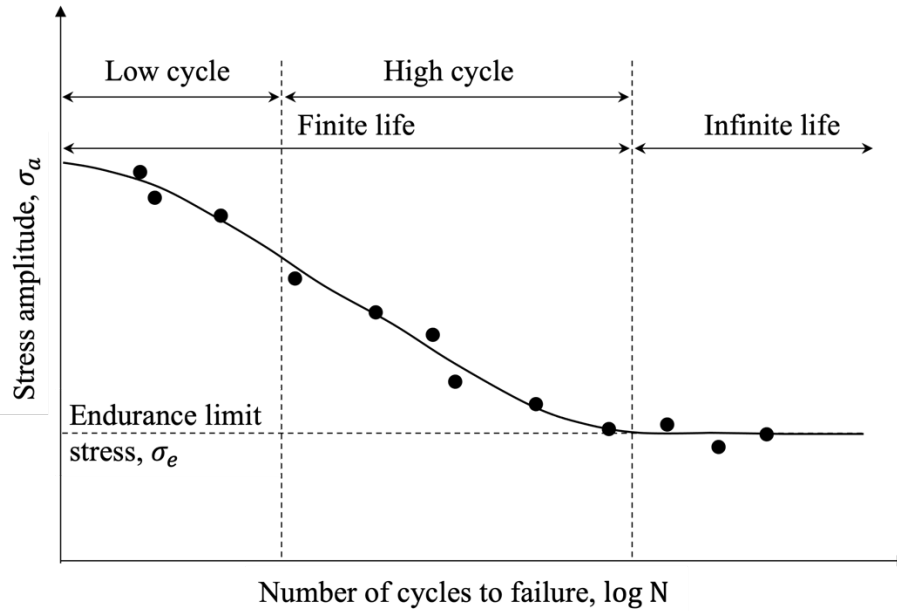
Figure 2.6 S-N curve.

2.3.2 *Fatigue crack propagation assessment*

As described in Section 2.3, the fatigue failure in a structure can be described by three stages: crack nucleation, propagation, and final failure. With this in mind, the structure's life should also be split into two parts: number of cycles to crack initiation and number of cycles to crack propagation until failure. Commonly researchers used those fatigue failure split in their studies, and when the dimensions of the micro-crack do not exceed $300\mu m$, the stage of damage nucleation is investigated.

Hobson [73] proposed the following relation on the micro-crack growth rate:

$$\frac{da}{dN} = A(\Delta\sigma)^n(d-a)^{1-\alpha}a^\alpha \tag{2.7}$$

where da/dN is the Fatigue Crack Growth Rate (FCGR), which is defined as the crack size increment da during the increment of corresponding cycles dN. a and d are the micro-crack length and grain dimensions, respectively. α, A and n are the material constants and $\Delta\sigma$ is the applied amplitude. For each material, several tests have to be

performed to identify the material constants, and Hobson [73] and Chopra [74] obtained the constants for carbon steels and aluminium alloy. Once micro-crack reaches the dimension of $300\mu m$, the crack is described as macro-crack and the crack propagation process occurs. This stage of the FCG phenomena is introduced by Irwin [27], who provided a powerful tool such as the Irwin SIF, K, where for the material under the static or monotonic loading, the stresses at the crack tip are proportional to SIF:

$$K = f\left(\sigma, \sqrt{a}\right) \tag{2.8}$$

where σ is the applied stress and a is the crack length. In the infinite plate the general solution of SIF is in Eq. (2.3), which for Mode I can be expressed as:

$$K_I = \sigma\sqrt{\pi a} \tag{2.9}$$

This means that crack tip stress is independent of geometry, and the intensity varies depending on the applied stress and the crack length. However, this approach assumes the ideal linear elastic behaviour of the material. This statement is the fundamentals of the LEFM, where the elastic stress field exists in front of the crack and is always self-similar. Even if the plastic zone is presented in real materials, but is less than 1mm, it can be neglected, and the SIF can be described as in Eq. (2.9). If the cyclic plastic zone is very small, then the crack tip is defined by K and the crack growth rate is characterised by K_{max} and K_{min}.

To predict the FCGR in the structures, Paris [75] demonstrated that FCGR depends on the applied SIF range, $\Delta K = (K_{max} - K_{min})$:

$$\frac{da}{dN} = f(\Delta K, R) \tag{2.10}$$

And after multiple number of tests, Paris discovered the power-law relationship that the FCGR are linear in a log-log scale versus ΔK, as shown in Figure 2.7 (Region II) and is widely known as Paris law or Paris-Erdogan equation in the following form:

$$\frac{da}{dN} = C\Delta K^M \tag{2.11}$$

where C and M are the material characteristics.
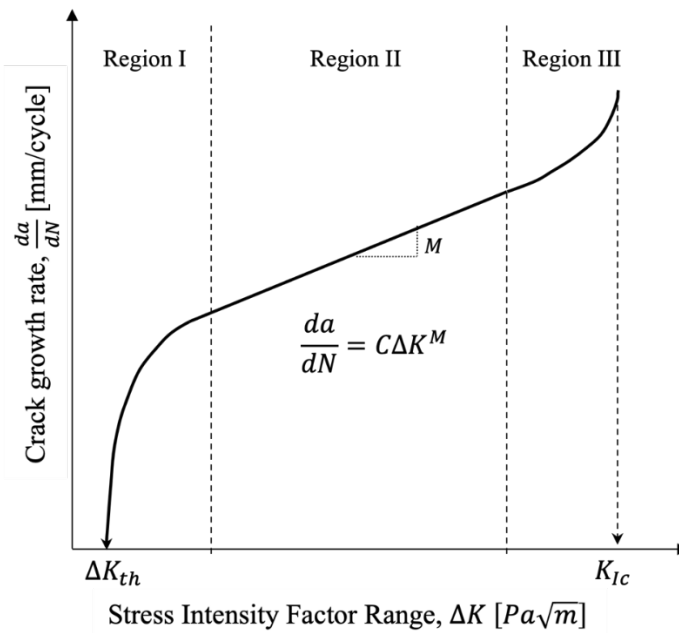
Figure 2.7 General behaviour of FCGR versus ΔK for metals.

As shown in Figure 2.7, the sigmoidal curve is the typical trend of da/dN versus ΔK. The Region II is the linear growth, governed by Paris law, Region I is the threshold zone, where the characteristic threshold of SIF ΔK_{th} under which the crack will not propagate if $\Delta K < \Delta K_{th}$. The Region III is where the crack growth is accelerated and when SIF approaches the toughness of the material K_{IC}, then the final failure occurs.

2.3.3 Fatigue damage prediction methods

There are a lot of models that are used for FCG predictions. The simplest way is the fatigue life predictions based on the material characteristics and the crack growth determined by the constant sinusoidal loading under different stress amplitudes, as discussed in Section 2.3. Paris and Erdogan [75] discovered the power-law relationship, represented by the SIF, and multiple refined models were introduced [76–81]. Paris law captures the linear part of $da/dN - \Delta K$ relationship, occurring in the Region II of the FCG curve, and the proposed refined models aimed to fit the entire sigmoidal curve, representing all three regions of curve. These models are based on linear damage accumulation and represent the LEFM, but the predicted curves are not accurate, especially for the variable amplitudes.

Fatigue experiments are a common practice of understanding the fatigue performance of the material but can be very time-consuming and expensive, so researchers looked at numerical tools for fatigue life predictions. As discussed in Section 2.2, FEM is the most common numerical tool for fracture mechanics problems. The researchers are utilising available commercial and non-commercial tools for fatigue life predictions, such as RANC2D [82], FRANC3D [83], ADAPCRACK3D [84], ABAQUS [85], ANSYS [86–89], with the following common crack growth procedure [85]: 1. define the initial crack geometries, 2. perform stress analysis, 3. calculate SIF for different crack opening modes, 4. predict crack growth direction (the direction of the incremental extension) by introducing the selected criterion, 5. determine the position of the new crack tip, 6. introduce of new crack faces, 7. re-meshing of the structure after the crack advance, 8. gain the relationship of the crack length and the SIF, 9. calculate the fatigue life by integrating the appropriate crack growth law (ex. Paris law). To predict the crack growth direction, the maximum principal stress criterion [90], where the crack growth is in the direction perpendicular to the maximum principal stress, is utilised, as well as maximum strain energy density criterion and minimum strain energy density criterion (S-criterion), where the direction of the crack growth at any point along the crack front is towards the region with the minimum value of the strain density factor [91]. For the crack growth direction under mixed-mode loading, the Maximum Tangential Stress (MTS) criteria is used, where cracks propagate along the radial direction, on which the tangential stress becomes maximum [92], and maximum Circumferential Stress (MCS) criterion and maximum Energy Release Rate criterion [93] are utilised. However, using FEM for FCG problems, FEM faces some difficulties in crack modelling, as the crack path has to be prescribed. Commonly it is assumed to be a straight line [54], re-meshing is required at each step of crack propagation which can result in expensive computational costs, due to the dense meshes [59]. FEM is not absolutely accurate for crack problems because of the stress singularities around the crack tip, which are not taken into account [90].

As shown in Figure 2.3, multiple mesh-free methods are developed to overcome problems in FEM for FCG analysis. In the used methods like Diffuse FEM [94],

Element-free Galerkin (EFG) [95, 96], Partition of Unity FEM (PUFEM) [97], Partition of unity (PoU) [98], Generalised FEM (GFEM) [99], XFEM [100], the cracks propagate along with the sets of nodes, where only mesh of nodes and a boundary description is needed, and the finite element mesh is unnecessary. XFEM is extensively used for the FCG, as it overcomes the problems in the re-meshing by introducing local enrichment functions to represent the discontinuity of the displacement across the crack lines [97]. In XFEM, the maximum principal stress criterion used to obtain the direction of the crack growth and domain-based interaction integral approach is used for SIF extraction, followed by a computation of the fatigue life utilising generalized Paris' law [101]. Also, developments are made for XFEM to improve the crack growth procedures, such as Coupled XFEM/ FMM (fast marching method) [102] and A-XFEM – Adaptive XFEM [103].

BEM is another common tool for FCG analysis, which is used to calculate the SIF and permits to simulate the crack propagation by adding new boundary elements along with crack extensions. The key feature of BEM is that only the boundary of the domain is discretised, which provides accurate results for stresses and no need for re-meshing the outer boundary during the crack growth [104–106]. BEM also follows the similar steps of the FCG model with the calculation of SIF, and selection of crack propagation law, the definition of crack growth parameters, crack propagation and calculating the fatigue life using Paris' law. BEM was improved by using the Galerkin weighted residual procedure for discretisation (Symmetric-Galerkin boundary element method (SGBEM)) [107] and intensively used Dual boundary element method (DBEM) [108–115], where the crack in the structure is presented by the "dual" elements that allow the stress and displacement fields to be computed on both crack faces without the need to subdivide the body along the crack boundary.

In all the developed finite element based methods and mesh-free methods, the problem arises of modelling the interaction of multiple micro- and macro-cracks in the structure and their effect on the FCGR. With the aim to overcome these limitations, a PD fatigue model is utilised. To the best of the author's knowledge, there is currently no study available in the literature concerning the PD modelling of the micro- defects

in the structure with the effect on the fatigue nucleation and propagation stages. This goal is achieved in [23] as a part of the research described in Chapter 5 and Chapter 6.

2.4   Additively manufactured structures

Metal AM is the newer field of AM technology, developed over the past 20 years, becoming a state-of-the-art manufacturing process of complex structural shapes [4, 116]. Titanium, aluminium, stainless steel and nickel super alloys are the most commonly used alloys in AM [7, 117]. Each of the materials has its applicability in different fields because of their mechanical properties, production challenges and costs. Titanium alloys Ti6Al4V are used in aerospace, energy, marine, automobile, biomedical and chemical industries [8] and are among the most attractive materials due to their outstanding combination of high specific strength, low density and corrosion resistance [118], good fatigue strength and quite good weldability [119], with the only drawback of its high cost of fabrication. Multiple studies, discussed in [118], are undergoing on AM of Ti6Al4V to reduce the manufacturing cost and widen its industrial applications. The studies' focus is on different Ti6Al4V AM process techniques, which could result in a good quality AM of fabricated metal with properties close to the standard cast and wrought product.

AM is the process which aims at building metallic parts layer-by-layer, as shown in Figure 1.1. The layered process provides flexibility and low-cost manufacturing of complex structures, which became more competitive than traditional manufacturing processes in the recent years [118]. Some of the most common techniques used for Ti6Al4V AM processes can be distinguished by the type of material used, like wires for the wire+arc AM (WAAM) (Figure 2.8) and the metallic powders for Selective Laser Melting (SLM) or Electron Beam Melting (EBM).
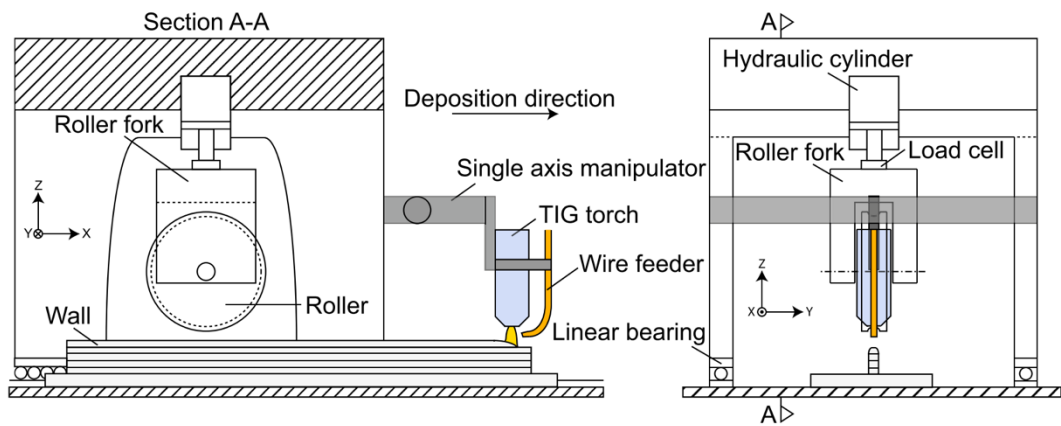
Figure 2.8 Principle of WAAM [120].

(a)   (b)
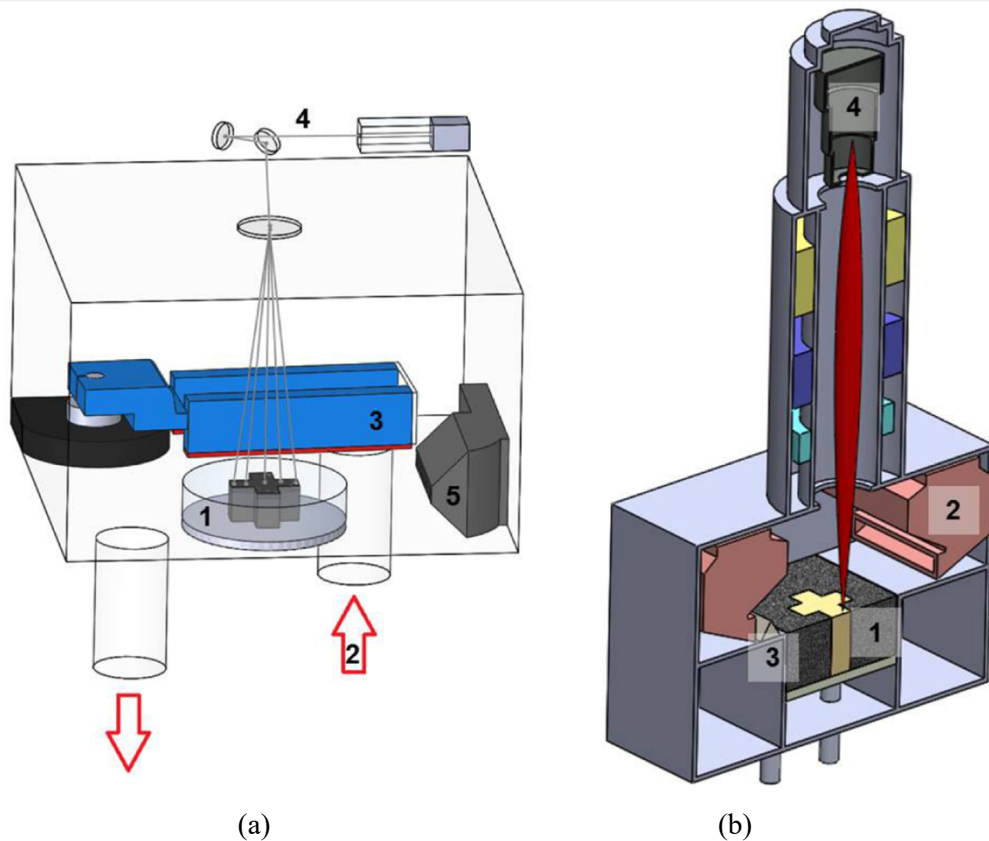
Figure 2.9 Schematics of (a) SLM and (b) EBM. The parts of the machines: 1. An object building platform, 2. A feed container, 3. A deposition unit, 4. A powder source, 5. An argon flow nozzle [121].

WAAM is a technique that manufactures parts by adding wire layer-by-layer, as shown in Figure 2.8. WAAM allows the building large size parts, but the surface quality and accuracy are not as good as those manufactured by SLM. The SLM process, shown

in Figure 2.9a, can result in a good surface finish, as the metal parts are usually created by melting metallic powder using a high-power-density laser. Therefore, SLM takes place in the chamber which contains the bed with controlled distribution of thin layers of powder. However, the bed dimensions limit the production capabilities, as the manufacturing of large parts would require large equipment with significant investments [121]. EBM is a process based on a layer of powder melting by an electron beam, shown in Figure 2.9b. The process is similar to SLM, where the powder is distributed on a platform, then it is melted, and the platform moves down; then another powder layer is distributed and melted and the process repeats until the desired part is built. The parts made by EBM also require high investments, but conductive metals and reflective alloys can be used in manufacturing[122].

All the AM processes require the designed 3D computer model, the processing steps, and the post-processing. The Computer-Aided Design (CAD) file is used for 3D part fabrication and the appropriate sensors are controlling the processing conditions. After the deposition process is over, the fabricated part requires post-processing operations, like chemical polishing, machining grinning and peening. The carefully controlled processing conditions such as a feed rate of the feedstock material, speed of the heat source and finishing operations can result in a desired product outcome [123, 124].

AM showed a great potential of titanium alloys manufacturing because of geometrical flexibility, repeatability, surface quality and productivity [7]. For example, manufacturing by SLM allows the production of complex geometries with high precision and the geometry output as one piece, which illuminates the production of multiple parts and their later assembly. Additionally, AM can be used to repair damaged, corroded, or worn-out parts. The AM technology has a high level of 3D precision, allowing parts identification and further addition of metal on damaged surfaces [118]. However, an important drawback of layer-by-layer manufacturing is the anisotropy of the material properties of the additively manufactured components [16]. The rapid and repeated heating and cooling of the AM process leads to variations in the microstructure, the properties (layer quality) and internal stresses in different regions [14, 15]. The variations in the microstructure occur due to the high-temperature

gradients, which are moving to the rapid solidification during the AM. Moreover, thermal gradients produce RS in the sample, and while the solidification of the layer mainly introduces the shrinkage of the sample, the 'printing' of the additional layer can change the RS from tensile to compressive and the other way around. The process of the rapid and repeated heating and cooling of layer by layer manufacturing is also resulting in variations of the RS where the stresses are larger in the scanning direction [19]. These quantities generally influence the fatigue performance of the material.

Another negative outcome of the AM is the occurrence of pores due to the powder [125] or wire [10] contaminations, vaporisation when the temperatures in the molten pool are very high [126], leading to the entrapped gases or vapours in the material [7]. Eventually, microstructure with the existence of pores that act as a strong stress raiser and RS impact the structure's performance under different loading conditions [127], especially under fatigue loading. Evaluation of the additively manufactured sample fatigue performance in the literature brought a lot of discussion on the crack initiation sites at the pores due to its drastic impact on the fatigue life, but the crack propagation profiles are more referred to the sample microstructure. Some test studies [19] indicated that pores did not have a great impact on the FCG of the samples with pores of a diameter of $d_p \leq 50 \mu m$. On the other hand, a review of fatigue performance of additively manufactured Ti6Al4V samples [128] mentioned the contribution of both the microstructure and the process-induced defects.

The rolling process is induced in WAAM, as shown in Figure 2.8, to overcome the issue of RS in the parts produced by AM [129]. The roller is placed behind the welding torch, and the rolling under the specified loads is applied as soon as the material solidifies [120]. The rolled WAAM has an effect on material granularity [120], as will be discussed in Section 2.4.2, and allowed to reduce the longitudinal RS [129] discussed in Section 2.4.3.

2.4.1   *Effects of the pores on fatigue life*

Due to the layer-by-layer manufacturing, the deposition process has to be carefully controlled as it could lead to entrapped gases or vapours in the material resulting in microscopic spherical pores [7]. Recent studies on WAAM and SLM, using in-situ X-

ray computed tomography scanning, evidenced the presence of the pores in the structures. The porosity volumes for each of the methods vary and are reported as 0.01-0.04% for WAAM [10, 11], as shown in Figure 2.10 and Figure 2.11, and 0.08-0.2% for SLM [130], shown in Figure 2.11. The variations of the porosity inclusions are the cause of cooling rates and temperatures of the AM process [120]. Pores are commonly observed in the regions of non-melted powder for SLM [125] and when the structure is manufactured with a contaminated wire during WAAM [10]. With this respect, it is essential to understand the cause of the mechanical property variations of the metal alloys produced by AM and the effect of porosities on Ti6Al4V fatigue properties.

(a) (b)
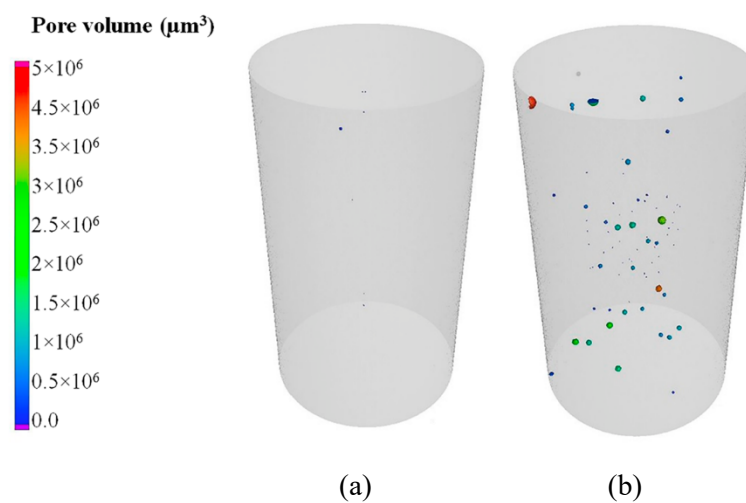
Figure 2.10 (a) X-ray computed tomography scan at specimen gauge section of the defect-free sample, density is 99.99%, and (b) wire+arc additively manufactured porosity specimen, density is 99.96% [10].

Additionally, the Ti6Al4V fatigue properties have significantly scattered experimental data. Besides, the pores in the structures have a significant influence on the fatigue life of additively manufactured samples. Experimental studies on Ti6Al4V fatigue properties showed that the crack nucleation starts at the process-induced pore and the lifetime to failure depends on location, size and pore volume [13, 19, 131–133]. Moreover, indicating the types of pores according to their location as on surface, subsurface and internal pores, the surface pores have a higher impact on the Ti6Al4V fatigue properties [11]. The surface roughness is the major drawback of the AM process, which limits fatigue performance. The studies [123, 124] showed that the post-processing of the samples increases the fatigue performance where the smoother

surface brings higher fatigue life. On the other hand, the surface pores or surface roughness can be removed by post-processing techniques, like chemical polishing, machining, grinding and peening. With the use of post-processing techniques and carefully controlled processing conditions, input parameters can avoid the surface pores and subsurface pores located in the vicinity of the free surface, specified as the most critical one [10, 134, 135]. It is important to note that crack initiation occurs at the areas with a more considerable amount of porosity or the pores located close to the free surface. Multiple tests [10, 12, 17, 18] indicated that the sub-surface pores are the dominant factor in limiting fatigue life. Also, the researchers identified the challenges for determining the additively manufactured Ti6Al4V fatigue properties, as layer by layer manufacturing results in heterogeneous microstructure and porosity defects distributions.
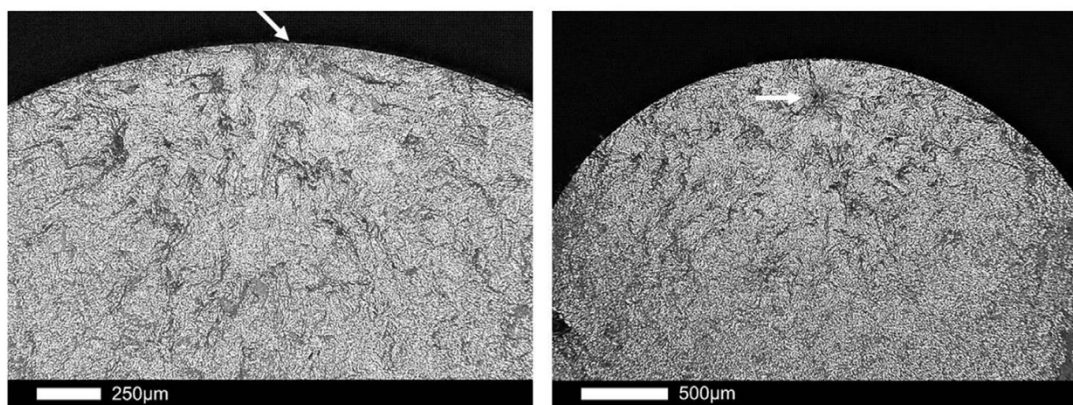
(a)
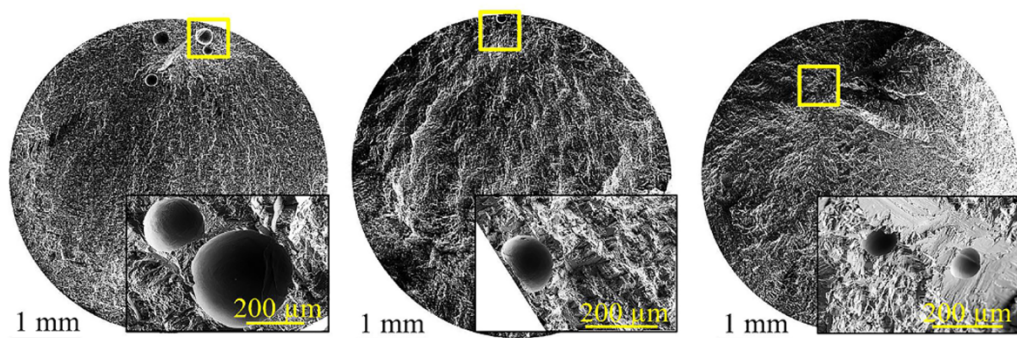
(b)

Figure 2.11 Damage initiation at pore locations for: (a) SLM [131] and (b) WAAM [10].

The porosities in Ti6Al4V alloys have a direct impact on mechanical behaviour [136]. Also, porosity affects the material's elastic properties, and the proposed empirical and semi-empirical expressions [137–145] relate Young's modulus to the total porosity of the sample. The proposed analytical solutions include the characterisation of the pore sizes, ratio, orientation, fraction, etc. However, the proposed equations have limitations and include assumptions about the real microstructure, including the parameters, which has to be measured experimentally for each type of material. The proposed analytical approaches showed a good fit to experimental values for brittle fracture, with the main focus on predicting the elastic properties of porous materials. While quasi-static properties are essential for the initial evaluation of the material, the prediction of the fatigue life of the material is more crucial.

The predictive model, based on the defect tolerant design approach, such as El-Haddad's [146], is widely used to predict the fatigue limit of additively manufactured materials. In this model, the defect is assumed as a crack, and later, Murakami and Endo [147] introduced a new parameter based on the projected area of the pore expressing the fatigue limit as a function of the porosity size and location. In addition, Beretta and Romano [148] adapted Murakami's parameter in El-Haddad's model for calculating the fatigue limit of the samples including pores. The analytical approaches [146–148] showed reasonable estimation of the endurance limit in comparison to the fatigue test of additively manufactured samples [10, 12, 132, 149], but in some cases can give conservative predictions. The numerical crack nucleation models can be developed for more accurate predictions of fatigue performance. The studies [13, 150] are modelling an individual pore using a FEM to compute the stress concentration factor. The performed [150] static analysis with a defined ratio of pore diameter to its distance to the free edge concluded that the stress concentration factor is higher for the pores located close to the free surface. Instead, in [13], the porosity defects of different shapes are identified by scanning the samples of SLM Ti6Al4V and evaluating the stress concentration factor by FEA. The fatigue nucleation is predicted at the pore by using the stress-strain response of the FE model. Nonetheless, the following numerical

studies focused on a single pore and did not include the global interaction on the multiple pores.

To overcome the problem of modelling the pores interactions and analysing the effect of the pores sizes and location on fatigue life, the study in Chapter 5 proposes a new method of micro pores initiation in the material and fatigue nucleation prediction by means of PD.
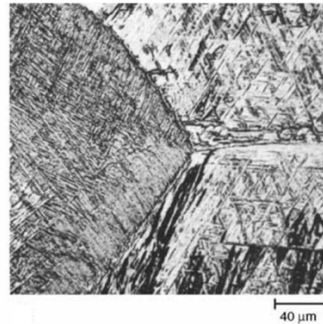
Figure 2.12 Microstructure of air cooled Ti6Al4V [151].

| (a) | (b) | (c) |
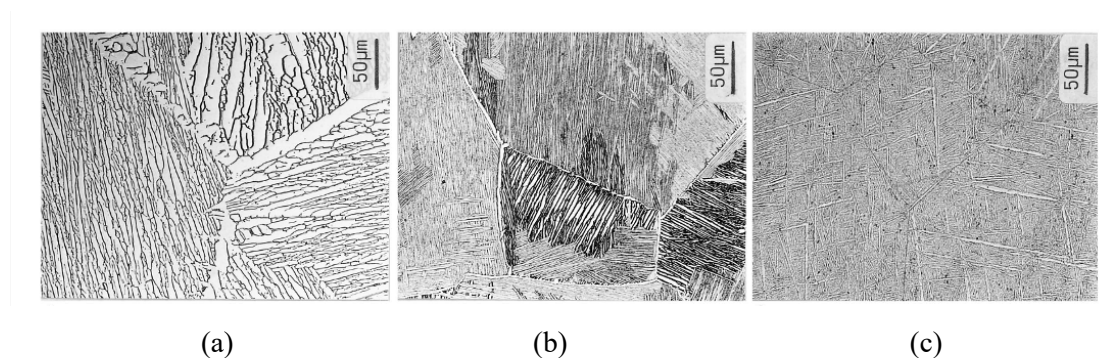
Figure 2.13 Effect of cooling rate on microstructure: (a) $1\,°C/min$, (b) $100\,°C/min$, (c) $8000\,°C/min$ [70].

2.4.2   Effects of granularity on FCGR

The studies on FCG in additively manufactured titanium alloys [16, 19, 68] indicated a strong impact of grain shape and size on fatigue crack performance. There has been an increasing amount of literature [133, 152–154] focused on finding the relationship between the AM process parameters and the mechanical properties of the final structures. Processing parameters such as heating and cooling rates, temperature gradients, the heat source, and layer thickness during the AM significantly impact the microstructural characteristics.
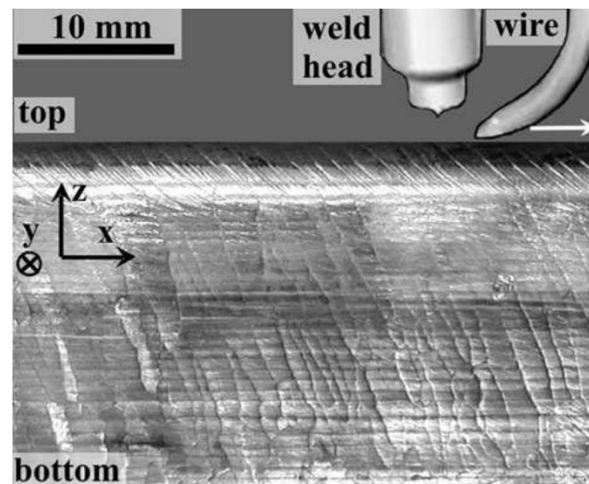
Figure 2.14 Prior β grains in additively manufactured Ti6Al4V alloy [156].

The microstructure of the titanium alloys is influenced by the processing type and the heat treatment [151]. The traditional Ti6Al4V is a $\alpha + \beta$ alloy. It has acicular α-grains, which are separated by prior β grain boundaries, as shown in Figure 2.12. The structure in Figure 2.12 is a basketweave structure, also named as 'Alpha Widmanstatten structure', which occurred due to the cooling of the metal from above the β transus temperature [151]. It is the most common microstructure of Ti6Al4V, but the morphology can be changed with the alternation of the alloy composition or increasing the cooling temperature. Figure 2.13 shows the changes in microstructure with different cooling rates, where the finer microstructure develops with the increased cooling rate [70]. Finer microstructures have better strength and ductility compared to the coarser microstructures but are less resistant to FCG [155].

The evaluation of the additively manufactured microstructure indicated the presence of elongated columnar prior β grains, shown in Figure 2.14, which are growing parallel to the build direction due to the rapid solidification process [15, 118, 120, 133, 153]. The epitaxial growth of grains in Figure 2.14, occurs during the solidification process from the previously deposited layer and is dependent on the temperature gradients and tilts in the laser scanning direction [125, 133]. The columnar prior β grains bring anisotropy in the mechanical properties and fatigue properties in different orientations [8]. However, in various AM processes, different morphologies were reported. For example, looking at the WAAM samples [120, 153], columnar prior

β grains with the thickness of the grains ranging from 1 to 3 mm have been noticed. On the other hand, the implementation of the rolling process in AM, as shown in Figure 2.8, showed a reduction of the prior β grains size with decreased size of increasing rolling load. This means that different processing and post-processing techniques can change the material microstructure and as a result its fatigue properties. The damage in SLM Ti6Al4V due to the cycling loading initiates at the grain boundaries α along the prior β grains with the intergranular α fracture mode [157, 158]. As the crack propagation mechanism is effected by the microstructure, the annealing process of the SLM structures is decreasing the size of $\alpha - phase$ with increased fatigue performance [19].
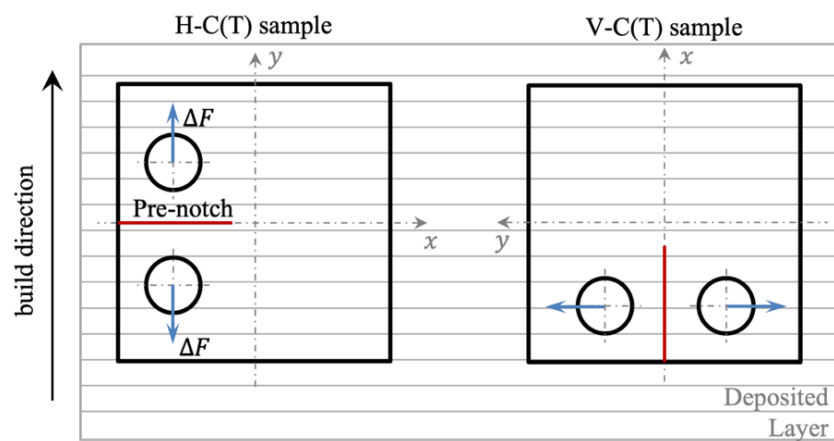
Figure 2.15 Horizontal compact tension H-C(T) and vertical compact tension V-C(T) specimen cut.

As reported in the experiments [19] on the Ti6Al4V alloys, produced by SLM, showed lower FCGR than forged Ti6Al4V, and only after employment of the heat-treated procedure, the FCGR were close to the conventionally processed alloy. Moreover, the test results [19] indicated the variations of the crack growth behaviour in the Horizontal Compact Tension (H-C(T)) and Vertical Compact Tension (V-C(T)) samples. In the H-C(T) samples, the crack growth is perpendicular to the build direction; instead, in V-C(T) samples, the crack is located perpendicular to the deposited layers, as shown in Figure 2.15. The tests' outcome indicated that the FCGR of the H-C(T) samples is greater than the ones in the V-C(T) samples. Instead, the experiment [16] on WAAM and EBM [14] titanium alloy samples showed contrary

results compared to SLM with the faster crack growth in H-C(T) samples. The evaluation of the SLM produced structures indicated that the fine-grained and martensitic microstructure tend to increase crack propagation, due to the higher brittleness and lower levels of crack-tip shielding primary by crack closure effects. [68]. The same pattern is noticed for the wrought titanium alloys [159], where the coarse-grained lamellar microstructure has higher FCG resistance. The coarse-grained lamellar microstructures consist of large β grains with a diameter of around 1 mm [159].

Although the columnar grains were observed in the SLM and WAAM systems, the microstructure of samples produced by the powder is finer compared to the wire fed system. The size of the columnar β grains could bring differences in the FCGR of SLM and WAAM samples, as the fatigue tests of the SLM C(T) sample indicated the intergranular propagation in both H-C(T) and V-C(T) samples [160]. The samples built with the EBM process showed the crack propagation through the prior β grains in the H-C(T) sample and along in V-C(T) samples [14].

As multiple experimental studies reported the anisotropy in the additively manufactured materials due to the existence of the columnar grains in the structure, it is important to understand the effect of the microstructure on the FCGR. The study in Chapter 6 numerically model and analyse how different types of microstructure contribute to the FCGR of the metals and how the combination of columnar microstructure and the existence of the pores affects the fatigue crack performance.

2.4.3 *Effect of Residual Stresses on FCGR*

The layer-wise manufacturing, discussed in Section 2.4.2, not only result in variations in the microstructure due to the high-temperature gradients, but also in RS in the sample. Vrancken et al. [161] reported anisotropy in FCGR of Ti6Al4V produced by SLM, where very high compressive stresses influenced the FCGR originated along with the building directions. On the other hand, the samples with dominated tensile RS showed the lowest fracture toughness. Multiple studies [162, 163] on the material outcome of the AM process showcased the residual stress distributions in the as-built samples with high compressive stresses at the centre of the samples and tension at the

edges. Syed et al. [163] also investigated the influence of the RS on FCGR and observed high dependency of RS on FCG behaviour. Moreover, it was showcased that the orientation of the sample cut had a different outcome of FCGR with higher RS resulting in a higher FCGR. All of the studies on Ti6Al4V samples produced by SLM observed the largest RS parallel to the scan direction, and the studies [161–163] outlined the importance of post-built annealing treatments to relieve the RS and reduce the anisotropy of mechanical properties.

The studies in the literature showcased two types of Compact Tension (C(T)) sample produced by AM for the FCG tests. The first type of specimens by SLM was built individually on the platform, and the second type involved the building of the continuous extended block, which later on is used to slice individual specimens [161]. Each of the produced samples was then machined to have the smooth sample surface according to ASTM standard E647 [164] and after the notch was produced. Looking at the production process of C(T) samples, Syed et al. [163] showed the changes in the RS with the applied surface and notch machining. Firstly, the as-built individual samples had very high compressive stresses in the middle of the sample and as twice as high tensile stresses at the sample edges. Secondly, after machining of the sample surfaces, the sample became slightly thinner, and the compressive stresses in the middle were released by 55% with some release to the tensile stresses at the edges of the sample. Moreover, the last machining of the notch resulted not only in the tensile stress reduction but also in the stress redistribution. The machining process had a noticeable effect on the stress release in the samples, but stresses still varied, with tensile and compressive stresses within the sample length.

On the other hand, the heat treatment resulted in almost negligible stresses in the samples or quite low constant stresses through the sample length. The fatigue tests of the SLM C(T) samples showed faster crack propagation with higher RS. A similar outcome in the fatigue propagation tests was showcased by other authors [19, 161], indicating the effect of anisotropy in the fatigue properties of the samples due to the higher RS in the build direction compared to the layer scanning direction. In each of the studies, the resultant RS have huge variations with some as-built samples having

very high tensile RS of up to 800 MPa [19, 161, 163], up to 300 MPa [19, 165, 166] and some with very high compressive stresses of up to $-400\ MPa$ [161–163, 167].

Despite multiple experimental studies performed to understand the mechanisms for the residual stress generation in SLM, several numerical studies were conducted to estimate the RS and distortions in the samples. Mughal et al. [168] developed a 2D finite element thermo-mechanical model with a moving heat source to predict the RS. Moreover, Alimardani et al. [169] proposed a 3D transient approach for layer-by-layer modelling and predicting the temperature redistributions and RS in the multi-layered samples. Mukherjee et al. [165] performed 3D thermo-mechanical models and evaluated the effect of the AM process parameters such as layer thickness and heat input on the residual stress distributions. Another study [170] also coupled 3D thermo-mechanical FE models and additionally analysed residual stress distributions due to the different laser scan strategies. However, to the best of the author's knowledge, no PD analysis is performed on the modelling of the RS in the material with the analysis of the effects of the stresses on FCGR. The description of the numerical model and the RS implementation is described in Chapter 6.

2.5   Environmental fatigue and SCC

The combination of two events of corrosion and fatigue can often be the most dangerous mechanisms of material failure and is known as environmental fatigue, or CF. Corrosion itself can generate a lot of damage in metals, but with the combination of fatigue, it can jeopardise the material strength and decrease the structure's life. The effect of environmental fatigue on the failure of metallic structures is summarised in [20].

Corrosion is a complex phenomenon and can be divided into generalized and localized. Generalized corrosion affects uniformly to the entire surface of metal exposed to the corrosion environment; instead, the localized corrosion initiates locally. For localized corrosion, initiation can be a very long process, but the growth is rapid once started. The localized corrosion process is often elevated by stresses and is referred to as SCC. SCC is possible only when the material is under the static load and is exposed to an aggressive environment. The combination of material, aggressive

environment (e.g. NaCL solution, methanol solution) and stress state results in SCC and corrosion crack propagation [20]. Many metals like titanium, stainless steel, high tensile steel, and aluminium alloys are corrosion-resistant in NaCl solution but are sensitive to SCC. Primarily it was noticed in the pre-notched Ti6Al4V when exposed to a very aggressive environment, like methanol solution or NaCl solution, the SCC occurs at the notch tip [171]. When the crack is already in the material, it triggers the SCC where the film rupture at the crack tip occurs with the dissolution process taking place. This process commonly occurs due to fatigue when the passivizing oxide film protecting the metal surface ruptures and does not have enough time to re-passivate.

As discussed in Section 2.3.2 SIF is the fundamental concept for FCG, and Smith et al. [172] discovered the threshold phenomenon for SCC, K_{ISCC}, below which the SCC does not occur. K_{ISCC} is one of the most important parameters of SCC definition and the researches use the threshold SIF for SCC, K_{ISCC} as a baseline for defining the categories of crack growth.

Coupling the fatigue with corrosion can be a devastating combination for structural components. When the events occur together, they are interdependent, as shown in Figure 1.4. CF and Corrosion Fatigue Crack Growth (CFCG) rates are of great interest for life prediction of engineering structures. McEvily and Wei [173] classified the CFCG with respect to K_{ISCC}, as shown in Figure 2.16 and discussed more in detail in Section 7.2. In the following classification when $K_{max} < K_{ISCC}$ the CF refers as TCF, where the crack growth is increased by environmental effects, for example, filiform, pitting, exfoliation [174] and the CFCG rate is in the form:

$$\left(\frac{da}{dN}\right)_{TCF} = \left(\frac{da}{dN}\right)_{Air} + \left(\frac{da}{dN}\right)_{Pitting} \tag{2.12}$$
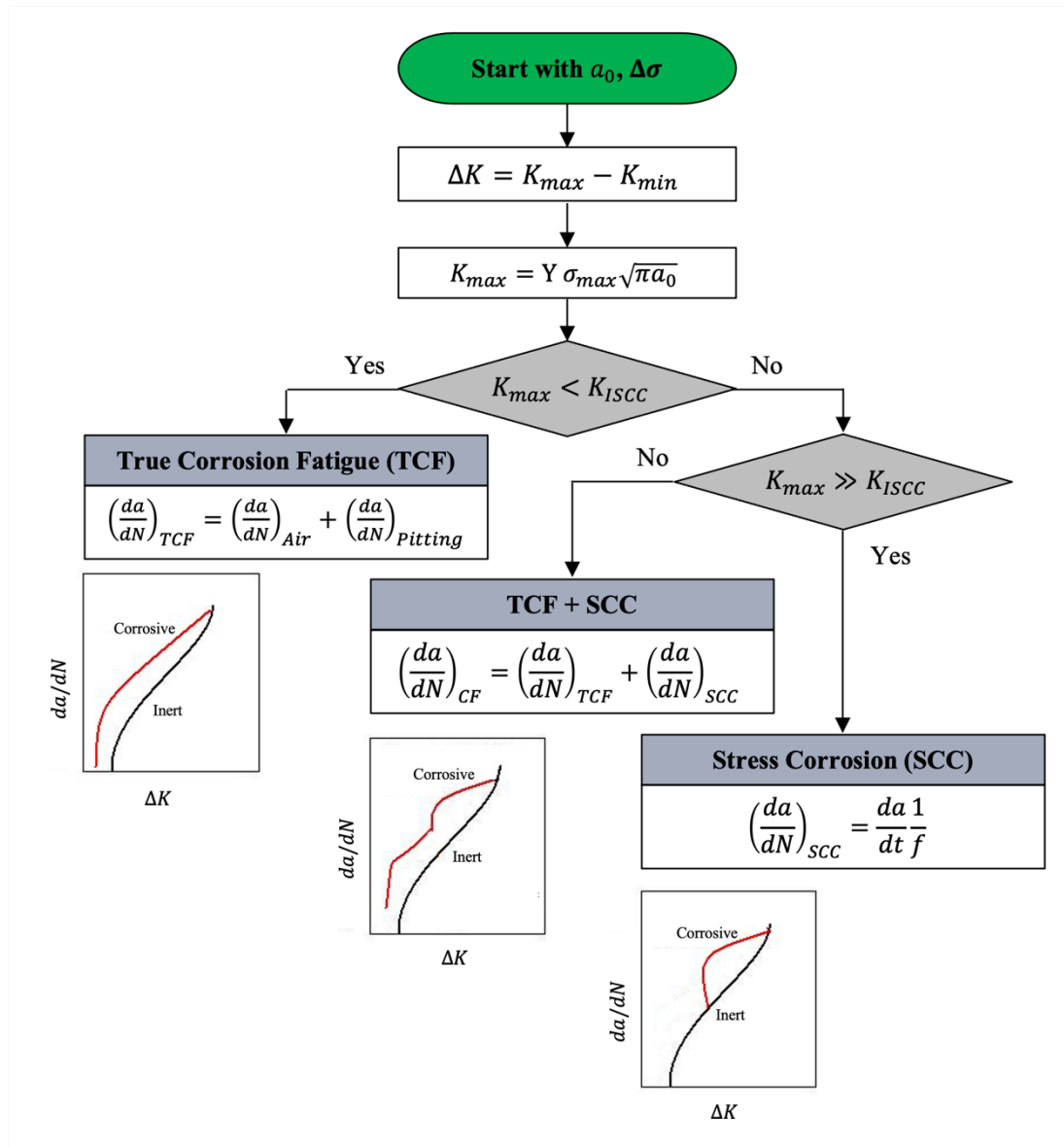
Figure 2.16 Block-scheme of CFCG categories (modified from [20]).

When $K_{max} > K_{ISCC}$, then the fatigue loading can activate the SCC with the FCG mechanism. The models at this stage are named as CF, and two types of models are introduced in the literature: the superposition model [175, 176] and the process-competition model [177]. The superposition model was introduced by Wei and Landers [175], where the CFCG rate, $\left(\frac{da}{dN}\right)_{CF}$, is equal to the sum of mechanical FCGR, $\left(\frac{da}{dN}\right)_{Air}$, and the contribution from SCC, $\left(\frac{da}{dN}\right)_{SCC}$:

$$\left(\frac{da}{dN}\right)_{CF} = \left(\frac{da}{dN}\right)_{Air} + \left(\frac{da}{dN}\right)_{SCC} \tag{2.13}$$

The SCC is time-dependent, and the shift from da/dN to da/dt can be evaluated in the following form:

$$\left(\frac{da}{dN}\right)_{SCC} = \frac{da}{dt}\frac{1}{f} \tag{2.14}$$

where f is the frequency of the loading cycle.

Another CF model proposed in [176] is including also the cycle-dependent corrosion term $\left(\frac{da}{dN}\right)_{cdc}$:

$$\left(\frac{da}{dN}\right)_{CF} = \left(\frac{da}{dN}\right)_{Air} + \left(\frac{da}{dN}\right)_{cdc} + \left(\frac{da}{dN}\right)_{SCC} \tag{2.15}$$

The authors in [176] identified several models of $\left(\frac{da}{dN}\right)_{cdc}$, but concluded that the process of finding the correct parameters for $\left(\frac{da}{dN}\right)_{cdc}$ definition is quite a complicated process.

The competition model proposed in [177] assumes that the CF is equal to the larger of two possible effects:

$$\left(\frac{da}{dN}\right)_{CF} = max \begin{cases} \left(\frac{da}{dN}\right)_{TCF} \\ \left(\frac{da}{dN}\right)_{SCC} \end{cases} \tag{2.16}$$

Some empirical engineering models [178–181] for CFCG are developed where the researchers take into account the effect of the environment on the FCG and express the CFCG rate as a function of the SIF range. However, most models follow the Paris law type equation by fitting the curves to the experimental data and obtaining the model constants based on the tests data for a given environment. Instead, a new numerical approach is proposed and discussed in Chapter 7, where the PD FCG model is combined with the PD diffusion model for CFCG rates predictions. The PD diffusion model is a specific SCC Hydrogen Embrittlement (HE) mechanism presented in detail in Chapter 7.

2.6   Summary

The following chapter gives a literature overview on the points of interest in the conducted research. It shows the available methods for failure problems evaluations and how the numerical approach, PD, can overcome the problems of discontinuities and be a beneficial tool for modelling and analysing the material failure. The literature review on additively manufactured materials showcased the drawbacks of layer-by-layer manufacturing and the importance of analysing factors like process-induced defects, granularity and RS on the fatigue performance of the material. Finally, the gaps in the available numerical models on fatigue and CF are identified, and new approaches of PD tools are investigated and presented in the next Chapters.

3   METHODOLOGY

3.1   Introduction

This chapter aims to introduce the main numerical technique – PD, used in this research study. There are three PD models exist: bond-based PD [65], ordinary state-based PD [182] and non-ordinary state-based PD [182]. The bond-based PD model has a limitation on material properties, especially Poisson's ratio is 1/3 in the 2D model and 1/4 in the 3D model for isotropic materials due to the assumptions of pairwise interactions of the same magnitude, as discussed in Section 3.3.2. Ordinary state-based PD eliminates this limitation and provides more realistic results, and Poisson's ratio is not restricted to 1/3 (2D model) and 1/4 (3D model). Ordinary state-based PD and non-ordinary state-based PD both have a mathematical object called 'force-vector state', but in the non-ordinary state-based PD, the bonds are not restricted to central forces, which can be in any direction. In the current research, bond-based PD and ordinary state-based PD are utilised. Ordinary state-based introduced in Section 3.3.1 is used on quasi-static and dynamic PD analyses in Chapter 4 to have more accurate results with respect to the materials with Poisson's ratio different from 1/3. Instead, the bond-based PD, described in Section 3.3.2, is used for fatigue and CF problems due to the simplicity of the formulation and the type of material considered in this research. A description of the numerical solution methods for static, quasi-static and dynamic problems is given in Section 3.4.

MATLAB is used as a main programming and computing platform for developing PD numerical tools for all the presented problems in Chapters 4-7.

3.2   Applications of Peridynamics

Starting from the day the PD was introduced to the scientific community by Silling [183] at Sandia National Laboratories, the applicability of the numerical tool on various problems widened progressively during the years. The PD mechanical formulation combines CCM and MDM, which allowed to overcome the problems, including discontinuities such as cracks. The development of the PD allowed the researchers to

analyse the structures on macroscopic, mesoscopic and nanoscopic levels. With the following advantages, active research started on brittle fracture problems, such as predicting crack nucleation and propagation [184–187], the interaction of the main crack with micro-cracks [188, 189] and the interaction between multiple micro-cracks [22]. The topics of research are not limited only to brittle fracture but also to plastic [182], viscoelastic [190], and viscoplastic materials [191]. Additionally, the applicability of the PD fatigue model [192] is shown on fatigue crack propagation problems in metals [193] and composites [194]. The development of PD numerical models has also been expanded to heat transfer [195], hydro-thermal diffusion [196], fluid-structure interaction [197] and corrosion problems [198]. The current research will also show the applicability of the PD tool on the CF problems explained in Chapter 7.

3.3 Peridynamic model for brittle damage

3.3.1 Ordinary state-based peridynamics

The ordinary state-based PD introduced by Silling [183] is a reformulation of the fundamental equations of continuum mechanics equations which are particularly suitable to solve problems including discontinuities. PD uses integro-differential equations instead of partial differential equations as in CCM. This widens the possibility of solving fracture mechanics problems, including cracks initiation and propagation [195].

The PD equation of motion can be written in the form of the integro-differential equation as:

$$\rho(\boldsymbol{x})\ddot{\boldsymbol{u}}(\boldsymbol{x},t) = \int_{H_x} \big(\boldsymbol{t}(\boldsymbol{u}'-\boldsymbol{u},\boldsymbol{x}'-\boldsymbol{x},t) - \boldsymbol{t}(\boldsymbol{u}-\boldsymbol{u}',\boldsymbol{x}-\boldsymbol{x}',t)\big)dV_{x'} + \boldsymbol{b}(\boldsymbol{x},t) \tag{3.1}$$

which can be discretised as:

$$\rho_{(i)}\ddot{\boldsymbol{u}}_{(i)} = \sum_{j=1}^{M} \Big(\boldsymbol{t}_{(i)(j)}\big(\boldsymbol{u}_{(j)} - \boldsymbol{u}_{(i)}, \boldsymbol{x}_{(j)} - \boldsymbol{x}_{(i)}, t\big)$$

$$- \boldsymbol{t}_{(j)(i)}\big(\boldsymbol{u}_{(i)} - \boldsymbol{u}_{(j)}, \boldsymbol{x}_{(i)} - \boldsymbol{x}_{(j)}, t\big) \Big) V_{(j)} + \boldsymbol{b}_{(i)}$$

(3.2)

from which the acceleration $\ddot{\boldsymbol{u}}_{(i)}$ of the material point i at a time t can be obtained. Each material point i interacts with other material points j within its horizon H_x with a total number M of the family members for the point i, as shown in Figure 3.1. The coordinates of a material point are represented as $\boldsymbol{x}$ with the incremental volume V. $\boldsymbol{u}$, $\boldsymbol{b}$ and ρ denote displacement vector field, body load and mass density of the material point, respectively.
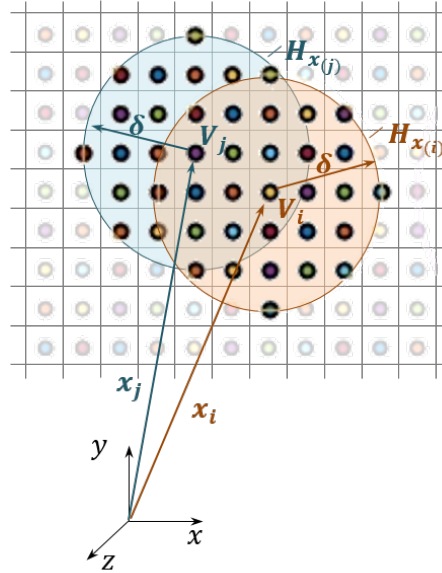
Figure 3.1 Peridynamic material points and interaction of material points i and j.

In the ordinary state-based PD, interacting material points can exert forces on each other with unequal magnitudes [64], and for the interacting material points i and j, PD force densities can be defined as:

$$t_{(i)(j)} = 2\delta \Bigg\{ d_{PD} \frac{\Lambda_{(i)(j)}}{|\boldsymbol{x}_{(j)} - \boldsymbol{x}_{(i)}|} \Big(a_{PD}\theta_{(i)} - \frac{1}{2} a_{2PD}T_{(i)} \Big)$$

$$+ b_{PD}\big(s_{(i)(j)} - \alpha T_{(i)}\big) \Bigg\} \times \frac{\boldsymbol{y}_{(j)} - \boldsymbol{y}_{(i)}}{|\boldsymbol{y}_{(j)} - \boldsymbol{y}_{(i)}|}$$

(3.3)

$$t_{(j)(i)} = -2\delta \left\{ d_{PD} \frac{\Lambda_{(i)(j)}}{|\boldsymbol{x}_{(j)} - \boldsymbol{x}_{(i)}|} \left(a_{PD}\theta_{(j)} - \frac{1}{2} a_{2PD}T_{(j)} \right) \right.$$
$$\left. + b_{PD}\left(s_{(i)(j)} - \alpha T_{(j)} \right) \right\} \times \frac{\boldsymbol{y}_{(j)} - \boldsymbol{y}_{(i)}}{|\boldsymbol{y}_{(j)} - \boldsymbol{y}_{(i)}|} \tag{3.4}$$

where δ is the horizon size, T is the temperature change at material point, α is the coefficient of thermal expansion, a_{PD}, b_{PD}, d_{PD}, a_{2PD} are the PD parameters, s - the stretch between material points, and θ - dilatation, which can be expressed as:

$$\theta_{(i)} = d_{PD}\delta \sum_{j=1}^{M} \Lambda_{(i)(j)}s_{(i)(j)}V_{(j)} \tag{3.5}$$

and the parameter $\Lambda_{(i)(j)}$ is defined as:

$$\Lambda_{(i)(j)} = \left(\frac{\boldsymbol{y}_{(j)} - \boldsymbol{y}_{(i)}}{|\boldsymbol{y}_{(j)} - \boldsymbol{y}_{(i)}|} \right) \cdot \left(\frac{\boldsymbol{x}_{(j)} - \boldsymbol{x}_{(i)}}{|\boldsymbol{x}_{(j)} - \boldsymbol{x}_{(i)}|} \right) \tag{3.6}$$

The stretch between material points i and j can be expressed as:

$$s_{(i)(j)} = \frac{|\boldsymbol{y}_{(j)} - \boldsymbol{y}_{(i)}| - |\boldsymbol{x}_{(j)} - \boldsymbol{x}_{(i)}|}{|\boldsymbol{x}_{(j)} - \boldsymbol{x}_{(i)}|} \tag{3.7}$$
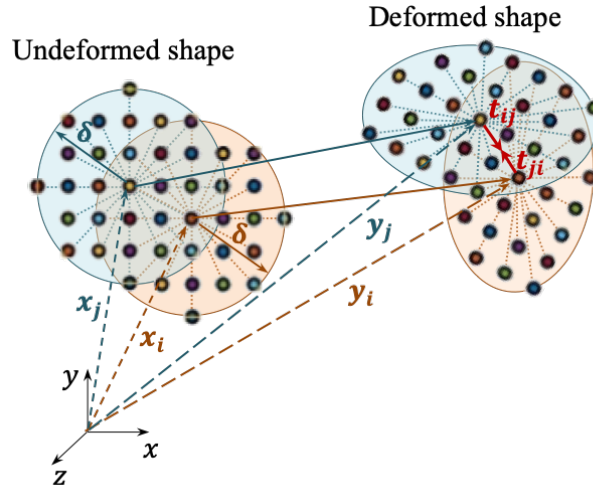
Figure 3.2 Peridynamic material points i and j in the deformed configuration and the ordinary state-based peridynamic forces between these material points.

Once a material point displaces to a new location as a result of deformation of the structure, its new location is specified as $\boldsymbol{y}$ in the deformed configuration, as shown in Figure 3.2.

PD parameters $a_{PD}, b_{PD}, d_{PD}, a_{2PD}$ can be related to material constants of CCM by equating strain energy density of a material point inside a body subjected to isotropic expansion and simple shear loading conditions calculated from CCM and PD [64]. For a 2-Dimensional (2-D) model with plane stress conditions, the plate is discretised with a single layer of material points in the thickness direction. Due to this, the PD parameters are expressed in terms of bulk modulus, κ, shear modulus, μ, thickness, h , and horizon size, δ, for a 2-Dimensional problem with plane stress conditions:

$$a_{PD} = \frac{1}{2}(\kappa - 2\mu), \qquad a_{2PD} = 4\alpha a, \qquad b_{PD} = \frac{6\mu}{\pi h \delta^4}, \qquad d_{PD} = \frac{2}{\pi h \delta^3} \qquad (3.8)$$

with

$$\kappa = \frac{E}{2(1 - v)}, \qquad \mu = \frac{E}{2(1 + v)} \qquad (3.9)$$

where E and v are Young's modulus and Poisson's ratio, respectively.
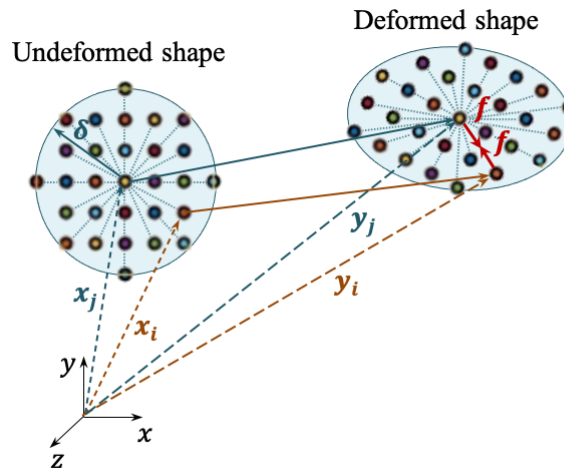
Figure 3.3 Peridynamic material points i and j in the deformed configuration and the bond based peridynamic forces between these material points.

3.3.2   Bond-based peridynamics

Bond-based PD is the first PD theory introduced by Silling [65], where the force densities $\boldsymbol{t}_{(i)(j)}$ and $\boldsymbol{t}_{(j)(i)}$ are not only aligned in the direction of the deformed position of bond, but also are equal in magnitude [64], as shown in Figure 3.3. So, the equation of motion given in Eq. (3.2) takes the form of:

$$\rho_{(i)}\ddot{\boldsymbol{u}}_{(i)} = \sum_{j=1}^{M} \boldsymbol{f}_{(i)(j)}V_{(j)} + \boldsymbol{b}_{(i)} \tag{3.10}$$

where $\boldsymbol{f}_{(i)(j)}$ is the pairwise force density, which can be defined as [183]:

$$\boldsymbol{f}_{(i)(j)} = 4\delta b_{PD}\big(s_{(i)(j)} - \alpha T_{(i)}\big)\frac{\boldsymbol{y}_{(j)} - \boldsymbol{y}_{(i)}}{\big|\boldsymbol{y}_{(j)} - \boldsymbol{y}_{(i)}\big|} \tag{3.11}$$

where $s_{(i)(j)}$ is defined by Eq. (3.7) and the material constant b_{PD} is defined by Eq. (3.8) for a plane stress condition and by Eq. (3.12) for a plane strain condition, when the thick samples are loaded symmetrically in a single plane.

$$b_{PD} = \frac{12E}{5\pi h\delta^4} \tag{3.12}$$

The pairwise force density $\boldsymbol{f}$ depends on the stretch s between the material points and the material constant b_{PD}. However, it can be seen from Eq. (3.12) that the bond constant depends on only one engineering constant instead of two in the case of an elastic isotropic material. In this way, the limitation is present in bond-based PD on the Poisson's ratio, which is 1/3 in the 2D model and 1/4 in the 3D model [64].

3.3.3   PD model discretisation

In the PD theory, the interaction between material points is limited by defined horizon size δ. Without the restriction of the number of interactions, the computational time of the models can be very large. With the following continuity assumption, each material point within the discretised body should have the same neighbouring points during the deformations. To make the computational PD model more efficient, determining the material points' family members can be done only once at the

beginning of simulations. Moreover, the uniform discretisation of the body is used, where the material points volumes do not vary, otherwise integration errors due to the changes in the grid would have to be fixed by special integration techniques implementations [199].

3.3.4 Correction terms

As described in Sections 3.3.1 and 3.3.2, a meshless scheme is used in PD governing equations, where the domain is discretised with smaller volumes. Each of the volumes is associated with material points, shown in Figure 3.1, which interact between each other if the location of material point j is within the horizon H_x of the material point i. However, it can be noticed in Figure 3.1, that within the horizon of H_x some volumes of material points are truncated and the 'volume correction factor', v_c, was proposed and explained in [64]. Thus, the discretized equations of motion for bond-based PD will be in the following form:

$$\rho_{(i)}\ddot{\boldsymbol{u}}_{(i)} = \sum_{j=1}^{M} \boldsymbol{f}_{(i)(j)}\left(V_{(j)}v_{c_{(j)}}s_{cf_{(ij)}}\right) + \boldsymbol{b}_{(i)} \tag{3.13}$$

and ordinary state-based PD:

$$\rho_{(i)}\ddot{\boldsymbol{u}}_{(i)} = \sum_{j=1}^{M} \Big(\boldsymbol{t}_{(i)(j)}\big(\boldsymbol{u}_{(j)} - \boldsymbol{u}_{(i)}, \boldsymbol{x}_{(j)} - \boldsymbol{x}_{(i)}, t\big)$$
$$- \boldsymbol{t}_{(j)(i)}\big(\boldsymbol{u}_{(i)} - \boldsymbol{u}_{(j)}, \boldsymbol{x}_{(i)} - \boldsymbol{x}_{(j)}, t\big)\Big)\left(V_{(j)}v_{c_{(j)}}s_{cf_{(ij)}}\right) + \boldsymbol{b}_{(i)} \tag{3.14}$$

Another correction term s_{cf} is added to Eq. (3.13) and Eq. (3.14), which is called 'surface correction factor', proposed and described by [64], due to the fact that some solution inaccuracies can arise as material points located close to the free surfaces has fewer bonds of interaction compared to the other material points. With this respect the s_{cf} is also added to the PD equation of motion. Moreover, the surface effects have to be also considered for dilatation term, and the discrete form of the dilatation is also described by [64] and proposed in the following form:

$$\theta_{(i)} = d_{PD}\delta \sum_{j=1}^{M} G_{(d)(i)(j)}\Lambda_{(i)(j)}s_{(i)(j)}\left(V_{(j)}v_{c_{(j)}}\right) \tag{3.15}$$

where $G_{(d)(i)(j)}$ is the correction factor for the material points i and j.

3.3.5 Damage in PD theory

The failure parameter introduced by [200] includes a history-dependent scalar-valued function ψ to represent broken interactions (bonds) between material points:

$$\psi\left(\boldsymbol{x}_{(j)} - \boldsymbol{x}_{(i)}, t\right) = \begin{cases} 1 & \text{if } s_{(i)(j)}\left(\boldsymbol{x}_{(j)} - \boldsymbol{x}_{(i)}, t'\right) < s_c \text{ for all } 0 < t' \\ 0 & \text{otherwise} \end{cases} \tag{3.16}$$

where for a 2-D problem, the critical stretch s_c in connection with the material fracture energy G_c is expressed as [64]:

$$s_c = \sqrt{\frac{G_c}{\left(\frac{6}{\pi}\mu + \frac{16}{9\pi^2}(\kappa - 2\mu)\right)\delta}} \tag{3.17}$$

The material fracture energy G_c, also known as energy release rate, for a mode I opening is related to the SIF, K_I in the following way:

$$G_c = \frac{K_I^2}{E} \qquad \text{plane stress} \tag{3.18}$$

$$G_c = \frac{K_I^2}{E}(1 - v^2) \qquad \text{plane strain} \tag{3.19}$$

The general solution of SIF is described in Section 2.1 and can be determined by experiments.

The introduced parameter of the critical stretch s_c predefines the limit of the bond stretch, at which the bonds between material points can be broken. According to [183], the bonds are broken irreversibly once they are stretched beyond the critical limit and the bond no longer sustains the tensile force. With the applied tension forces on the

sides of the plate, the fracture energy G_c in PD model is required to break the bonds connected at the opposite halves of the crack, shown in Figure 3.4.

After defining the failure parameter in the PD theory, the local damage of the material point i is introduced to indicate the crack formation in the body. The local damage ranges from 0 to 1 and can be defined as:

$$\varphi(\pmb{x}_{(i)}, t) = 1 - \frac{\sum_{i=1}^{M} \psi(\pmb{x}_{(j)} - \pmb{x}_{(i)}, t) V_{(j)}}{\sum_{i=1}^{M} V_{(j)}} \tag{3.20}$$

Local damage is dependent on the relationship between the horizon size δ and the distance between the material points Δx:

$$\delta = m\Delta x, \qquad m = 3, 4, 5 \tag{3.21}$$

As shown in Figure 3.4, for an initial crack, the failure parameter becomes zero if a bond is passing through the crack represented by a red line. As the horizon size increases, the material point interacts with an increased number of points within the horizon. The local damage φ at a material point on the crack plane will converge to a value of 0.5 as m parameter increases.
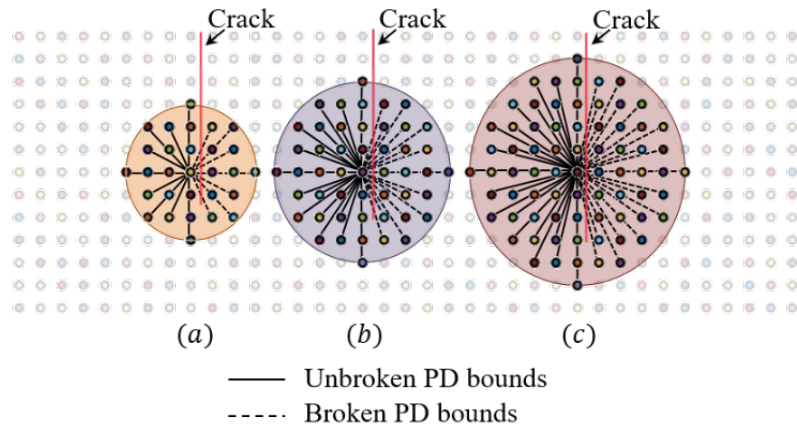
Figure 3.4 Local damage at a material point on the crack plane, when horizon size is a $\delta = 3\Delta x \rightarrow \varphi = 0.38$, b $\delta = 4\Delta x \rightarrow \varphi = 0.41$, c $\delta = 5\Delta x \rightarrow \varphi = 0.43$.

3.3.6   PD model boundary conditions

In the PD equation of motion, there are no spatial derivates, and the displacement and velocity Boundary Conditions (BC) cannot be applied directly to the body. Due to this, a fictitious boundary layer R_f of thickness equal to horizon size δ [64] is initiated in the body, and the BC are applied in the following form:

$$u_f(\boldsymbol{x}, t) = u \qquad \text{for} \quad \boldsymbol{x} \in R_f \tag{3.22}$$

$$\dot{u}_f(\boldsymbol{x}, t) = \dot{u} \qquad \text{for} \quad \boldsymbol{x} \in R_f \tag{3.23}$$

where u is displacement and $\dot{u}$ is velocity BC in x -direction.

The external loads can be applied as body loads through the material layer with the width of Δ and the body load is calculated according to the applied type of the load (e.g., distributed pressure, point load) [64].

The implementation of the BC in PD numerical model will be discussed and showcased more in detail within the next chapters considering the problems of interest.

3.4   Numerical solution method

In Section 3.3, PD theory is presented, including different types of equations of motion. The PD governing equations can be solved by various numerical methods in order to solve the problem in a more efficient way. First of all, the type of solution have to be defined, whether the problem has to be solved using the dynamic solution or static/quasi-static solution. If the problem is dynamic, the acceleration and inertia effects are important, and the solution is carried out by the explicit method. Instead, static or quasi-static problems are solved by the Adaptive Dynamic Relaxation (ADR) method or directly with matrix equations.

3.4.1   Dynamic solution

Explicit time integration scheme, described in [183], is used to solve dynamic problems, where Eq. (3.13) or Eq. (3.14) are used to evaluate the acceleration $\ddot{\boldsymbol{u}}_{(i)}$ for the material point i at the time step n_t. Then the velocity and the displacement are

predicted for the next time step n_{t+1}, using the forward difference method [64] for velocity $\dot{\boldsymbol{u}}_{(i)}^{n_t+1}$:

$$\dot{\boldsymbol{u}}_{(i)}^{n_t+1} = \dot{\boldsymbol{u}}_{(i)}^{n_t} + \ddot{\boldsymbol{u}}_{(i)}^{n_t}\Delta t \tag{3.24}$$

and then backward difference method to obtain displacement $\boldsymbol{u}_{(i)}^{n_t+1}$ for the next time step:

$$\boldsymbol{u}_{(i)}^{n_t+1} = \boldsymbol{u}_{(i)}^{n_t} + \dot{\boldsymbol{u}}_{(i)}^{n_t+1}\Delta t \tag{3.25}$$

where Δt is the time step size, which has to be sufficiently small so that the numerical solution is stable. In particular, [183] proposed to calculate the limit on the time step size based on the von Neumann stability analysis in the following form:

$$\Delta t < \sqrt{\frac{2\rho_{(i)}}{\sum_j \frac{4b_{PD}\delta}{\left|x_{(j)} - x_{(i)}\right|}\left(V_{(j)}v_{c_{(j)}}\right)}} \tag{3.26}$$

3.4.2   Static or quasi-static solution

Most of the studies on PD static or quasi-static solutions use explicit time integration. Moreover, Eq. (3.13) and Eq. (3.14) are introduced in the dynamic form, and a commonly used technique, ADR, is implemented in PD theory to solve static or quasi-static problems. Using the explicit method, the convergence of the static solution can be time-consuming, as too many time steps are required to reach a stable solution. Such a method, for example, fatigue analysis, can be very costly, and some studies are performed using a direct solution [193].

3.4.2.1   Adaptive Dynamic Relaxation Technique

The possibility of using the PD equation of motion on static or quasi-static problems is applicable by using the dynamic relaxation technique, where artificial damping is introduced in a system [195]. The chosen artificial damping guides the dynamic equation of motion towards convergence to a steady-state solution. Therefore, it is not easy to identify the effective fictitious damping coefficient that ensures the

convergence and the solution becomes a static problem. In this respect, Underwood introduced the ADR technique [146], where the damping coefficient is determined at each time step. Madenci and Oterkus [64] introduced ADR in the PD theory in the following form:

$$\boldsymbol{D\ddot{U}} + c_d \boldsymbol{D\dot{U}} = \boldsymbol{F} \tag{3.27}$$

with

$$\boldsymbol{F}_{(i)} = \sum_{j=1}^{M} \left(\boldsymbol{t}_{(i)(j)} - \boldsymbol{t}_{(j)(i)} \right) \left(V_{(j)} v_{c_{(j)}} \right) + \boldsymbol{b}_{(i)} \tag{3.28}$$

where $\boldsymbol{\ddot{U}}$ and $\boldsymbol{\dot{U}}$ are the acceleration and velocity matrices, $\boldsymbol{D}$ is the fictitious diagonal density matrix, which is chosen based on Greschgorin's theorem and c_d is the damping coefficient. A more detailed explanation of the ADR technique is described in [64].

ADR technique got wide applicability on static and quasi-static problems, but it can be time-consuming to reach the convergence of the static solution and quite a lot of time steps are required to solve the problem. Moreover, for some problems, like fatigue analysis that includes multiple static simulations, explicit time integration with ADR is quite prolonged and direct solution is more beneficial.

3.4.2.2 Direct Solution

To solve a static problem using the direct method, the acceleration term $\boldsymbol{\ddot{u}}$ is omitted from the equation of motion, and the equation will have the following form:

$$\sum_{j=1}^{N} \boldsymbol{f}_{(i)(j)} V_{(j)} + \boldsymbol{b}_{(i)} = 0 \tag{3.29}$$

and PD force function $\boldsymbol{f}_{(i)(j)}$ for a 2-D problem is expressed in the matrix form [201]:

$$\begin{Bmatrix} f_x \\ f_y \end{Bmatrix} = \frac{4\delta b}{|\xi|^3} \begin{bmatrix} \xi_x \xi_x & \xi_x \xi_y \\ \xi_y \xi_x & \xi_y \xi_y \end{bmatrix} \begin{Bmatrix} \eta_x \\ \eta_y \end{Bmatrix} \tag{3.30}$$

where ξ is a relative position between material points, $\boldsymbol{\xi} = \boldsymbol{x'} - \boldsymbol{x}$, ξ_x, ξ_y are the reference lengths in x and y directions and η_x, η_y are the relative displacements between material points in x and y directions, which for example for the fatigue problems with loading cycles of N, are evaluated as:

$$
\begin{aligned}
\eta_x &= u_x(\boldsymbol{x'}, N) - u_x(\boldsymbol{x}, N) \\
\eta_y &= u_y(\boldsymbol{x'}, N) - u_y(\boldsymbol{x}, N)
\end{aligned}
\tag{3.31}
$$

Eq. (3.30) is a local stiffness for each material point, interacting with other material points. The combination of local stiffness matrices results in the global static PD equation written in the matrix form as:

$$
\boldsymbol{KU} = \boldsymbol{B}
\tag{3.32}
$$

where $\boldsymbol{K}, \boldsymbol{U}$ and $\boldsymbol{B}$ are the global stiffness matrix, the material points displacements and the body load matrices. Eq. (3.29) is solved to find the displacements of each material point by taking the inverse stiffness matrix $\boldsymbol{K}^{-1}$. For the models with fine discretisation, the global stiffness matrices can be very massive, and it is time-consuming to calculate the $\boldsymbol{K}^{-1}$. Also, an ill-conditioned stiffness matrix may arise due to the bond breaking and the number of material points within the horizon. To overcome this issue, the stabilised biconjugate gradients method (BiCG) [202] is used. BiCG improves the capabilities of the PD solver by making it faster and smoother convergence. For all the presented simulations, in particular, for fatigue problems, the BiCG method is used with the convergence tolerance of 10^{-6} and a maximum number of iterations of 5000.

3.5   Summary

This chapter introduced the formulation of bond-based and ordinary state-based PD utilised in this research study. Due to discretising the material with points and modelling the interactions between material points, the PD numerical models are used in the next chapters for damage predictions and life assessment of the materials due to various loading and environmental conditions.

4   FRACTURE OF BRITTLE MATERIALS

4.1   Introduction

This chapter aims to investigate the dynamic fracture mechanisms in brittle materials by ordinary state-based PD and to understand the effect of defects in the form of holes, macro- and micro-cracks on toughening and degradation mechanisms in brittle structures. The results obtained from the quasi-static and dynamic PD analysis are presented and compared with FEM and experimental studies. Concerning the brittle fracture due to the tensile loading, firstly, in Section 4.3.3, the analysis of the structure is performed under different dynamic loading conditions and the evaluated crack propagation speeds, crack branching patterns, and branching angles from the PD model are compared with experimental results [203]. Secondly, in Section 4.3.4, PD simulations are performed for the main crack interacting with the micro-cracks problem. Five different cases of micro-crack presence under quasi-static BC are presented, and the determined critical loads are compared against analytical solutions [58]. Considering the importance of the micro-cracks on main crack propagation behaviour, the influence of the parameter K_I / K_0 on critical load is analysed to understand the "micro-crack toughening phenomena" (Section 4.3.4.1). Furthermore, the PD models with varying micro-crack distribution and orientation are analysed under dynamic BC. The obtained PD numerical results of crack propagation patterns and crack propagation speeds are presented (Section 4.3.4.2). Concerning the brittle fracture due to bending, firstly, in Section 4.4.3.1, the PD model is verified with FEM and validated with experimental results [204] in Section 4.4.3.2, where five types of hole-defects are allocated in the plate. Secondly, the validated PD model is applied for the prediction of mechanical failure in a concrete structure (Section 4.4.3.3). Finally, Section 4.5 provides a summary of the major information contained in this Chapter.

The study here described can be found in self-authored papers [21] and [22], and to the best of the author's knowledge, this is the first time influence of the parameter K_I/K_0 on critical load is analysed, which is an important factor for modelling porosity defects in the next chapters. It is important because it allows us to consider the

interaction of the multiple pores in the system and analyse their effect on the fatigue performance of the samples. Additionally, the presented validation studies with the experimental data available in the literature prove the capability of the developed numerical model to be applicable to fracture problems and give confidence in the developed numerical model and the PD parameters set up.

4.2   Background and motivation

The failure of engineering structures has always been a topic of engineering practice. One of the common types of mechanical failure is a brittle fracture [205–208]. Considering that brittle materials, such as Polymethyl Methacrylate (PMMA), concrete, ceramics and rocks, are widely used in various industries, it is important to investigate their structural behaviour.

Firstly, the brittle fracture of the crack development through the structure depends on the loading conditions, and a crack can propagate as a single crack, change its original trajectory, or split into two or multiple branches [28]. Theoretical studies [209] have proposed to introduce the limiting velocity of the crack, where the crack accelerates until arriving to the Rayleigh wave speed c_R. Experimental studies indicated variations of the critical velocities for different brittle materials. It was observed [210] that crack instabilities in brittle materials occur at velocities $V_c \sim 0.6c_R$ and similar crack branching behaviour was noticed in different numerical [211] and experimental studies [212, 213]. In [28], it is observed that the branching velocities for PMMA are about $V_c \sim 0.78c_R$ and instead [214] determined the critical velocities of up to $V_c \sim 0.9c_R$ with non-steady crack propagation. Multiple experiments on brittle fracture showed the occurrence of the crack instabilities with different fracture patters. The studies in [28, 203, 213] observed micro-branching phenomena with variation of branching angles of 10-15 degrees and [212] instead showed the macro-branching angles of 30 degrees. Similar microscopic branches were observed in the other brittle materials like Homalite-100 [215] and polystyrene [216]. When the crack propagation speed is reaching the critical velocity, the crack branches in two or multiple micro- and macro-cracks. But the mentioned experiments indicated a big variation of critical velocity

criteria, which could be affected by the size of the samples, as well as the dynamic loading. The literature review undertaken for this study can be found in Section 2.2.

Secondly, mechanical failure and defects in brittle materials can lead to weakening and the sudden collapse of the structure. Brittle materials can consist of randomly distributed small-size defects such as voids, micro-cracks and holes [47]. These defects can have a significant influence on the propagation behaviour of macro-cracks. Various experimental studies in the literature investigate the interaction between macro-cracks and small-size defects [48–51]. Different studies suggest that the existence of micro-cracks enhance or suppress crack propagation [52–54]. The problem of the defects attracted multiple researchers to proceed with experiments and numerical analysis, but still, investigation of the dual role of holes and micro-crack arrays on toughening and degradation mechanisms in brittle structures can be quite challenging. The literature review undertaken for this study can be found in Section 2.2.

4.3 Brittle fracture due to tensile loading

4.3.1 Material data

Two types of materials are employed in the presented studies for brittle fracture analysis, subjected to tensile loading. PMMA is considered for the dynamic crack propagation problems, and concrete is evaluated in dynamic and quasi-static problems. The material properties are summarised in Table 4.1. Concrete is considered as an isotropic material with the homogeneous properties in all directions.

Table 4.1 Material data for brittle fracture due to tensile loading

Material	Young's modulus, E [GPa]	Poisson's ratio, ν	Energy release rate, G_0 [J/m^2]
PMMA [217]	3.24	0.35	570
Concrete [58]	17	0.15	110

4.3.2 Geometry and boundary conditions

4.3.2.1 Dynamic analysis

The pre-notched thin rectangular plate in Figure 4.1 is chosen for the crack propagation study presented in Sections 4.3.3 and 4.3.4.2. The following geometric parameters are selected: length $L = 0.22\ m$, width $W = 0.3\ m$ and thickness $h = 0.003\ m$. The plate has a pre-crack at the left side with a size of $2a = 0.07\ m$.

The velocity BC are enforced in the fictitious boundary layer R_f (Figure 4.1b) as [218]:

$$u_f\left(x_f, y_f, t + \Delta t\right) = u(x, y, t) \text{ with } y_f \in R_{f\left(y = \frac{W}{2}\right)} \tag{4.1}$$

$$v_f\left(x_f, y_f, t + \Delta t\right) = 2\dot{v}^*\left(x, y = \frac{W}{2}, t + \Delta t\right) \times \Delta t - v(x, y, t) \tag{4.2}$$

$$u_f\left(x_f, y_f, t + \Delta t\right) = u(x, y, t) \text{ with } y_f \in R_{f\left(y = -\frac{W}{2}\right)} \tag{4.3}$$

$$v_f\left(x_f, y_f, t + \Delta t\right) = 2\dot{v}^*\left(x, y = -\frac{W}{2}, t + \Delta t\right) \times \Delta t - v(x, y, t) \tag{4.4}$$
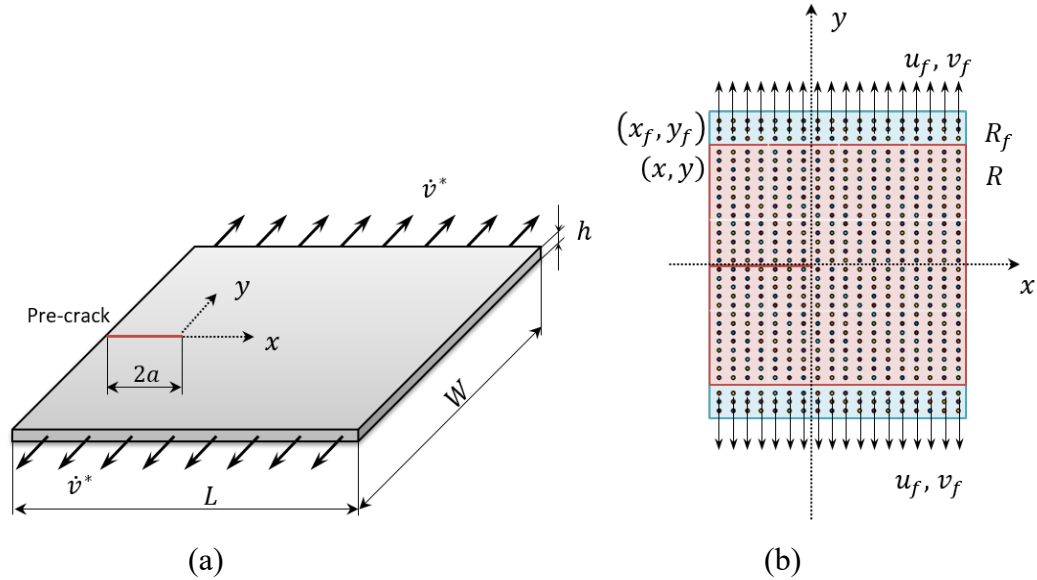
Figure 4.1 Pre-cracked rectangular square plate (a) under velocity BC and (b) its spatial discretisation under imposed BC.
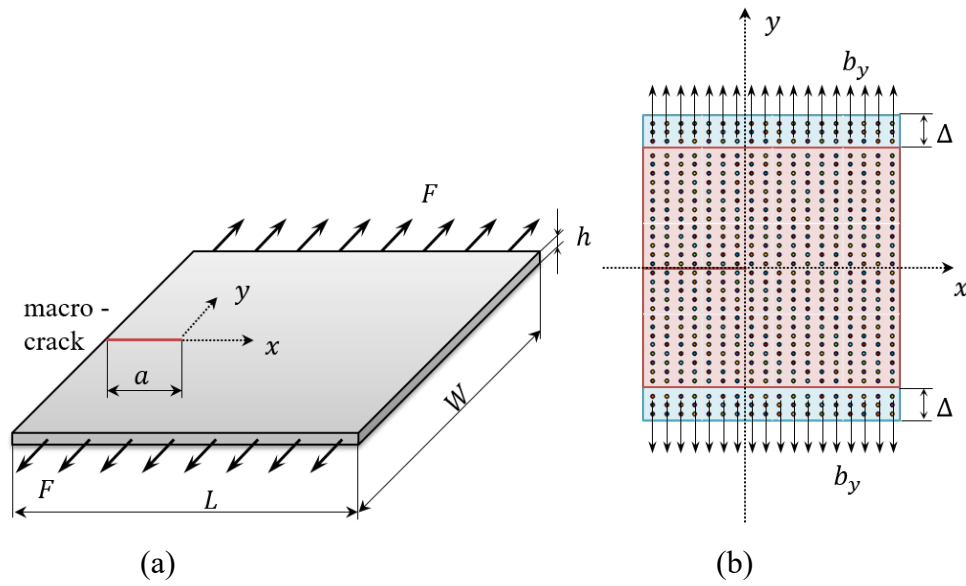
Figure 4.2 Sample geometry: (a) square plate with a macro-crack under quasi-static loading; (b) spatial discretisation of the square plate with a macro-crack under body force density BC.

4.3.2.2   Quasi-static analysis

The pre-notched thin rectangular plate described in Section 4.3.2.1 is selected for quasi-static analysis in Section 4.3.4, and the plate is loaded symmetrically by applying tensile force in the y-direction as shown in Figure 4.2.

A quasi-static loading is applied as a body force density:

$$b_y = \frac{F}{\Delta V_\Delta} \tag{4.5}$$

where F is the force and ΔV_Δ is the volume of the boundary layer, $\Delta V_\Delta = 1.98 \times 10^{-6}\ m^3$.

4.3.3   Numerical results and validation of crack propagation in PMMA plate

In this section, a comparison between PD simulations and experimental tests [203] is carried out. In particular, the crack propagation speeds and bifurcation angles are evaluated in order to assess the accuracy of the numerical model with the constant value of critical fracture energy. The other focus is on the response of the structure to the small changes in tensile loads.

The properties of the PMMA [217] are specified in Table 4.1 in Section 4.3.1, with the geometric parameters and BC described in Section 4.3.2.1. An impulsive loading is applied to obtain fast crack propagation and further bifurcation. To investigate the crack response to the tensile loads, multiple cases of the velocity BC are selected, starting with $\dot{v}^* = 1.00 \, m/s$ and increased by 0.2 m/s. The velocity is applied on the boundary edges at $y = W/2$ and $y = -W/2$ ranging from $\dot{v}^* = 1.00 \, m/s$ to $\dot{v}^* = 6.8 \, m/s$.

The PD models in Figure 4.1 are discretised with 275440 material points with uniform spacing between them $\Delta x = 5 \times 10^{-4}$ m and horizon size of $\delta = 3.015\Delta x$. A uniform time step size of $\Delta t = 2 \times 10^{-7}$ sec is used.

Based on the damage plots given in Figure 4.3 under different velocity BC, it is remarkable to see the dependency of the crack propagation behaviour on the applied loading conditions. As the intensity of the loading increases the thickening of the damage zone is observed, which is followed with further branching (Figure 4.3, from $\dot{v}^* = 1.4 \, m/s$ to $\dot{v}^* = 2 \, m/s$) or fish-bone pattern with multiple micro-branches or/and macro-branches (Figure 4.3, from $\dot{v}^* = 2.2 \, m/s$). Similar behaviour of crack propagation was observed by Bobaru and Zwang [198] for brittle materials for Soda-lime glass and Homalite 100 under velocity BC. It was also observed that the increase of the loading intensity speeds up the crack propagation and branching. Figure 4.3 presents the damage maps of all the simulations. Note that the negative x-axis indicates the pre-crack location.

Firstly, evaluating the crack propagation behaviour of a single crack bifurcation, the comparison is made with the brittle fracture experiments on PMMA performed by Suzuki and Sakaue [203], where the fracture speeds were evaluated within 5 mm before and after bifurcation as well as the bifurcation angle. It was mentioned that the mean crack speed before the bifurcation is $V_c = 688 \pm 45 \, m/s$ which drops by 42 m/s after the bifurcation with the mean crack speed of $V_c = 647 \pm 35 \, m/s$ and the bifurcation angle of 15 degrees.
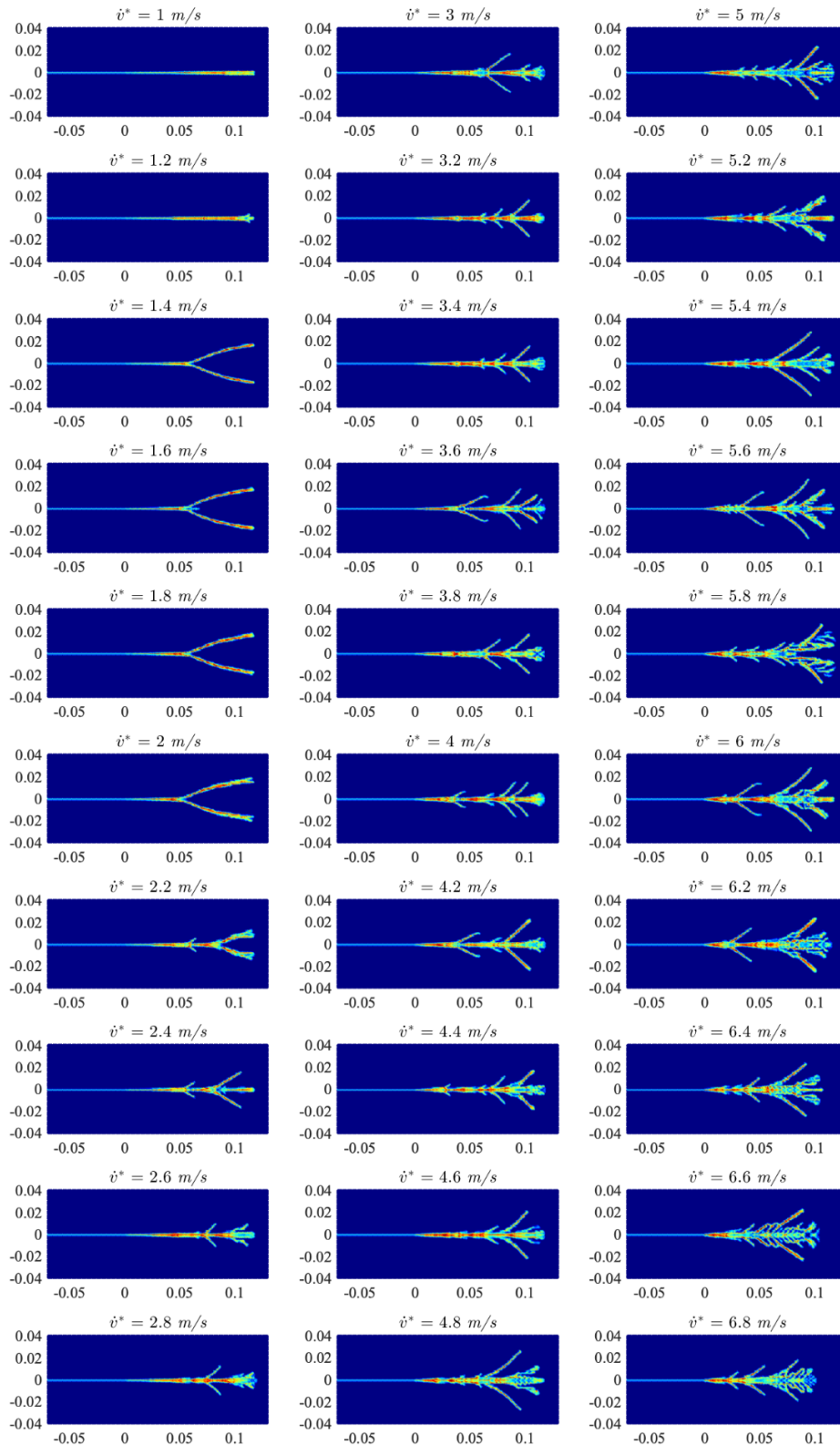
Figure 4.3 Damage maps for PMMA plate under different velocities BC. The applied velocities are specified on top of each figure.
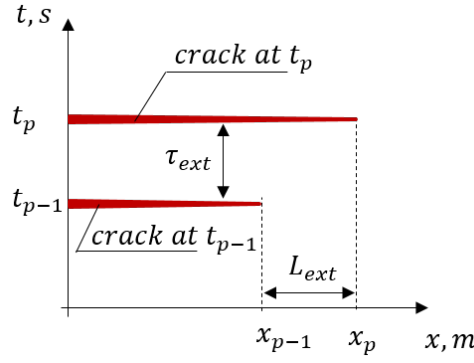
Figure 4.4 Crack propagation speed V_c evaluation.

The crack propagation speed from the numerical PD simulations is calculated as (see Figure 4.4):

$$V_c = \frac{x_{tp} - x_{tp-1}}{t_{tp} - t_{tp-1}} = \frac{L_{ext}}{\tau_{ext}} \tag{4.6}$$

where x_{tp} and x_{tp-1} are the crack tip positions at the current time t_{tp} and the previous time t_{tp-1}. L_{ext} represents the extension length of the crack propagation during the time interval τ_{ext} between t_{tp} and t_{tp-1}. For the crack propagation speed calculations, the extension length is specified as $L_{ext} = 5$ mm, which means that data-dumps are performed every 5 mm of crack tip progression.

Based on the crack behaviour under the applied loading BC between $\dot{v}^* = 1.40 \; m/s$ and $\dot{v}^* = 2.0 \; m/s$ when the crack is bifurcating, it can be seen from Figure 4.5a that the crack propagation speeds from the numerical PD model are in the range of the fracture speeds from the experimental results [203]. Under specified loading conditions, the thickening of the damaged area is noticed before the bifurcation with the mean crack propagation speed of $V_c = 500 \pm 5 \; m/s$. The bifurcation occurs when the mean crack propagation speed is $V_c = 560 \pm 10 \; m/s$. The predicted crack branching angles around 16-20 degrees is noted for all four loading BC between $\dot{v}^* = 1.40 \; m/s$ and $\dot{v}^* = 2.0 \; m/s$. The predicted crack speeds and crack bifurcation angle are quite close to the experimental observations.

Based on the experimental studies, a large decrease of crack propagation speeds relative to the single crack speeds is observed. Döll [32] and Ramulu and Kobayashi

[31] stated that before the bifurcation occurs, the crack propagation speed may accelerate, and after bifurcation, it drops by 5-10%. The recent experiments on Soda-lime glass by Sundaram and Tippur [219] showed the same pattern of the crack propagation behaviour with a drop of crack propagation speed by 30% prior to bifurcation and followed by a significant increase at branching and a fast drop by 30% after the bifurcation. Numerical studies, by means of PD [220, 221], showed a similar trend of fracture speeds in the bifurcation zone. Evaluating the crack bifurcation of PMMA in Figure 4.5 from the numerical PD model, the crack propagation speed decreases when the thickening occurs and increases rapidly before bifurcation following by a drop of 6% after bifurcation for both loading conditions. Moreover, two branches propagate with higher crack speeds than a single crack. The results for the crack propagation speed and crack growth distance after the bifurcation are analysed for the upper crack branch.

Secondly, the dynamic stretch of the plate under higher velocity BC in Figure 4.3 showed the formation of multiple micro-branches. It can be noticed, as the velocity of the crack is increasing, the length of the branches, as well as their number is increasing. The branching angles vary, and in most cases, lower crack speeds result in smaller angles. For example, the PD damage plot with the velocity BC increase of $\dot{v}^* = 2.4 \, m/s$ resulted in the first crack branching of around 30 degrees and at $V_c \sim 0.57 c_R$ (Figure 4.5b), followed by a longer branch of around the same angle of 30 degrees, but the second branch initiated at a higher crack speed of $V_c \sim 0.76 c_R$ with the distance between two branches is 0.03 m. On the other hand, the velocity of $\dot{v}^* = 3.2 \, m/s$ resulted in three branches (Figure 4.5b): the first one at crack tip location of $x_{tp} = 0.058 \, m$ with branching angle of 30 degrees at $V_c \sim 0.74 c_R$ and the other two branches with increasing branching angles by 5 degrees at $V_c \sim 0.75 c_R$ $(x_{tp} = 0.07 \, m)$, and 10 degrees at $V_c \sim 0.77 c_R$ $(x_{tp} = 0.085 \, m)$. The trend of higher branching angle with the longer branches can be noticed in all the simulations, as well as the occurrence of micro-branches with 12 degrees angles, followed by the long crack bifurcation, shown in Figure 4.5c. All the results of crack propagation have the same trend of the crack bifurcation, starting at $V_c \sim 0.57 c_R$ and upper with further drop and after the recovery.

The variation in branching patterns and angles is dependent on fluctuations in crack velocity, and when the velocity reaches the critical value, the crack is branching.

The comparison of the numerical crack propagation speed to the Rayleigh wave speed is shown in Figure 4.5, where PD numerical velocities are normalised by the Rayleigh wave speed c_R of the material which is $c_R \approx 934 \, m/s$ for the PMMA material.

The evaluation of c_R is performed by the approximate expression for the Rayleigh wave speed c_R [209]:

$$\frac{c_R}{c_2} = \frac{0.862 + 1.14\nu}{1 + \nu} \tag{4.7}$$

where ν is the Poisson's ratio. In terms of shear modulus μ and material density ρ, the speed of shear waves is defined as:

$$c_2 = \sqrt{\frac{\mu}{\rho}} \tag{4.8}$$

The performed PD simulations showed the dynamic instability of the propagating crack. It can be seen that the branching is a function of the crack velocity and the branching is not observed below the critical velocity. The experiments performed by [212] analysed the effect of the crack velocity on the occurrence of branching, showing that the increase of the velocity results from the micro-branching instability. The following nature can be explained as the energy release from the potential energy with the increased crack speed resulting in creating new crack branches. While the energy is distributing over the new cracks, the crack propagation velocity is decreasing. Moreover, the PD study showed the relation between the branch initiation and the branching angles and lengths, as the higher crack propagation speeds bring wider and longer crack bifurcations. On the other hand, the constant critical elongation parameter was used in the presented numerical simulations, which is simplified and not dependent on the loading condition and crack propagation speeds.

(a)

(b)

(c)
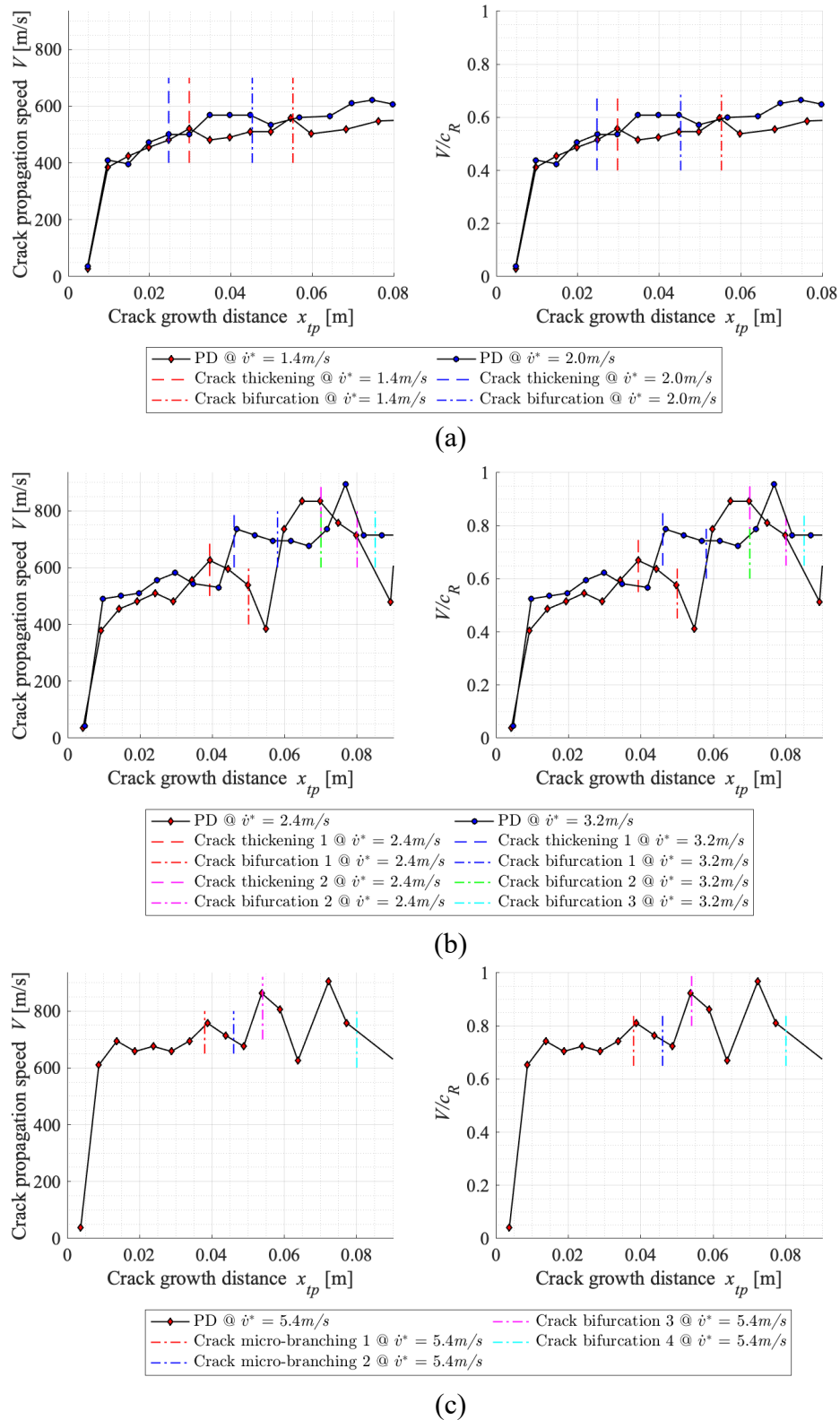
Figure 4.5 Crack propagation speeds and the ratios of numerically computed speed to the Rayleigh wave speed for PMMA plate under velocity BC of: (a) $\dot{v}^* = 1.4\,m/s$ and $\dot{v}^* = 2.0\,m/s$ (b) $\dot{v}^* = 2.4\,m/s$ and $\dot{v}^* = 3.2\,m/$ and (c) $\dot{v}^* = 5.4\,m/s$.

4.3.4   Numerical analysis and validation of concrete plate containing microcracks

In this section, the impact of the micro-cracks on the main (macro-) crack behaviour is analysed. The geometric parameters characterising the interaction of the macro- and micro-cracks are the dimensions of the cracks, distances between the micro-cracks, and the micro-cracks orientation.
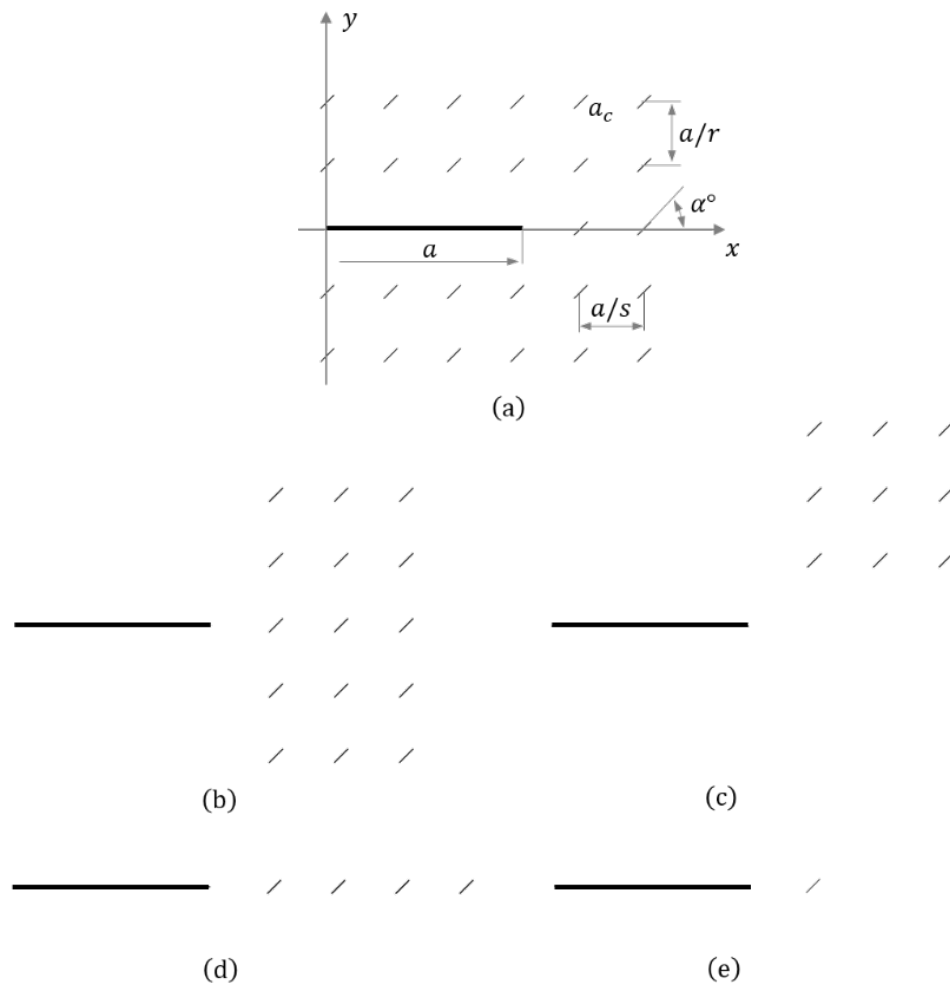
Figure 4.6 Micro-crack distribution diagrams [58]: (a) micro-cracks surrounding the main crack tip; (b) micro-cracks ahead of the crack tip; (c) asymmetrical arrangement of micro-cracks (+y domain) ahead of the main crack tip; (d) a set of micro-cracks ahead of the crack tip; (e) single micro-crack ahead of the main crack tip.

Figure 4.6 shows the PD model, which consists of a macro-crack with a size of $a = 0.045\ m$ at the left side of the plate with five different cases of distributed micro-cracks are considered with a length of $a_c/a = 0.1$. The distances between the micro-cracks are a/s and a/r with $s = r = 3$ and they are located in front and/or around the macro-crack tip, as shown in Figure 4.6. The parameters a_c, s, r and micro-cracks distributions are selected the same as in the study on the interaction of large crack with the array of micro-cracks [58] in order to compare the PD numerical results with analytical results in [58]. For each of the cases from (a) to (e), micro-crack configurations are analysed with the crack inclination of α varying from 0 to 90 degrees. Micro-cracks are regularly located in +y and/or –y domains and/or in front of the main crack tip. Firstly, the study in Section 4.3.4.1 is performed to investigate if the presence of the defects ahead of the macro-crack tip facilitates its further propagation. Secondly, Section 4.3.4.2 presents the study of how micro-cracks affect macro-crack propagation.

The allocation of micro-cracks in the PD numerical model is performed by breaking the bounds between material points. The principle is the same as discussed in Section 3.3.5 and as shown in Figure 3.4. When the bond between two material points is passing through the micro-crack, the failure parameter $\psi = 0$. If the bond between two points is intact, then $\psi = 1$. The intact bonds can be broken in time only if the stretch of the bond exceeds the pre-defined critical stretch s_c.

4.3.4.1   Quasi-static analysis of the critical load

The numerical model is set up for the concrete plate with the material properties specified in Table 4.1 in Section 4.3.1 and the geometric parameters and BC described in Section 4.3.2.2. The PD model is discretised with 69520 material points (Figure 4.2b) with uniform spacing between them $\Delta x = 0.001$ m and $\delta = 3.015\Delta x$. The plate is loaded symmetrically by applying quasi-static tensile loading in the y-direction (Figure 4.2). The quasi-static analysis is performed under an explicit time integration scheme with a stable time step size of $\Delta t = 1$ and a total time step of 3000 is sufficient to reach a stable solution by means of ADR technique [195], described in Section

3.4.2.1. After applying an initial loading of $F = 90\ N$ and reaching the steady-state solution the applied force is increased by $\Delta F = 1\ N$ for each 3000-time steps. The stretch of the bonds between material points is evaluated and when the first bond is broken if the stretch exceeds the critical stretch, i.e. $s > s_c$, the applied force is referred to as the critical load p. The critical loads are identified as p^0 for a plate with only a single macro-crack and p^* for the plate with a macro-crack and distributed micro-cracks.

The PD numerical models are analysed based on the relationship between the SIF of the case with a macro-crack K_0 and cases including micro-cracks K^* for all PD numerical models. First, constant fracture energy of $G_0 = 570\ \text{J/m}^2$ is considered for all cases. In this respect, the numerical model is evaluated under constant critical stretch based criteria, $s_c^* = s_c = 0.0038$ for all five cases of micro-crack distributions with s_c^* as well as for the case with only one macro-crack with s_c. Furthermore, critical stretch is not influenced by micro-crack configurations and crack inclination angles α varying from 0 to 90 degrees.

The results of the PD simulations are presented in Figure 4.7 based on the ratio of the critical loads p^* and p^0. Although a similar pattern of the micro-crack influence on main crack propagation is noticed by analytical solutions [58], analytical results have lower ratios of the critical loads for the inclination angles from 0 to 45 degrees compared to the PD simulations. The reason for the difference in the critical loads is the critical stretch which is constant in all PD simulations. The authors in [222] illustrate that the SIF decreases when the main crack is surrounded by multiple micro-cracks. Furthermore, Kachanov [53, 223] showed the influence of the micro-crack arrays and the inclination of the cracks on the geometry, which results in shielding effects or weakening.
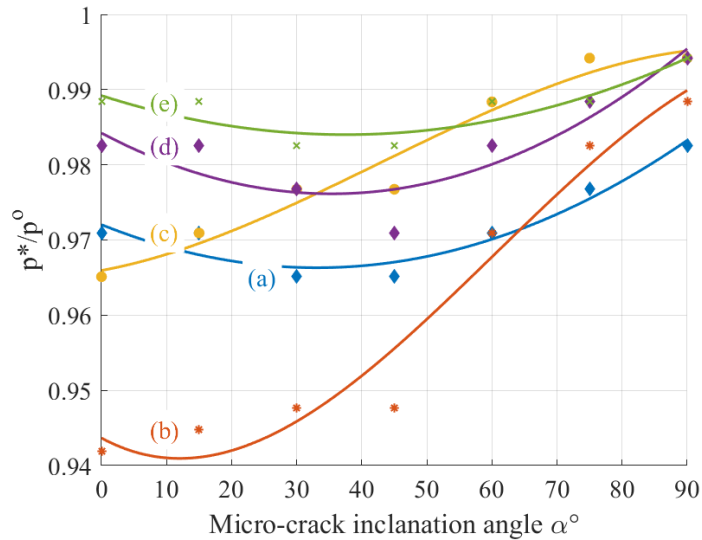
Figure 4.7 The ratios of the critical loads as a function of micro-crack orientation when constant critical stretch is considered for micro-crack distribution cases from (a) to (e). Markers present the PD scatter data and solid lines – PD polynomials for cases from (a) to (e).

Kachanov [223] evaluated two configurations of the micro-crack distributions: collinear cracks and stacked ones. He demonstrated in his work that the collinear cracks showed the stress amplification effect, which leads to an increase of SIF; contrary, the stacked configurations showed the stress shielding effect with the decrease of SIF. The further evaluation of the distributed cracks by Kachanov showed the influence of the crack dimensions and distances on the amplifying or shielding outcome and depending on the crack distributions, these two phenomena can compete. The author states that for traction BC (mode I), if the distances between the collinear a/s and stacked a/r configurations are higher than the length a_c of the cracks, the shielding effect is dominant. In order to get the amplifying effect of the cracks in the structure, the distance a/s should be much smaller than a/r [223]. In addition, other factors have an influence on the SIF, such as the crack number in the periodic coplanar row of cracks, periodic stack of parallel cracks, and the rotation of the cracks. According to Kachanov, with the increased number of parallel stack cracks, the SIF is decreasing, instead for the coplanar row of cracks SIF is increasing and $K^*/K_0 \approx 1$. Moreover, the distribution of the micro-cracks around the main-crack brings stress shielding effect. Similar effects of the arrays on the macro-crack tip, causing SIF amplification is found by multiple authors [56, 224, 225]. When the micro-cracks are rotated by $90^0 \geq \alpha^0 > 0$, high

impact is noticed of micro-cracks on macro-crack. The surrounding distribution of the micro-cracks leads to an increase of SIF with the micro-crack rotation from 0 to 90 degrees.

Evaluating the selected micro-crack distribution diagrams for PD analysis, the distances between the micro-cracks are bigger than the length of the cracks $a/s \gg a_c$ and the effect of the shielding is dominant in the structure. Thus, SIF for the cases, including micro-cracks, should be smaller than the cases with only one macro-crack, resulting $K^* < K_0$. Considering the outcome of the analytical solutions from [223] for the impact of the micro-cracks with rotational angles $\alpha^0 = 0$ degrees on SIF of the macro-crack tip, the following relationships K^*/K_0 are considered in the PD model: (a) $K^*/K_0 = 0.90$, (b) $K^*/K_0 = 0.84$, (c) $K^*/K_0 = 0.93$, (d) $K^*/K_0 = 0.96$, (e) $K^*/K_0 = 0.98$.

The selected K^*/K_0 are implemented in the numerical model by factorising the critical stretch values by K^*/K_0 ratios, where $s_c^* < s_c$. Furthermore, to include in the PD model the influence of the micro-crack inclinations on a macro-crack tip, critical stretch ratios are gradually increasing, resulting in the cases at $\alpha^0 = 90 \, deg$: (a)-(c) $s_c^* \approx 0.0036$, (d)-(e) $s_c^* \approx s_c = 0.0038$. The difference in the applied critical stretch values between the cases (a)-(c) and (d)-(e) results from the location of the micro-cracks, as the micro-crack distribution behind and above the macro-crack tip with the angle of rotation $\alpha^0 = 90^0$ leads to $K^*/K_0 < 0.96$ [223]. The employment of the relationship of K^*/K_0 in the PD model (Figure 4.8) showed more reasonable results compared to the analytical results in [58], which are based on asymptotic analytical solutions and the series solution to describe the macro- and micro-cracks interaction problems. The PD results with the implemented relationship of $K^*/K_0 \neq 1$ confirm the crack propagation's dependency on micro-crack distribution and deviation angle.
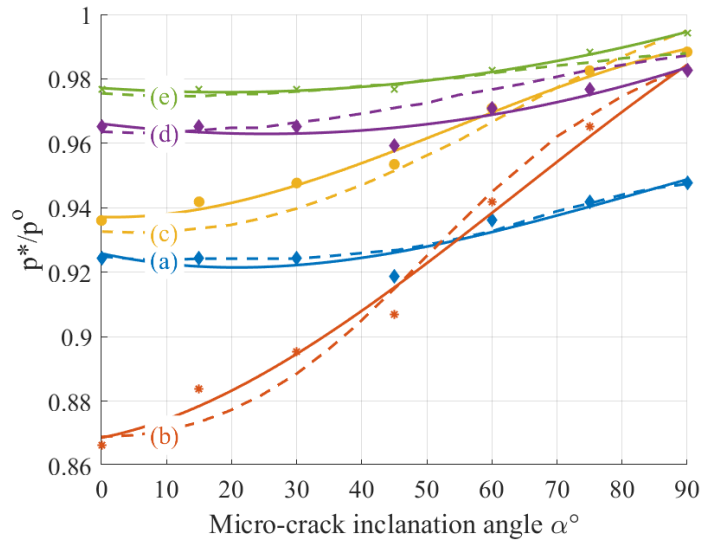
Figure 4.8 The ratios of the critical loads as a function of micro-crack orientation when K^*/K_0 for micro-crack distribution cases: (a) $K^*/K_0 = 0.90$, (b) $K^*/K_0 = 0.84$, (c) $K^*/K_0 = 0.93$, (d) $K^*/K_0 = 0.96$, (e) $K^*/K_0 = 0.98$. Markers present the PD scatter data, dashed lines – PD polynomials for cases from (a) to (e), and solid lines – Analytical solution for the cases from (a) to (e) [58].

4.3.4.2 Crack propagation behaviour in a plate containing micro-cracks

According to the study in Section 4.3.4.1, it is numerically demonstrated the influence of the micro-cracks on SIF of the macro-crack tip and their impact on the critical load. The interest of this section is to evaluate the influence of the micro-cracks on macro-crack propagation behaviour and speed. To calculate the crack propagation speeds, the concrete plate in Figure 4.1 is subjected to dynamic BC and loaded symmetrically by applying velocity constraints of $\dot{v}^* = 0.4 \ m/s$ on the plate edges at $y = \frac{W}{2}$ and $y = -\frac{W}{2}$. The BC, proposed in [218], are applied to the fictitious boundary layer R_f. The size of the R_f region is equal to the horizon size, which is $\delta = 3.015 \ \Delta x$. The BC are enforced as indicated by Eqs. (4.1)-(4.4) in Section 4.3.2.1.

The Peridynamic model in Figure 4.1b is discretised with 272800 material points with uniform spacing between them $\Delta x = 0.0005$ m. All simulations are performed with a time step size of $\Delta t = 0.2 \mu s$ and stopped at $t = 300 \mu s$.

In Section 4.3.4.1, it is noted that factorising the critical stretch values for the cases (a)-(e) in Figure 4.6 with micro-cracks distribution in the plate provided the results of

the ratios of critical loads, which are very close to the analytical solutions. Another important point is to see if the SIF at the macro-crack tip influences the crack propagation behaviour and speeds. It should be noted that the relation between K^*/K_0 is presenting the influence of the micro-cracks on the SIF of the macro-crack tip and is not speed dependent. This means that a constant fracture energy model is used, and critical fracture energy is not changing with the crack propagation speed [32, 226].

Firstly, the PD numerical models for the cases (a)-(e) in Figure 4.6 are analysed with the relation between the SIF of the case with macro-crack K_0 and the cases including micro-cracks K^* by using a constant critical stretch, which is dependent on critical fracture energy and evaluated by Eq. (3.17). Secondly, the relation between K^*/K_0 is varied in the PD model according to the cases: (a) $K^*/K_0 = 0.90$, (b) $K^*/K_0 = 0.84$, (c) $K^*/K_0 = 0.93$, (d) $K^*/K_0 = 0.96$, (e) $K^*/K_0 = 0.98$. The relations K^*/K_0 are implemented in the numerical model in the same way as described in Section 4.3.4.1 by factorising the critical stretch values by K^*/K_0 ratios.

Figure 4.9 presents the damage plots for all cases when constant critical stretch is considered and Figure 4.10 is for $K^*/K_0 \neq 1$ and the micro-crack inclination angles are $\alpha^0 = 0°, 45°$ and $90°$. It can be noted that the micro-crack inclination angles have an influence on the macro-crack propagation behaviour, where the macro-crack tends to follow the orientation of the micro-cracks. Moreover, when the micro-crack is located at the front and perpendicular to the macro crack, $\alpha^0 = 90°$, this leads to bifurcation of the macro-crack. Both types of critical stretch implementation showed a similar pattern of crack propagation, but the difference in the crack propagation and speeds can be noticed in Figure 4.11 and Figure 4.12. The adjusted critical stretch value according to SIF cases show higher crack propagation speeds as in Figure 4.13.
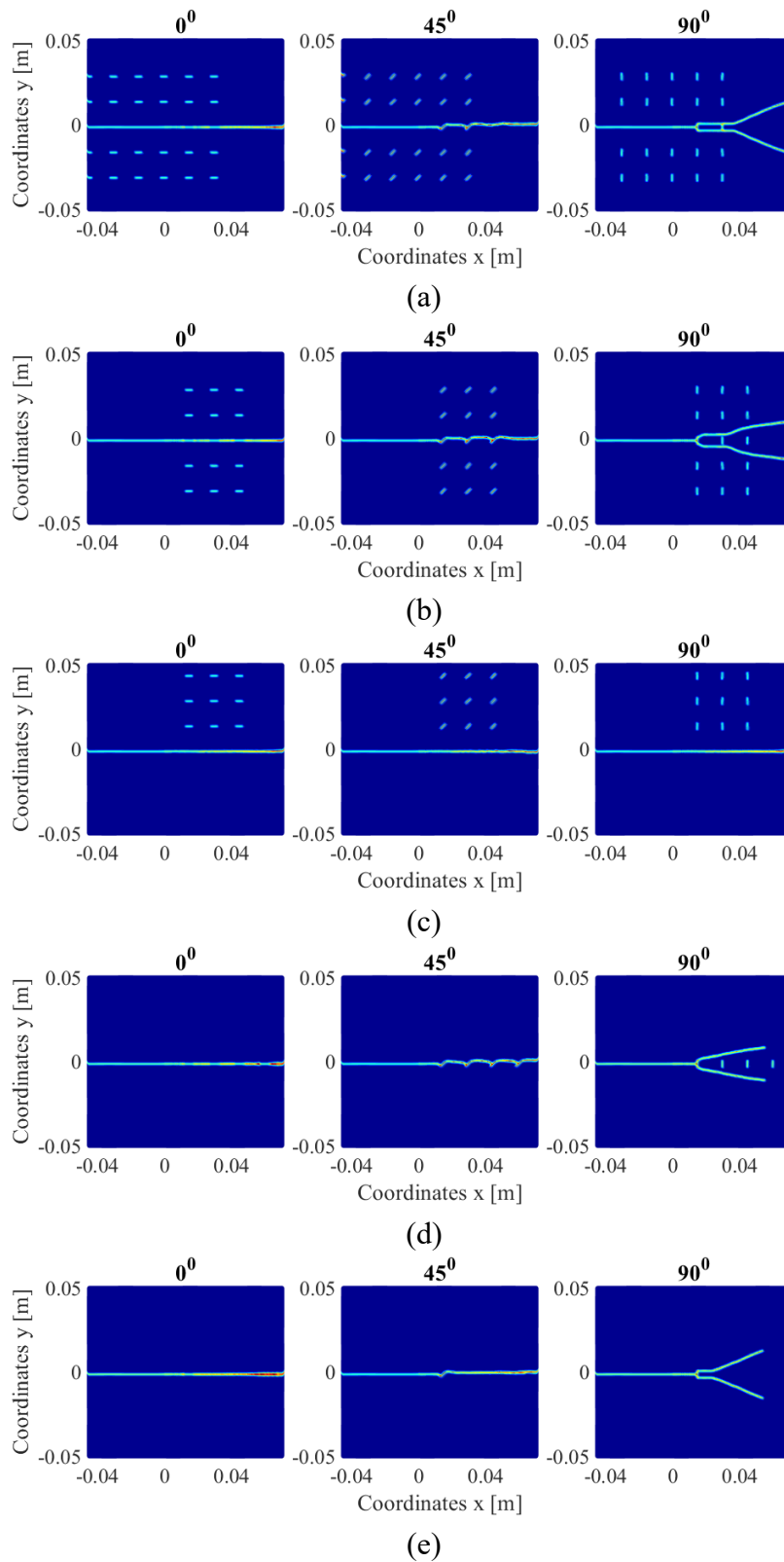
Figure 4.9 Damage plots of the crack propagation, when constant critical stretch is considered for the cases from (a) to (e) with multiple micro-cracks with the crack inclination of $\alpha^o = 0°, 45°$ and $90°$.

(a)

(b)

(c)

(d)

(e)
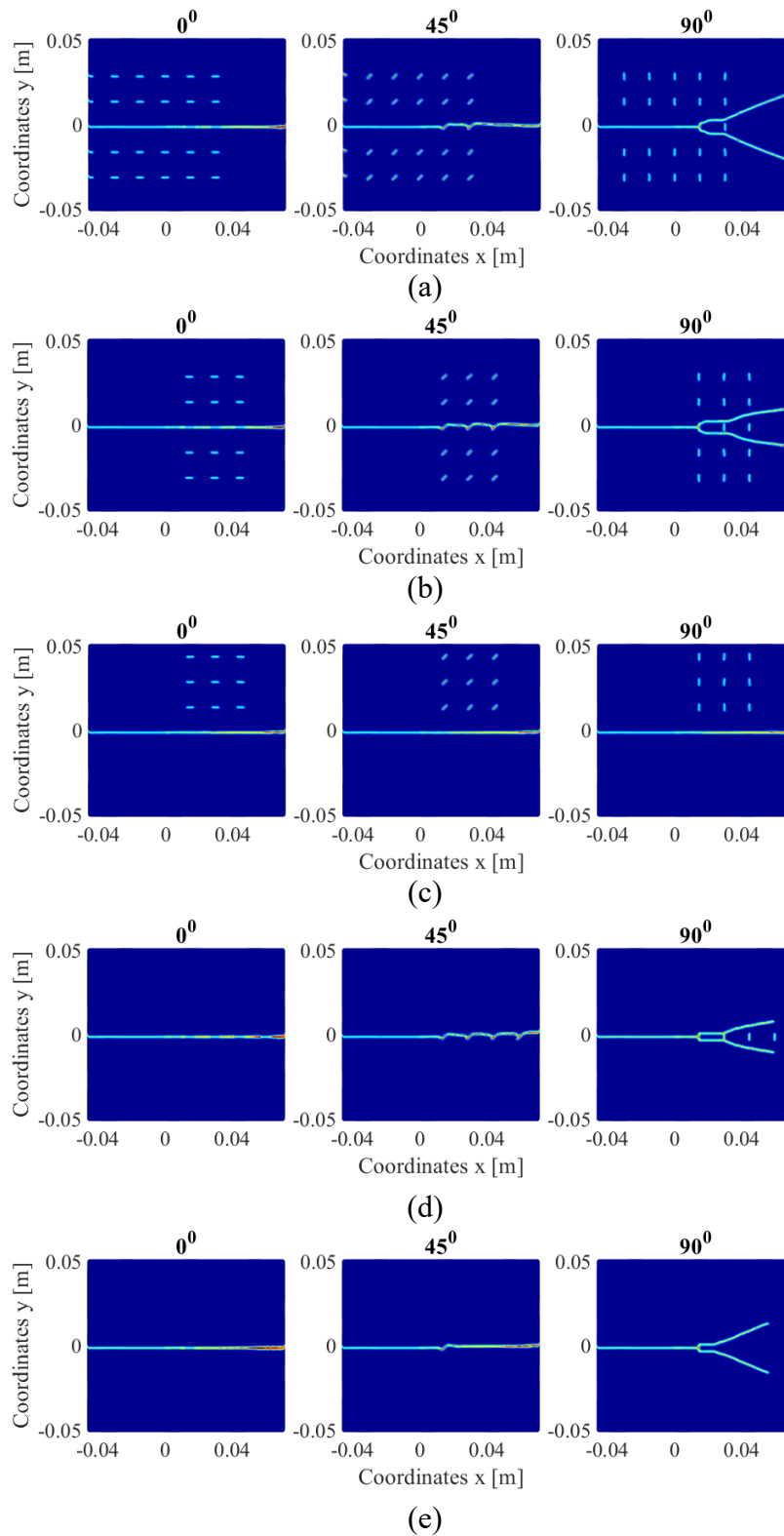
Figure 4.10 Damage plots of the crack propagation for the cases from (a) to (e) when K^*/K_0 for micro-crack distribution: (a) $K^*/K_0 = 0.90$, (b) $K^*/K_0 = 0.84$, (c) $K^*/K_0 = 0.93$, (d) $K^*/K_0 = 0.96$, (e) $K^*/K_0 = 0.98$, with the crack inclination of $\alpha^o = 0°, 45°$ and $90°$.

The crack propagation speed is evaluated by Eq. (4.6), when the macro-crack tip location becomes at $x = 0.05\,\mathrm{m}$. From Figure 4.11 and Figure 4.12 it can be noticed that the micro-cracks parallel to the macro-crack leads to an increase in crack propagation speed. On the other hand, the micro-cracks perpendicular to the macro-crack yields a shielding effect [188] leading to a decrease in crack propagation. Moreover, the crack opening of surrounding micro-cracks leads to energy dissipation and an increase in crack propagation resistance. When the micro-cracks are not distributed in front of the macro-crack, as in case (c), the crack propagation speed is similar to the case with only macro-crack is allocated. The micro-cracks act as the suppressors of the macro-crack propagation in the case (a) of micro-crack distribution (inclination $\alpha^o = 0^o$) which decreases the crack speed compared to the case (b).

The other point to mention is the crack propagation over time. Figure 4.13 presents results for each case (a) to (e) of micro-crack distributions with inclination angles α varying from 0 to 90 degrees ahead of the main crack tip when the relation $K^*/K_0 \neq 1$ is implemented. The numerical results show that only co-linear distribution of the micro-cracks, case (d) and (e), in front of the macro-crack delaying the crack propagation at the initial stage. Moreover, for most of the studied cases, the bigger crack inclination angle increases the propagation time. On the other hand, the hold off time is very small, around 30 μs, and after pathing through the micro-crack, the crack continues fast propagation. Only the crack bifurcation in all the cases showed a major impact on crack delay. Based on the performed PD simulation results, it can be concluded that the types of micro-cracks, their sizes, distributions and orientations have a remarkable influence on the toughening mechanisms in the system.
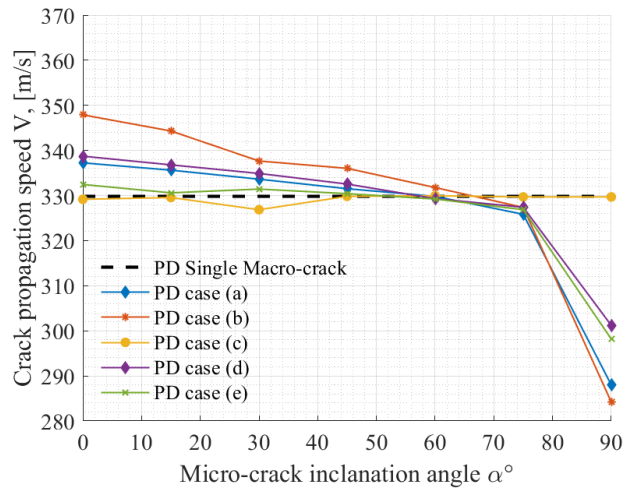
Figure 4.11 Numerical results for the concrete plate under velocity BC $v_l = 0.4$ m/s for a crack speed as a function of micro-crack orientation and when constant critical stretch is considered. Crack speed is evaluated at the crack tip location $x = 0.05\ m$.
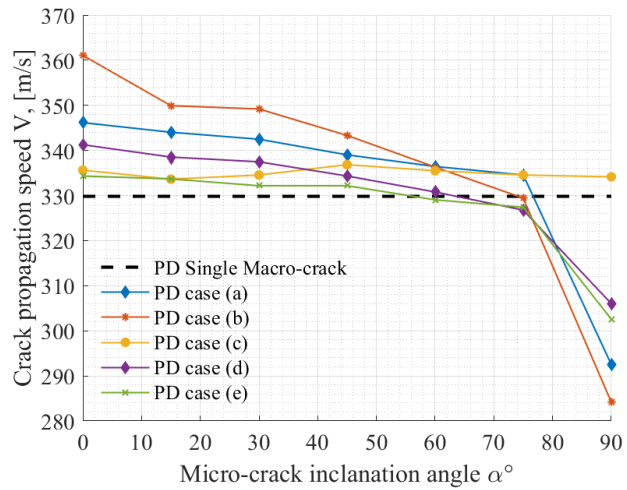
Figure 4.12 Numerical results for the concrete plate under velocity BC $v_l = 0.4\ m/s$ for a crack speed as a function of micro-crack orientation. The parameter $K^*/K_0 \neq 1$: (a) $K^*/K_0 = 0.90$, (b) $K^*/K_0 = 0.84$, (c) $K^*/K_0 = 0.93$, (d) $K^*/K_0 = 0.96$, (e) $K^*/K_0 = 0.98$. Crack speed is evaluated at the crack tip location $x = 0.05\ m$
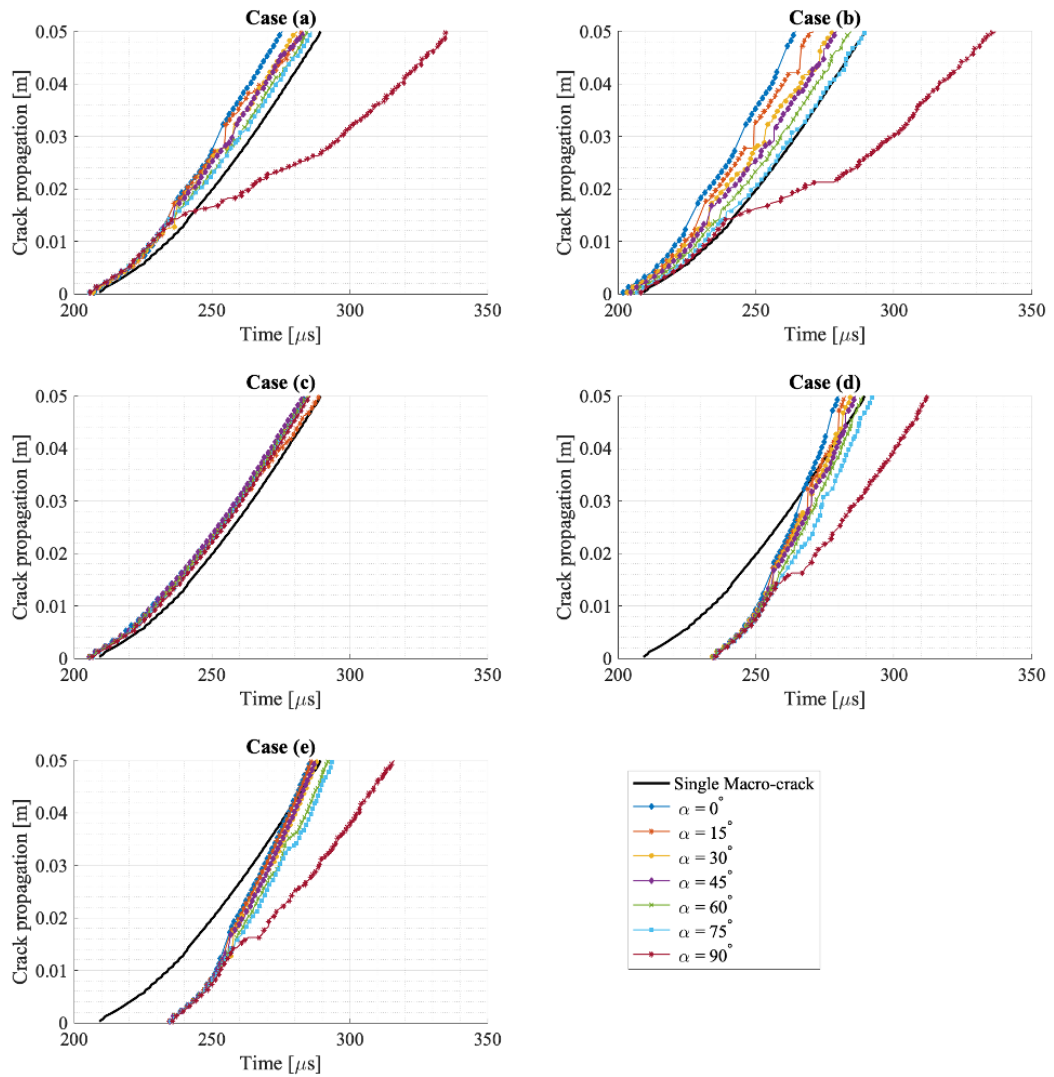
Figure 4.13 Numerical results for the concrete plate under velocity BC $v_l = 0.4\, m/s$ for a crack propagation as a function of time for all the cases (a) to (e) of the micro-crack distribution with different micro-crack inclination angles α. The parameter $K^*/K_0 \neq 1$ for cases: (a) $K^*/K_0 = 0.90$, (b) $K^*/K_0 = 0.84$, (c) $K^*/K_0 = 0.93$, (d) $K^*/K_0 = 0.96$, (e) $K^*/K_0 = 0.98$.

4.4   Brittle fracture due to bending

In this section, a three-point bending test is considered to analyse the crack propagation behaviour when hole defects exist in the structure. Firstly, the PD model under static load is verified with FEM to set up the BC. Secondly, the solution is presented for crack propagation behaviour under dynamic loading with the presence of defects. Five different types of holes are selected for the numerical analysis. The effect of the hole in the structure is investigated for a PMMA plate in order to verify the

numerical PD model with the experimental tests [204]. Besides, the validated model is applied on a concrete plate for a crack behaviour analysis.

A series of PD simulations are conducted to:

- study the influence of Young's modulus, density, Poisson's ratio, and fracture energy on crack behaviour in the presence of the hole defects;

- investigate and analyse the influence of the hole dimensions on crack propagation and crack-arrest phenomena;

- analyse the impact of different velocity BC on the crack path and crack propagation speed.

4.4.1 Material data

For brittle fracture analysis of the plate, subjected to three-point bending loading, two types of materials are employed in the presented studies. PMMA and concrete are both considered for the dynamic crack propagation problems. The material properties are summarised in Table 4.2.

Table 4.2 Material data for brittle fracture due to bending

Material	Young's modulus, E [GPa]	Poisson's ratio, ν	Energy release rate, G_0 [J/m^2]
PMMA [204]	6.1	0.31	220
Concrete [58]	17	0.15	110

4.4.2 Geometry and boundary conditions

4.4.2.1 Static analysis

A plate with a length of $L = 0.2\ m$, a width of $W = 0.05\ m$ and thickness of $h = 0.005\ m$ in Figure 4.14a is subjected to three-point bending loading. The supports are located $L_s = 0.14\ m$ from each other. The pre-existing crack of $2a = 0.005\ m$ is located at the bottom edge of the plate.

(a)

(b)
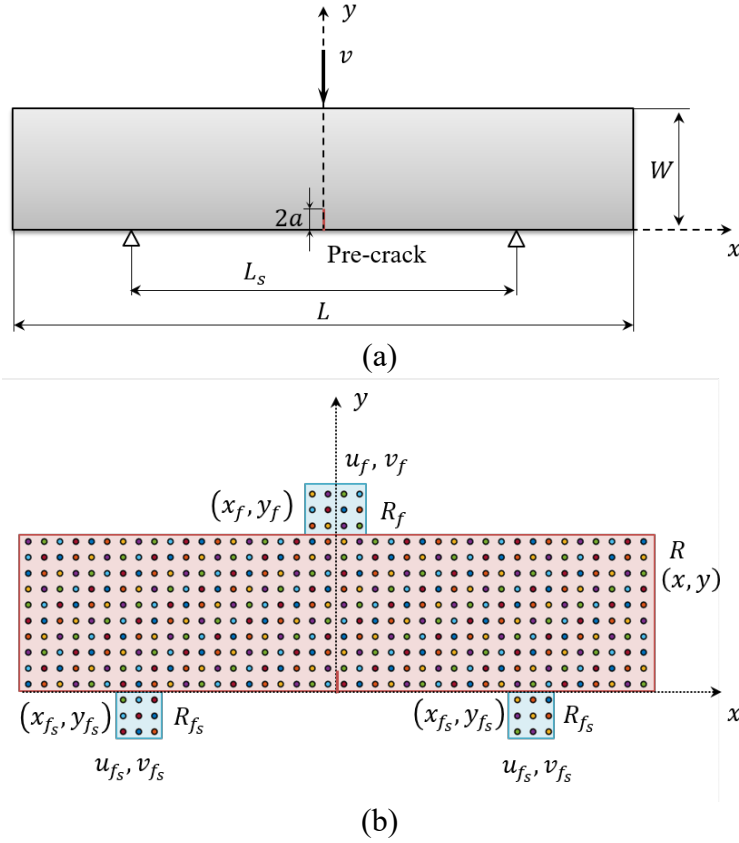
Figure 4.14 (a) Pre-cracked rectangular plate under bending loading and (b) its discretisation.

The plate is subjected to the displacement constraints of $v(x, y = W, t)$ and fully fixed supports at $y = 0$. The BC are enforced in the fictitious boundary layer R_f in the following way (Figure 4.14b):

$$u_f\left(x_f, y_f, t + \Delta t\right) = 0 \text{ at } -2\Delta x \leq x \leq 2\Delta x \text{ with } x_f \in R_{f(-2\Delta x \leq x \leq 2\Delta x)} \quad (4.9)$$

$$v_f\left(x_f, y_f, t + \Delta t\right) = -v(x, y, t + \Delta t) \text{ at } W \leq y \leq W + \delta$$

$$\text{with } y_f \in R_{f(W \leq y \leq W + \delta)} \quad (4.10)$$

$$u_{f_s}\left(x_{f_s}, y_{f_s}, t + \Delta t\right) = 0 \quad (4.11)$$

$$v_{f_s}\left(x_{f_s}, y_{f_s}, t + \Delta t\right) = 0 \quad (4.12)$$
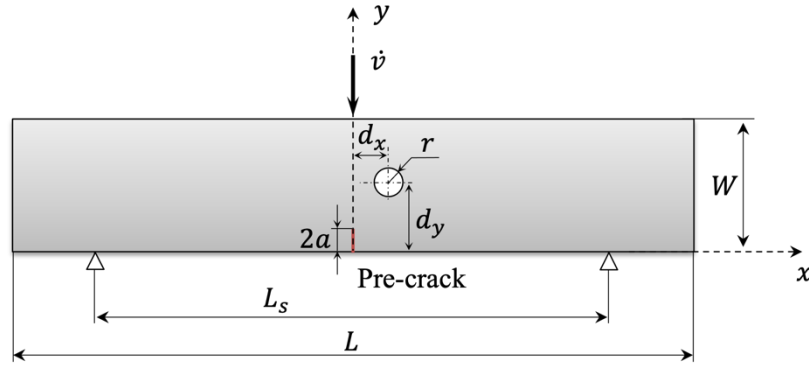
Figure 4.15 Pre-notched rectangular plate with a hole defect under bending.

4.4.2.2   Dynamic analysis

The plate in Figure 4.15 is subjected to dynamic loading conditions with a hole of the radius R. Hole is located at a distance of $d_x = 0.003 + r\ m$ and $d_y = 0.025\ m$ from the origin of the main coordinate system located at the bottom of the crack. Velocity BC of $\dot{v}$ are applied at the fictitious region at the top edge of the plate (Figure 4.14b) as following:

$$u_f\left(x_f, y_f, t + \Delta t\right) = 0 \text{ at } -2\Delta x \leq x \leq 2\Delta x \text{ with } x_f \in R_{f(-2\Delta x \leq x \leq 2\Delta x)} \qquad (4.13)$$

$$v_f\left(x_f, y_f, t + \Delta t\right) = -\dot{v}(x, y, t + \Delta t) \times \Delta t \text{ at } W \leq y \leq W + \delta$$
$$\text{with } y_f \in R_{f(W \leq y \leq W + \delta)} \qquad (4.14)$$

The fully fixed supports at $y = 0$ are enforced by Eqs. (4.11) and (4.12).

4.4.3   Numerical results and validation

4.4.3.1   Benchmark problem

In order to set up the numerical model for the dynamic crack propagation problem in three-point bending plate, the initiation of the BC in PD model are validated with FEM. The PMMA plate with material properties from Table 4.2 and the geometry from Section 4.4.2.1 is subjected to the displacement constraints of $v(x, y = W, t) = 5 \times 10^{-3}$ m . The BC are enforced by Eqs. (4.9)-(4.12). Displacement BC are applied at the fictitious region R_f located in the middle of the top edge of the plate. The PD

model is discretised with 430 material points with uniform spacing between them $\Delta x = 0.005\,m$ m and horizon size of $\delta = 3.015\Delta x$. A total time step of 2000 is sufficient to reach the quasi-static loading condition by means of ADR method with a time step size of $\Delta t = 1\,sec$ [195]. The supports are set up as a fully fixed displacement and velocity BC in a fictitious region R_{f_s} at the bottom side of the plate. The R_{f_s} regions are equal to the horizon size $\delta = 3.015\,\Delta x$. The PD results are compared against FEM results obtained by using ANSYS, a commercial finite element software. As shown in Figure 4.16, the PD results are in good agreement with FEM results for the displacements along the centre lines of the plate.

4.4.3.2   Hole defects in PMMA

PMMA plate described in Section 4.4.2.2 is investigated under dynamic loading conditions and including a pre-existing crack, as shown in Figure 4.15 [204], and five cases of different hole radiuses r: $r = 0$, only pre-existing crack is allocated, $r = 0.002\,m$, $r = 0.003\,m$, $r = 0.004\,m$, $r = 0.005\,m$. The model is analysed under velocity BC of (a) $\dot{v} = 3$ m/s and (b) $\dot{v} = 5$ m/s

The PD models are discretised with 160000 material points with uniform spacing between them $\Delta x = 0.00025$ m and horizon size of $\delta = 3.015\Delta x$. Uniform time step size of $\Delta t = 0.072\mu s$ is used. The critical stretch is specified as $s_c = 0.01072$ corresponding to an energy release rate of $G_0 = 220\,J/m^2$.

(a)   (b)
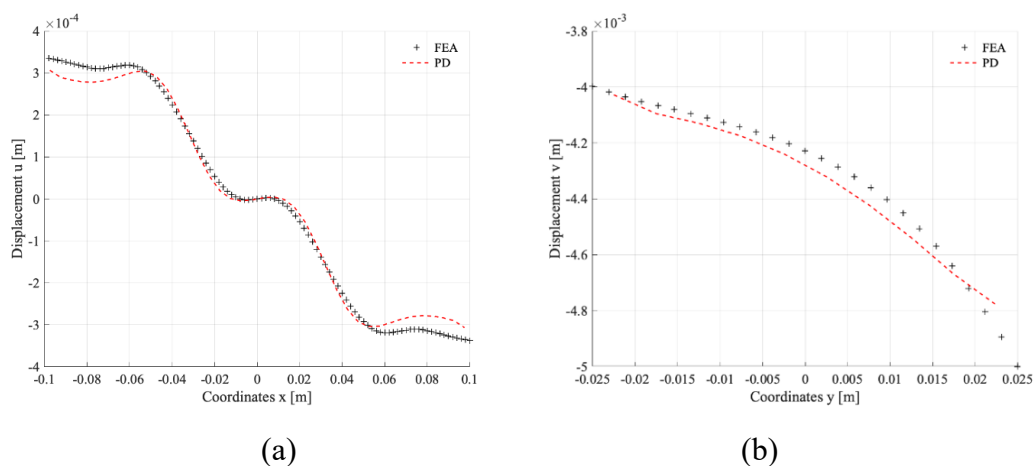
Figure 4.16 Displacement variations along the centre lines (a) $u\,(x,\ y = 0)$ and (b) $v(x = 0,\ y)$.

The crack propagation behaviour for different loading conditions from PD analysis is shown in Figure 4.17a,b. When there is no hole defect in the structure, the crack propagates in a self-similar fashion. On the other hand, when hole defects are allocated in the structure, the crack path changes and deflects towards the holes. The same pattern of crack propagation is noticed during the experimental tests [204], shown in Figure 4.17c. A higher deflection is observed for larger holes where the crack approaches the defect and after propagating close to the defect, it restores its original path. A curved crack trajectory can be noticed which is almost symmetrical with respect to the local axis of the hole. For both velocity BC, the crack moves towards the hole and then it is momentarily arrested at the boundary of the hole without intersecting with the hole. It then moves further towards the location of the applied BC [60].
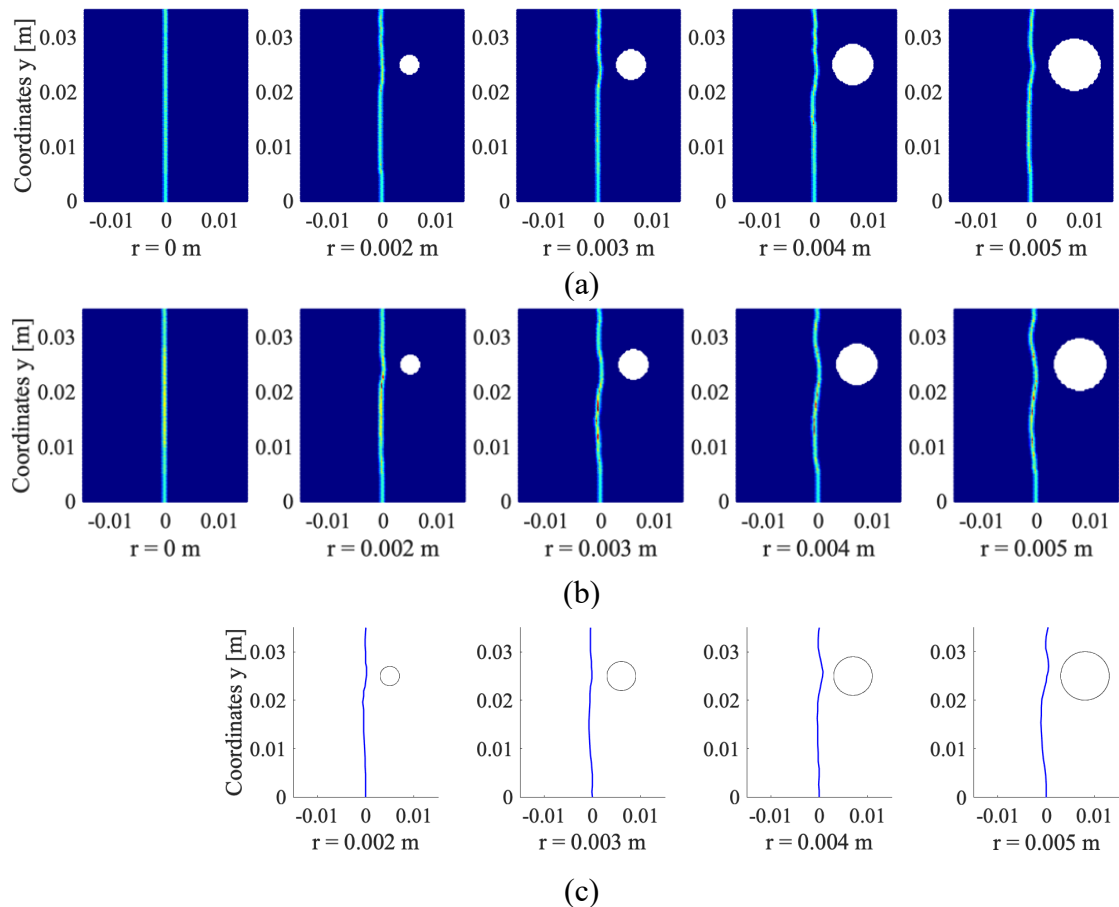
Figure 4.17 PD Damage maps of the PMMA plate with different values of the hole radius r and under velocity BC: (a) $\dot{v} = 3$ m/s at time $t = 360 \mu s$ and (b) $\dot{v} = 5$ m/s at $t = 230 \mu s$; (c) Crack path based on the tests [204].

The crack propagation speed is calculated by Eq. (4.6) as shown in Figure 4.4. Figure 4.18a shows the variation of the crack propagation speed with an increase in crack growth for velocity BC of $\dot{v} = 3$ m/s when a hole with a radius of $r = 0.005\ m$ is inserted on the structure. It can be noticed that the crack propagation speed increases to the value of $V_c = 500$ m/s as the crack tip is at $x = 0\ m$, $y = (d_y - 0.01)\ m$ with the crack approaching the hole. As the crack propagates further and the crack trajectory approaches to the hole, the crack propagation speed gradually decreases up to $V = 100$ m/s. When the crack tip location is at $x = 6 \times 10^{-4}\ m$, $y = d_y = 0.023\ m$ (the local axes of the hole is at $d_x = 0.007\ m$, $d_y = 0.023\ m$) the crack is being arrested for around $10\mu s$ (Figure 4.18b) and then recovers its original trajectory with continually increasing speed. A similar variation of the crack propagation speed is noticed for the velocity BC of $\dot{v} = 5$ m/s (Figure 4.18a) where the crack propagation speed is higher and reaches $V_c = 600\ m/s$. Furthermore, the crack is curving towards the hole with a gradually dropping speed to $V_c = 250\ m/s$ and after a very small crack arresting period of $3\mu s$ (Figure 4.18b) it leads to further recovery of the crack speed while propagates away from the hole. The phenomena of the crack-arrest were noticed in the multiple tests [60, 61], where the crack propagation behaviour is very similar to the results achieved by PD simulations with the drop of the crack propagation speed and the delay of crack propagation when the crack deflects towards the hole. It is not easy to detect the crack arrest phenomena, as the crack arrest period is very short. Moreover, it can be noticed the crack arrest is force-dependent (Figure 4.18b) with the increased delay of crack propagation for lower velocity BC. Additionally, Figure 4.18c shows the results of the crack propagation speed and time when velocity BC of $\dot{v} = 3$ m/s is applied on a plate with a hole radius of $r = 0.003m$. In this case, the crack-arrest is more clear and is around $13\mu s$ starting at the time $t = 148\mu s$ when the crack tip is at $d_y = 0.023m$. At the same moment, the crack propagation speed is dropping to $V_c = 110$ m/s with further recovery. One of the reasons for the clear crack arrest period can be that the crack propagates as a straight line and deflects only towards the hole (Figure 4.17a, $r = 0.003m$).
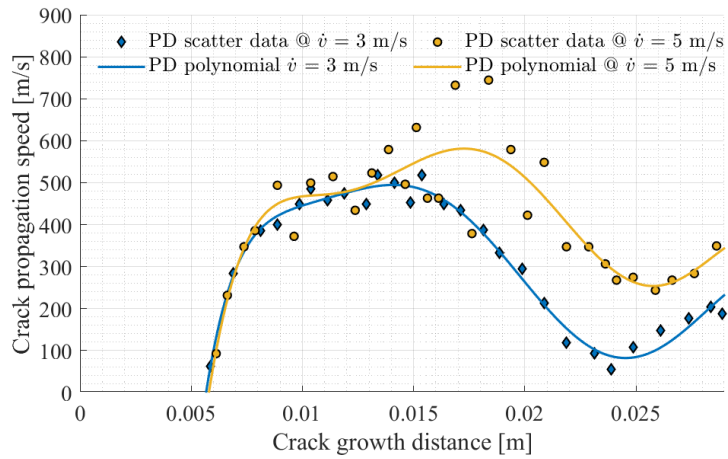
(a)
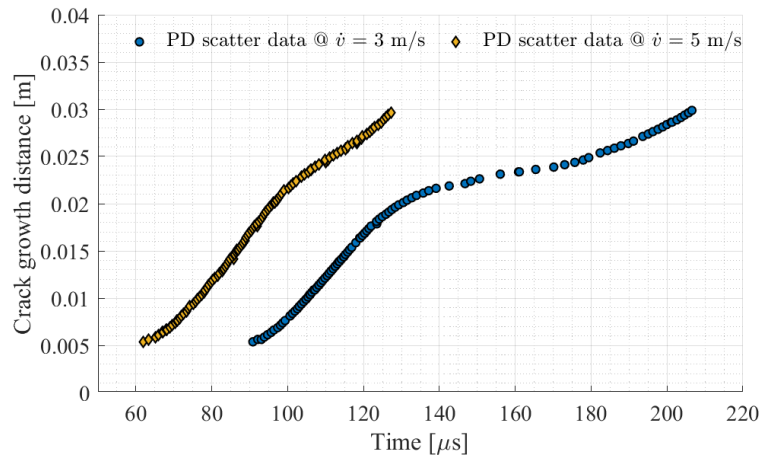
(b)
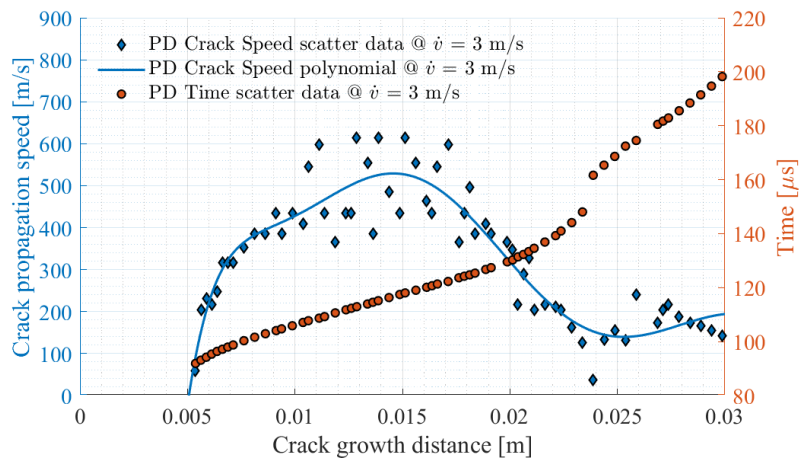
(c)

Figure 4.18 PMMA plate with the hole radius of $r = 0.005\ m$ under velocity BC of $\dot{v} = 3$ m/s and $\dot{v} = 5$ m/s: (a) Variation of the crack propagation speed with increasing crack growth distance. (b) Variation of the crack length with time. (c) Variation of the crack propagation speed and time with increasing crack growth distance for PMMA plate with the hole radius of $r = 0.003\ m$ under velocity BC of $\dot{v} = 3$ m/s.

4.4.3.3 Hole defects in Concrete

PD simulations of PMMA material showed good agreement with experimental tests for the crack propagation behaviour in the structure, including a hole defect as described in Section 4.4.3.2. Having this in mind, another type of brittle material, concrete, is considered for fracture analysis for the three-point bending problem. The dimensions of the rectangular plate, the sizes and the location of the defects are selected the same as described in Section 4.4.3.2. The material properties of the concrete are specified in Table 4.2. The geometry of the plate and the application of the BC is described in Section 4.4.2.2. The concrete plate is subjected to three different velocity BC: (a) $\dot{v} = 0.5$ m/s, (b) $\dot{v} = 0.75$ m/s and (c) $\dot{v} = 1$ m/s.
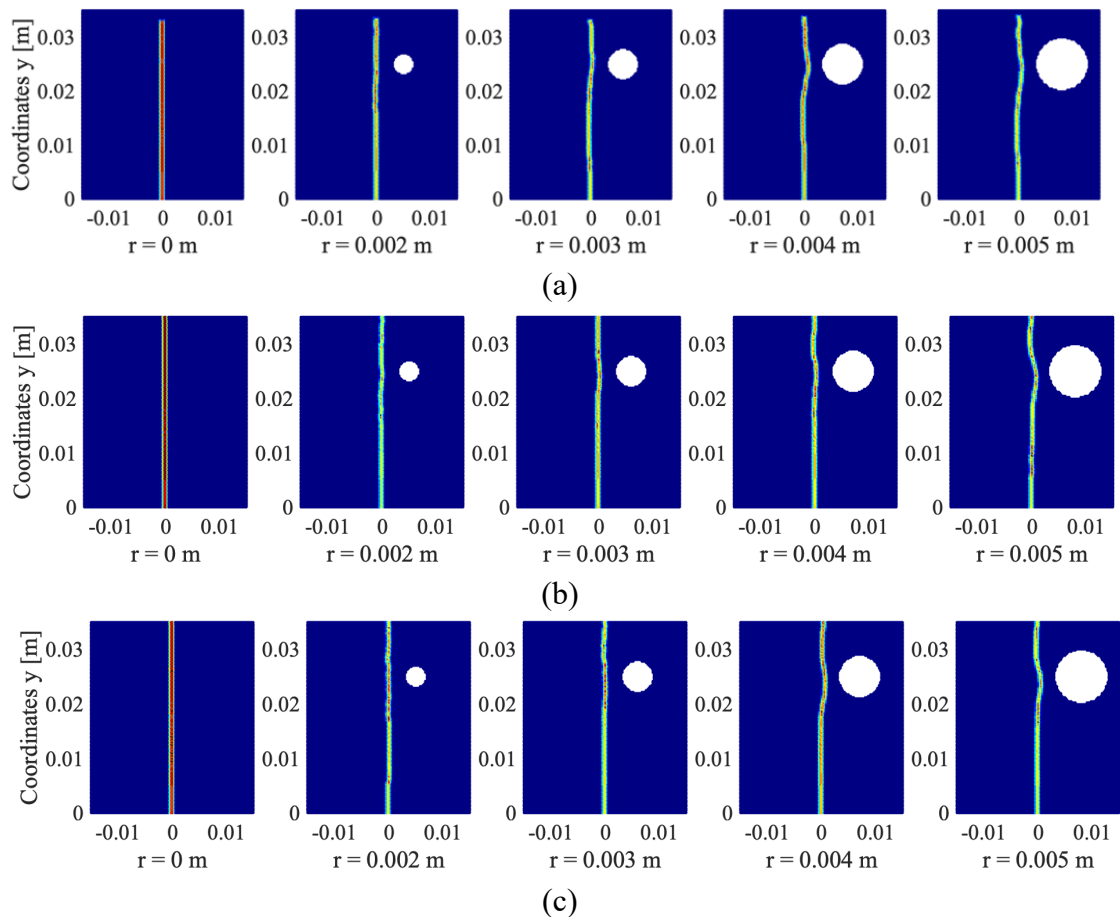
Figure 4.19 Damage maps of the concrete plate with different values of the hole radius r under velocity BC: (a) $\dot{v} = 0.5$ m/s at time $t = 485.56s$, (b) $\dot{v} = 0.75$ m/s at $t = 285.63\ s$, (c) $\dot{v} = 1$ m/s at $t = 228.5\ s$.

The PD models are discretised with 160000 material points with uniform spacing between them $\Delta x = 0.00025$ m and horizon size of $\delta = 3.015\Delta x$. Uniform time step size of $\Delta t = 0.057\mu s$ is used.

Figure 4.19 represents the damage maps for concrete plate subjected to the bending loading. Five cases are analysed with a varying radius of the hole defects: $r = 0$, only pre-existing crack is allocated, $r = 0.002\ m$, $r = 0.003\ m$, $r = 0.004\ m$, $r = 0.005\ m$. The fracture behaviour of the concrete plates is similar to the PMMA material where the crack is curving towards the holes and an increase in hole radius leads to an increase in curvature of the crack. Moreover, the existence of a hole in the plate influences the crack propagation speed and evaluating the crack speed at the location of the crack tip at $y = dy = 0.025\ m$ (area of curvature) demonstrates a decrease in crack speeds with an increase in hole radius. The propagation speed of the crack towards the location of the applied velocity BC is presented in Figure 4.20a. The arrest mechanism in the concrete structure with the presence of the holes ahead of the propagating crack can be noticed (Figure 4.20b). The period of the crack arrest in Figure 4.20b is very small and after the crack propagates away from the hole, the crack propagation speeds are even higher than the crack speeds before the crack arrest. For all simulations, a constant increase in crack propagation speed is observed first. However, as the crack approaches closer to the hole approximately 0.01 m behind the location of the hole, i.e. the crack tip is at $x = 0\ m, y = (d_y - 0.01)\ m$, leads to the curvature of the main crack and a gradual drop of speed on average by 70 %.

Numerical results utilizing PD showed a similar pattern of brittle fracture with the existence of the holes in the pre-cracked plate under three-point bending conditions. The crack is propagating very fast towards the location of the load application with the crack propagating speeds reaching up to $V_c = 600\ m/s$ for the load cases of $\dot{v} = 5$ m/s for PMMA and $\dot{v} = 1$m/s for a concrete plate. On the other hand, more brittle material as concrete showed faster crack propagation under the lower velocity BC.
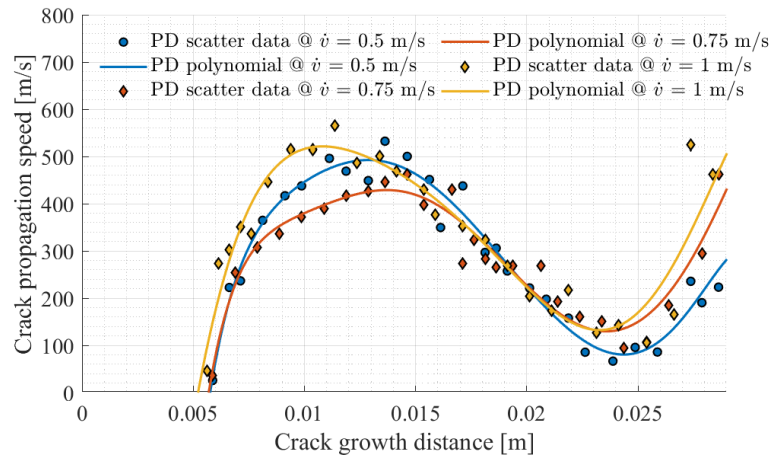
(a)
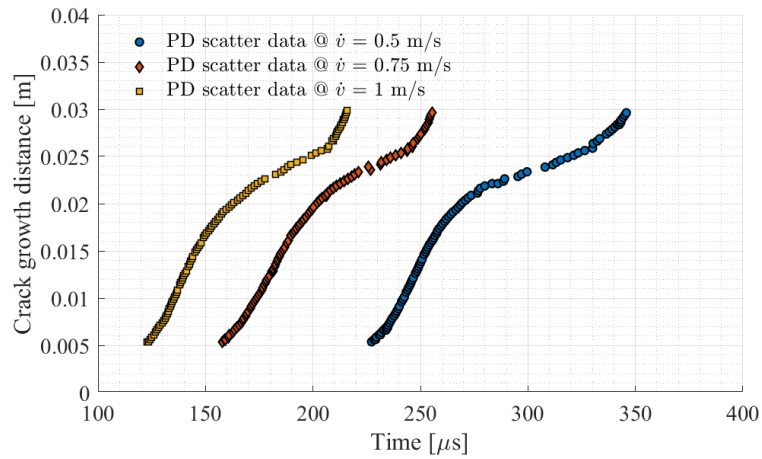
(b)

Figure 4.20 Concrete plate with the hole radius of $r = 0.005\ m$ under different velocity BC: (a) Variation of the crack propagation speed with increasing crack growth distance. (b) Variation of the crack length with time.

4.5 Summary

The results of this chapter demonstrated that PD model using a critical stretch based failure criterion captures the fracture phenomena in brittle materials, such as PMMA material, under dynamic loading conditions including both crack propagation and crack branching. The comparison of PD simulations with experiments showed a remarkably close agreement of the crack propagation speeds, with a 6 % difference, and captured similar patterns of the crack behaviour. PD model represents the crack propagation accurately with the increase of crack propagation speeds which leads to further branching. Moreover, in both experimental literature and PD model, the speed of crack

propagation reduces when thickening occurs, and after a sharp increase of the speed before bifurcation follows a drop in the crack speed after branching, and further recovery occurs with the rise of the crack propagation speeds in both branches.

Additionally, the numerical results for the critical load in macro- and micro-crack interaction problems showed remarkable results compared to analytical solutions. PD model accurately captured the influence of the micro-crack inclination angles on the critical loads that a plate can withstand. It is concluded that the application of the parameter K^*/K_0 has a substantial impact on the results, as SIF is dependent on crack distribution and inclination angles. The application of the updated $K^*/K_0 \neq 1$ for different micro-crack distributions showed close agreement with the analytical solutions. It can be noticed that the allocation of the micro-cracks in front of the macro-crack facilitates further propagation of the crack. Moreover, macro-crack has a tendency to follow the micro-cracks orientation and in the case of the perpendicular orientation of micro-crack with respect to the macro-crack leads to a further bifurcation. Analysing the crack propagation speeds showed that in the presence of the micro-cracks ahead of the macro-crack the shielding effect is present, and the crack speeds drop by approximately $10\ \%$. On the other hand, the parallel distribution of micro-cracks increases the crack speeds by approximately $6\ \%$.

Lastly, the results of the PD numerical model of the three-point bending of the pre-cracked plate with a hole defect show that the crack-arrest phenomena with the decrease of the crack propagation speed by 70% occurs when the crack deflects towards the hole. However, shortly after, the crack restores its original trajectory with an increase in speed. The increase in velocity BC leads to larger deflections of the crack towards the hole. Similar characteristics were observed during the experiments which show the reliability of the performed simulations by means of PD numerical model.

The results of this study have been published in [21] and [22] with additional work on stretch based failure criterion, convergence studies for different horizon and discretisation sizes and studies on Crack Opening Displacement (COD).

5   FATIGUE NUCLEATION

5.1   Introduction

The aim of this chapter is to evaluate the effect of the pores in Ti6Al4V dog-bone samples produced by AM, and propose a methodology to estimate the fatigue life reduction due to the internal pores. The bond-based PD, described in Section 3.3.2, together with the fatigue model described in Section 5.3, is utilised to influence the pores on the HCF crack initiation. Considering the duration of the fatigue simulations, the direct solution with stabilised BiCG is used to improve the computational efficiency (Section 3.4.2.2). In Section 5.4, the defect-free titanium alloy is used to calibrate PD parameters using the test data from [11], and the convergence study of fatigue nucleation in a dog-bone specimen is performed. In Section 5.5, the impact of the porosity on Young's modulus is analysed by the proposed fatigue model with a "concentration-dependent damage" (CDD) [198] implementation of porosities. In Section 5.6, the fatigue nucleation analysis is performed for additively manufactured Ti6Al4V samples with two different porosity levels. The porosity in fatigue models is introduced with gamma distributions, discussed in Section 5.6.2, in order to reach the required porosity levels. Firstly, the porosities in the fatigue model are implemented with a CDD approach and fatigue life is predicted. Secondly, a new PD porosity model is proposed to model the low porosity in the samples, which improves the prediction accuracy of the fatigue nucleation. Both of the models are validated against the tests. Lastly, the sensitivity study is performed on the reduction of material life with the located single pore and changing its diameter and location. Finally, the discussions are given in Section 5.6.5 with the followed by conclusions.

The study here described can be found in [23], and to the best of the author's knowledge, this is the first time the predictive HCF nucleation model has been developed to investigate the influence of process-induced defects like pores on the fatigue life of titanium alloys. Additionally, this chapter presents a numerical approach to assess the influence of the pore location and size on the fatigue life of Ti6Al4V. The PD predictions indicated the critical pore characteristics and the applicability of the developed PD model on samples with low porosity for HCF-loaded applications.

5.2   Background and motivation

Additively manufactured Ti6Al4V got attention in multiple fields, as discussed in Section 1.1, due to its high strength to weight ratio, and a lot of studies are focused on Ti6Al4V fatigue properties. The investigations showed that factors like AM processing parameters, geometry, and the surrounding environment directly impact Ti6Al4V mechanical properties [227]. Some experimental studies showed the existence of the process-induced defects and the differences in the product quality of the structures produced by ALM, which can have an influence on the fatigue performance of the additively manufactured parts [10–13]. The type of process-induced defects and the porosities in additively manufactured materials are discussed in Section 2.4.1.

In the current studies, the AM processing parameter variations and its processing-property relationships are not taken into account, as well as the potential anisotropy of mechanical properties. Therefore, the resulting process-induced pores in the dog-bone samples and their effect on the Ti6Al4V fatigue properties are investigated. In this respect, the defect-free Ti6Al4V sample with isotropic properties is selected as a reference specimen, and different methods of pores implementation in PD model are presented with its effect on the fatigue performance.

5.3   PD fatigue model

The first PD fatigue model was proposed in [228], which is suitable only for the crack growth phase. Instead, the formulation in [192] describes the possibilities to deal with three stages of fatigue: crack nucleation, crack growth and final failure, as discussed in Section 2.3. The authors in [192] introduced the damage variable called the "remaining life", which is degrading over the fatigue cycles. Each bond of the material points interactions in the PD model is identified by initial remaining life $\lambda(0) = 1$ and the bond is breaking irreversibly when $\lambda(N) \leq 0$. The irreversible bond breakage for fatigue cracking can be implemented by the failure parameter [200] presented by Eq. (3.16), which includes a history-dependent scalar-valued function ψ to represent broken interactions (bonds) between material points within the loading cycles N:

$$\psi\big(\boldsymbol{x}_{(j)} - \boldsymbol{x}_{(i)}, N\big) = \begin{cases} 1 & \text{if } \lambda(N) > 0 \text{ for all } 1 < N \\ 0 & \text{otherwise} \end{cases} \tag{5.1}$$

To monitor the accumulated damage of the bonds over the loading cycles N, the local damage of each material point i is defined as:

$$\varphi\big(\boldsymbol{x}_{(i)}, N\big) = 1 - \frac{\sum_{i=1}^{M} \psi\big(\boldsymbol{x}_{(j)} - \boldsymbol{x}_{(i)}, N\big) V_{(j)}}{\sum_{i=1}^{M} V_{(j)}} \tag{5.2}$$

Due to the nature of the cycling loading with the two extremes of the loading conditions F_{max} and F_{min}, shown in Figure 2.4, the PD fatigue model includes the minimum s^{min} and maximum s^{max} bond stretches between material points, so the bond strain is defined as [192]:

$$\varepsilon = \big|s^{max} - s^{min}\big| = |(1 - R)s^{max}| \tag{5.3}$$

According to [192], the cyclic bond strain ε is proportional to the cyclic SIF, which leads to the relationship between the PD FCG parameters and the Paris law, reported in Eq. (2.11). And with the correlation of ΔK to the ε, the introduced evolution law in [192] for the remaining life of the bond can be rewritten as:

$$\begin{cases} \dfrac{d\lambda(N)}{dN} = -A_1 \varepsilon^{m_1} \text{ (Phase I)} \\ \dfrac{d\lambda(N)}{dN} = -A_2 \varepsilon^{m_2} \text{ (Phase II)} \end{cases} \tag{5.4}$$

where the cyclic bond strain ε is expressed by Eq. (5.3) and the load ratio $R = s^{min}/s^{max}$.

The presented numerical fatigue model in Eq. (5.4) includes two phases of fatigue, where PD fatigue parameters A_1, m_1 are for crack nucleation (Phase I) and A_2, m_2 are for crack propagation (Phase II). The fatigue parameters for both phases are calibrated with the experimental data. Since the initial remaining life of each bond is $\lambda_1(0) = 1$, integrating Eq. (5.4) leads to:

$$A_1 \varepsilon^{m_1} N_1 = 1 \tag{5.5}$$

This means that the crack nucleation occurs at:

$$N_1 = \frac{1}{A_1 \varepsilon^{m_1}} \tag{5.6}$$
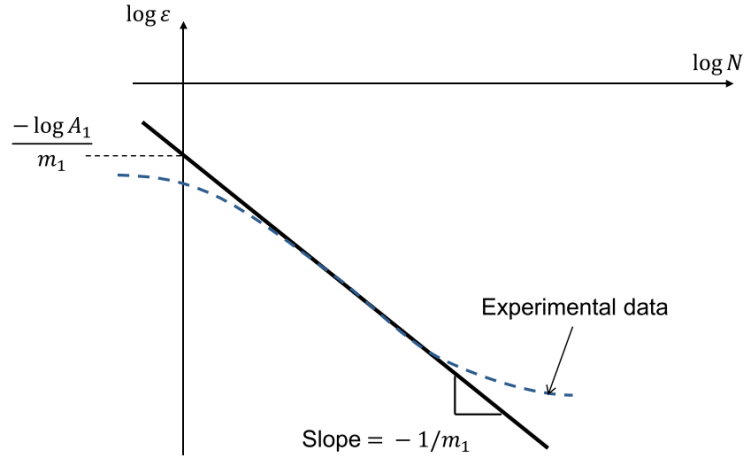
Figure 5.1 Calibration of PD fatigue parameters A_1 and m_1 for Phase I [192].

Presenting Eq. (5.6) on a log-log scale, the A_1 and m_1 can be determined by a linear fit to experimental data presented by strain-life relation in log-log scale [192], as shown in Figure 5.1. The obtained parameters of A_1 and m_1 are used for static solutions to calculate the fatigue life of the sample at the nucleation phase. The remaining life of the bond is in the Phase I only until the local damage is $\varphi < 0.4$, otherwise, the fatigue damage is moving from Phase I to Phase II. The FCG model for Phase II can be presented by rewriting the Eq. (5.4) in the following form [229]:

$$\frac{\lambda_{ij}^n - \lambda_{ij}^{n-1}}{N(n) - N(n-1)} = -A_2 \left(\varepsilon_{ij}^n \right)^{m_2} \tag{5.7}$$

where the remaining life λ_{ij}^n of the bond between the material points i and j at the cycle range n is evaluated. For Phase II, the cyclic bond strain ε is proportional to the cyclic SIF [192] and the PD fatigue parameters are calibrated by matching $\frac{da}{dN} - \Delta K$ curves

with experimental data [192], where PD parameter $m_2 = M$ can be obtained directly from the Paris' law data. Moreover, the parameter A_2 has to be calibrated, where the single PD FCG simulation is performed with an arbitrary value of A'_2 and already calibrated value of m_2. After evaluation of the PD FCGR $\left(\frac{da}{dN}\right)'$ with the estimated value of A'_2 and because the FCGR linearly depends on A_2, the calibrated value of A_2 can be computed in the following way [192]:

$$A_2 = A'_2 \frac{da/dN}{(da/dN)'} = A'_2 \frac{C\Delta K^M}{(da/dN)'} \tag{5.8}$$

If the sample has already a pre-existing crack, then the PD FCG model has both phases, and the material points located in the vicinity of the crack tip are treated as in Phase II. In the presented studies in Chapter 5, only the crack nucleation phase is investigated, so PD fatigue model is solved only for Phase I. Instead, the studies in Chapters 6 and 7 include both phases of fatigue and the calibration procedure for both phases is further discussed.
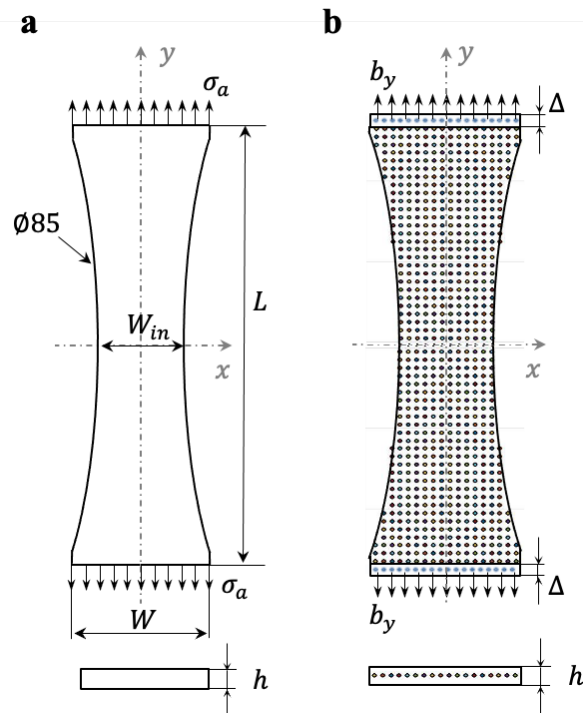
Figure 5.2 (a) Dog-bone titanium alloy plate under uniaxial tensile loading and (b) its discretisation.

5.4   Fatigue life of defect-free sample

5.4.1   Properties of PD model

The 2-D PD fatigue model is considered for a dog-bone plate with a total length of $L = 30 \times 10^{-3} m$, a width of $W = 10^{-2}\ m$ and $W_{in} = 5 \times 10^{-3} m$, the thickness of $h = 5 \times 10^{-3} m$ shown in Figure 5.2a. The following homogeneous material properties of the plate are specified: Young's modulus $E = 110\ GPa$ and Poisson's ratio $\nu = 1/3$.

Using the test data [11] for the defect-free sample, the calibration of the parameters $A_1 = 2.9 \times 10^{24}$ and $m_1 = 13.56$ are utilized for PD numerical model [192], as shown in Figure 5.1. The specimen is under HCF with the load ratio of $R = 0.1$ and the stress amplitudes of $\sigma_a = 360, 316$ and $270\ MPa$ are considered. A static loading, using the direct method described in Section 3.4.2.2, is applied as a body force density, b_y (Figure 5.2b.):

$$b_y = \frac{\sigma_y W h}{\Delta V_\Delta} \tag{5.9}$$

where ΔV_Δ is the volume of the boundary layer, and σ_y is a tension loading, evaluated in the following way:

$$\sigma_y = \begin{cases} \sigma_y^{max} = \dfrac{2\sigma_a}{1 - R} \\ \sigma_y^{min} = \sigma_y^{max} R \end{cases} \tag{5.10}$$

Please note that the no-damage zone is introduced in all numerical models in order to avoid the crack initiation in the area of the abrupt changes in the cross-sectional area. In that matter, the accumulated damage of the bonds is allowed only for the points located in the midsection of the sample $(-2.5 \times 10^{-3} m \le y \le 2.5 \times 10^{-3} m)$.

5.4.2   Numerical study of convergence

Three types of convergence studies are identified in [230]. In this work, the δ - convergence study is performed for a fixed horizon factor $m = 3$, where $\delta = m\Delta x$. The problem set up is stated in Section 5.4.1 and the dog-bone plate is under the stress

amplitude of $\sigma_a = 360\ MPa$. Three different horizon sizes δ with corresponding uniform grid spacing and the total number of material points of $\Delta x = 0.2 \times 10^{-3}m\ (4656\ nodes)$, $\Delta x = 0.15 \times 10^{-3}m\ (8352\ nodes)$, $\Delta x = 0.1 \times 10^{-3}m\ (18784\ nodes)$ are selected. The parameters A_1 and m_1 are kept constant for δ -convergence studies, as they are obtained from the test data and are not dependent on the horizon size. The focus of δ - convergence is to observe the crack nucleation phase in a specimen and the fatigue life. The PD simulations are stopped when the nucleation of the damage occurs, meaning that the local damage is $\varphi \geq 0.4$. Figure 5.3 shows the comparison of damage plots, where the fatigue damage is at the midplanes of the specimen. With the increased number of material points within the sample, the damaged area is smaller, but there is no major impact on the fatigue life, where the difference in life predictions is <1%. Considering that the outcome of this study showed quite close results for all three horizon sizes, PD models with $\delta = 0.45 \times 10^{-3}m$ and $m = 3$ will be utilised for numerical efficiency.
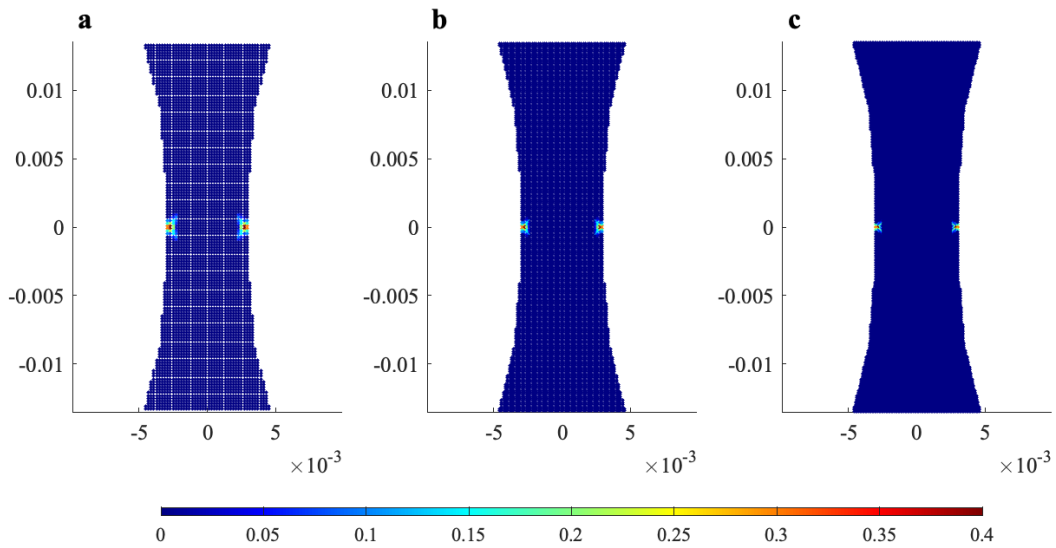
Figure 5.3 δ - convergence of PD fatigue crack nucleation for three different horizon sizes and the corresponding predicted life N_f: (a) $\delta = 0.6 \times 10^{-3}m, N_f = 194571\ cycle$; (b) $\delta = 0.45 \times 10^{-3}m, N_f = 194059\ cycles$; (c) $\delta = 0.3 \times 10^{-3}m,\ N_f = 193240\ cycles$.
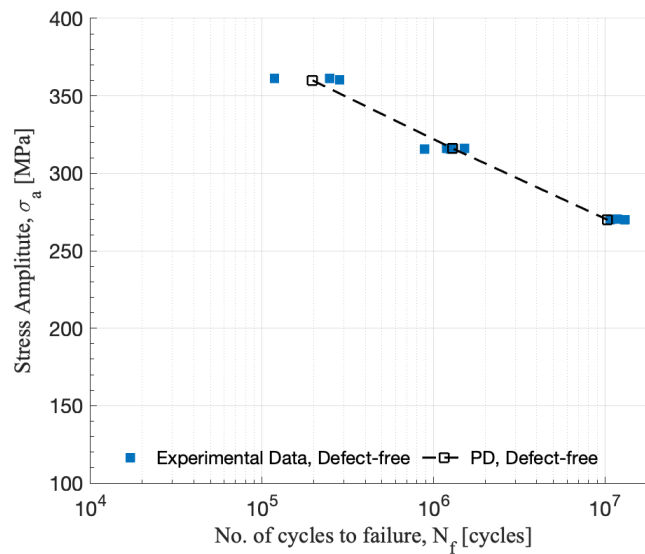
Figure 5.4 Stress amplitude as a function of the loading cycle at which nucleation occurs. PD results in comparison with the experimental data [11].

5.4.3   Crack nucleation prediction

As observed in [11], the type of wire used for WAAM of titanium alloy resulted in different porosity in the samples and moreover, in the variations of the fatigue life. Due to this, the reference PD model is set up for a defect-free Ti6Al4V alloy specimen, and Figure 5.4 shows the S-N data of the numerical results in comparison with the experimental data [11]. All the HCF nucleation life predictions are presented in logarithmic scale. It can be seen in Figure 5.4 that the predicted crack initiation life N_f for three different amplitudes $\sigma_a = 360, 316$ and $270\ MPa$ are in good agreement with the experimental data and the developed numerical model is used as the reference one for the porosity implementations in the next presented studies.

5.5   Impact of porosity on Young's modulus

There is a great importance of the material properties, like Young's, shear and bulk moduli, as well as Poisson's ratio on the mechanical behaviour of the material. Multiple studies were developed to relate porosity and elastic properties of the material and the authors developed analytical [137, 140] and semi-empirical [141, 231] expressions

where the general expression of the dependence of Young's modulus on the porosity is of the following form:

$$E = E_0 f(P) \tag{5.11}$$

where E and E_0 are Young's modulus of porous material and fully dense material, respectively, and $f(P)$ is the function that relates Young's modulus and porosity P.

Therefore, analytical solutions are based on some assumptions, such as treating the properties of all phases as isotropic, even if the material is anisotropic, which could introduce some error to analytical solutions.

Five different analytical solutions, presented in Table 5.1, are selected to estimate the relation between porosity and Young's modulus. The models in Table 5.1 are the general expressions which can be used for porous materials. Therefore, the constants depend on the type of material, types of pores and porosity levels and have to be calibrated using experimental data. In the current study, the focus is on Ti6Al4V alloy which includes spherical pores, and all the presented constants in Table 5.1 are selected accordingly.

Table 5.1 Analytical models to estimate the relation of porosity and Young's modulus

Model	Equation	Constants
1. Phani and Niyogi [143]	$\dfrac{E}{E_0} = \left(1 - \dfrac{P}{P_c}\right)^n$	$P_c = 0.85$ $n = 2$ [232]
2. Pabst and Gregorova [144]	$\dfrac{E}{E_0} = (1 - aP)\left(1 - \dfrac{P}{P_c}\right)$	$a = 1$ (spherical pore) $P_c = 0.75$ [232]
3. Knudsen and Spriggs [141, 231]	$\dfrac{E}{E_0} = e^{-bP}$	$b = 3.36$ [232]
4. Boccaccini et al. [138]	$\dfrac{E}{E_0} = \left(1 - P^{\frac{2}{3}}\right)^{1.21\,s}$	$s = 1$ (spherical pore)
5. Nielsen [142]	$\dfrac{E}{E_0} = \dfrac{1 - P}{1 + P/\mu}$	$\mu = \mu_0(1 - P)$ $\mu_0 = 0.5$ (coarse pore systems)

where P_c is the critical porosity at which $E = 0$, a, b and s are packing geometry factors, μ and μ_0 are shape function and shape factor, respectively.
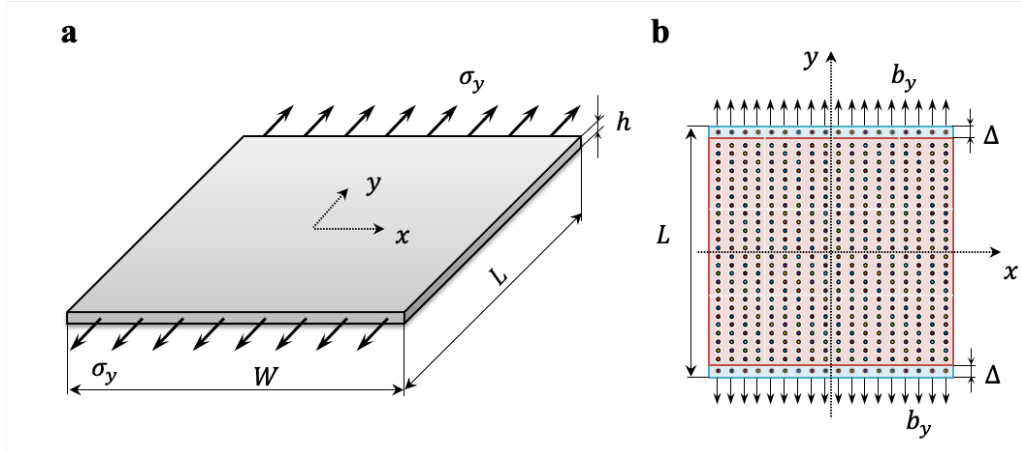
Figure 5.5 (a) Square titanium alloy plate under uniaxial tensile loading and (b) its discretisation.

The analytical models presented in Table 5.1 are used to validate the CDD [198] approach of pores implementation in PD model and if the relation between porosity and Young's modulus occurs.

To evaluate the fraction of void space in the material, the following porosity ratio is used:

$$P = \frac{V_p}{V_T} \tag{5.12}$$

where V_p is the volume of void-space and V_T is the bulk volume of material.

Considering the effect of the pores on Young's modulus of the material based on the mathematical apparatus of continuum mechanics, it is necessary to implement the porosity in the 2-D PD numerical model. For a validation study, a square plate with a length and width of $L = W = 10^{-2}\ m$, and thickness of $h = 5 \times 10^{-4} m$ in Figure 5.5a is selected and subjected to uniaxial tensile loading in the y-direction. The following material properties of the titanium alloy plate are specified: Young's modulus, $E_0 = 110\ GPa$ and Poisson's ratio, $v = 1/3$ [233].

The PD model is discretised with 10000 material points (Figure 5.5b) with uniform spacing between them $\Delta x = 1 \times 10^{-4} m$ and $\delta = 3\Delta x$. A static loading is applied as a body force density b_y and the BC are enforced as stated in Eq. (5.9), where $\Delta V_\Delta = 5 \times 10^{-10}\ m^3$ and σ_y is a tension loading, $\sigma_y = 220\ MPa$.
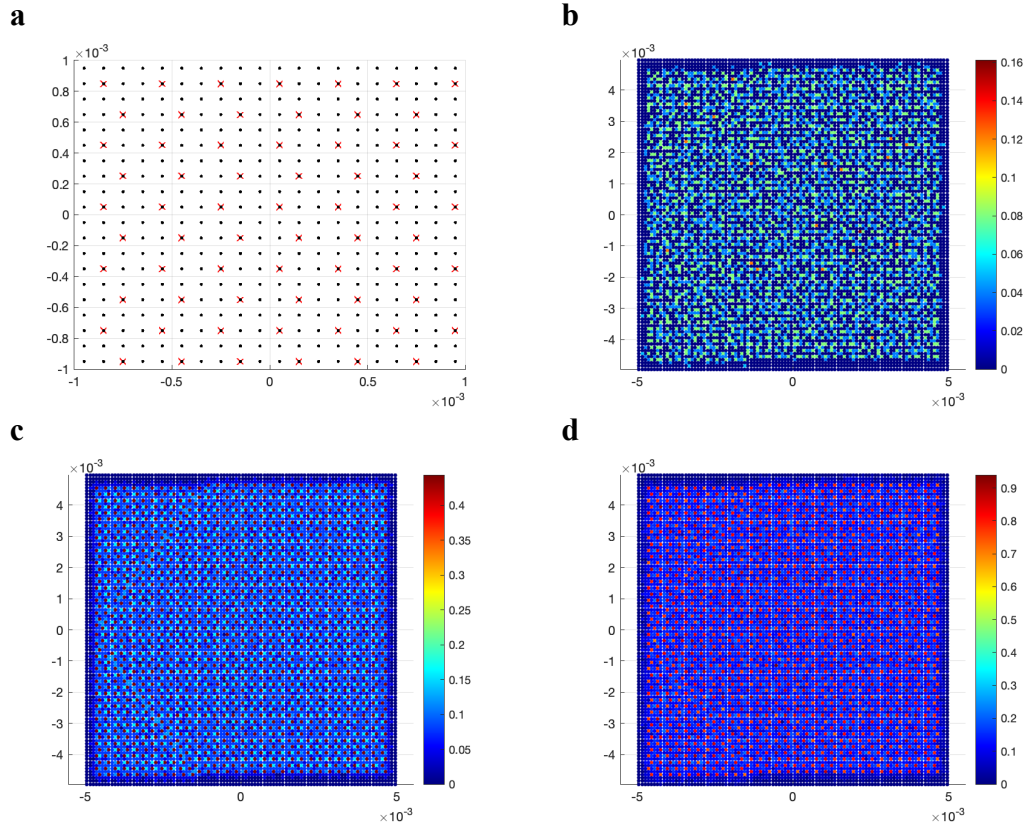
Figure 5.6 (a) PD pores allocation, where 'cross' represents pores; Damage maps of the plate with different pore ratio P: (b) $P = 1\%$, $E/E_0 = 0.97$; (c) $P = 5.7\%$, $E/E_0 = 0.86$; (d) $P = 10\%$, $E/E_0 = 0.74$

In PD, the failure in the material is calculated as N_b/N_T , where the ratio between the number of broken bonds is N_b and the total number of the bonds is N_T. To implement the existence of the pores in the square plate, the CDD [198] model is used, which was initially utilised for the damage that occurred by corrosion [198] and later on implemented in elastic porous materials like glass and rock [234], which are subjected to force pulses to evaluate the wave propagation. In the current study, the CDD model is used to assess the effect of the internal defects, like pores, in the titanium alloy plate on Young's modulus of the material.

To implement pore in the system, we assume that the damage index at the point is linearly dependent on its porosity, where the porosity ratio for each material point x_i can be represented as:

$$P\left(x_{(i)}\right) = \frac{N_{b(i)}}{N_{T(i)}} \tag{5.13}$$

and the total porosity of the plate is evaluated in the following form:

$$P = \frac{\sum_{i=1}^{M} \frac{N_{b(i)}}{N_{T(i)}} V_{(i)}}{\sum_{i=1}^{M} V_{(i)}} \tag{5.14}$$

This means that initial damage is initiated in the model and implemented by breaking bonds in order to match the specified porosity. The material properties are kept constant through all the simulations and only the bond breakage between material points is implemented. In the numerical model, 1492 material points are selected to represent the pores in the plate, as shown in Figure 5.6a. The selection of 1492 points is only for the purpose of numerical simulations and do not represent the actual pore distributions in the actual samples. The actual samples have random pore locations and variations in porosity levels, so with the variation of porosity levels in the PD model, the location of the pores is constrained. A number of simulations ($sim = 1,2 \ldots ,27$) are performed, where for each selected material point x_i a random bond is broken with $N_{b(i)} = sim$. It is an incremental process, and with each simulation, the number of broken bonds between the selected material point and its family members is increased by 1. After each simulation the strain of the plate is checked to evaluate Young's modulus, E of the plate with implemented porosity P. For example, Figure 5.6b-d represents the damage plots of the plate with the porosity levels of $P = 1.0, 5.7$ and 10%. Numerical simulations show the decrease of the Young's modulus with the porosities in the system with the relative Young's modulus of $E/E_0 = 0.97, 0.86$ and 0.74. All peridynamic results are compared against analytical solutions presented in Table 5.1. Note that in the current study, the interest is in low porosity of the metals and not in the porous materials. This is the reason why Figure 5.7 shows the analytical and PD plots only until the porosity of $P = 10\%$. Moreover, due to the random breakage of bonds in the specified material points (Figure 5.6a), the bonds connecting two material points with the pores will stay intact. It means that if material point x_i and material point x_j are selected for the representation of the pore, then the bond $x_i - x_j$ will not be broken, and the bond-breakage moves to the next bond of the family members of point x_i. With the stated bond-breakage system, the assumptions of

the "isotropic" pore shapes and distribution, and the linear dependency of local damage on its porosity, the local damage of each material point is evaluated by Eq. (3.20).

As it can be noticed in Figure 5.7, the mentioned analytical approaches give the variation of the relative Young's modulus. The certain simplifying assumptions about the shape, size and distribution of the pores cause the difference in the results. The outcome of the PD numerical model in Figure 5.7 is within the range of analytical solutions.
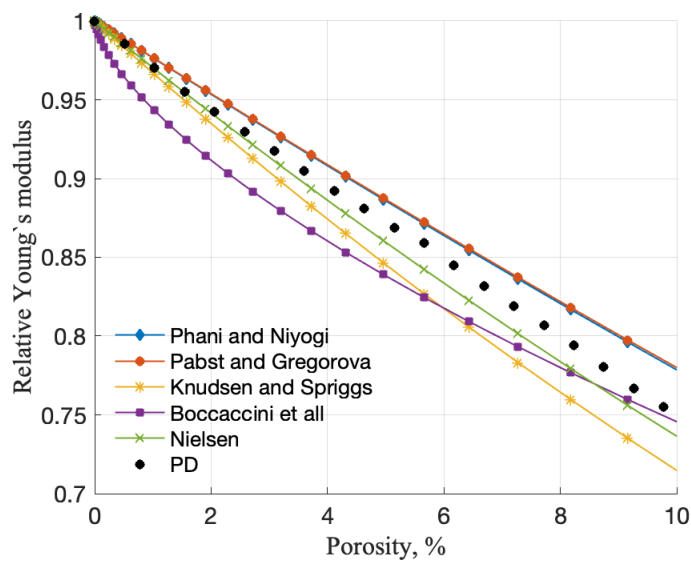
Figure 5.7 Variation of the relative Young's modulus with increasing porosity in the plate. PD vs Analytical models [138, 141–144] in Table 5.1

5.6   Fatigue life of sample with micro-pores

In this section, the CDD [198] approach of porosity implementation is utilised in PD fatigue model, followed by a new method for pores representation.

5.6.1   Numerical model assumptions

The material exposed to cyclic loading undergoes different phases with a particular behaviour, as discussed in Section 2.3. Each of the phases is load-dependent, where the damage nucleation in the material is initiated from the fractions of 10 nm leading to the development of micro-cracks in the crystallographic planes initiated by the shearing stress. During the LCF, the material is exposed to plastic deformations due to the large

and continuous plastic slips in the grains. In the HCF the shear stress is also activating the localised plastic slips in some crystals and on a surface of the material, where the damage nucleates in the form of pores or cavities. The crack nucleation is a complex process that is dependent on the loading and the material composition, where a very small fraction can initiate the material damage and reduce the fatigue life. The damage on sub-microscopic level initiated with slip bands was investigated in theoretical studies [235] and, the studies [236, 237] of fatigue behaviour of the material with different inclusion sizes, shapes and location indicated the stress concentrations at inclusion apex, where the inclusions with dimensions of $d_p > 10 \mu m$ at sub-surface level originated the crack nucleation. Even perfectly round defects artificially induced in the sample had an effect on crack nucleation and the loss of fracture ductility during LCF investigation [238]. The in-situ X-ray CT scanning of additively manufactured materials evidenced the presence of the spherical pores in the structures, which were immediately below the surface of the sample and/or inside the sample, and the damage nucleation occurred directly from the pore. Due to this, the assumptions were put in place in the presented PD model, where the evolution of the crack nucleation starts at the pore and not at plastic slips, so the pore is always in the elastic domain and no plastic flow occurs.

5.6.2 Problem setup

All the presented numerical studies are performed on the Ti6Al4V alloy dog-bone specimen (Figure 5.2) with the geometrical and material properties stated in Section 5.4.1. Moreover, the PD numerical model from Section 5.4 is selected as a reference defect-free model. The specimens are under HCF with the load ratio of $R = 0.1$ and the stress amplitudes of $\sigma_a = 360, 316$ and $270\ MPa$. For each load, a number of simulations are performed with varying pore distributions within the midsection of the sample. As the current interest is at nucleation of the damage, the solver is stopped when local damage is $\varphi \geq 0.38$, as discussed in Section 3.3.5.

It is evidenced by the tests [10] that the damage nucleation occurred at the pores located immediately below the surface of the sample, and the study in Section 5.6.4.1

is performed to identify the importance of pore dimension and location on fatigue performance of the sample. In this section, the pores are randomly distributed in the sample, as schematically shown in Figure 5.8. Gamma distribution with the shape parameter of $a = 2$ is selected. The scale parameter and the total number of pores $N_{p_{tot}}$ are implemented with variations in order to achieve the desired porosity ratio in a sample. The flowchart of porosity evaluation and pore assignment is shown in Figure 5.9. After the desired total porosity is reached, a set of pores $N_{p_{tot}}$ with the optimal pore diameters are randomly allocated in the sample. Eq. (5.12) is used to evaluate the fraction of void space in the material.
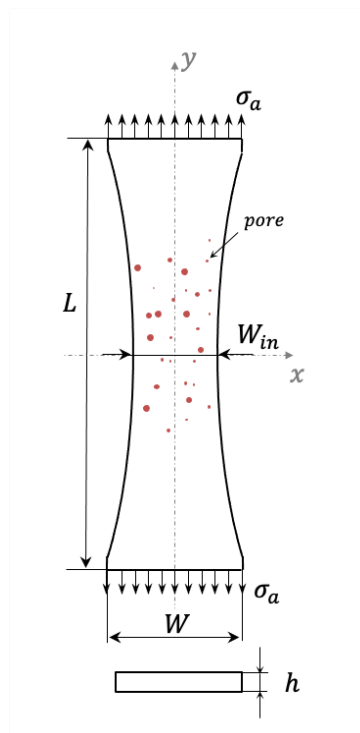
Figure 5.8 Sample geometry with randomly distributed pores.
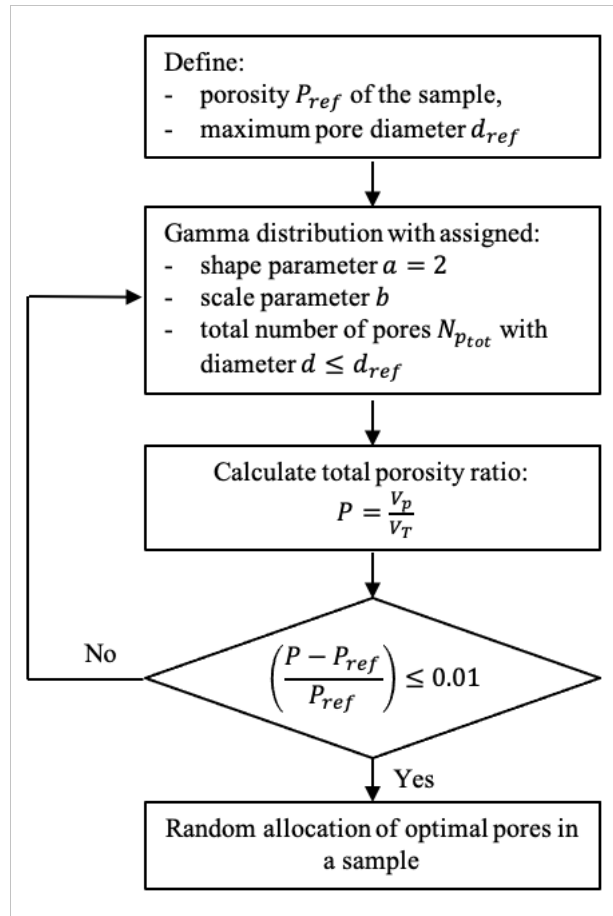
Figure 5.9 Flowchart of porosity evaluation.

(a)   (b)
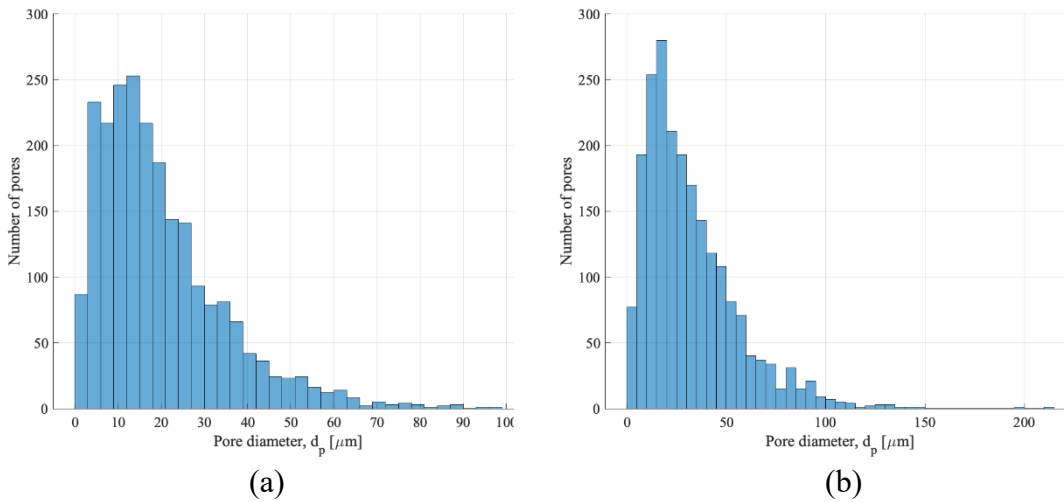
Figure 5.10 Gamma distribution: (a) $a = 2, b = 10, N_{p_{tot}} = 2256 \rightarrow P = 0.01\%$; (b) $a = 2, b = 15, N_{p_{tot}} = 2488 \rightarrow P = 0.04\%$.

Two types of porosities are selected for verification study of PD numerical model with the tests [10]. During the experiments and analysis of the additively manufactured samples [10], the porosity specimens are deposited with contaminated wire, and the porosities of $P = 0.01\%$ and $P = 0.04\%$ are identified. Moreover, looking over the microstructure of the specimens, it is observed that the specimens with porosity of $P = 0.01\%$ include pores with diameters below $100\mu m$. Having this in mind, two types of simulations are performed using Gamma distribution of the pores in order to reach the optimal pore diameters with the porosities of $P = 0.01\%$ and $P = 0.04\%$. Multiple cases of gamma pore distributions were run (13 simulations), and in some of them, the pore diameter could reach $d_p \leq 400\mu m$. Figure 5.10 shows the examples of the pore distributions with the pore diameters $d_p \leq 250\mu m$.

5.6.3 *"Concentration-dependent damage" PD model*

According to the study in Section 5.5, it is numerically demonstrated that implementing the CDD model in PD to initiate the pores in the system has a great impact on Young's modulus of the sample. Moreover, PD results are within the range of mentioned analytical solutions presented in Figure 5.7. Instead, in the following section the interest is in the evaluation of the pores influence on the fatigue life of the dog-bone specimen (Figure 5.2) and if the CDD model can be used for HCF problems.

Using the CDD model, the number of broken bonds have to be evaluated for each pore. Combining Eq. (5.13) and Eq. (5.14) the number of pre-broken bonds for each material point is evaluated as:

$$N_{b(i)} = \frac{V_{p(i)}}{V_{T(i)}} N_{T(i)} \tag{5.15}$$

where $V_{p(i)}$ is the volume of the pore assigned for the material point x_i , $V_{T(i)}$ and $N_{T(i)}$ are the bulk volume and the total number of bonds of the material point, respectively.

All the pores are treated as spherical, and for a 2-D sample, the volume of the pore with a diameter d_p is evaluated as $V_p = \frac{4}{3}\pi \left(\frac{d_p}{2}\right)^3$. Utilising Eq. (5.15) for analysis of the number of the pre-broken bonds to be assigned in the selected material points with

the allocated pore of diameter $d_p \leq 400\mu m$, the relationship between $N_{b(i)}$ and $d_{p(i)}$ can be evaluated, shown in Figure 5.11. It should be noted that the bonds can be fully and partially broken. For example, if the pore diameter of $d_p = 300\mu m$ is allocated for material point, then three bonds are fully broken with $\psi = 0$ and one partially broken with $\psi = 0.519$ based on the pore diameter and the number of broken bonds. This means that a history-dependent scalar-valued function ψ in Eq. (3.20) for pre-broken interactions (at cycle $N = 0$) between material points will be $\psi = 1$ if $d_p = 0$ and $\psi < 1$ for $d_p > 0$. Due to the fact that the scanned samples in the experimental studies [10] showed porosities of $d_p < 400\mu m$, the number of pre-broken bonds per node is $N_b < 9$ (Figure 5.11). The bond-breakage system is described in Section 5.5
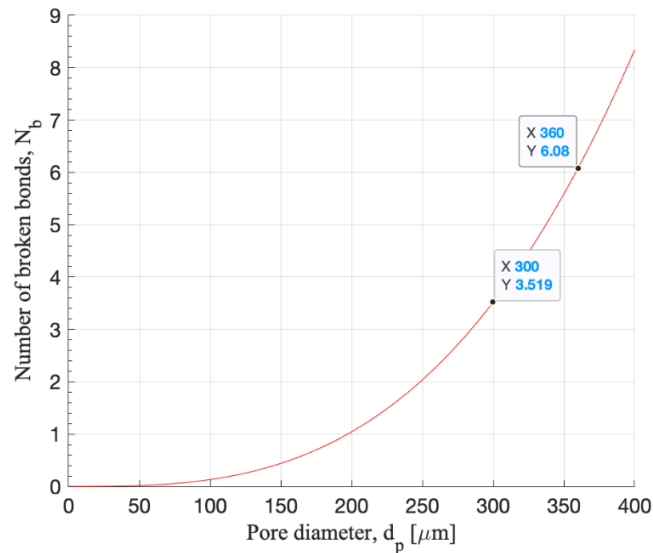
Figure 5.11 Pore diameter and the number of broken bonds relationship.

The numerical results of the CDD model implementation of porosities in the dog-bone sample have shown that the damage starts at the pore located close to the edge of the sample. The bigger the pore and closer it is to the edge, the faster the damage initiates. Figure 5.12 represents the damage maps of three solutions under different loading conditions with the porosity of $P = 0.04\%$ in the samples. Figure 5.13 shows the numerical results and comparison to experiments [10]. For the lower porosities (Figure 5.13a), with the implemented CDD method, the fatigue life N_f is quite close to

experimental data. However, for the porosity of $P = 0.04\%$, the fatigue life is overpredicted (Figure 5.13b).

The presence of the pores with the implemented CDD model result in local stress concentrations at the location of the pore with the crack initiation at the pore. In reality, a similar trend of pore initiation is noticed during the experiments on additively manufactured samples [239]. Therefore, the employment of the CDD method in PD HCF fatigue model did not show good applicability on fatigue problems due to the different nature of the fatigue crack nucleation and the processes developing in the material under the cycling loading. Due to this, additional porosity models are investigated with the effect of the pores on fatigue limit.

5.6.4   New PD porosity model

Evaluating the fatigue life of the structures, porosity defects has a noticeable effect on fatigue strength and multiple models, summarised and classified in [240], were proposed to predict the impact of the small cracks or inclusions on fatigue life. El Haddad et al. [146] presented a model in Eq. (5.16) in order to use the LEFM theory for short cracks and introduced the fictitious crack length l_0 in Eq. (5.17), which is increasing with a very short length of the crack.
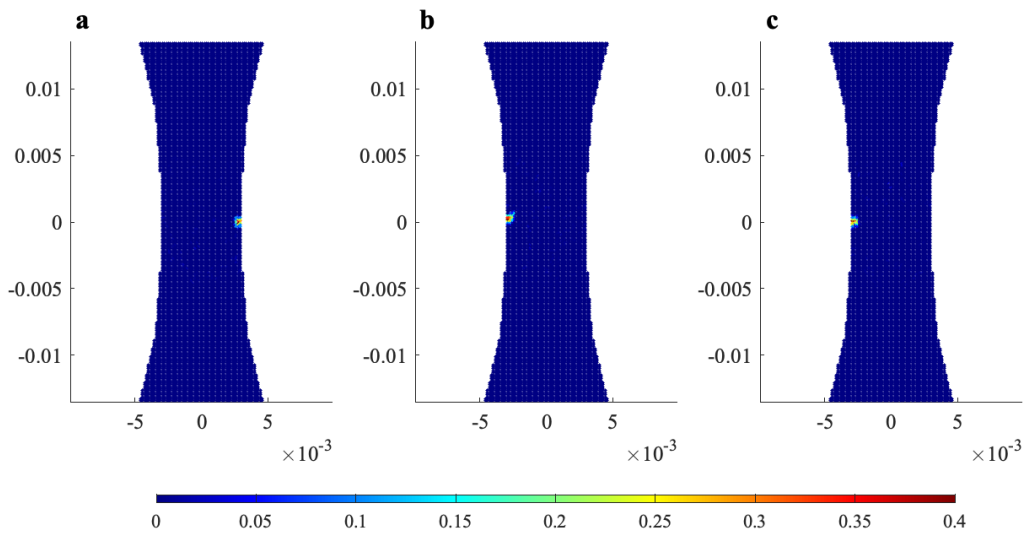
Figure 5.12   Damage maps: (a) $\sigma_a = 360MPa, N_f = 441174\ cycles$;   (b) $\sigma_a = 270MPa, N_f = 910241\ cycles$; (c) $\sigma_a = 225MPa, N_f = 9837299\ cycles$.

a

b

c

Figure 5.13 Experimental [10] and PD results of fatigue life prediction for porosities: (a) $P = 0.01\%$; (b) $P = 0.04\%$; (c) Combined results for all three models.

$$\Delta K = \Delta\sigma\sqrt{\pi(l + l_0)} \qquad (5.16)$$

$$l_0 = \frac{1}{\pi}\left(\frac{\Delta K_{th}}{\Delta\sigma_e}\right)^2 \qquad (5.17)$$

where ΔK and $\Delta\sigma$ are the SIF range and the applied stress range, l and l_0 are the short crack length and El Haddad parameter. ΔK_{th} and $\Delta\sigma_e$ are the threshold SIF and the fatigue limit of the material at which the small cracks do not propagate.

Murakami [147] adopted a new parameter $\sqrt{S}$ to obtain the relationship between the SIF range and the porosity size, where the spherical pore is treated as a crack with a size equal to the square root of the projected area of the pore and the SIF range can be estimated in the following form:

$$\Delta K_p = C \Delta \sigma \sqrt{\pi \sqrt{S}} \tag{5.18}$$

The parameter C depends on the porosity defects location, where $C = 0.5$ is for internal pores and $C = 0.65$ is for external pores [147].

Beretta and Romano [148] expressed El Haddad parameter l_0 by Murakami's parameter $\sqrt{S}$ in Eq. (5.19) to have a smooth transition from the porosity defects to the long cracks, and introducing the SIF limit for the specimens with crack nucleation at the pore by Eq. (5.20).

$$\sqrt{S_o} = \frac{1}{\pi} \left(\frac{\Delta K_{th,LC}}{C \, \Delta \sigma_e} \right)^2 \tag{5.19}$$

$$\Delta K_{th} = \Delta K_{th,LC} \sqrt{\frac{\sqrt{S}}{\sqrt{S} + \sqrt{S_0}}} \tag{5.20}$$

$\Delta K_{th,LC}$ is the threshold SIF range for the long crack and according to the tests in [10] $\Delta K_{th,LC} = 4.5 \, MPa\sqrt{m}$ for the additively manufactured Ti6Al4V with the intrinsic fatigue limit of $\Delta \sigma_e = 540 \, MPa$, when load ratio $R = 0.1$.
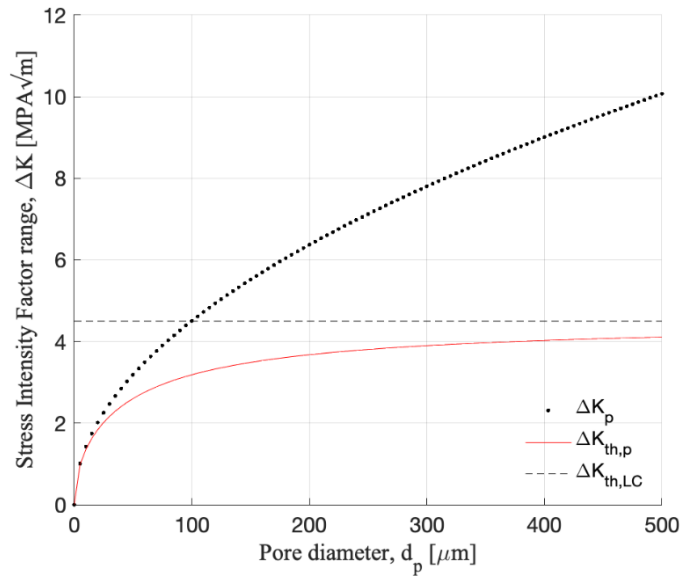
Figure 5.14 K-T diagram for Ti6Al4V alloy.

The fatigue strength in the presence of the small defects can be described by Kitagawa and Takahashi diagram (K-T diagram) [241]. K-T diagram can be presented in terms of fatigue limit or SIF in the presence of the porosity defects, and the study in [148] shows its good applicability. To analyse the effect of the porosity on the fatigue life of the sample, Eq. (5.18) is used to calculate the SIF range ΔK_p for the pores with diameter $0 \leq d_p \leq 400 \, \mu m$ and Eq. (5.20) – to find the SIF range limit $\Delta K_{th,p}$ for specified pores. The calculated ΔK_p and $\Delta K_{th,p}$ are presented by K-T diagram in Figure 5.14.

As discussed in Section 5.3, the evolution law of the remaining life in Eq. (5.4) is expressed in terms of cyclic bond strain, and following the Paris law, the evolution law for the crack nucleation phase is presented in the following form:

$$\frac{d\lambda(N)}{dN} = -A_1 \Delta K^{m_1} \qquad (5.21)$$

Because the SIF range is proportional to the strain, the $\Delta K_{th,p}$ is used as a SIF limit for crack nucleation phase and the effect of the pore on strain can be introduced in the following equation:

$$\chi = \frac{\Delta K_p}{\Delta K_{th,p}} \qquad (5.22)$$

And the evolution law of the remaining life will be modified in the following way:

$$\frac{d\lambda(N)}{dN} = -A_1 (\varepsilon \chi)^{m_1} = -A_1 \left(\varepsilon \frac{\Delta K_p}{\Delta K_{th,p}} \right)^{m_1} \qquad (5.23)$$

The enforced parameter χ represents the pores with different diameters of d_p in the relation between the SIF range ΔK_p and the SIF range limit $\Delta K_{th,p}$ for specified pores. In this way, the pores with different diameters can be added to the numerical model, and their effect can be analysed on the nucleation phase of fatigue life.

Murakami's concept of correlation between the geometrical parameter $\sqrt{S}$ and the threshold SIF is applicable for different shapes of the defects and cracks for the region $\sqrt{S} \leq 1000 \mu m$ [240]. Moreover, it includes one pore, which is evaluated as the 'fatal'

pore with the fatigue fracture nucleation. But the location of the 'fatal' pore in the specimen and the size is very important and plays a significant role in the fatigue life of the sample. Due to this, Section 5.6.4.1 presents the PD numerical results of the effect of one pore on the fatigue life of the Ti6Al4V sample.
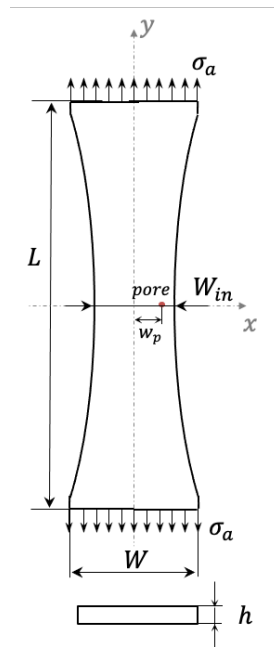
Figure 5.15 Sample geometry with the allocation of one pore.

5.6.4.1   *Pore size and location effect on fatigue life*

The analysis is performed on the effect of pore diameter and location on the fatigue life of the sample, using the proposed PD fatigue model of porosity implementation described in Section 5.6.4. The PD study is conducted with the allocation of one 'fatal' pore with a diameter d_p at the distance w_p from the sample centre line, as shown in Figure 5.15. The specimen is under tension-tension loading condition with stress amplitude of $\sigma_a = 270\ MPa$. PD results in Figure 5.16, showing that the closer the pore is to the free edge with a higher pore diameter, the lower the life of the sample is. It can be seen that the critical pore diameter is around $d_p = 100 \mu m$, which means that the samples with pore diameters $d_p < 100 \mu m$ result in a small decrease of the titanium alloy fatigue strength.
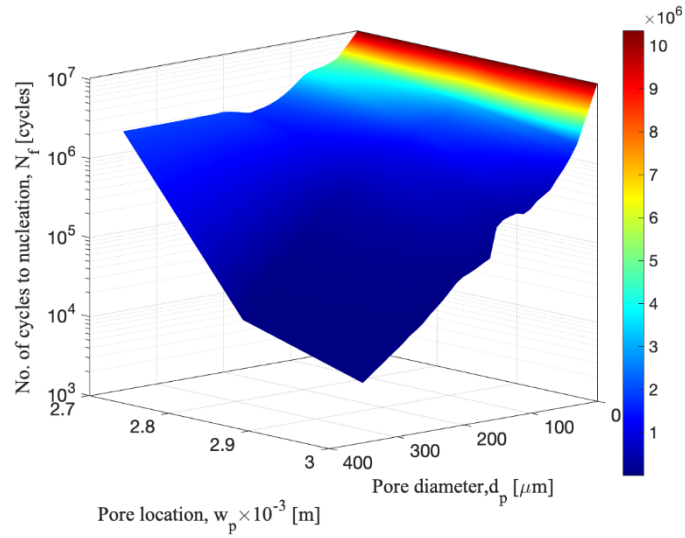
Figure 5.16 Effect of pore location and diameter on fatigue life.

5.6.4.2 Fatigue life of low porosity samples

The experiments [10] present a wide variation of the sample life under the same loading conditions. Moreover, various experimental studies [10, 11, 18, 131, 242] have indicated that the lowest fatigue life is noticed when multiple pores are present close to the free surface. The sub-surface pores are the most critical case for damage initiation, as shown as well in Section 5.6.4.1. Having this in mind, the PD fatigue numerical model was implemented for a system with multiple pores. Considering the study of the existence of the multiple micro-cracks in the system [22] presented in Section 4.3.4, in this study, it is assumed that if two pores are interacting with each other, meaning if both material points x_i and x_j are selected for the representation of the pore, then the interaction between the pores i and j is effecting the remaining life of the bond as:

$$\frac{d\lambda_i(N)}{dN} = -A_1\left(\varepsilon_i \chi_i \chi_j\right)^{m_1} \tag{5.24}$$

Eq. (5.24) indicates the amplifying effect on the crack nucleation process. The following concept includes the interaction of the pores and if the pores are located close to each other, at a distance between them $\leq 450\mu m$ (horizon sizes of PD models is $\delta = 0.45 \times 10^{-3}m$), then the faster crack nucleation will be noticed and a more significant impact on the fatigue life.
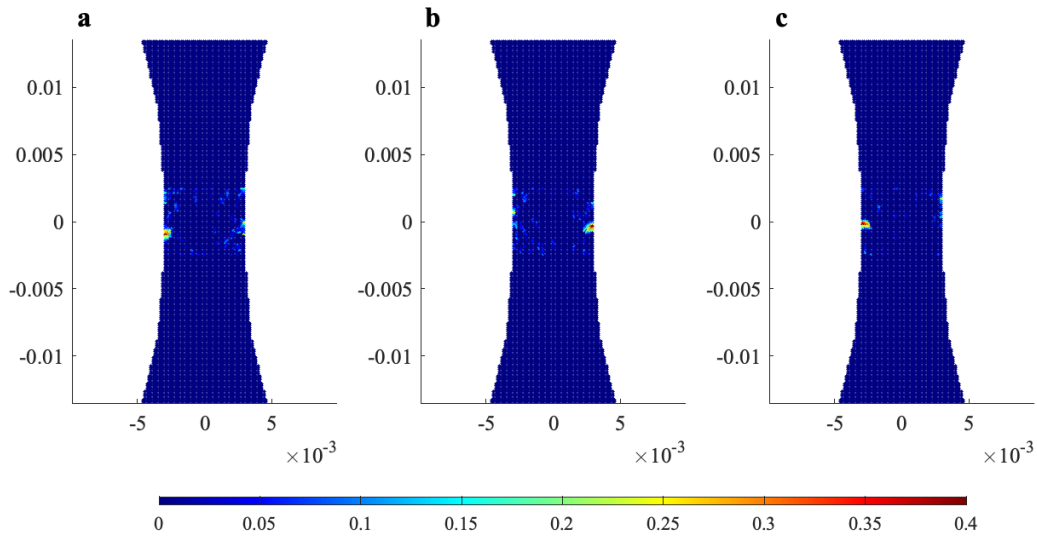
Figure 5.17 Damage maps for samples with $P = 0.01\%$: (a) $\sigma_a = 360MPa, N_f = 33135\ cycles$; (b) $\sigma_a = 316MPa, N_f = 130872\ cycles$; (c) $\sigma_a = 270MPa, N_f = 1297377\ cycles$.

Instead of using the pre-breaking bond model applied in Section 5.6.3, only the SIFs of each pore is evaluated, and Eq. (5.24) is used for pores representation in a sample. Note that the proposed relationship is applied to all bonds $N_{T(i)}$ for material point x_i. Figure 5.17 represents the damage maps of three solutions under different loading conditions with the porosity of $P = 0.01\%$ in the samples. The pattern of the damage is similar to the pre-broken bond method, where the damage is initiated at the pores located in the vicinity of the plate edge. The comparison of the numerically predicted fatigue life for porosity values of $P = 0.01\%$ and $P = 0.04\%$ and tests data is presented in Figure 5.18. Multiple simulations were performed for the samples with $P = 0.04\%$ and Figure 5.18 shows the scatter of the PD results due to the different pore distribution in the sample. The damage initiates at the pore, closest to the sample surface, where the higher diameter of the pores and their interaction showed lower fatigue life, summarised in Table 5.2. The 'fatal' pore is the pore where the crack nucleates and additional contribution to the crack initiation come from secondary pore located at close proximity.
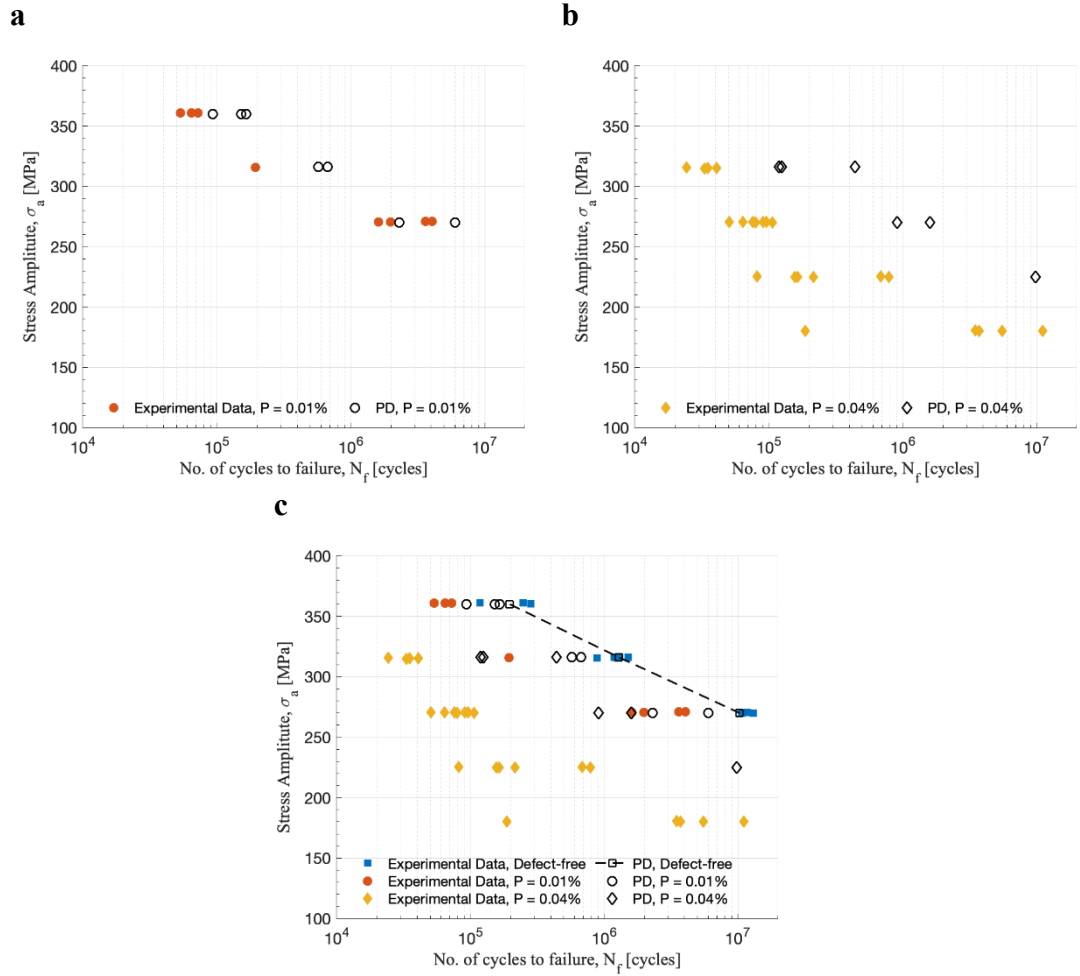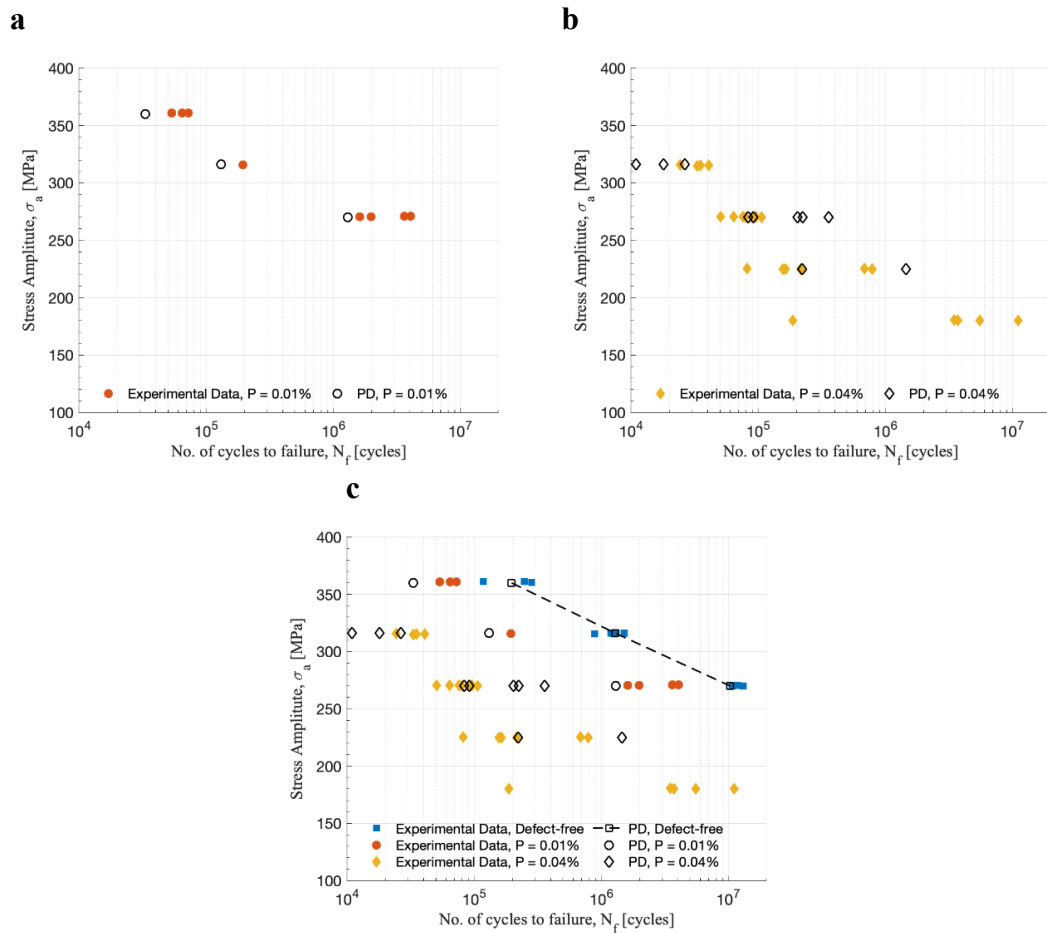
Figure 5.18 Experimental [10] and PD results of fatigue life prediction for porosities: (a) $P = 0.01\%$; (b) $P = 0.04\%$; (c) Combined results for all three models.

Table 5.2 PD results of the effect of porosity diameter on fatigue life with $P = 0.04\%$

Stress amplitude σ_a, MPa	Fatigue life $N_f, cycles$	'Fatal' pore Diameter $d_p, \mu m$	Location $w_p, 10^{-3}m$
316	10894	210	3
316	18053	160, 35	2.85, 2.7
316	26418	17, 124	3, 2.85
270	83228	21, 250	3, 2.85
270	91750	162,47	3, 2.85
270	203853	164,60	2.85, 2.7
270	223221	222	2.85
270	357848	55, 93	3, 2.85
225	222554	350	2.85
225	1461034	200	2.85

The proposed approach of pores initiation in the sample provides fatigue life predictions close to the experiments [10]. Moreover, for the porosity value of $P = 0.04\%$, the new peridynamic porosity model performs better than the CDD model.

5.6.5 Discussion and future work

The distribution, size, shape, location, and density of the process-induced critical defects impact the performance of additively manufactured structures. The samples with a similar manufacturing process, microstructures and smooth surface could result in different fatigue life due to the high dependency on the initial defects size and stress levels, which brings the high scatter of the test fatigue data [13, 19, 131–133]. Due to this, it is important to understand the impact of process-induced porosities of fatigue life of additively manufactured samples.

The fatigue studies have been conducted for the additively manufactured Ti6Al4V under load controlled constant amplitude conditions with a load ratio of $R = 0.1$. One of the challenges of investigating the AM materials fatigue life is the implementation of the porosity defects in the numerical model. For the numerical purpose, the developed PD fatigue model has been set up for the defect-free Ti6Al4V sample using the test data for the PD parameters' calibration process. This approach indicated the workability of the developed model, which is named as a reference one. Although several assumptions are made in the PD model, like the material is treated as elastic with isotropic properties even when the pores are initiated in the model, the numerical results showed good fatigue life predictability.

It is also well known that the sample undergoes cyclic plastic deformations on microscopic levels and controls the material's fatigue life. The cracks are starting to initiate at the share of the persistent slip bands due to the development of stress concentrations [235–237]. On the other hand, the existence of the pores or inclusions is becoming the critical factor for crack initiation. The defects located at the close vicinity to the surface have had high local stresses, and with the inclusions of $d_p > 10\mu m$ originated the crack nucleation [238]. Flat elongated defects have higher stress concentrations and are more critical for fatigue performance. But even perfectly round

defects have an effect on crack nucleation. Based on these observations in the literature, the phenomena such as stress relaxation, strain hardening, phase transformation are excluded from the current PD fatigue model, and the evolution of the crack nucleation is starting at the pore, so the pore is always in the elastic domain, and no plastic flow occurs.

The performed numerical investigation has demonstrated the vital reduction in the fatigue life of the Ti6Al4V dog-bone specimen caused by the presence of the pores in the sample. The early failure in the samples was influenced by a few large pores (with a diameter of $d_p > 100 \, \mu m$) located close to the surface or the multiple pores located in close proximity. The CDD approach of porosity implementation results in local stress concentrations at the pre-damaged zone, developing in crack initiation. But the following concept overpredicted the fatigue life of the sample and required further investigation on its applicability on fatigue nucleation problems. However, the adopted Murakami's formulation in the PD fatigue model, the SIF of the pore defect was evaluated with the assumption that all the pores are spherical. The numerical model was simulated for the two types of porosities of $P = 0.01\%$ and $P = 0.04\%$ and the results are quite close to the test results available in the literature. Note that the model is treated as elastic, and plastic slips and dislocation processes are omitted, where crack nucleation starts directly at the allocated pore in a sample. Nevertheless, the proposed method with the adopted assumptions of pores allocation in the PD model has shown an ability to estimate the most critical defect's size and location.

S-N curves are generated under constant amplitude loading the load ratio of $R = 0.1$, while the loads can often be with variable amplitudes in nature. Under various loading conditions, such as load sequence and interactions is becoming important. Using linear cumulative damage rule in the PD studies for fatigue life predictions needs to be investigated for additively manufactured structures under variable amplitude or under different load ratios. If periodic overloads exist in the structure, then the cycling hardening or softening can occur in the structure. The PD model has to be extended and includes both elastic and plastic processes in the material.

The insight provided by the PD analyses can be used for fatigue life predictions considering both internal and surface defects, with the study of different defect shapes, subjects of future works.

5.7   Summary

This chapter presents the numerical results considering the porosity effect and pore defects on the fatigue nucleation of additively manufactured Ti6Al4V material. Those effects were evaluated based on the porosity levels publicly available in the literature. The results of this study have been published in [23], where the outcome of the work shows successful implementation of PD theory to model pores in 2-D dog-bone titanium alloy specimen and taking into account the interaction between the pores. The study included two types of porosity implementations. The CDD model was used with pre-broken bonds in the sample and a new PD porosity model with the enforced coefficient in the evolution law of the remaining life of the bonds. The porosity of the sample was accounted for by gamma distribution, where the identified diameters of the pores were randomly distributed in the samples. Firstly, the verified CDD approach was applied in the fatigue model, where the fatigue life was overpredicted for the samples with the higher porosities of $P = 0.04\%$. Secondly, the new PD porosity model-based life prediction method demonstrated the improved capability of capturing the effect of both porosities on fatigue nucleation. The presented S-N curves show that the PD fatigue life prediction is in good agreement with the test data. The dependency of the fatigue life on pore location and size was evaluated, and it was showcased that the subsurface pores with the pore diameter are the most critical. The larger pore located in the vicinity of the sample surface has a high contribution to fatigue life reduction. The developed PD fatigue model showed its capability to predict the fatigue life of the defect-free samples, as well as of the samples with different types of porosities.

6   FATIGUE CRACK GROWTH

6.1   Introduction

The aim of this chapter is to evaluate the effect of the microstructure, pores and RS in Ti6Al4V C(T) samples produced by AM. The bond-based PD fatigue model, described in Section 5.3, is utilised to analyse the FCGR titanium alloy sample, including crack nucleation and propagation phases. In Section 6.3, the defect-free wrought titanium alloy is used to calibrate PD parameters using the tests data from [18] for Phase I and from the Paris' law data [159] for Phase II. In Section 6.4, the review of the studies regarding the microstructure of AM and its effect on FCG is investigated. The variations of FCG due to different grain shape and size because of the layer-by-layer process is numerically analysed by PD. In addition, the effect of porosities on the FCG is discussed by the numerical implementation of porosities discussed in Section 5.6.4 and analysed in Section 6.5. The effect of both factors like columnar grains and porosities in the material is combined in the PD numerical model, and the fatigue performance is analysed in Section 6.6. Lastly, in Section 6.7, the numerical PD FCG model is developed to predict the fatigue performance of additively manufactured Ti6Al4V alloy with implementation of the internal stresses in the model by different temperature profiles. Thus, the FCGR are analysed and compared to the test data available in the literature. Finally, the studies about the RS formed in the additively manufactured samples as a consequence of the repeated heating and cooling processes are reviewed. The developed PD model with the thermal stress implementation will illustrate the great impact on the FCGR. The presented numerical results in the FCG studies are verified with FEA.

6.2   Background and motivation

The fabrication process of AM is based on the layer-by-layer adding of material according to the designed 3D geometry [3]. Thus, the AM process provides a lot of advantages over the conventional processing methods such as prototyping, rapid fabrication, product customisation and material efficiency. On the other hand, the layer-

wise production results in material anisotropy, process-induced defects and residual stress development. It is recognised that the disadvantages of AM exist due to the high impact on the mechanical behaviour of the final product with properties worse than the conventionally produced components [14–16]. More detailed literature review on additively manufactured materials is in Chapter 2.4.

In this respect, it is important to evaluate the impact of microstructure, porosities and RS on the FCG performance of additively manufactured Ti6Al4V. Firstly, the current study aims to predict the fatigue fracture in C(T) samples and analyse the contribution of different types of microstructures and different levels of porosities on FCG by using PD. PD has been successfully applied to fatigue problems to predict crack nucleation and propagation [192, 193, 228], as well as the influence of the porosity on the fatigue life of the metal samples [23], as presented in Chapter 5. In Chapter 5, a numerical approach of implementation of the pores in the PD fatigue model is proposed and showed good predictability of fatigue life of dog-bone samples under HCF. In this respect, the proposed approach is applied to FCG problems and analysed the effect of the additively manufactured columnar microstructure and the existence of process-induced defects in the structures on the FCG. Secondly, the numerical PD fatigue model is developed to predict the fatigue performance of Ti6Al4V alloy after introducing the internal stresses in the model by different temperature profiles. The literature review undertaken for this study can be found in Section 2.4.

6.3   PD fatigue defect-free model setup and validation

In the presented studies for fatigue damage prediction in C(T) titanium alloy samples, PD is utilised as a main numerical tool. As described in Section 5.3, PD fatigue model requires PD parameters A_1, m_1, A_2 and m_2 calibration and the wrought titanium alloy Ti6Al4V [18, 159] is selected for this purpose. The wrought Ti6Al4V is identified as a reference model with the following homogeneous material properties: Young's modulus $E = 110\,GPa$ and Poisson's ratio $\nu = 1/3$. Moreover, all simulations are performed under Very High Cycle Fatigue (VHCF) loading with assumptions that no plastic flow occurs.
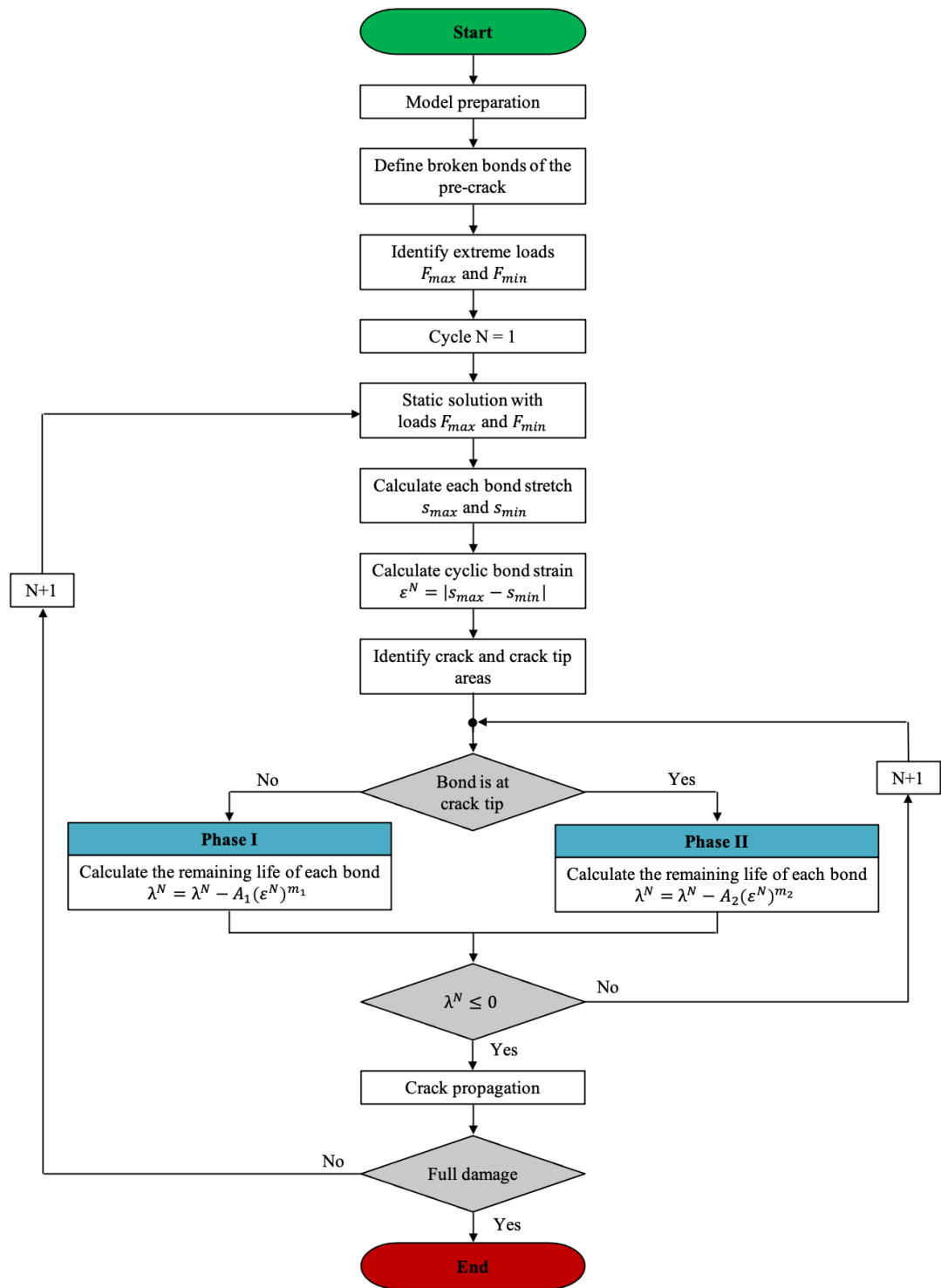
Figure 6.1 Flowchart of PD fatigue model.

The PD fatigue model contains crack nucleation and propagation phases. Looking at the PD model, which is discretised with the material points, the points located in the vicinity of the crack tip in the C(T) sample will already be at the propagation phase, whereas the other ones are at the nucleation phase. The flowchart of PD fatigue model is shown in Figure 6.1. Firstly, the PD parameters A_1 and m_1 are calibrated from the experimental data [18] in Section 5.4.1. Secondly, in Section 6.3.2, the PD parameters A_2 and m_2 are obtained from the Paris' law data [159], and the crack growth curves compared with experimental results.
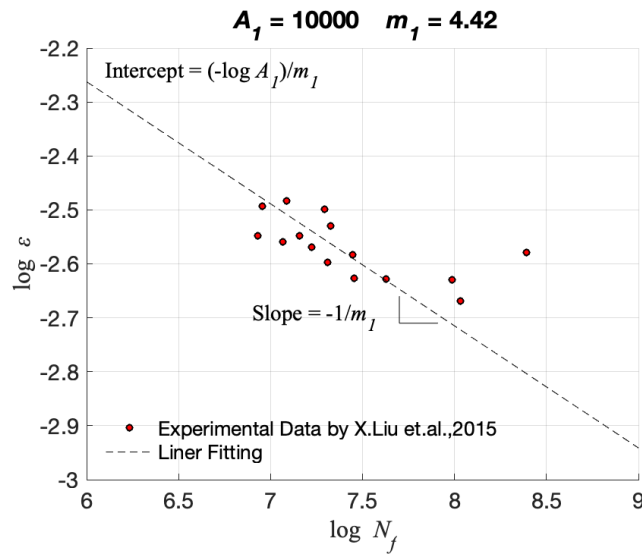
Figure 6.2 Loading cycles N_f as a function of bond strain ε for the crack nucleation phase. PD parameters calibration utilising the S-N experimental data [18].

6.3.1   Properties of crack nucleation PD model

The experimental work [18] is performed for solid cylindrical specimens of Ti6Al4V under the VHCF loading with different loading ratios and load amplitudes. To simplify the computational model, a 2-D dog-bone plate is used in the PD fatigue crack nucleation simulations, as shown in Figure 5.2 (Section 5.4), with the total length of $L = 50 \times 10^{-3} m$, width of $W = 20 \times 10^{-3}\ m$ and $W_{in} = 6 \times 10^{-3} m$, thickness of $h = 4 \times 10^{-3} m$. The PD models are discretised with 6600 material points having a uniform spacing of $\Delta x = 0.3 \times 10^{-3}$ m and horizon size of $\delta = 3.015 \Delta x$. Following the procedure in [192] of parameters calibration utilising the S-N test data [18], shown

in Figure 6.2, the parameters for the PD fatigue crack nucleation are identified as: $A_1 = 1 \times 10^4$ and $m_1 = 4.42$.

The plate is subjected to VHCF with the load ratio of $R = 0.1$ and the stress amplitudes of $\sigma_a = 373,\ 322, 297$ and $244 MPa$. A static loading, using the direct method described in Section 3.4.2.2, is applied as a body force density at the upper and lower edges of the sample and enforced by Eq. (5.9).
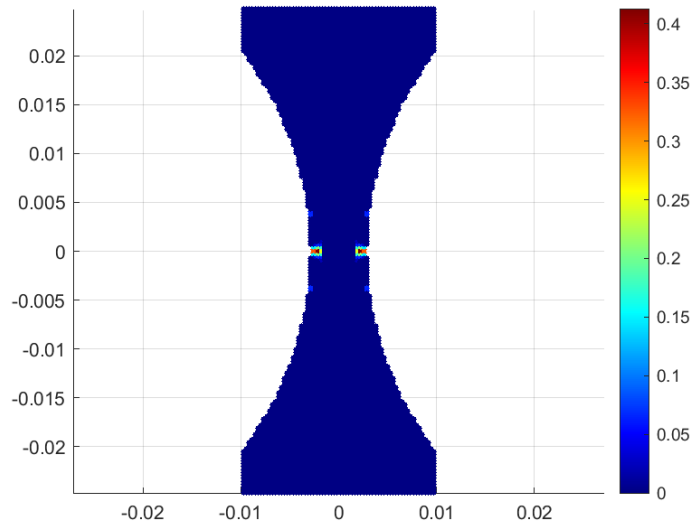
Figure 6.3 Damage map for the dog-bone plate under stress amplitudes of $\sigma_a = 244\ MPa$ at $N_f = 8 \times 10^7\ cycles$.
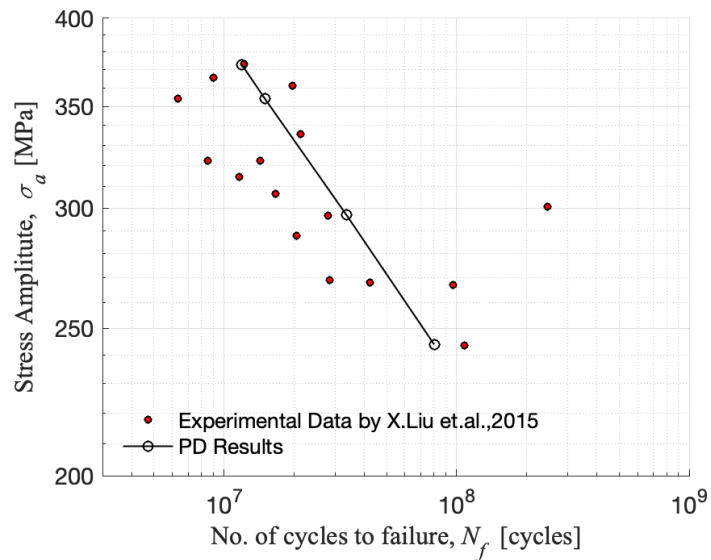
Figure 6.4 Stress amplitude as a function of the loading cycle. Calibrated PD model versus experimental data [18].

Solving the PD discretised model with identified parameters A_1 and m_1 have resulted in fatigue crack initiation at the midplane of the plate shown in Figure 6.3, and the number of cycles N_f to crack nucleation due to different stress amplitudes in Figure 6.4. The implementation of calibrated parameters showed that the numerical results are in line with the experimental data [18].
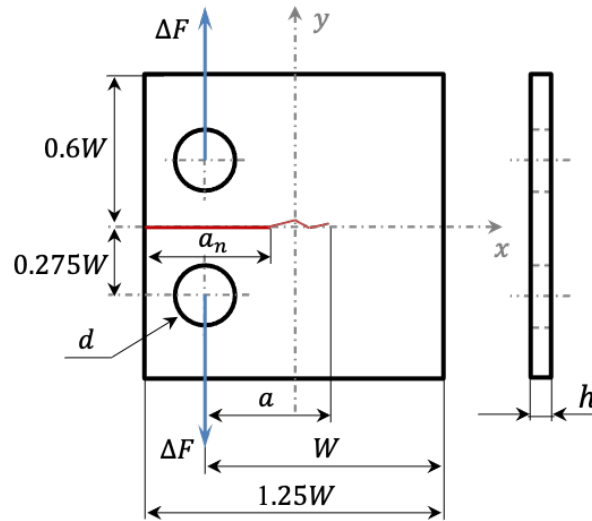
Figure 6.5 Square titanium alloy C(T) plate under uniaxial tensile loading.

6.3.2 Properties of Fatigue Crack Growth PD model

The PD FCG model is set up for C(T) sample, shown in Figure 6.5, with the effective width of $W = 25 \times 10^{-3} m$, thickness of $h = 5 \times 10^{-3} m$ and the pre-notch length of $a_n = 12.4 \times 10^{-3} m$. The crack propagation is analysed for five different cyclic loads of $\Delta F = 6.25, \ 5.4, \ 4.5, \ 3.6$ and $3.15 \ kN$ with the load ratio of $R = 0.1$. The loads are applied at the pins with the diameter of $d = 6.25 \times 10^{-3} \ m$ as a body force density in the following form:

$$b_y = \frac{F_y}{\Delta V_\Delta} \tag{6.1}$$

where ΔV_Δ is the volume of the pin area, and F_y is the applied load, which is defined as:

$$F_y = \begin{cases} F_y^{max} = \dfrac{2\Delta F}{1-R} \\ F_y^{min} = F_y^{max}R \end{cases} \tag{6.2}$$

where F_y^{max} and F_y^{min} are the cyclic load extremes, respectively.

PD model is discretised with 10400 material points with uniform spacing between them $\Delta x = 0.3 \times 10^{-3}$ m and horizon size of $\delta = 3.015\Delta x$. Calibrated PD parameters $A_1 = 1 \times 10^4$ and $m_1 = 4.42$ are used for the nodes in crack nucleation phase and PD parameters $A_2 = 0.52 \times 10^6$ and $m_2 = 4.757$ are obtained from the Paris law data [159]. The FCGR for the mid-region of the crack propagation are evaluated, and the SIF is obtained from ASTM standard E647 [164]:

$$\Delta K = \frac{\Delta F(2+\zeta)}{h\sqrt{W}(1-\zeta)^{\frac{3}{2}}}(0.886 + 4.64\zeta - 13.32\zeta^2 + 14.72\zeta^3 - 5.6\zeta^4) \tag{6.3}$$

where $\zeta = \frac{a}{W}$, a is the crack length from the location of the applied load as shown in Figure 6.5, h is the thickness of the specimen, and W is the distance between the applied load and the edge of the specimen.
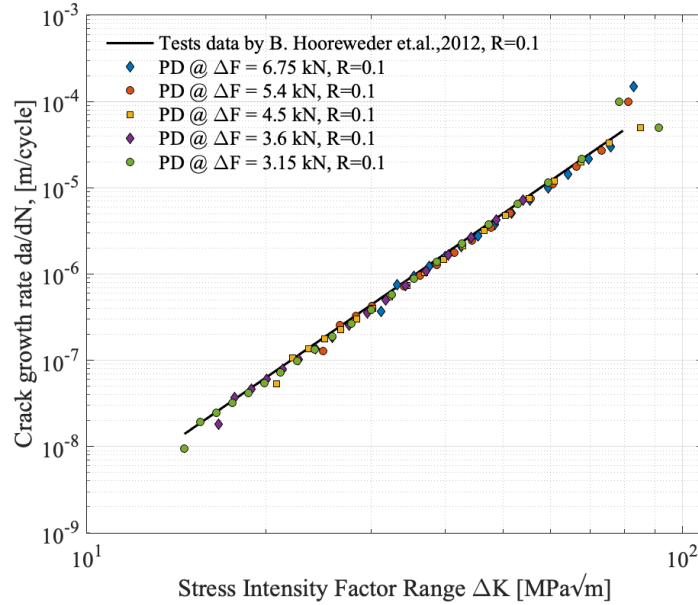
Figure 6.6 Crack growth rate versus SIF range. PD parameters calibration utilising the test data [159].
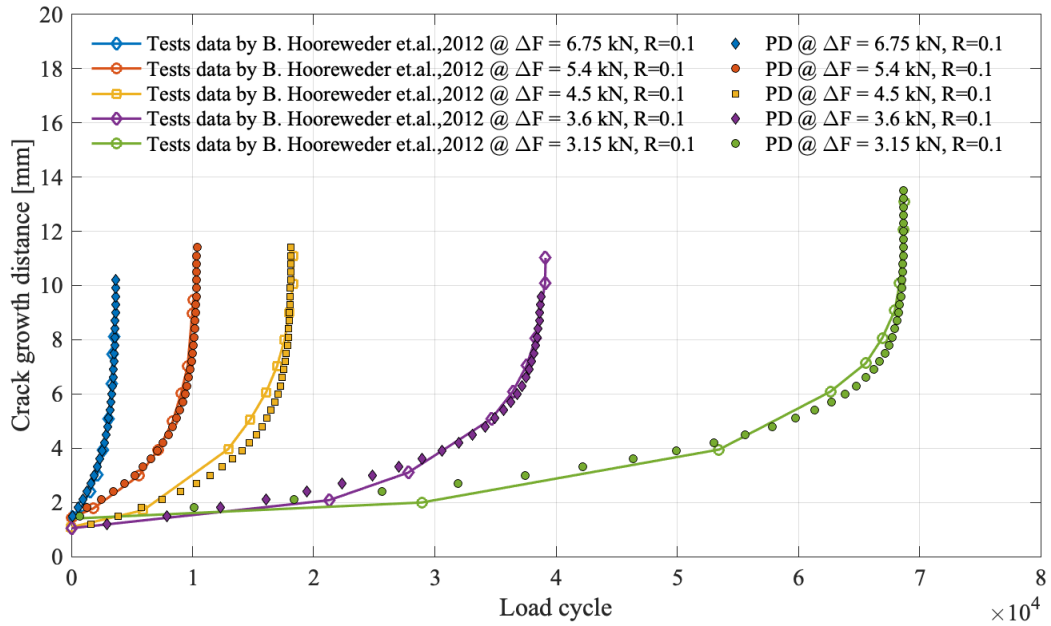
Figure 6.7 Crack growth distance versus load cycle for five different load cases. Comparison between PD and test data [159].

The numerical simulations in Figure 6.6 are evaluated after crack propagated around 1mm in order to analyse only the linear region of the $\frac{da}{dN} - \Delta K$ curve, where the fracture toughness can be calculated from Eq. (6.3), which is applicable when $\zeta > 0.2$ [164]. The crack growth curves for five different load cases are compared with the experimental results [159], where Figure 6.7 illustrates the capability of the PD fatigue model to capture the crack growth behaviour.

6.4 Influence of microstructure of the FCG

In order to understand the impact of microstructure on FCG in additively manufactured titanium alloys, different polycrystalline models are generated by the Voronoi tessellation method and are analysed under the constant cycling loading of $\Delta F = 3.15kN$ with the load ratio of $R = 0.1$, where the cyclic load extremes are $F_y^{max} = 7kN$ and $F_y^{min} = 0.7kN$. The loads are applied at the pins as shown in Figure 6.5 as body force density, evaluated by Eq. (6.1). The PD FCG model for wrought Ti6Al4V is validated with the experimental data in Section 6.3 and used to analyse the influence of material microstructure on crack propagation behaviour due to the AM

process. The geometry, shown in Figure 6.5, material properties of the C(T)-sample and PD parameters are kept the same as stated in Section 6.3.

Voronoi tessellation method or Voronoi diagram is a subdivision of a plane into regions. The centroidal Voronoi diagram is utilised, where the centroids are the generators of the Voronoi tessellation. For each centroid, the corresponding area is generated, called a Voronoi cell. For example, the Voronoi diagram is generated for 15 centroids in Figure 6.8, where MATLAB 'voronoi' function is used to plot the bounded cells of the diagram for assigned coordinates of 2D centroids (points).
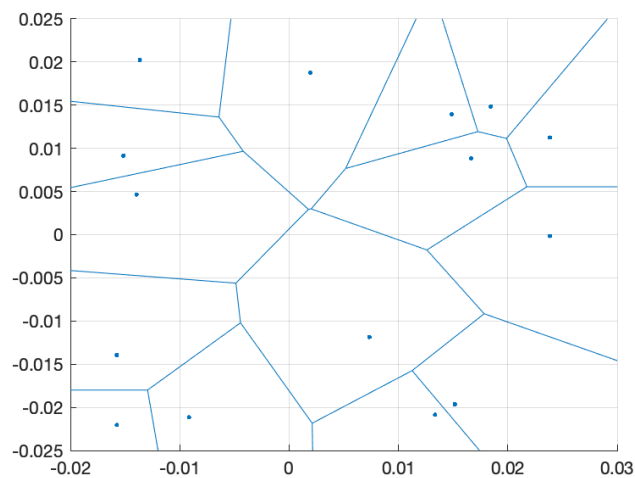
Figure 6.8 Voronoi cells for 15 points.

6.4.1   Modelling of grains in PD

The materials' microstructure is quite a complex phenomenon, which results in different fracture behaviour. The experiments [16, 19, 68] showed reported intergranular and transgranular crack propagation and, additionally, crack deflections. It is essential to understand the cause of the particular behaviour of the crack and the reason for variations in FCGR in the H-C(T) and V-C(T) samples produced by AM, discussed in Section 2.4.2 and shown in Figure 2.15. Thus, additively manufactured titanium alloys' failure modes are analysed due to the cycling loading, different types of the polycrystalline model with a variation of the grain and grain boundary strength. The polycrystalline model is generated by the Voronoi tessellation method, where each cell of the Voronoi diagram represents a grain. Therefore, the grains have different

properties of the Grain Boundaries (GB) and the Grain Interior (GI). The introduced "interface strength coefficient" [243] for the bonds in a system was used for various fracture problems. PD fatigue model can be expressed as:

$$
\begin{cases}
\dfrac{\lambda_{ij}^n - \lambda_{ij}^{n-1}}{N(n) - N(n-1)} = -kA_1\left(\varepsilon_{ij}^n\right)^{m_1}, & \text{for Phase I} \\[2mm]
\dfrac{\lambda_{ij}^n - \lambda_{ij}^{n-1}}{N(n) - N(n-1)} = -kA_2\left(\varepsilon_{ij}^n\right)^{m_2}, & \text{for Phase II}
\end{cases}
\tag{6.4}
$$

where

$$
k = \begin{cases} k_{GI}, & \text{for GI} \\ k_{GB}, & \text{for GB} \end{cases}
\tag{6.5}
$$

Eq.(4.6) accounts for two phases of fatigue, including crack initiation (Phase I) and crack propagation (Phase II), with Eq. (6.5) for the bonds between material points located inside the same grain and inside different grains. Figure 6.9 provides a visualisation of points distribution within the plate, where different colours indicate the nodes which belong to a particular grain. Firstly, if the material point is close to the crack with the length of a and in the red region as shown in Figure 6.9, then the interactions of the material point with the other 'family members' will be at Phase II of fatigue analysis with parameters A_2 and m_2. Secondly, the coefficient k is assigned as k_{GI} for the PD bonds of the material point interacting with the other 'family members' which belong to the same grain. Otherwise, coefficient k_{GB} is assigned for the bonds that pass over the grain boundary, as visualised in Figure 6.9. As the coefficient k is introduced to the evolution law in Eq. (6.4), the change in strength of the GB or GI is introduced with the weaker response than the initial structure. For example, suppose the bond connects two material points that belong to different grains, and it is assigned that the GB are weaker than the GI ($k_{GI} < k_{GB}$). In that case, the bond's life decreases faster and going to break earlier compared to the bonds between two points located within the same grain.
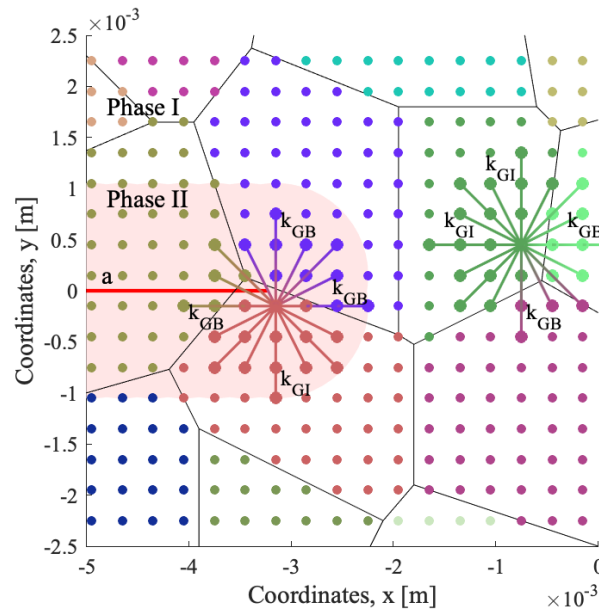
Figure 6.9 Interaction between material points and corresponding bond constants.

6.4.2 Effect of the grain size

The experimental studies [16, 19, 68] showed an impact of grain shape and size on fatigue crack performance of the titanium alloys. In this section, the effect of the grain size on the fatigue performance of the Ti6Al4V plate is analysed. Based on the observation from the material microstructure, random coordinates are generated to represent the centroids for the Voronoi grains. The selected number of the generated centroids represents the total number of grains in the system. Firstly, the PD polycrystalline models are generated for four configurations with the total number of grains within the sample: a. 500, b. 350, c. 200 and d. 50. Secondly, all four models are simulated under four conditions.

The GB are weaker than the GI with:

C1: $k_{GI} = 1, k_{GB} = 5$

C2: $k_{GI} = 1, k_{GB} = 10$.

The GI is weaker than the GB with:

C3: $k_{GI} = 5, k_{GB} = 1$

C4: $k_{GI} = 10, k_{GB} = 1$.

The parameters k_{GI} and k_{GB} are selected to numerically demonstrate the impact of different grain sizes, shapes and grain boundary effects on FCGR as well as to show that the elongated grains in the AM materials are one of the factors bringing the material anisotropy. To have the deeper knowledge of the grain boundary effects, the parameters k_{GI} and k_{GB} have to be calibrated.
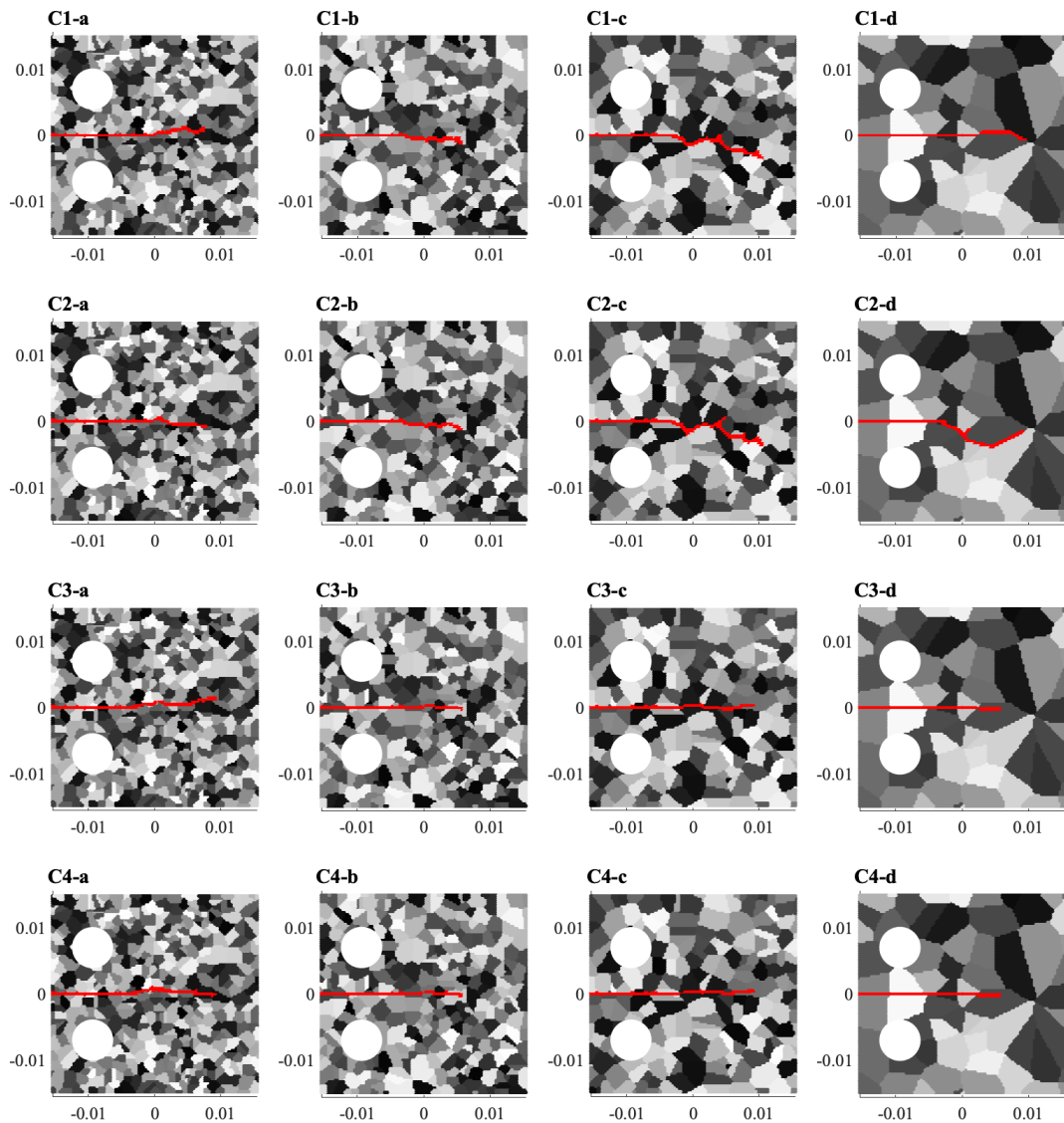
Figure 6.10 Damage plots for C(T)-samples under different grain coefficient conditions: C1: $k_{GI} = 1, k_{GB} = 5$, C2: $k_{GI} = 1, k_{GB} = 10$; C3: $k_{GI} = 5, k_{GB} = 1$ and C4: $k_{GI} = 10, k_{GB} = 1$, for the samples with total number of grains: a. 500, b. 350, c. 200 and d. 50.

128

The damage maps in Figure 6.10 show the intergranular crack propagation for conditions C1 and C2, where the strength of the GB is lower than the GI and transgranular for C3 and C4 where the strength of the GB is greater than the GI. The intergranular crack propagation can be seen for all grain sizes, which occurs due to the weakness of the bonds crossing the boundaries of the grain. Instead, with a transgranular fracture pattern, the crack is propagating through the grain with an almost straight crack path. The grey palette in Figure 6.10 indicates the randomly distributed grains, and the crack propagation pattern is displayed in red. The samples with the higher grain coefficients of $k_{GB} = 10$ (C2) or $k_{GI} = 10$ (C4) resulted in a faster crack propagation, as the bonds are weaker compared to the conditions C1 and C3.
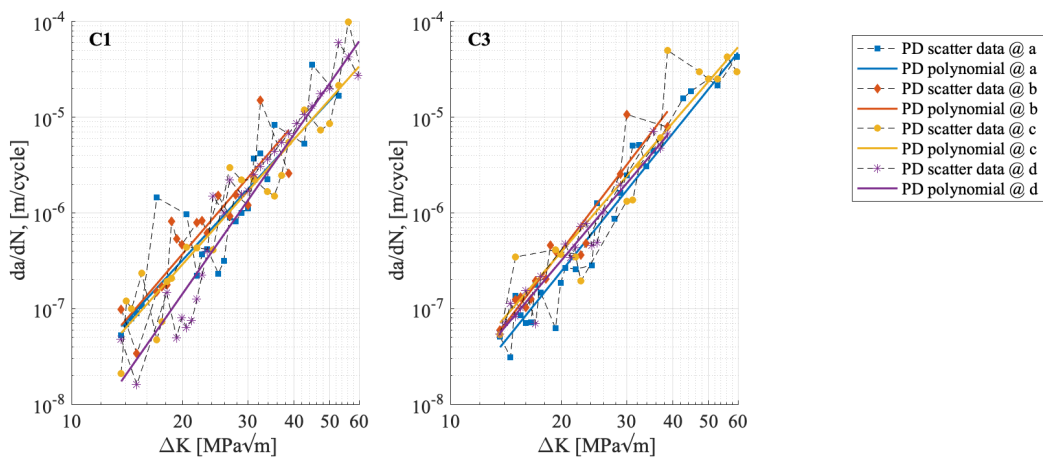
Figure 6.11 Crack growth curves for C(T)-samples under different grain coefficient conditions: C1: $k_{GI} = 1, k_{GB} = 5$ and C3: $k_{GI} = 5, k_{GB} = 1$ and for the samples with total number of grains: a. 500, b. 350, c. 200 and d. 50.

The PD results obtained from the FCG samples with condition C1 indicated that the coarser microstructures are more resistant to FCG. Figure 6.11 illustrates that the model with the coarse grain distribution of 50 grains requires a higher number of cycles compared to the model with a more significant number of grains. The models with fine microstructures (a. 500 grains) have a higher number of weak grain boundaries, which results in faster crack propagation. The investigations of the titanium alloy microstructures in [155] concluded that the finer microstructures lead to high FCGR. Hence, the evaluation of the samples under condition C3, where the GB are stronger than the GI, shows a very similar crack growth response for all grain models. The crack

is suppressed when it reaches the grain boundary and continues propagation through the next grain. (Figure 6.11, C3).

As the production of the materials can result in different types of microstructures, it is essential to understand the FCG response with intergranular or transgranular crack propagation. Figure 6.12 illustrates the comparison of FCGR for the models with different granularities. The numerical results clearly show that the coarser is the model, the better is the response of the samples with an intergranular crack propagation behaviour (sample C1-d). On the other hand, fine granularity models (a. 500 grains) show very close FCGR (Figure 6.12) for the samples C1-a and C3-a, even if the crack propagation for C1-a is intergranular and for C3-a is transgranular (Figure 6.10).
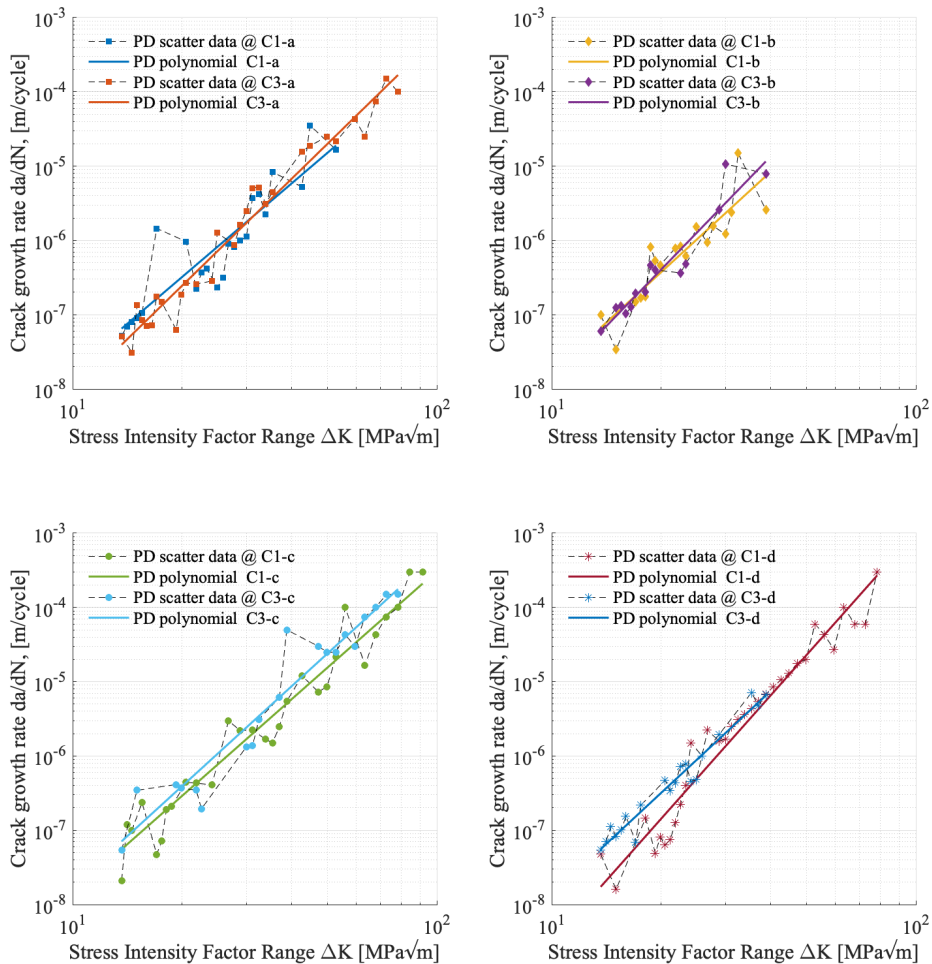
Figure 6.12 Crack growth curves comparison for C(T)-samples with different granularity: a. 500, b. 350, c. 200 and d. 50 and under different grain coefficient conditions: C1: $k_{GI} = 1, k_{GB} = 5$ and C3: $k_{GI} = 5, k_{GB} = 1$.

6.4.3 Effect of columnar grains

Due to the layered process of AM, the layers of the welding are annealed several times, which causes the anisotropy of the alloy microstructure. The difference in the grain sizes and elongated structure in the additively manufactured parts brings the anisotropic characteristics and the differences in the fatigue properties in different sample orientations. The microstructure analysis of the produced titanium alloy parts showed the columnar prior-β grains, which are growing parallel to the build direction. To introduce the columnar structure to PD polycrystalline model, the polycrystalline structure is generated by implementing the Voronoi tessellation technique. Similar to another study [244], the random coordinates are generated representing the centroids of the Voronoi grains and after contracted in x- or y-direction. For example, Figure 6.13 shows the steps of PD polycrystalline model generation, starting from the Voronoi tessellation technique, followed by step 2 of contraction in x-direction by a factor of 0.1. Finally, the last step is finding the material points located within the specified grain boundaries, followed by identifying the points located within the specified C(T) sample dimensions and assignment of material points associated with the grain. The contraction of the structure in x-direction presents the H-C(T) sample (Figure 2.15), where the columnar grains are allocated perpendicular to the deposited layer and for the representation of the V-C(T) sample structure, the contraction of the grains is in y-direction. Moreover, the third type of structure is generated with the columnar grain inclination by 45 degrees. For all three types of samples (a. H-C(T), b. V-C(T) and c. 45-C(T)), the grains are generated randomly, and, for the given domain, the number of grains is controlled by the overall of 120 columnar grains per sample with the grain size of around 10 mm in length and 1 mm in width. The numerical study is performed for the samples with assigned C1: $k_{GI} = 1, k_{GB} = 5$; C2: $k_{GI} = 1, k_{GB} = 10$; and C4: $k_{GI} = 10, k_{GB} = 1$.
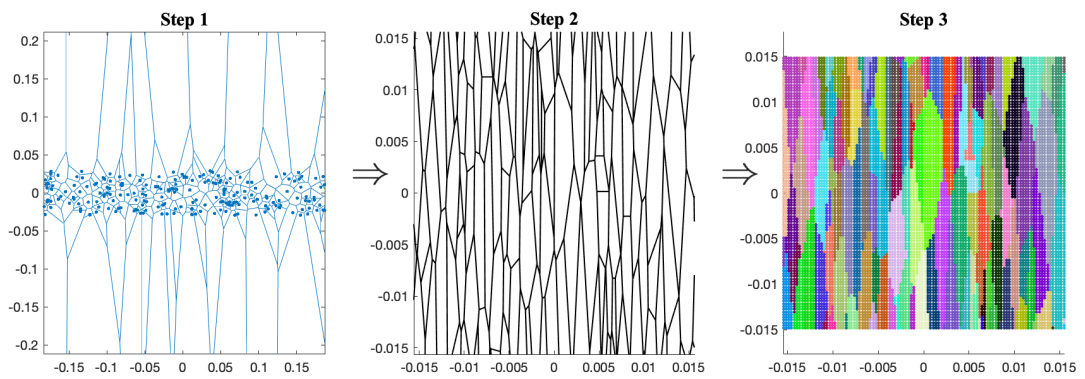
Figure 6.13 Generation of columnar grains from Voronoi tessellation technique.
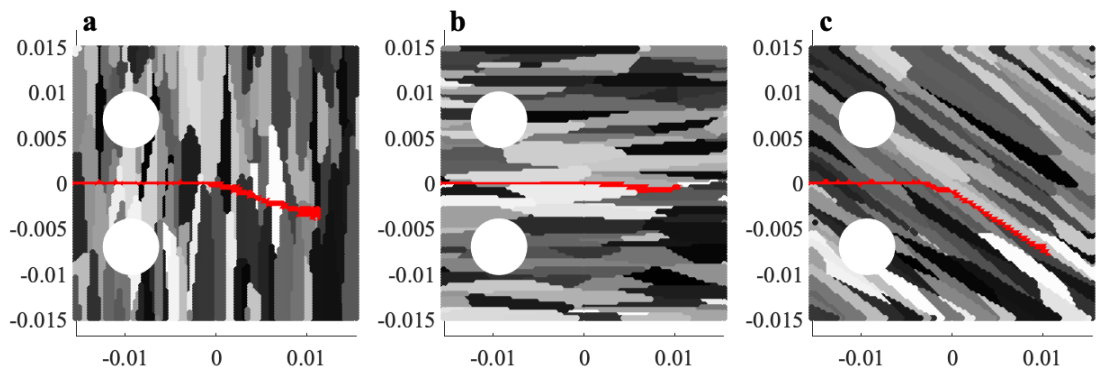
Figure 6.14 Damage plots for C(T)-samples under C1 with $k_{GI} = 1, k_{GB} = 5$: (a) H-C(T), (b) V-C(T) and (c) 45-C(T).
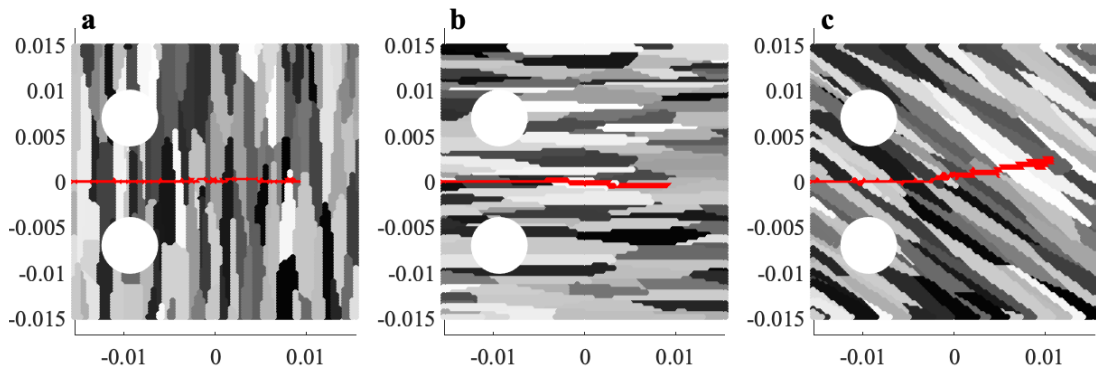
Figure 6.15 Damage plots for C(T)-samples under C4 with $k_{GI} = 10, k_{GB} = 1$: (a) H-C(T), (b) V-C(T) and (c) 45-C(T).
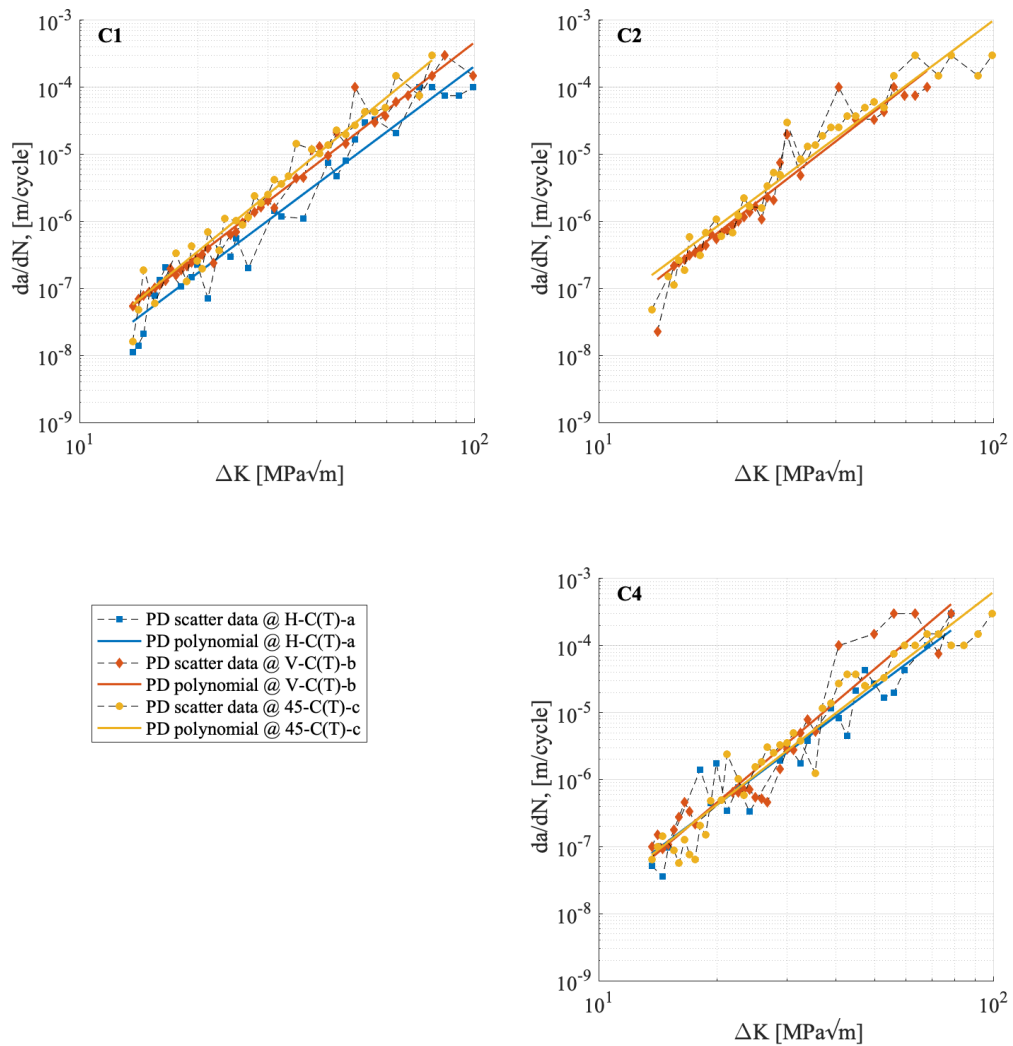
Figure 6.16 Crack growth curves comparison for CT-samples with different granularity: (a) H-C(T); (b) V-C(T) and (c) 45-C(T), and under different grain coefficient conditions: C1: $k_{GI} = 1, k_{GB} = 5$, C2: $k_{GI} = 1, k_{GB} = 10$ and C4: $k_{GI} = 10, k_{GB} = 1$.

The damage maps in Figure 6.14 show the transgranular crack propagation in H-C(T) samples, where the crack (indicated in red) passes through the multiple long grains (indicated in the grey scheme). Instead, when the columnar grains are distributed parallel to the initial crack (V-C(T) samples) or with 45 degrees of inclination (45-C(T) samples), the crack propagation is intergranular. Moreover, if the crack tip of the pre-crack is located inside the grain, the crack will move towards the closest GB and follow the path in-between two long grains. For the model with grains located perpendicular to the pre-crack (Figure 6.14a), the crack selects the path with the thinnest grains having

the higher number of weak GB on its way. Furthermore, as the crack repeatedly passes through multiple grains in the H-C(T) sample, this brings some resistance to the crack path, and the crack propagates longer (Figure 6.16). In the areas when the crack tip is passing through the grain, the FCGR of the sample H-C(T)-a is close to the reference material [18], indicated by the black line (Figure 6.16). The V-C(T) and 45-C(T) samples (Figure 6.16, C1) showed very close results of crack growth rates with the decreased scatter data.

Additionally, the FCGR are evaluated for the models with the grain coefficient $k_{GI} = 1, k_{GB} = 10$ (Figure 6.16, C2), where the crack propagation path is similar to the model with $k_{GI} = 1, k_{GB} = 5$ (C1), but the crack is propagating faster. The columnar grain model is simulated for the structures with strong grain boundaries, meaning $k_{GI} = 10, k_{GB} = 1$ (Figure 6.16, C4), where the grain direction does not have a big effect on the crack behaviour with the transgranular propagation for all models, shown in Figure 6.15, and the obtained crack growth rate curves almost coincide (Figure 6.16, C4).

6.4.4   Discussion

Modelling the grain structure by means of PD and evaluating the FCG behaviour and the FCGR in the C(T) Ti6Al4V samples show the anisotropy in the FCG properties. The columnar grains in Section 6.4.3 are a good representation of the WAAM samples, where elongated β grains are growing parallel to the additively manufactured layer build direction [120, 153]. The representation of the columnar grains in the H-C(T) sample, which are perpendicular to the crack propagation path (Figure 6.14) showing the crack pathing repeatedly through the grains on its way and indicating that more resistance is occurring on the crack path (Figure 6.16, C1). On the other hand, the V-C(T) samples show the weaker response of the sample to the fatigue loading with the fast-propagating crack along the columnar grains due to the fact that the pre-crack is parallel to the columnar grains. The same pattern of crack propagation in the different cuts of C(T) samples is noticed in the WAAM Ti6Al4V tests [16] where the H-C(T) sample has higher FCG resistance compared to V-C(T) sample due to the elongated β grains. On the other hand, since high pressure rolling of each additively manufactured

layer can be applied to reduce the grain size and as a result, to reduce the anisotropy in the material [120], the microstructure will no longer be columnar and β grains size is reduced to the one shown in Figure 6.10, where the C(T) sample with the higher number of grains is indicating the rolled structure under higher rolling load. Due to the rolling procedures of WAAM, the effect of changed microstructure is noticed during FCG tests [245], where rolled samples show the FCGR close to the wrought Ti6Al4V and reduced scatter of FCGR properties in both H-C(T) and V-C(T) samples. Due to this, the PD grain model from Figure 6.10 is the closest representation of the rolled WAAM samples, with the corresponding FCGR in Figure 6.11 due to different sizes of the grains.

In addition, the samples produced by SLM without any heat treatment [19] show contrary results compared to WAAM samples. The crack propagates faster in H-C(T) samples, even if the structure has elongated β grains parallel to the layer build direction. The cause for such an outcome in FCGR could be the existence of very high RS in the direction of crack propagation in H-C(T) sample. The applied heat-treatments show not only coarsening of the microstructure but also a huge reduction in RS, which results in very close FCGR for both layer orientations. The coarsening of microstructure shown in Figure 6.10d and numerical simulations of the fatigue propagation indicate that the coarser grain in a sample is more resistant to FCG. In this respect, the FCGR are closer to the wrought Ti6Al4V with the fatigue properties close to the isotropic sample Figure 6.11d.

6.5   Influence of pores on FCG

Another important effect to consider on FCGR is the existence of the pores in additively manufactured Ti6Al4V samples. Firstly, the porosities are initiated in the PD fatigue model, and the effect on the FCG behaviour is analysed. Secondly, the PD fatigue analysis is performed for C(T) specimen, which includes columnar grains and different levels of porosities. The porosities are initiates in the C(T)-sample, shown in Figure 6.5, with material properties and PD parameters described in Section 6.3. C(T)

sample is under the load ratio of $R = 0.1$ with the cyclic load extreams of $F_y^{max} = 7kN$ and $F_y^{min} = 0.7kN$, applied to the sample by Eq.(6.1).

6.5.1   Modelling of pores in PD FCR model

Three major factors affect the fatigue life of the structure: microstructure, pores and RS. In Section 6.4, it is numerically showcased the effect of the material microstructure on the fatigue crack propagation, and the developed model of the columnar grains had a different fatigue performance with respect to the grain orientation. In this section, the interest is on the influence of the pores on the crack propagation behaviour.

The study in Chapter 5 was performed on the effect of the pores on the fatigue crack nucleation in additively manufactured Ti6Al4V. The proposed numerical model for pores implementation in the PD fatigue nucleation showed good predictability of fatigue life of dog-bone samples under HCF. Moreover, the model provided an estimation of critical pore sizes and their locations. In this respect, a similar PD fatigue model is applied to the FCG problem in the C(T) sample. The proposed model for pores initiation in the numerical model adopts Murakami's formulation [147], where the relation between the SIF and the porosity size is analysed with the porosity coefficient enforcement in the cumulative damage rule of fatigue PD model, shown in Figure 5.14. Following that the Paris law can be expressed in terms of the cyclic bond strain ε, because ε is proportional to the SIF, a PD porosity model is implemented for both

of fatigue crack nucleation and propagation stages, where the porosity coefficient added in Eq. (6.4) as:

$$\begin{cases} \dfrac{d\lambda(N)}{dN} = -kA_1(\varepsilon\chi)^{m_1} = -kA_1\left(\varepsilon\dfrac{\Delta K_p}{\Delta K_{th,p}}\right)^{m_1}, & \text{for Phase I} \\[4mm] \dfrac{d\lambda(N)}{dN} = -kA_2(\varepsilon\chi)^{m_2} = -kA_2\left(\varepsilon\dfrac{\Delta K_p}{\Delta K_{th,p}}\right)^{m_2}, & \text{for Phase II} \end{cases} \tag{6.6}$$

where parameter k is the strength coefficient introduced in Eq. (6.5) for GB and GI presentation. The enforced parameter χ represents the pores with different diameters

of d_p in the relation between the SIF range ΔK_p and the SIF range limit $\Delta K_{th,p}$ for specified pores, as discussed in Chapter 5, Section 5.6.4, is increasing with the bigger pore diameter [23].

The analysis is performed for four different porosity levels of $P = 0.01, 0.04,$ 0.08 and 0.2%. The indicated porosities are selected due to the sample observations in the published works [11, 125, 130]. The reference model is the C(T) sample from Section 6.3 with the porosity of $P = 0$.

To initiate the porosity in the PD model, Gamma distribution with the shape parameter of $r = 10$ is selected, as shown in Figure 6.17. The assignment of the pores within the sample and the proposed method to reach the porosity levels is described in Section 5.6.4. Figure 6.17 shows an example of the plate with the porosity level of $P = 0.01\%$, the total number of $N_{p_{tot}} = 2324$ pores are randomly allocated in the sample with the maximum pore diameter of $d_p = 220\mu m$. The first row of Figure 6.17 showing the Gamma distributions for each of the assigned porosities with the indication of the total number of the pores $N_{p_{tot}}$ within a sample. The second row shows the random porosity distributions corresponding to each of the porosity levels, where the samples with the $P > 0.01\%$ has more dense porosity distributions with the total number of pores of $N_{p_{tot}} > 4300$. Note that the size of pores in Figure 6.17 are scaled only for visualisation purposes. Multiple crack interaction between neighbouring pores is taken into account, where the amplifying effect is considered and discussed in Chapter 4, meaning that the interaction between the pores i and j is effecting the remaining life of the bond as:

$$\begin{cases} \dfrac{d\lambda_i(N)}{dN} = -kA_1\big(\varepsilon_i \chi_i \chi_j\big)^{m_1}, & \text{for Phase I} \\ \dfrac{d\lambda_i(N)}{dN} = -kA_2\big(\varepsilon_i \chi_i \chi_j\big)^{m_2}, & \text{for Phase II} \end{cases} \qquad (6.7)$$
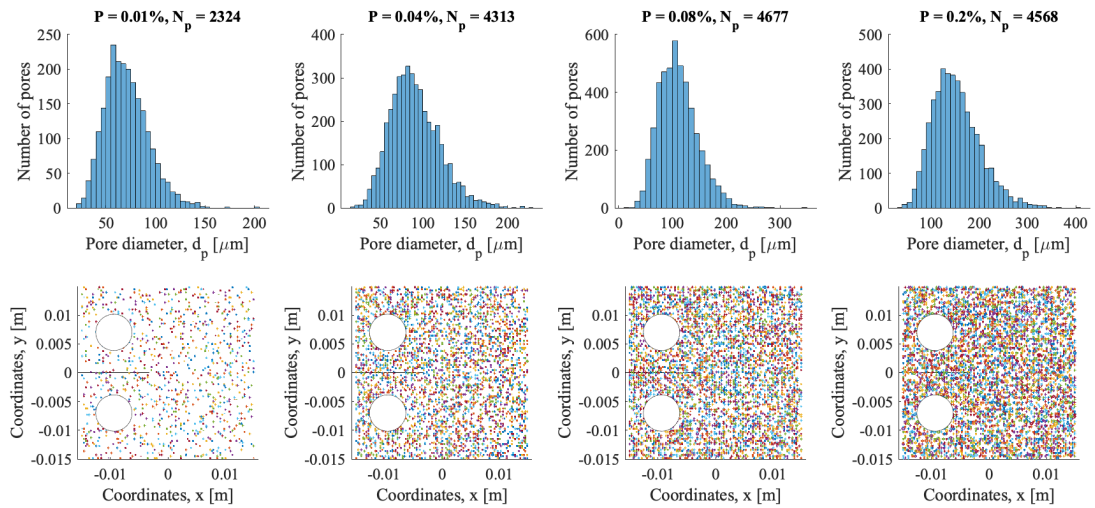
Figure 6.17 Gamma distribution of the pores with porosities of $P = 0.01, 0.04, 0.08$ and 0.2%, and its corresponding distributions in C(T) sample.
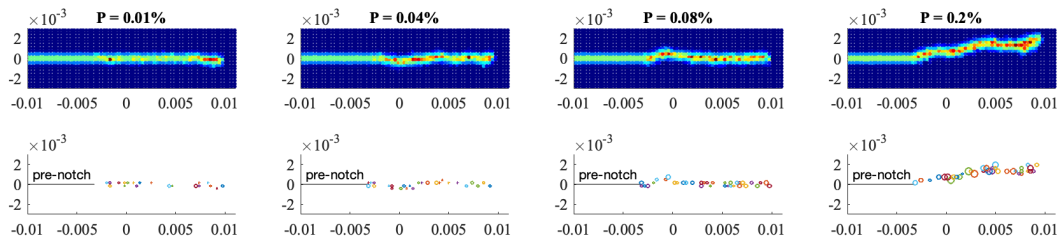
Figure 6.18 Crack propagation plots and pore distributions in front of propagating crack in C(T) sample with different porosity levels.

6.5.2 Results and discussion

The fatigue simulations are performed under the cyclic load of $\Delta F = 3.15\ kN$ with the load ratio of $R = 0.1$, and the material properties are same as stated in Section 6.3 by omitting the influence of material microstructure ($k_{GI} = 1, k_{GB} = 1$). In all of the simulated cases, crack is following the path with a higher density of pores and deflecting towards the pores with a bigger diameter, as shown in Figure 6.18. Only for the sample with the lowest porosity of $P = 0.01\%$ the crack growth is straight with the small deflection at the end of its path. The small effect on crack propagation is noticed due to the small porosities and low densities of the pores in front of the crack tip. The second row in Figure 6.18 shows the pores that the crack is propagating through, where only 20 pores with the mean pore diameter of $d_p^{mean} = 77 \mu m$ are noticed in the sample

with $P = 0.01\%$. On the other hand, the samples with the porosities of $P = 0.04$, 0.08 and 0.2% have higher clusters of the pores on the crack path with the number of pores of 26, 35 and 37, and mean pore diameter of $d_p^{mean} = 86, 121$ and $168 \ \mu m$, respectively. The samples with the higher porosity levels are weakening the sample's integrity and have a higher effect not only on the crack growth behaviour but also on the crack growth rates. The $da/dN - \Delta K$ curves in Figure 6.19 for C(T) sample with different porosity levels show the reduction of the fatigue strength due to the dense presence of the pores. Only the areas with pores of $d_p < 50 \mu m$ or where the distance between the pores is more then $0.3 \times 10^{-3} \ m$, the FCGR are very close to the wrought Ti6Al4V (Figure 6.19, calibrated PD model with $P = 0$) and the effect of the pores on the FCGR is minimal, as shown in Figure 6.19 for $P = 0.01\%$.
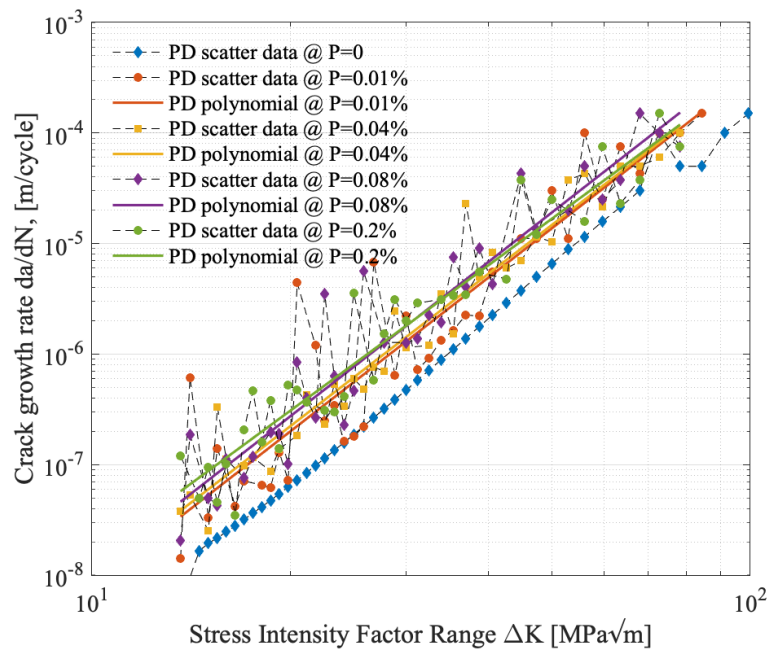
Figure 6.19 Crack growth curves comparison for C(T) samples with different porosity.

6.6   Effect of microstructure and pores on FCG

From the presented numerical study in Section 6.5.2, the effect of the porosities on the FCGR is clear with the low impact of the pores on crack growth behaviour only in the samples with low porosity densities and small sizes of pores. This could be the reason why the test studies [19] showed a minor impact of the pores of the diameter of $d_p \leq 50 \mu m$ on FCGR. Moreover, the study [14] of EBM Ti6Al4V alloy samples showed non-uniform defect distributions in the additively manufactured part with different fatigue performances of the H-C(T) and V-C(T) samples. It was indicated that the core part of the built was mostly defect-free, and the highest concentration of the pores were closer to the edges of the built [14]. Therefore, it was concluded that the porosities did not have a significant contribution to FCG properties. Instead, the review in [128] had the contrary outcome with a definitive effect of the pores on the fatigue performance where it is stated that fatigue crack behaviour is dependent not only on microstructure but also on process-induced defects, with the effect on the FCGR. With this respect, it is important to analyse the fatigue response of the C(T) specimen by considering the microstructure and process-induced defects, like pores.
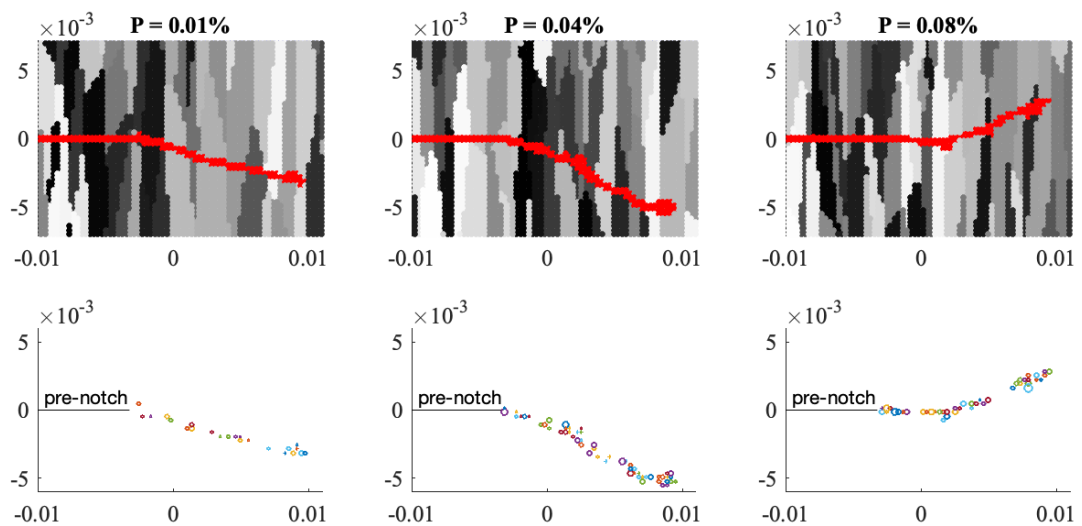
Figure 6.20 Crack propagation plots and pore distributions in front of propagating crack in H-C(T) samples with different porosity levels of P.
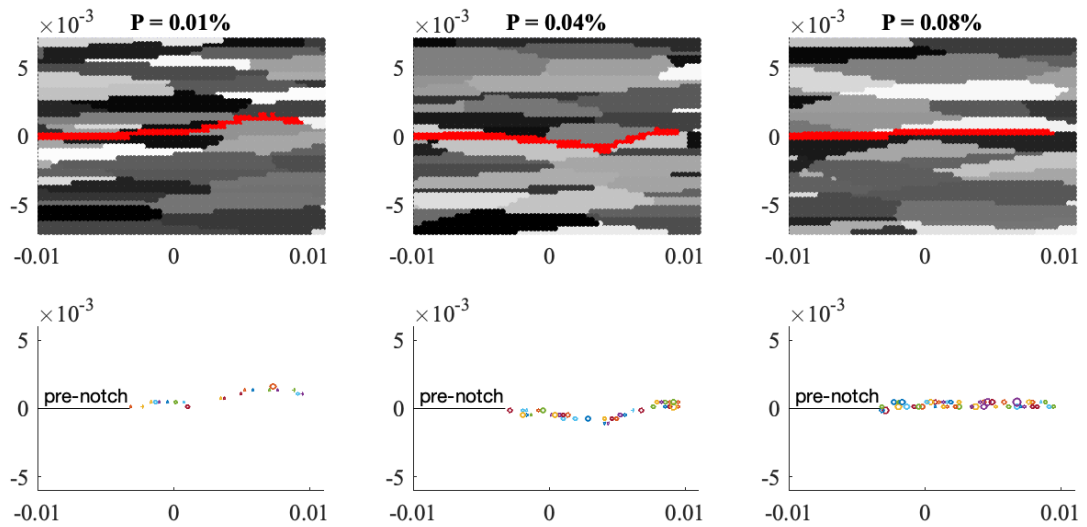
Figure 6.21 Crack propagation plots and pore distributions in front of propagating crack in V-C(T) samples with different porosity levels of P.

The PD fatigue model includes the two types of C(T) samples, shown in Figure 6.20 and Figure 6.21 with the granularity of C1 ($k_{GI} = 1, k_{GB} = 5$), described more in details in Section 6.4, and three levels of porosity $P = 0.01, 0.04$ and 0.08%. As shown, in Figure 6.20 and Figure 6.21, the H-C(T) samples has the long grains allocated perpendicular to the pre-notch; on the other hand, sample V-C(T) has the grain distribution parallel to the pre-notch. The long grains are presented in a grey pattern. The performed PD simulations for all porosity levels have shown transgranular crack propagation for H-C(T) and intergranular crack propagation for V-C(T) samples. In all the cases for H-C(T) samples, crack deflects toward the weakest areas with the higher densities of the pores but still propagates through the grains (in Figure 6.20). Evaluating the FCGR, the porosities have a clear effect on the fatigue performance, where in both types of samples, H-C(T) and V-C(T), the higher levels of porosities initiate the faster crack propagation resulting in the worth FCGR, shown in Figure 6.22. Moreover, comparing the fatigue performance of H-C(T) and V-C(T) samples in Figure 6.23 shown that H-C(T) samples are still more resistant to the FCG.
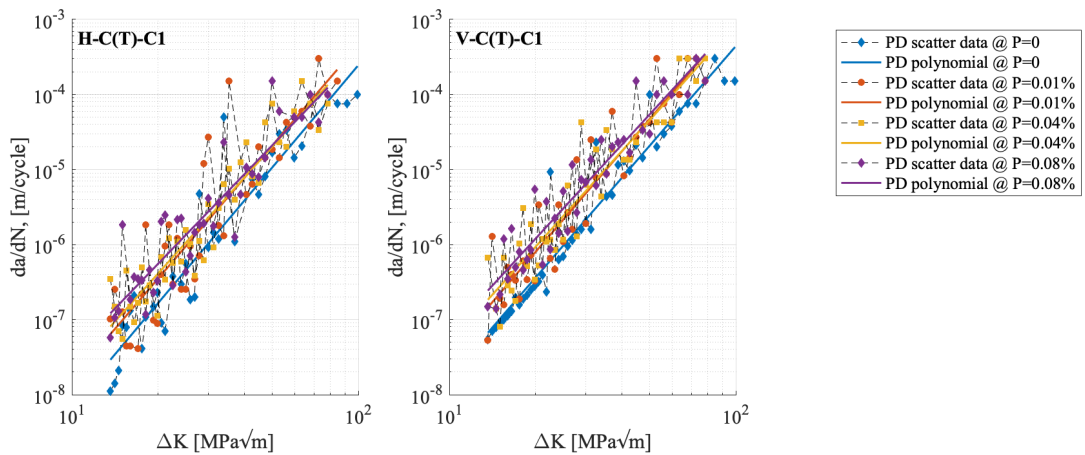
Figure 6.22 Crack growth curves comparison between samples with different porosity levels of P and granularity of H-C(T) and V-C(T) samples.
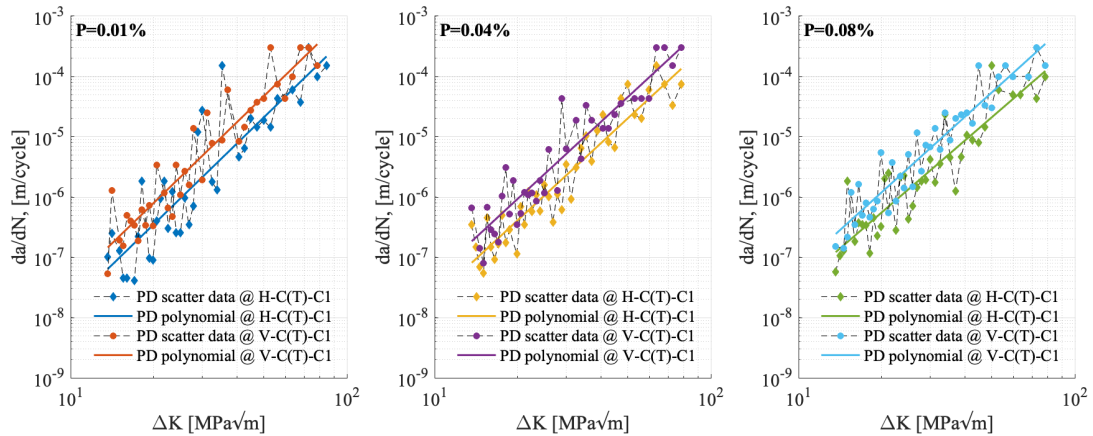
Figure 6.23 Crack growth curves comparison between H-C(T) and V-C(T) samples with porosity of $P = 0.01, 0.04$ and 0.08%.

The PD study showed good assessment and indication of the porosity effects on the FCG even if the model is treated as elastic and the plastic deformations are neglected. All the pores are treated as spherical, and the cavities in the samples are evaluated, taking the pore diameter into account. The following assumption is made based on the test observations [7, 126], where the most common process-induced defects are spherical pores. Thus, the PD fatigue model accurately captures the small changes in the material structure and the effect of the small defects on the FCGR and crack propagation behaviour due to the pore existence. The initiation of granularity and porosity in the numerical model indicated the influence of both factors on fatigue

142

performance. Firstly, it is showcased by means of numerical modelling the importance of porosity reduction in the samples, as even the small porosity levels of $P = 0.01\%$ with the distribution all over the sample have a noticeable impact on FCGR. Secondly, the numerical investigation on the columnar grains in the structure showed the anisotropy in the fatigue properties due to the development of a long-grained structure during the AM process.

6.7   Effect of residual stresses on FCG

The last major factor in evaluating is the effect of the RS on the FCG. In general, the AM process results in very high RS due to repeated heating and layered cooling process. The stresses depend on the temperature distributions, especially when the produced deposit cools down. The RS tend to change from compressive to tensile in the middle of the samples and from tensile to compressive between the layers, with a non-uniform distribution of RS within the sample [165].

The PD fatigue model consists of multiple static tension-compression cycles. Due to this, the implementation of the RS was simplified and a pre-tension or pre-compression model due to thermal deformation is introduced. Moreover, the applied temperature distributions are the same in each cycle and the RS will be readjusted due to the crack propagation only. In this section, the model is treated as elastic and the RS are compressive in both x and y directions or tensile in both directions.

Firstly, the FEA of the thermally deformed structure is performed using the commercial software ANSYS to identify the residual thermal stresses due to the heat source. Secondly, FEA is used to evaluate the maximum RS in the C(T) sample under different temperature distributions, and PD numerical model is verified with FEA. Lastly, the fatigue crack propagation analysis by means of PD is performed on a titanium alloy C(T) sample with initial stresses due to the applied temperature profile.

6.7.1   FEA of residual stresses in C(T)-sample

FEA is conducted to evaluate the RS in the C(T) specimen. In order to introduce the RS in titanium alloy C(T) specimen, the temperature BC should be specified. Figure 6.24 shows the configured temperature distribution. Note that the selected paraboloid temperature distribution does not represent the real temperatures in the additively manufactured C(T) samples but are selected by the iterative procedure to reach the specific levels of RS in the numerical sample. Four types of parabolic temperature distributions are selected with $T_{\max}$ equal to $-250,\ 250,\ 500,$ and $1000\ K$ with the resulting RS shown in Figure 6.25.
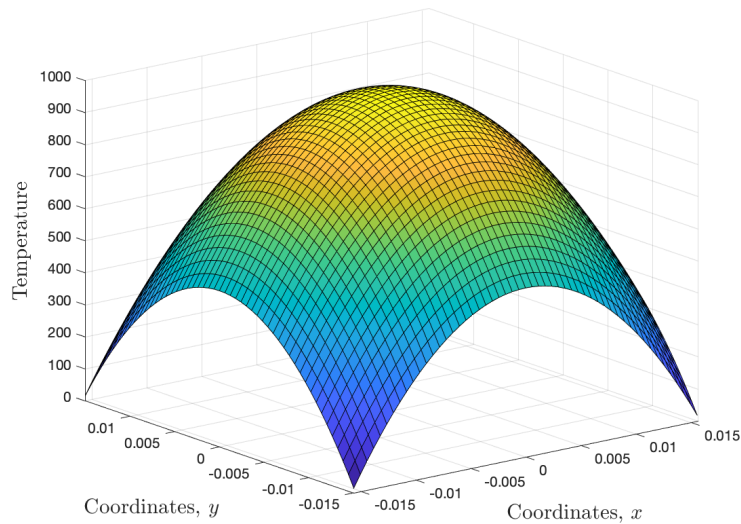
Figure 6.24 Parabolic temperature distributions in C(T) sample with $a = 0$ under $T_{\max} = 1000\ K$.

The calculated RS by means of FEA at the centre line of the sample in Figure 6.25 indicating the high tensile stress concentrations near the crack tip with higher longitudinal RS σ_x^{rs} for the higher $T_{\max} > 0$. The sample without the crack with $a = 0$ is in a compression state, but as the crack is initiated in the sample, high tension stress area develops at the crack tip. Similar changes from compressive to tensile RS were noticed during the pre-notch machining process of the C(T) sample preparation, as discussed by Syed et al. [163]. Moreover, the distribution of the transverse RS σ_y^{rs} in Figure 6.25 is very close to the residual stress distributions in [163, 166], where the sample without pre-notch is under tensile RS at the areas close to the edges. On the

other hand, with the initiation of the notch, the maximum tensile stresses for $T_{\max} > 0$ are in front of the notch tip, followed by compressive stresses.
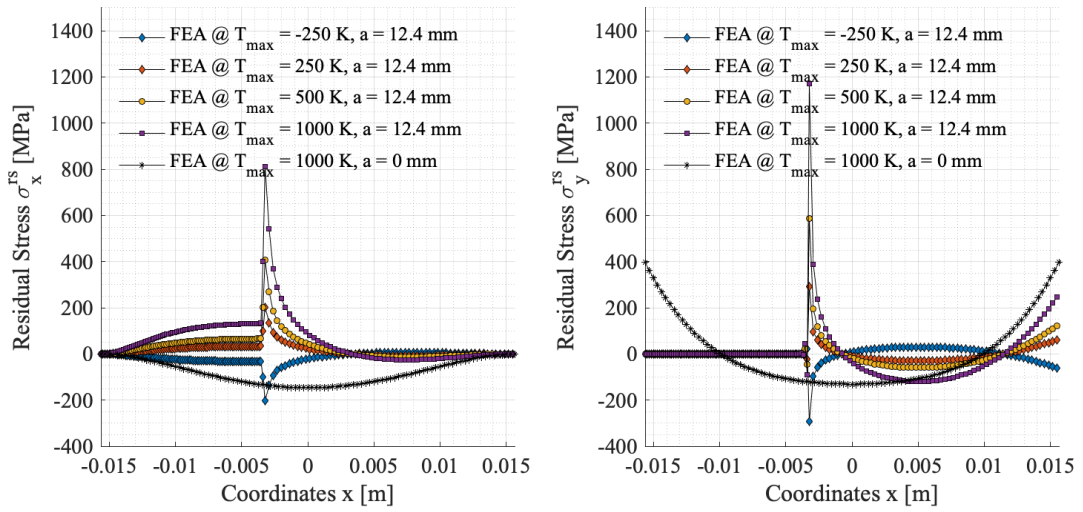
Figure 6.25 Residual stress distribution in the C(T) sample along the centre line $y = 0$ for a crack length of $a = 0$ and $a = 12.4\ mm$ due to the different temperature profiles.
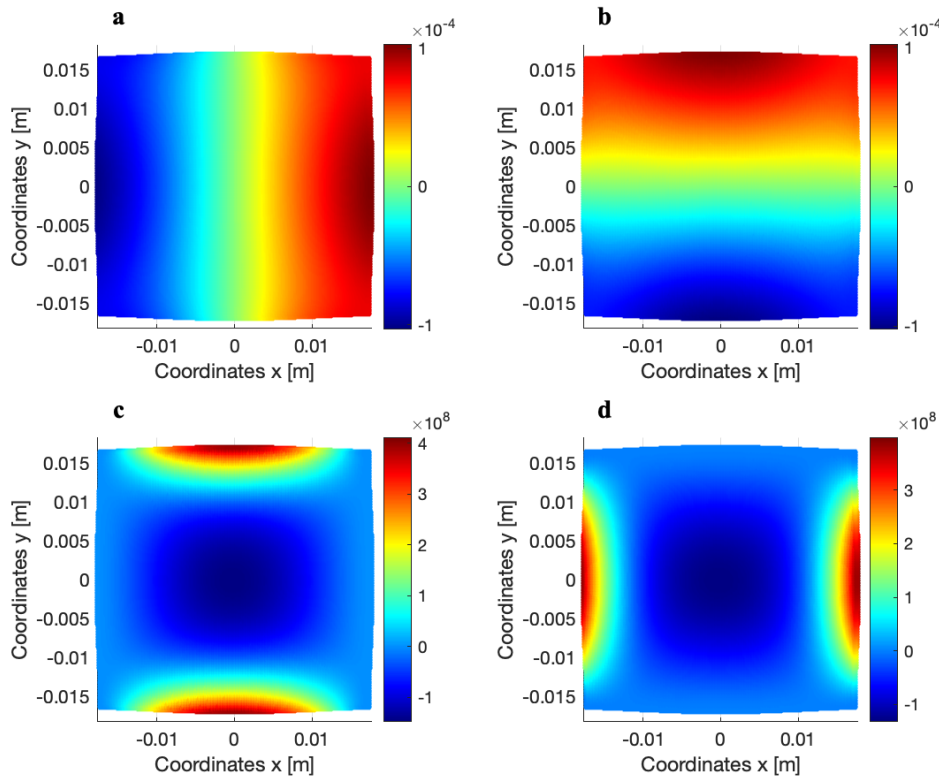
Figure 6.26 Displacements in (a) x-direction $u\ [m]$ and (b) y-direction $v\ [m]$. RS (c) $\sigma_x^{rs}\ [Pa]$ and (d) $\sigma_y^{rs}\ [Pa]$ of the plate with a crack length of $a = 0$ under temperature distribution of $T_{\max} = 1000\ K$.
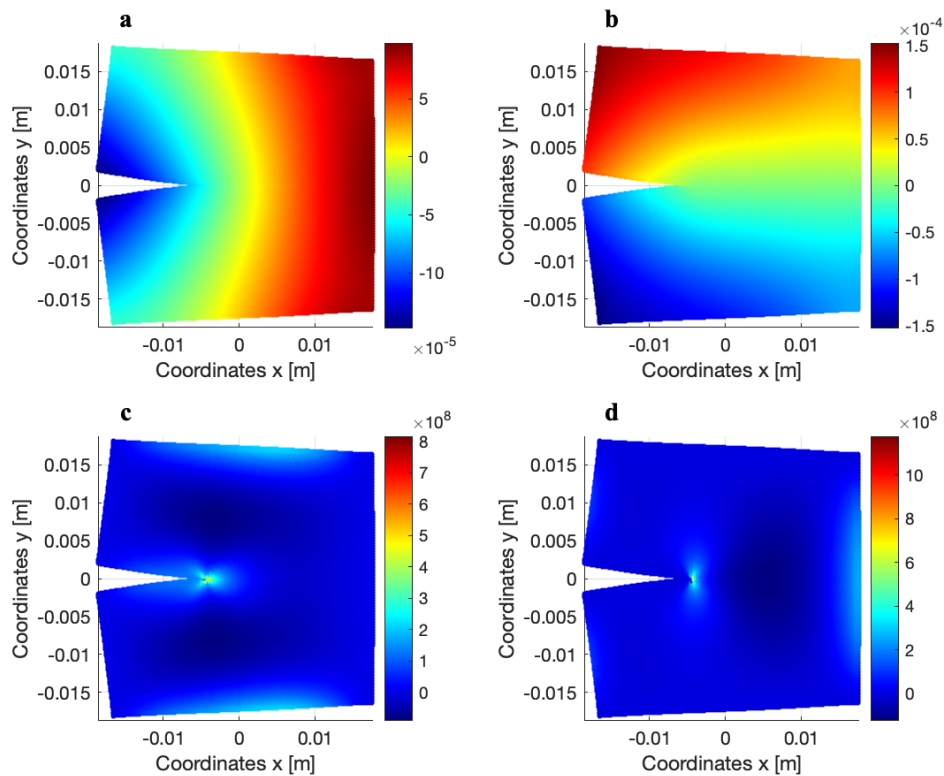
Figure 6.27 Displacements in (a) x-direction u $[m]$ and (b) y-direction v $[m]$. RS (c) σ_x^{rs} $[Pa]$ and (d) σ_y^{rs} $[Pa]$ of the plate with a crack length of $a = 12.4\ mm$ under temperature distribution of $T_{\max} = 1000\ K$.

In Figure 6.26c,d, the compressive RS in the plate without a crack are due to the applied parabolic temperature profile where the peak temperatures are in the middle of the plate and the gradual decrease of the temperatures are closer to the plate edges. Compressive stresses happen due to the non-uniform heating and cooling of the plate, where the plate tends to expand due to the heat at the centre, as shown in Figure 6.26a,b, but cooling constraining boundaries at the edges are restraining the expansion. On the other hand, when the crack is initiated in the plate, peak RS in Figure 6.25 are noticed at the crack tip due to the thermal expansion of the plate when $T_{\max} > 0$ as shown in Figure 6.27, followed by the compressive stresses closer to the plate edge with the cooling temperatures. Instead, when $T_{\max} < 0$ the crack closure takes place (Figure 6.28a,b) with high compressive stresses at the crack tip (Figure 6.28c,d). The increased difference between the heating and the cooling temperatures (parabolic profile) in the plate results in the higher stresses in front of the crack tip, as shown in Figure 6.25. The non-uniform temperature distribution in the plate resulting in a subsequent expansion

and contraction is the cause of the non-uniform stresses with the peak stress concentrations at the crack tip.
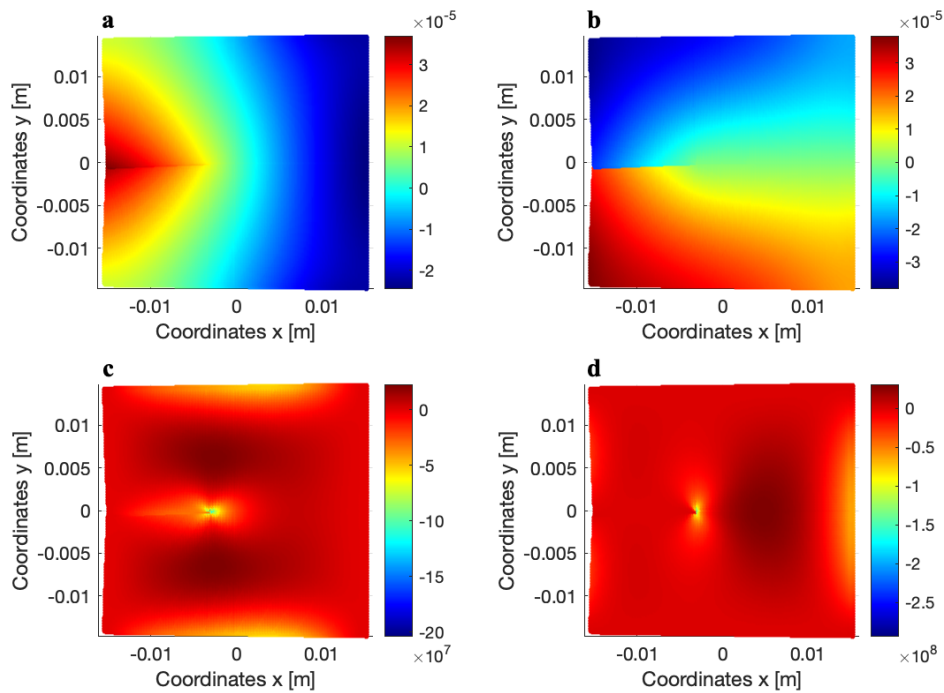
Figure 6.28 Displacements in (a) x-direction $u\ [m]$ and (b) y-direction $v\ [m]$. RS (c) $\sigma_x^{rs}\ [Pa]$ and (d) $\sigma_y^{rs}\ [Pa]$ of the plate with a crack length of $a = 12.4\ mm$ under temperature distribution of $T_{\max} = -250\ K$.
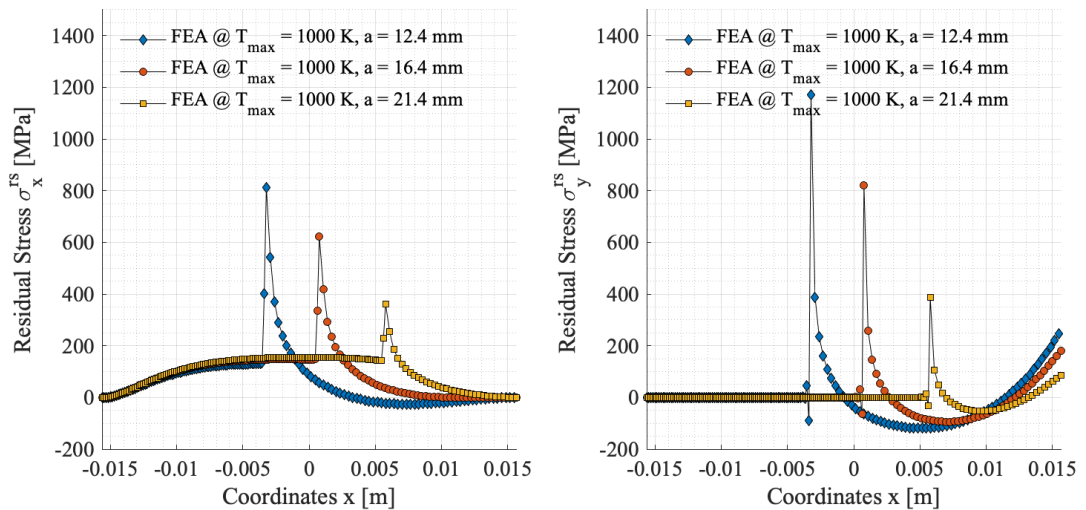
Figure 6.29 RS at the crack tip in the C(T) sample along the centre line $y = 0$ for an increasing crack length of a.

The thermally deformed pre-cracked structure in Figure 6.25 will be used for fatigue crack propagation analysis and the stresses at the crack tip will be referred to as maximum RS in the sample. With this respect, four models are identified with an initial maximum RS of $\sigma_x^{rs} = -203.3, 203.3, 406.6$ and $813.2 \; MPa$, under temperature distributions of $T_{\max} = -250, 250, 500$ and $1000 \; K$, respectively.

Figure 6.29 presents calculated RS by means of FEA versus the crack length along the crack propagation line in the plate under temperature distribution of $T_{\max} = 1000 \; K$. The tensile stress area can be noticed near the crack tip for both longitudinal and transverse directions, at the crack length of $a = 12.4, 16.4$ and $21.4 \; mm$, with the release of RS as the crack propagates.

It can be noted in Figure 6.29 that the RS are decreasing with the increased crack length in a plate under the applied parabolic temperature distribution shown in Figure 6.24. The following outcome is contrary to the increasing stresses in the plate as the crack propagates due to the tension loading conditions. The decrease in the RS occurs due to the applied temperature profile, as shown in Figure 6.30. The cooling temperatures at the edges of the plate result in high RS at the crack tip and compressive RS ahead of the crack. As crack length is increasing, the applied temperatures ahead of the crack tip are lower, compared to the initial crack length of $a = 12.4 \; mm$ and the RS are decreasing. The application of different temperature profiles results in a different outcome of RS. For example, the temperature profile in Figure 6.31a results in lower RS in Figure 6.31b,c than applied parabolic distribution in Figure 6.29. The temperature distribution in Figure 6.24 with the resulting RS in Figure 6.29 is the first iteration of the simplified implementation of initial RS in the additively manufactured structure, where the stresses within the sample are not constant and decrease as the crack propagates. Multiple variations of the temperature distributions, which could represent the initial RS in the additively manufactured samples due to the layer-by-layer process, are in the interest of further studies.
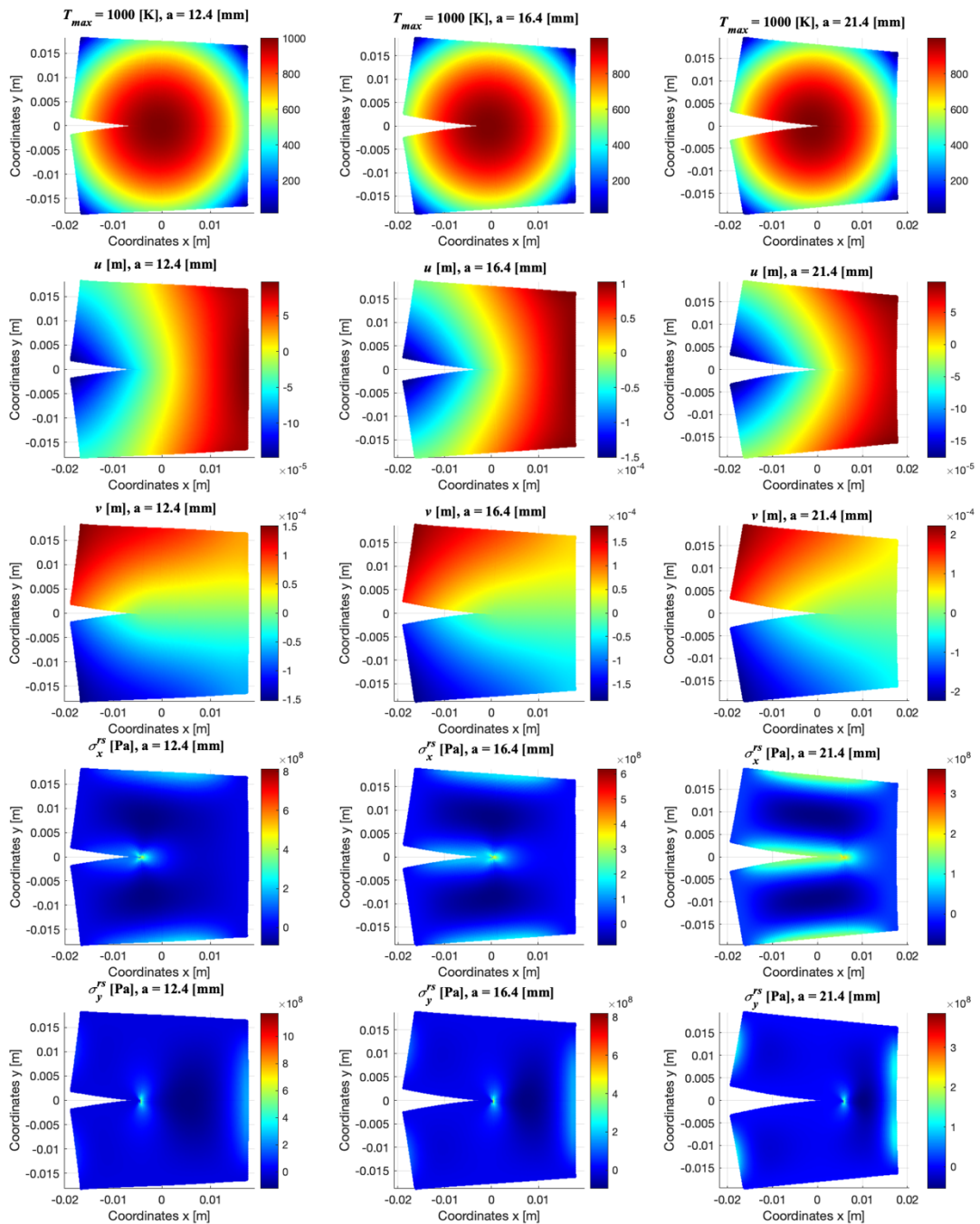
Figure 6.30 Temperature distribution, displacements in x-direction (u) and y-direction (v), RS σ_x^{rs} and σ_y^{rs} of the plate with a crack length of $a = 12.4, 16.4$ and $21.4\ mm$.
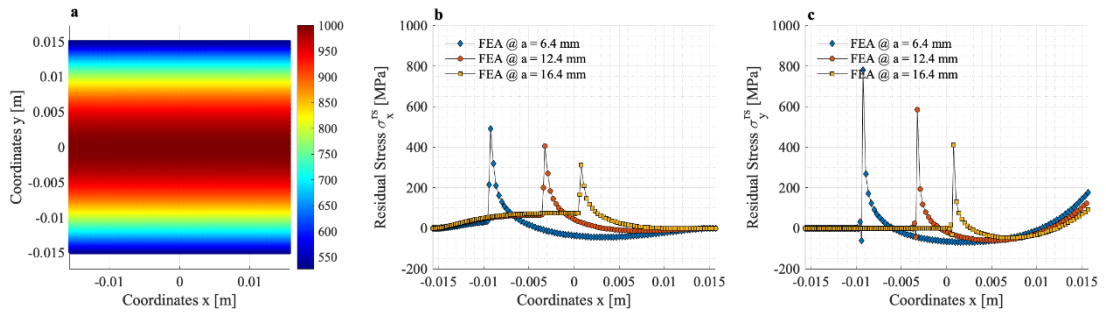
Figure 6.31 (a) Temperature distribution, RS (b) σ_x^{rs} and (c) σ_y^{rs} of the plate with a crack length of $a = 6.4, 12.4$ and $16.4\ mm$.

6.7.2   PD model verification with FEA

The FCG analysis is performed by means of PD and the model is verified with FEA so that the implemented temperature profiles described in Section 6.7.1 will result in the same maximum RS distributions. The PD fatigue model is described in Section 5.3 and the flowchart of the tension-tension loads and temperature distribution implementation in the PD FCG model is shown in Figure 6.32. The parameters and material properties of the titanium alloy Ti6Al4V C(T) sample are specified in Section 6.3. The thermal expansion coefficient is $\alpha = 8.78 \times 10^{-6}\ 1/K$.

Both FEA and PD models are simulated under the parabolic temperature distribution with $T_{\max} = 1000\ K$ (Figure 6.24) as shown in Figure 6.33 the PD results are in good agreement with FEA results for the displacements along the centre lines of the plate.

Utilising PD for the fatigue simulations, the temperature distribution with $T_{\max}$ is initiated at each cycle to represent RS in the sample, as shown in Figure 6.32. This means that at each cycle of tension-tension with the load ratio of $R = 0.1$ and with the load amplitude of ΔF, the parabolic temperature is introduced. Figure 6.34 shows PD models, where only the maximum tension load of $F_{max} = 7\ kN$ is applied at the cut outs (Figure 6.5), only temperature distribution with $T_{\max}$ is introduced and the combined model with both $F_{max} + T_{\max}$. When the tension load of F_{max} occurs together with $T_{\max}$, the displacements are superimposed. In this respect, in Figure 6.34, the application of the tension load together with the temperature of $T_{\max} = 1000\ K$, higher displacements are noticeable in the thermally deformed structure under tension

loading. The application of temperatures of $T_{\max} > 0$ leads to the sample expansion, shown in Figure 6.34, and crack opening. Instead, when the temperatures are $T_{\max} < 0$, the crack closure occurs and under the combined loads of $F_{max} + (T_{\max} = -250\ K)$, the sum of the displacements is lower compared to the condition with F_{max} only.

It should be noted that PD FCG simulations for the samples without initial RS (wrought Ti6Al4V in Section 6.3) is solved by PD equations of motion and the crack propagation is controlled by fatigue damage model described in Section 5.3. In this way, the stresses in the plate are occurring due to the externally applied loading, which affects crack tip stress fields. Instead, the experimental checks of additively manufactured samples [14, 15, 19] showed the RS in the material before the crack initiation and propagation processes. With this respect, to initiate the initial RS in the plate due to AM process, it is proposed to apply parabolic temperature distribution, which results in tensile or compressive stresses in front of the crack tip before the tensile load is applied. It is a simplified method of initiation of pre-tension or pre-compression of the model with the representation of RS. As shown in Figure 6.34, the applied loading occurred together with RS (due to the applied temperature distribution), which favours crack opening and promotes the crack propagation, discussed in the next Section 6.7.3. The current numerical model assumes that the material is linearly elastic, and the effects of the RS due to the temperature distribution and the applied stresses due to the tension loading are superimposed. The following assumption is not an absolutely accurate criterion as the existence of the RS effects on the crack tip stress field and when the sample is loaded, the distribution of plastic strain in the crack tip field occurs [246]. The non-uniform distribution of the RS in the additively manufactured structures [14, 15, 19] and the internally self-equilibrating stresses due to the crack initiation complicates the prediction of FCGR. It is beneficial for future works to check other temperature profiles for the implementation of initial stresses in the samples due to AM. Still, additional tests and data should be available on initial RS, redistribution of RS due to crack propagation and the effect of the RS on FCGR. Nevertheless, the proposed PD combining RS and applied loading shows promising results in Section 6.7.3.
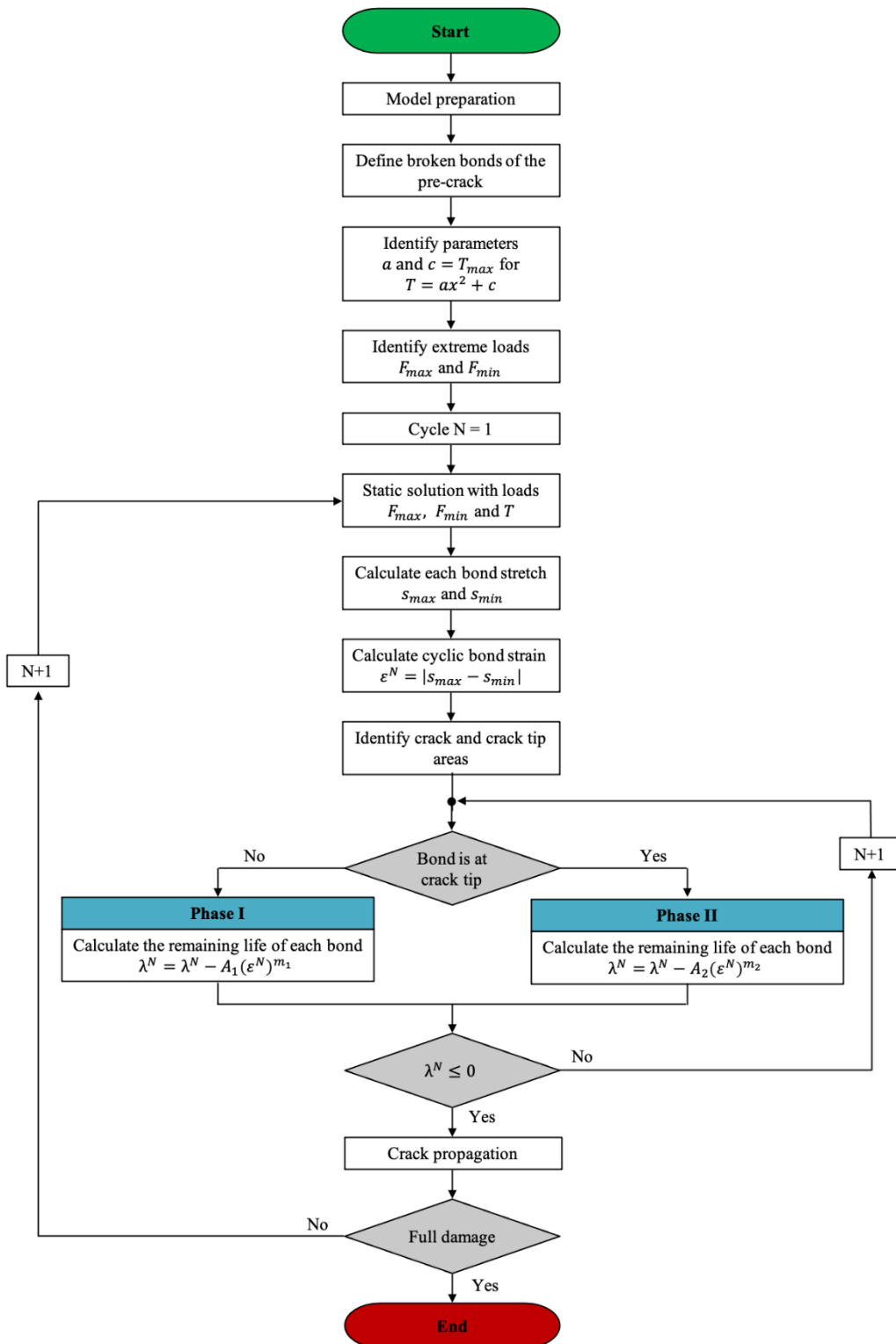
Figure 6.32 Flowchart of PD fatigue model with initiated tension-tension loads of F_{max} and F_{min} and temperature distribution with $T_{\max}$.
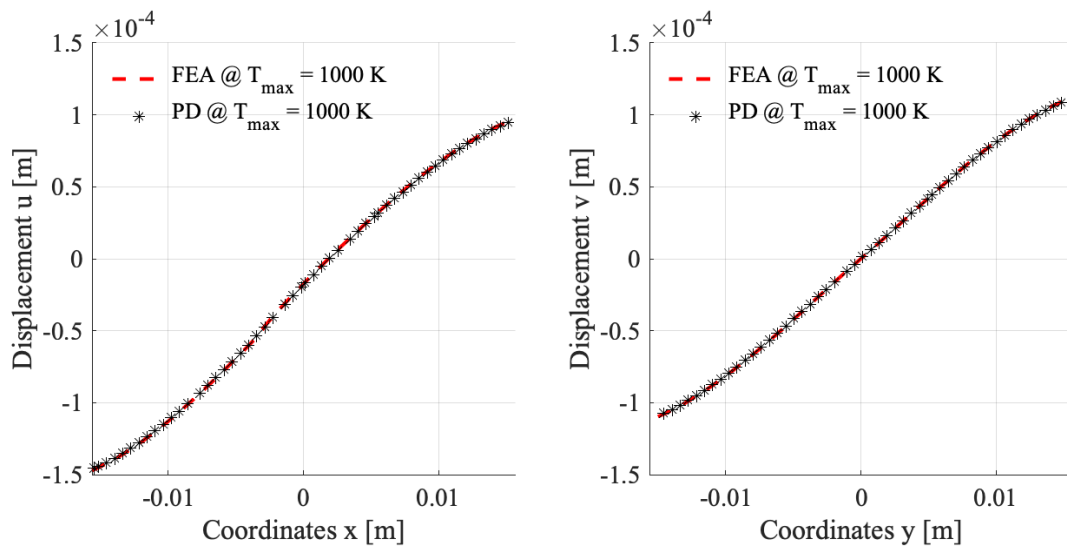
Figure 6.33 Displacement variations along the centre lines in a plate with a crack length of $a = 0$.
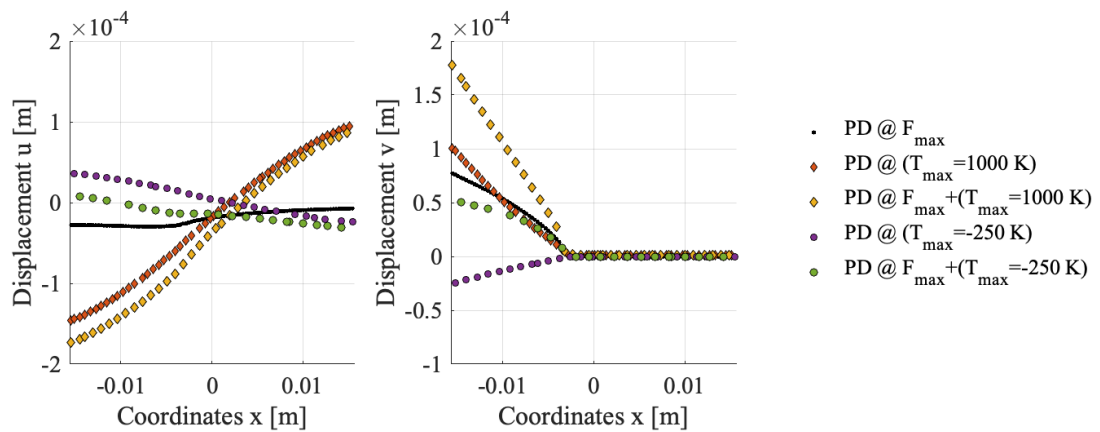
Figure 6.34 Comparison between PD predictions of the displacement variations along the centre line $y = 1.5 \times 10^{-4}$ at: tension load $F_{max} = 7\ kN$ only, temperature distribution with $T_{max} = 1000\ K$ only, and combined $F_{max} + T_{max}$.

6.7.3 PD FCG model results and discussions

The PD fatigue model from Section 6.3 is selected for the study of the FCG in the C(T) sample. The geometry, material properties of the C(T) sample and PD parameters are kept the same. The cyclic load of $\Delta F = 3.15\ kN$ with the load ratio of $R = 0.1$ is selected.

The simplified model of RS implementation includes the temperature distribution profile from Figure 6.24 for each cycle load of ΔF. The following approach of modelling initiates high tensile RS near the crack tip in the plate as described in Section

6.7.1. The sample is analysed under three tensile and one compressive RS. The load cases and the resulting stresses in front of the crack tip are summarised in Table 6.1.

The PD FCG model uses the Paris' law described in Section 5.3, where cyclic bond strain ε is proportional to the cyclic SIF and the life of the bonds evolves according to Eq.(5.7). The applied Paris–Erdogan equation does not explicitly include the crack closure phenomena as it is done by Elber [80, 247], which defines an effective stress intensity range when partial crack closure occurs after unloading the sample. In the current study, the tension-tension loads are applied with the load ratio of $R = 0.1$ and the model is treated as elastic where the phenomena of plasticity-induced crack closure is neglected.

Table 6.1 Load cases and RS at a crack length of $a = 12.4 \times 10^{-3}\ m$

Type	Parabolic temperature distribution with $T_{\max}, K$	RS due to temperature $T_{\max}$, σ_x^{rs}, MPa	RS due to temperature $T_{\max}$, σ_y^{rs}, MPa	Cyclic load, $\Delta F, kN$
1	1000	813.2	1173	
2	500	406.6	586.3	3.15
3	250	203.3	293.1	
4	-250	-203.3	-293.1	
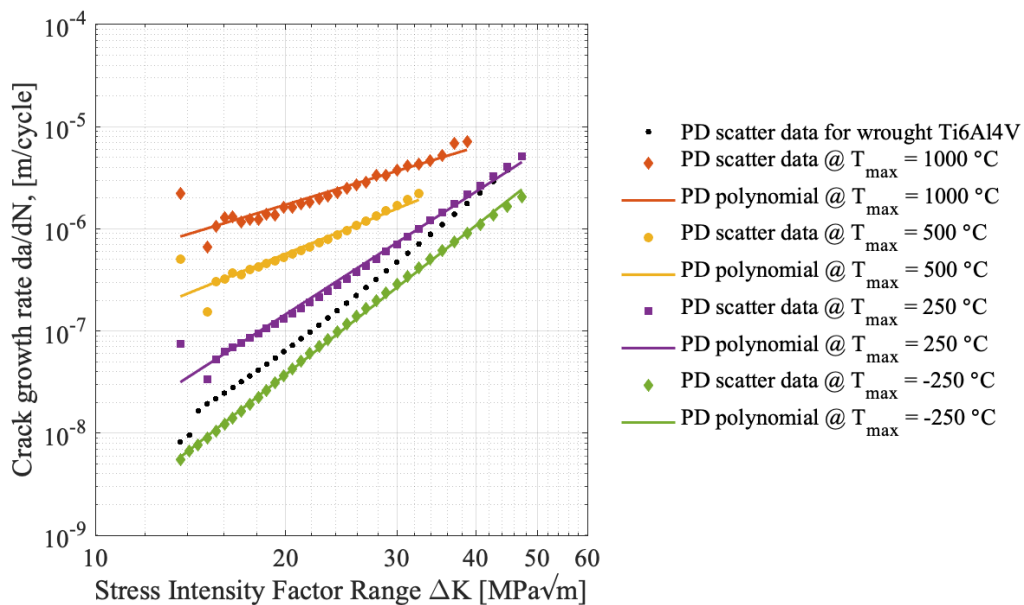
Figure 6.35 Crack growth curves comparison for C(T) samples under different temperature distributions.

The PD numerical results in Figure 6.35 show a great impact of RS on FCGR. The models with high tensile RS cause higher stress concentrations near the crack tip, resulting in a greater FCGR compared to the wrought Ti6Al4V. This means that the tensile RS in front of the propagating crack add to the tensile loading resulting in faster fracture. Moreover, the existence of the compressive stresses in x and y directions are enhancing the fracture resistance. The compressive stresses are acting to close the crack and reduce the tensile load so that the FCGR is the lowest. The studies of the additively manufactured Ti6Al4V C(T) samples show that the crack growth is faster in the presence of high RS.

Figure 6.36 shows the data obtained from the crack growth rate curves at SIF range of $\Delta K = 16\ MPa\sqrt{m}$, reported in the literature [19], where the tests are performed at a load ratio of $R = 0.1$, and the maximum tensile residual stress values are estimated from the reported stress distributions. The PD results in Figure 6.36 are presented when the SIF range is $\Delta K = 16\ MPa\sqrt{m}$ and the longitudinal σ_x^{rs}, MPa and the transverse σ_y^{rs}, MPa RS are evaluated by performing the FEA described in Section 6.7.1. The SIF of $\Delta K = 16\ MPa\sqrt{m}$ has occurred when the crack propagated and the length of the crack is $a = 14\ mm$. The combined results of PD fatigue model and residual stress evaluations from FEA are presented in Figure 6.36. The PD numerical results predicted the FCGR close to the experimental data [19, 163, 248]. The PD FCRG in the samples with lower RS shows slower crack propagation compared to the tests data. One of the reasons could be microstructure and the process-induced porosities of the samples [19], which are not included in the current study, as well as the simplifications applied in the PD numerical model. On the other hand, the simplified numerical PD model of initiating the RS in the C(T) samples by introducing the temperature profiles in each of the fatigue cycles is capable of predicting the FCGR behaviour and the influence of stresses on the fatigue performance. For example, the study by Leuders et al. [19] reported very high tensile internal stresses of $775\ MPa$ in the built direction and $265\ MPa$ in the scanning direction. The PD results with the stresses in the C(T) sample are close to the experimental studies, and FCGR show quite close results to the test data in Figure 6.36.
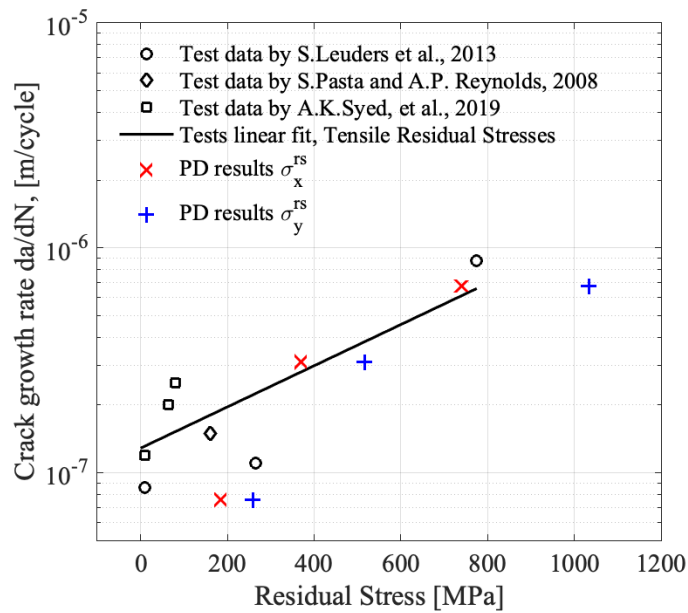
Figure 6.36 FCGR as a function of maximum RS. PD results vs test data [19, 163, 248].

Both of the tests [19, 163, 248] and the PD simulations show the dependency of the fatigue performance on the RS with faster crack propagation in the presence of the higher RS. The existence of the RS and different levels of RS developed in the AM SLM process are major factors in the anisotropic fatigue behaviour of the samples.

6.8   Summary

This chapter presents the numerical studies on the effects of material microstructure, the existence of the pores and RS on the FCGR. The main focus is on the additively manufactured Ti6Al4V alloy where, firstly, the effects on FCGR are evaluated based on the types of microstructure due to the layer-by-layer manufacturing developed in the material. Secondly, the porosity levels in additively manufactured structures are analysed, and fatigue performance is numerically predicted. Lastly, the numerical approach of modelling the RS in the C(T) samples by means of PD to predict the fatigue response of the additively manufactured Ti6Al4V samples is presented.

The employment of PD theory in fatigue problems showed the PD fatigue model's capability to capture the FCG behaviour, and the results of the validated model are in line with test data. The following conclusions can be derived from the conducted studies:

- The crack propagation behaviour is directly dependent on the material microstructure, and coarse-grained microstructure has higher FCG resistance. Moreover, the columnar type of microstructure developed during AM brings the anisotropy into fatigue properties. The samples with the elongated β grains located parallel to the crack propagation path have a weaker response with the fast-propagating crack along the columnar grains.

- The pores in the presented samples impact the crack propagation behaviour, where the crack moves through the areas with a higher density of the pores with bigger diameters. The porosities weaken structural integrity with faster FCGR for the samples with higher levels of porosities.

- The model with implemented porosities and columnar microstructure showed the effect of both factors on the FCGR. The cut of the samples with different columnar grains orientation contributes to the anisotropy of FCG performance. Even small levels of porosities (P = 0.01%) are increasing the FCGR.

- The implementation of the parabolic temperature profile resulted in high RS in front of the crack tip leading to the pre-tension or pre-compression of the sample. The thermal deformations of the plate in the PD model are verified with FEA. A good agreement is found between the PD and FEA simulations, and the model is used for further fatigue analysis. The PD fatigue model with the initial RS shows good predictability of the FCGR, which is consistent with the experimental data available in the literature. The C(T) samples with the high tensile RS have very high-stress concentrations in front of the crack tip, leading to fast crack propagation. On the other hand, compressive RS have a contrary effect on FCGR with lower fracture levels because of the pre-compression of the sample, which is acting to close the crack. The proposed numerical approach of RS implementation in the PD FCG model showed its capability to capture fatigue damage evolution and applicability on predictions of FCGR of additively manufactured Ti6Al4V samples.

The results of these studies have been published in [24] and [25].

7   CORROSION FATIGUE CRACK GROWTH

7.1   Introduction

In this chapter, the PD framework for modelling the CFCG is presented. The proposed numerical model combines the PD FCG model and PD diffusion model in order to couple the mechanical and diffusion fields existing in the material due to the impact of environmental fatigue. The mechanical field is responsible for the characterisation of the changes to the structure due to the fatigue loading conditions. The diffusion field is based on the modelling of the adsorbed-hydrogen SCC, in particular, the HE model is considered. The novelty of the presented study in the coupling of mechanical and diffusion fields by means of PD, and identifying the effect of hydrogen on material strength and susceptibility of Ti6Al4V to hydrogen-induced cracking.

In this chapter, Section 7.2 provides the background and motivation of this study. Section 7.3 provides an overview of hydrogen diffusion adapted from [249] and the coupling of mechanical and diffusion fields in the PD numerical model for CFCG predictions, as explained in Section 7.4. Section 7.5 describes the PD CFCG model procedure, followed by Section 7.6, where the model set-up is introduced. Numerical results of the CFCG rates for the cast Ti6Al4V alloy are presented in Section 7.7 and for the additively manufactured Ti6Al4V alloy in Section 7.8. The results of the PD FCGR in the Ti6Al4V subjected to the corrosive environment are validated against the experimental data available in the literature. The gaps, future work, and the summary of the chapter are provided in Section 7.9 and Section 7.10, respectively.

7.2   Background and motivation

The CFCG rate is of great interest for life prediction and the safety assessment of engineering structures. It is a complex combination of the interaction mechanisms of the metallurgical factors, cycling loading and the corrosive environment [173, 250]. The researchers working on the FCG of Ti6Al4V in the corrosive environment showcased the decrease of the fatigue strength and faster FCGR compared to the inert

environment [251–254]. Due to the wide applicability of Ti6Al4V in various industries like biomedical, automotive, aerospace, marine and others, it is important to understand the effect of the material-environment combination on FCGR.

For the FCG in the corrosive environment, several mechanisms are likely possible. FCG in the air has a characteristic sigmoidal shape of relation between $da/dN - \Delta K$ and occurs above the threshold SIF range ΔK_{th} with further linear dependence of da/dN on ΔK and final rapid growth when SIF is approaching the critical value. Instead, FCG behaviour in a corrosive environment is a more complex process that includes three different categories classified by [173]. All three categories of crack growth depend on the threshold SIF for SCC and can be defined with respect to ΔK_{ISCC} The general block-scheme of CFCG categories, CFCG models and schematics of CFCG curves are presented in Figure 2.16, where a_o is the initial crack length and $\Delta\sigma$ is the load amplitude. The different models for CFCG predictions is discussed in Section 2.5.

The first category is the TCF, with the FCGR increasing due to the corrosive environment. The crack propagation is relatively immune to the SCC and occurs below the corresponding K_{ISCC} with no influence of stress corrosion mechanism. With the applied stress intensity excursion $\Delta K = K_{max} - K_{min}$ the TCF occurs if $\Delta K_{max} < \Delta K_{ISCC}$.

The TCF is demonstrated by an increased FCGR and lower ΔK_{th}. Generally, the process of TCF happens when fatigue cycles break the passivizing film and activate the anodic dissolution of the crack tip. As the cycles continue, the material does not have enough time to permanently re-passivise, and crack growth rates in corrosive environments are higher than those in inert environments [20]. Other common types included in TCF are pitting, intergranular, filiform and exfoliation, dissolution, and each of them affect the FCG [174].

The second category shown in Figure 2.16 is SCC, in which the system is more sensitive to SCC and when the ΔK_{ISCC} for SCC is much lower than the critical SIF, K_C. Generally, the SCC is the result of a combination of 3 factors: exposure to a corrosive environment, susceptible material and tensile stresses above a threshold value [20]. Additionally, the reduction of frequency of the cycles or the increase of the load ratio

triggers the SCC mechanism [174, 255]. There is no unified mechanism for SCC in the literature. Various models have been proposed, which are based on damage by passive film rupture [216, 256], adsorption models [257] when the specific chemicals adsorb on the crack surface and lowers the fracture stress, and the HE model [258–261] where hydrogen atoms diffuse to the crack tip and embrittle the metal.

The contribution of each mechanism in TCF and SCC on CFCG depends on the metallurgical, environmental variables and loading. The experimental studies [254, 261, 262] on CFCG in conventional casting Ti6Al4V tested in several environments indicated the increase in FCGR in 3.5%wt NaCl solution and distilled water, and the frequency-dependent behaviour. A few studies [263, 264] were performed on additively manufactured Ti6Al4V alloy, where the corrosion behaviour of SLM and WAAM Ti6Al4V subjected to 3.5%wt NaCl solution was investigated. The authors concluded the effect of microstructure on corrosion resistance where the order of corrosion resistance was identified as SLM<WAAM<rolling<SLM+heat treatment, with pitting corrosion as the main failure mechanism. Regarding the understanding of the contribution of the corrosion on FCG in additively manufactured Ti6Al4V, a very limited number of studies were performed. Jesus et al. [252] performed a study on FCGR in Ti6Al4V specimens produced by SLM under a corrosive environment with the outcome of faster FCG when the tests are performed in 3.5%wt NaCl. Neikter et al. [265] analysed the Ti6Al4V samples produced by EBM, investigated the HE phenomena, and concluded the susceptibility of EBM Ti6Al4V alloys to HE with the increased FCGR.

HE is an important mechanism of SCC and in particular for CFCG in steels, aluminium, titanium and nickel-based alloys. In this study, Ti6Al4V is considered, and hydrogen-based SCC mechanisms, together with the samples' fatigue performance, are analysed. The study showcased the applicability of the developed numerical model of CFCG predictions on both cast/wrought and additively manufactured Ti6Al6V alloys.

7.3   PD hydrogen diffusion model

Hydrogen enrichment in the Ti6Al4V is leading to HE with the phenomena observed in multiple studies. Similar to the approach adopted in [249] on hydrogen grain boundary diffusion, in this study, the reduced model [266] of Fisher's mechanism [267] of diffusion is used in the following form:

$$\frac{dC_H}{dt} = D_H \nabla^2 C_H \qquad (7.1)$$

where D_H is hydrogen diffusion coefficient or diffusivity, m^2/s and C_H is the hydrogen concentration. Eq (7.1) describes the evolution of C_H in time t. Ti6Al4V can contain mixed phases, which can have different hydrogen diffusivities. Hydrogen diffusion coefficient in α-phase is $D_{H_\alpha} = 1.45 \times 10^{-16} m^2/s$ and for the β-phase is $D_{H_\beta} = 5.45 \times 10^{-12} m^2/s$ at room temperature [268]. According to [259], hydrogen diffusion depends on the microstructure of the titanium, where the hydrogen absorption rate is higher in the microstructures with continuous β-phase. Additionally, in $\alpha + \beta$ alloys, hydrogen prefers to diffuse in β-phase and with an α-phase in the structure hydrogen diffuses along the β/α grain boundaries. For this study, the simulated Ti6Al4V alloys are assumed homogenous and D_{H_β} for β-phase is considered. Please note that the effect of α-phase is neglected together with the microstructural effect on the hydrogen diffusion in this study which may have an effect on the CFCGR.

PD governing equation for hydrogen diffusion mechanism is based on Fisher's model in Eq. (7.1) and is given in the following form [249]:

$$\dot{C}_H(\boldsymbol{x}, t) = \int_{H_x} \boldsymbol{f_H}(C_H(\boldsymbol{x}', t) - C_H(\boldsymbol{x}, t), \boldsymbol{x}' - \boldsymbol{x}) dV_{x'} \qquad (7.2)$$

where $\dot{C}_H(\boldsymbol{x}, t)$ is the time derivative of hydrogen concentration for a material point $\boldsymbol{x}$ and V is the incremental volume of material point $\boldsymbol{x}'$. Eq. (7.1) in the discretised form is:

$$\dot{C}_{H(i)} = \sum_{j=1}^{M} \boldsymbol{f}_{H(i)(j)} V_{(j)} \qquad (7.3)$$

where the interaction of material points i and j are in place within the horizon H_x with a total number M of the family members for i. f_H is the hydrogen diffusion response function and defined as:

$$f_H = d_{bc} \frac{C_H(x', t) - C_H(x, t)}{|x' - x|} \tag{7.4}$$

In Eq. (7.4) d_{bc} is the diffusion bond constant, defined as:

$$d_{bc} = \frac{6D_H}{\pi h \delta^3} \tag{7.5}$$

where δ is the horizon size.

The hydrogen diffusion model is simulated in the time domain where the backward difference method is used to obtain hydrogen concentration for the next time step n_{t+1}:

$$C_{H(i)}^{n_t+1} = C_{H(i)}^{n_t} + \dot{C}_{H(i)}^{n_t+1} \Delta t \tag{7.6}$$

where Δt is the time step size which can be expressed in terms of cyclic period $T = 1/f$ (f is the frequency, Hz) and the total number of time steps n_F within one period:

$$\Delta t = \frac{T}{n_F} \tag{7.7}$$

A more detailed explanation of the effect of the time step size and frequency on the CFCG is introduced in Section 7.6.3.

To represent the hydrogen adsorption in the sample, the concept of hydrogen coverage θ_H is introduced in the PD diffusion model [249]:

$$\theta_H = \frac{C_{Htip}}{C_{Hsat}} \tag{7.8}$$

where C_{Htip} is the surface hydrogen concentration at the crack tip and C_{Hsat} is the surface hydrogen concentration saturation value.

7.4   Coupling of mechanical and diffusion field

The coupling of mechanical and diffusion fields is necessary to identify the effect of hydrogen on material strength and susceptibility of Ti6Al4V to hydrogen-induced cracking. With this respect, the test data [269] was considered where the decrease of

critical SIF was noticed with the increased hydrogen level in the material. The test data is adapted and presented in Figure 7.1a indicating the sample embrittlement. For the purpose of integrating the phenomena of local embrittlement in the material as hydrogen is adsorbed and diffused within the sample, the hydrogen-embrittlement model is adopted.

In the PD model, the influence of hydrogen is accounted by a decrease of a critical stretch s_c with increasing hydrogen coverage θ_H. To find the coupling between θ_H and dependent s_c, Langmuir-McLean isotherm [270] is utilised, which relates hydrogen coverage to the bulk hydrogen concentration C_H (unit mol H/mol Ti) in the following form:

$$\theta_H = \frac{C_H}{C_H + \exp(-\Delta G_b^0/RT)} \tag{7.9}$$

where ΔG_b^0 is the Gibbs energy difference between surface and bulk material, and in the current model is the trapping energy of hydrogen at a Ti grain boundary, $\Delta G_b^0 = 40 kJ/mol$, R and T are gas constant and absolute temperature, respectively.

As shown in Figure 7.1b, utilising Eq. (7.9) to convert test data to the relation between the θ_H and s_c, resulted in the following equation:

$$K_c(\theta_H) = 5.4\theta_H^{-0.409} \tag{7.10}$$

and $s_c(\theta_H)$ is evaluated by [271]:

$$s_c(\theta_H) = \sqrt{\frac{5\pi G_c(\theta_H)}{12E\delta}} \tag{7.11}$$

where E is Young's modulus, G_c can be calculated for a plane strain configuration according to the critical SIF:

$$G_c(\theta_H) = \frac{K_c(\theta_H)^2}{E/(1-v^2)} \tag{7.12}$$
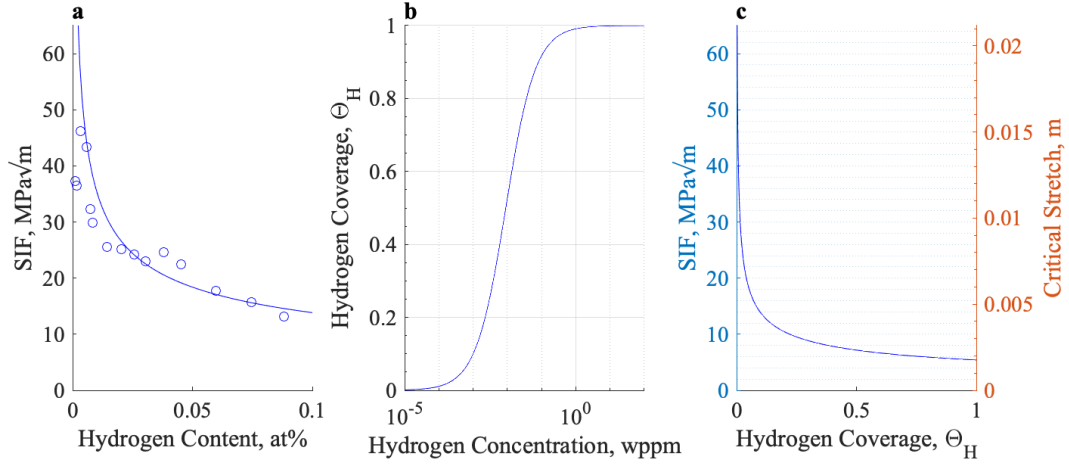
Figure 7.1 a. Effect of Hydrogen content on the critical SIF, adapted from [269], b. Hydrogen Coverage, θ_H as a function of Hydrogen Concentration [270] for $\Delta G_b^0 = 40\ kJ/mol$, c. SIF and Critical stretch as a function of θ_H.

The study [269] indicates the effect of the strain rates on the HE process. It is suggested that during slower rates with a longer time, creep deformation occurs. With added hydrogen to the samples, the embrittlement occurred at the lower hydrogen content, compared to the samples strained at faster rates. This means that slower rates of the applied loads resulted in the loss of the overall ductility and increased HE process due to hydrogen.

The important effect of the load frequency is noticed during FCGR tests on Ti6Al4V, where low-frequency fatigue is more sensitive to the environment. To consider the effect of the load frequency on the HE process, the following relationship is introduced in the PD model:

$$K_c(\theta_H) = \frac{K_{Ic}(1-R)}{\Delta K_{scc}} \theta_H^{-0.409} \tag{7.13}$$

where K_{Ic} is the critical SIF, which is selected for Ti6Al4V as $K_{Ic} = 105\ MPa\ \sqrt{m}$, and ΔK_{scc} is selected from the available test data [272]: $\Delta K_{scc} = 17.6\ MPa\ \sqrt{m}\ (f = 1Hz)$, $\Delta K_{scc} = 13.2\ MPa\ \sqrt{m}\ (f = 5Hz)$ and $\Delta K_{scc} = 11.0\ MPa\ \sqrt{m}\ (f = 10Hz)$. Figure 7.2 shows the critical stretch values as a function of θ_H for different load frequencies. The relation in Eq. (7.13) effects on crack propagation, where at the same amount of hydrogen coverage in the metal, the fatigue progression of the crack is faster at low-frequencies, as shown in Figure 7.2. With the following assumption, the study

in Section 7.7 shows the effect of the frequencies in CFCGR, where after the $K_c(\theta_H)$ reaches the ΔK_{Iscc}, the differences of FCGR for different frequencies are noticeable. If the relationship in Eq. (7.13) is not introduced, then the frequency effect is not visible, and CFCGR will be the same for all frequencies.

Moreover, to take into account that the SCC occurs when $\Delta K > \Delta K_{SCC}$ with abrupt changes in the behaviour of $log\left(\frac{da}{dN}\right) - \log(\Delta K)$, the K_{th}^{max} value is introduced in the model, below which the crack growth is not occurring due to SCC. For the given load frequency, the K_{th}^{max} is determined from the test data, where:

$$K_{th}^{max} = \frac{\Delta K_{scc}}{(1 - R)} \tag{7.14}$$

The resulting plots can be seen in Figure 7.2, where the critical stretch decreases with the increase hydrogen concentration, evaluated by Eq. (7.13). And when the stretch of the bond is $s < s_{th}^{max}$ (s_{th}^{max} evaluated from K_{th}^{max} by Eq. (7.11)), then there is no effect of HE process, and the bonds are breaking only by the decreasing life over the fatigue cycles.
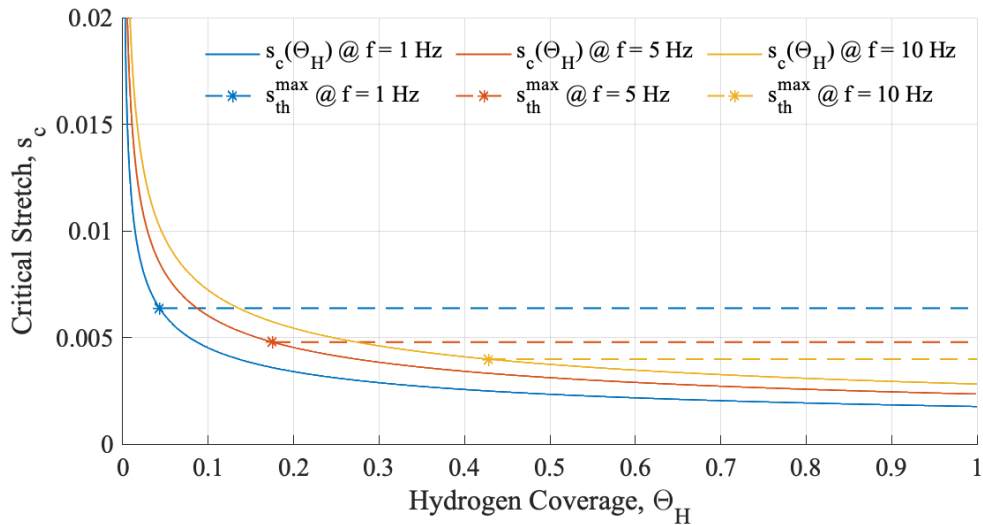
Figure 7.2 Variation of critical stretch with hydrogen coverage.

Start with a_0, ΔF

$$\Delta K = K_{max} - K_{min}$$

Yes $\qquad\qquad$ $K_{max} < K_c(\theta_H)$ $\qquad\qquad$ No

True Corrosion Fatigue (TCF)

$$\left(\frac{da}{dN}\right)_{TCF} = \left(\frac{da}{dN}\right)_{Air}$$

No $\qquad$ $K_{max} \gg K_c(\theta_H)$

Yes

TCF + SCC

$$\left(\frac{da}{dN}\right)_{CF} = \left(\frac{da}{dN}\right)_{TCF} + \left(\frac{da}{dN}\right)_{SCC}$$

Stress Corrosion (SCC)

$$\left(\frac{da}{dN}\right)_{SCC} = \frac{da}{dt}\frac{1}{f}$$
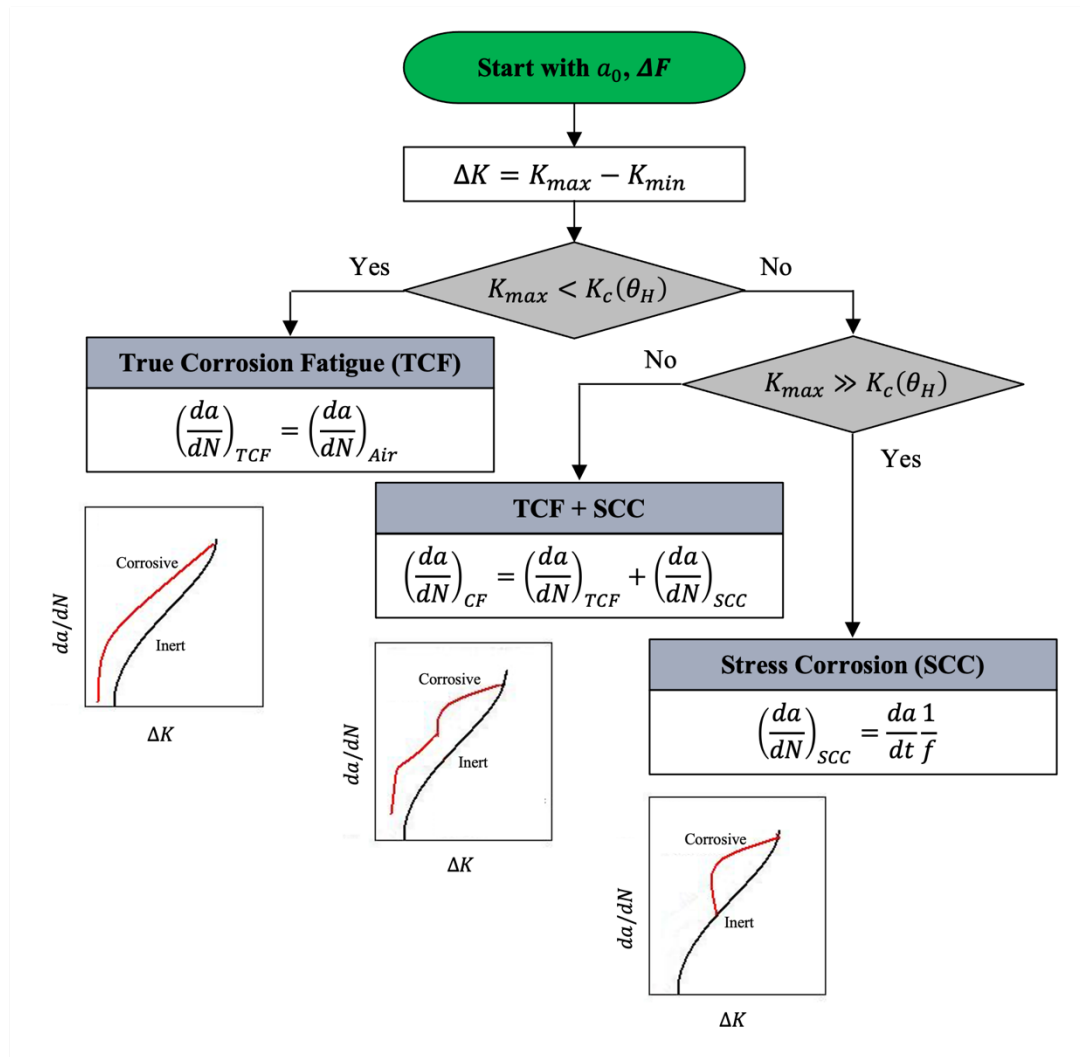
Figure 7.3 Block-scheme of CFCG categories in PD model.

7.5 PD CFCG model procedure

In the current studies for CFCG prediction in C(T) titanium alloy samples, PD is utilised as the main numerical tool. As described in Section 2.5, according to the CF model proposed by Wei and Landers [175] that the CFCG, $\left(\frac{da}{dN}\right)_{CF}$, is the sum of the mechanical FCGR, $\left(\frac{da}{dN}\right)_{Air}$, and the contribution from the SCC, $\left(\frac{da}{dN}\right)_{SCC}$. The following CFCG model is developed utilising the PD numerical model, where Figure 7.3 shows the general scheme of the model when C(T) sample is with the crack length of a_0 and the load of ΔF is applied. The model is classified relative to the $K_c(\theta_H)$.

When $K_{max} < K_c(\theta_H)$, then $\left(\frac{da}{dN}\right)_{CF} = \left(\frac{da}{dN}\right)_{Air}$. When $K_{max} > K_c(\theta_H)$, then $\left(\frac{da}{dN}\right)_{CF}$ is a result of interaction between the mechanical fatigue and time-dependent corrosion contribution, $\left(\frac{da}{dN}\right)_{CF} = \left(\frac{da}{dN}\right)_{Air} + \left(\frac{da}{dN}\right)_{SCC}$. The environmental contribution is set up as a HE model, and FCG is in the air considering the effect of the environmentally-assisted crack growth. And when $K_{max} \gg K_c(\theta_H)$, the crack growth is occurring due to the HE and SCC is the main contributor to the failure.

In this respect, PD model is set up for fatigue damage predictions, which is $(da/dN)_{Air}$ and numerical diffusion model, which is the HE model, $(da/dN)_{SCC}$. Both models have to be integrated to predict the CFCG and Figure 7.4 shows the three stages of the PD model:

1. PD model initiation and parameters identification: model preparation, discretisation, assignment of the material properties, identification of the fatigue and diffusion model parameters, identification and assignment of the fatigue loads.

2. PD HE model:

2.1 Hydrogen coverage step: assignment of the unit value of the hydrogen coverage, $\Theta_H = 1$, at the crack tip and zero value $\Theta_H = 0$ is assigned for all remaining surfaces of the specimen. The unit value of hydrogen coverage corresponds to saturated hydrogen surface concentration of $6549\ mol/m^3$.

2.2 Diffusion step: PD hydrogen diffusion model described in Section 7.3 is used to predict the hydrogen diffusion in the material at each time step.

2.3. Embrittlement step: relation in Figure 7.1 is used to quantify the local hydrogen concentration on the material strength. The relation between the hydrogen concentration and hydrogen coverage is used to evaluate the critical stretch of the bond, $s_c(\Theta_H)$, as shown in Figure 7.2. The bond is broken if the stretch of the bond is greater than the current critical stretch, $s_c > s_c(\Theta_H)$.

3. PD fatigue model: static solutions for the extreme loads and the degrading life of the bonds over the cycles. The bond is broken when its remaining life is $\lambda^N \leq 0$.

During Stage 2 and Stage 3, the accumulated damage of the bonds is monitored, and if the local damage occurs at any of the two stages, then the algorithm moves to the beginning of Stage 2 with the location of a new position of the crack tip and the

processes of Stages 2 and Stage 3 repeat until the full damage of the sample. As the crack propagates, the constant unit value of hydrogen coverage is applied at the new crack tip and the hydrogen concentrations at the crack surfaces.
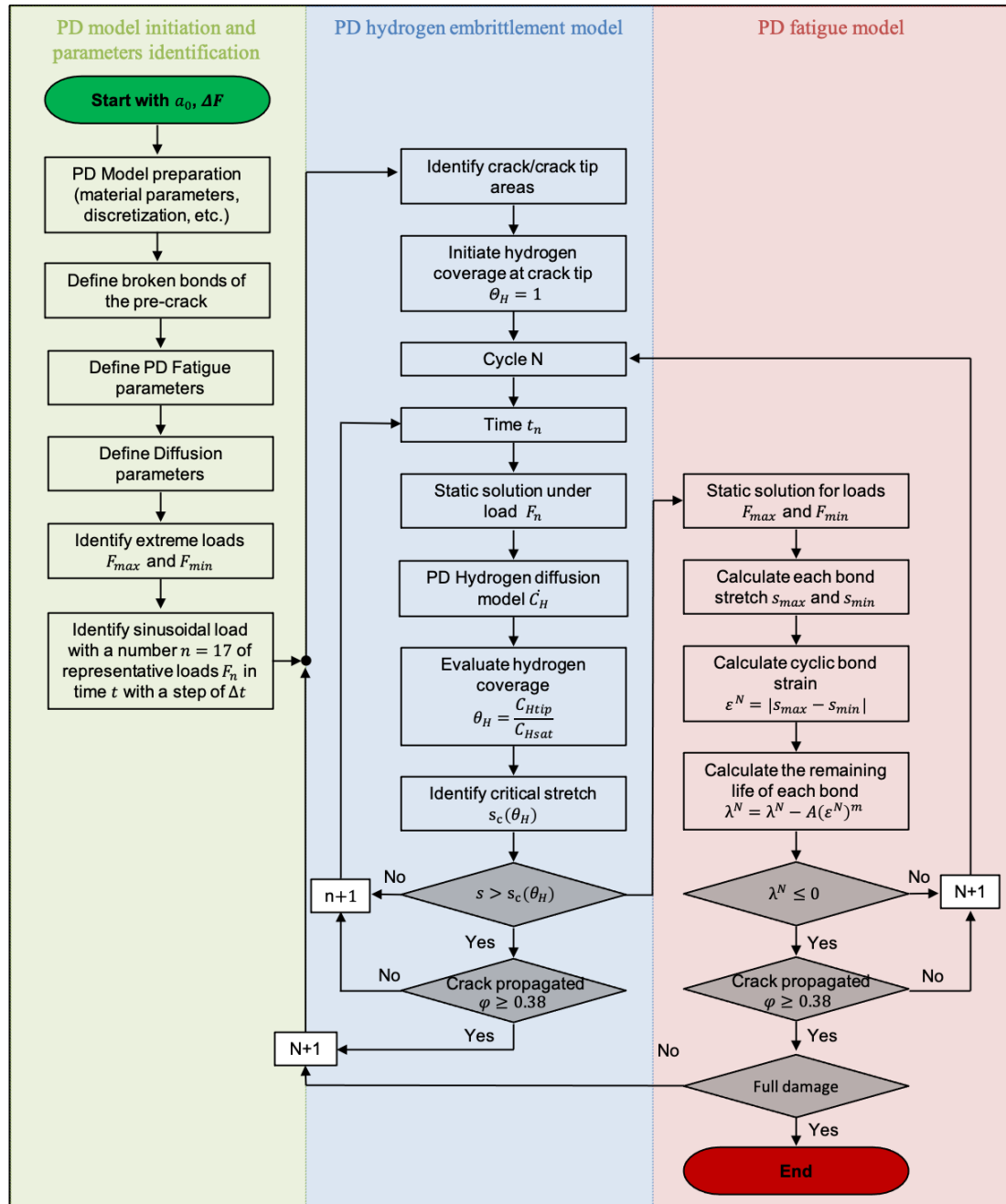
Figure 7.4 Solution procedure.

7.6 PD CFCG model set up

7.6.1 Problem set up

Similar to the experimental study [273], the Ti6Al4V samples are subjected to cyclic loading in NaCl solution, the PD model is set up for a C(T) sample, shown in Figure 6.5, subjected to a cyclic load of $\Delta F = 2.25\ kN$ with a load ratio of $R = 0.1$. The material properties of Ti6Al4V are homogeneous and can be found in Section 6.3. The dimensions of the C(T) sample and PD model discretisation parameters are the same as described in Section 6.3.2.

The results of FCGR in NaCl solution are compared to the FCGR in the air, where the authors [273] showcased that the fatigue behaviour in the air is frequency independent. Instead, the samples tested in NaCl solution showed frequency dependence with the abrupt increase of FCGR. For this reason, numerically, it is beneficial to look at the complex corrosion - fatigue phenomena. Firstly, the numerical model set-up is performed for Ti6Al4V in the air, which is described in Section 7.6.2. Secondly, the fatigue load determination for SCC is described in Section 7.6.3 And lastly, hydrogen diffusion plots are presented in Section 7.6.4.

7.6.2 PD FCG model in the air

As discussed in Section 6.3, in the PD fatigue model, the parameters A_2 and m_2 have to be calibrated using the Paris' law data [159]. For this purpose, the data in [273] for the sample tested in the air is selected, where the constant m_2 is obtained directly from the $log\left(\frac{da}{dN}\right) - \log(\Delta K)$ curve, and A_2 is identified by running first model with random parameter A_2' and then calibrated by Eq. (5.8).

After the calibration procedure, the PD FCG model parameters are $A_2 = 22 \times 10^3$ and $m_2 = 3.87$ and the computed results of $log\left(\frac{da}{dN}\right) - \log(\Delta K)$ are in line with the experimental data, shown in Figure 7.5. It means that the parameters for the PD FCGR model are set up correctly, and the model tested in the air can be used as a reference one for the next studies.
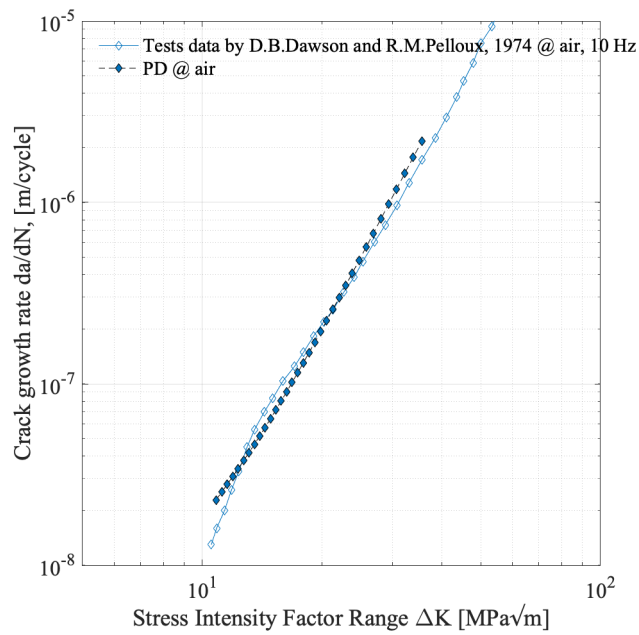
Figure 7.5 FCGR versus SIF range for a sample tested in the air. Calibrated PD model utilising test data in [273].

7.6.3 Fatigue load determination for SCC

For the sinusoidal waveform employed in the current study, it is assumed that the loading cycle starts from the minimum load of F_{min}:

$$
\begin{aligned}
F &= \frac{F_{max} - F_{min}}{2} + \frac{\Delta F}{2} \sin\left(2\pi\omega t - \frac{\pi}{2}\right) \\
&= \frac{\Delta F}{2}\left[\frac{1 + R}{1 - R} + \sin\left(2\pi\omega t - \frac{\pi}{2}\right)\right]
\end{aligned}
\tag{7.15}
$$

where ω is the loading frequency, t is the time, R is a load ratio and ΔF is force range, $\Delta F = F_{max} - F_{min}$.
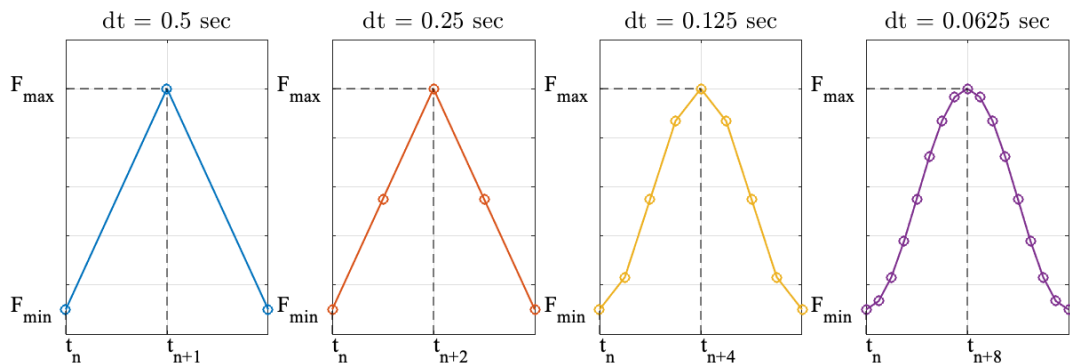
Figure 7.6 Load initiation according to a time-step size.

170
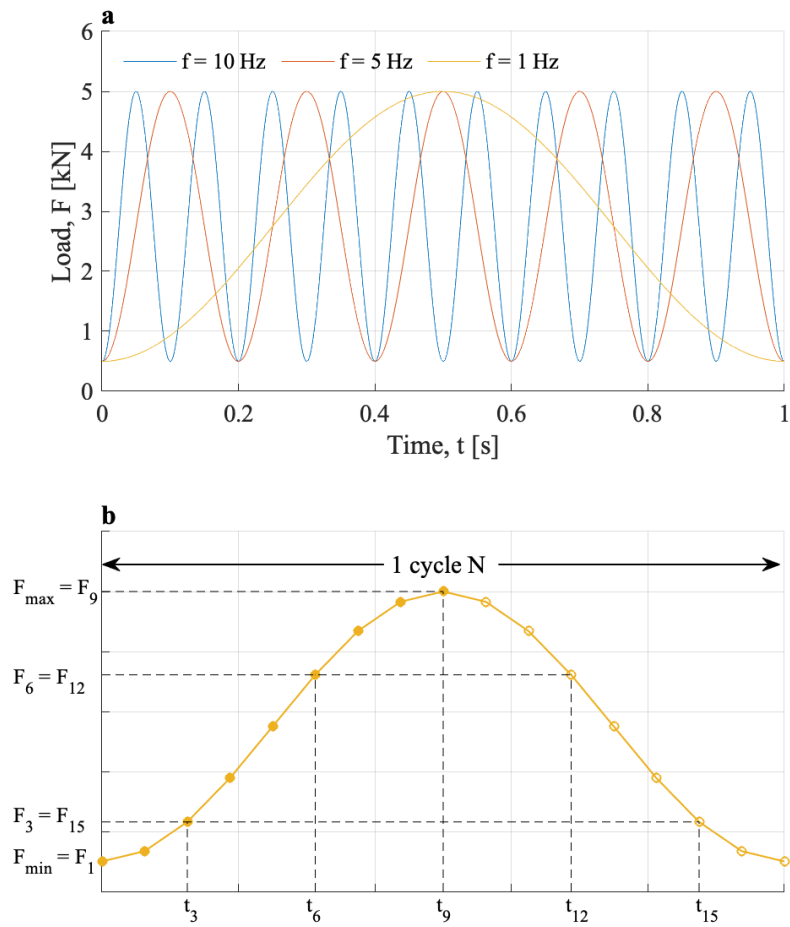
Figure 7.7 (a) Load vs time for different loading frequencies; (b) Discretisation of the sinusoidal load F under frequency of $f = 1\ Hz$ by a time-step of $dt = 0.0625\ sec$.

For metals, as high strength steels, titanium alloys, mostly attributed to HE ahead of the crack tip, the diffusion of hydrogen into the material is produced by an anodic reaction at the crack tip [268]. The process is time-dependent, and the frequency of the cyclic loading affects the FCG. Due to this, the analysis for SCC is performed in the time domain, as shown in Figure 7.4, and the plate is subjected to the sinusoidal load. As it is time-consuming to solve the PD under a very small load time-step, the effect of the time-step size, dt on FCGR is analysed. Four time-step sizes are selected: $dt = 0.5, 0.25, 0.125$ and $0.0625\ sec$, as shown in Figure 7.6. The smaller the time-step size is, the better representation of the sinusoidal load, but the longer the simulations are.
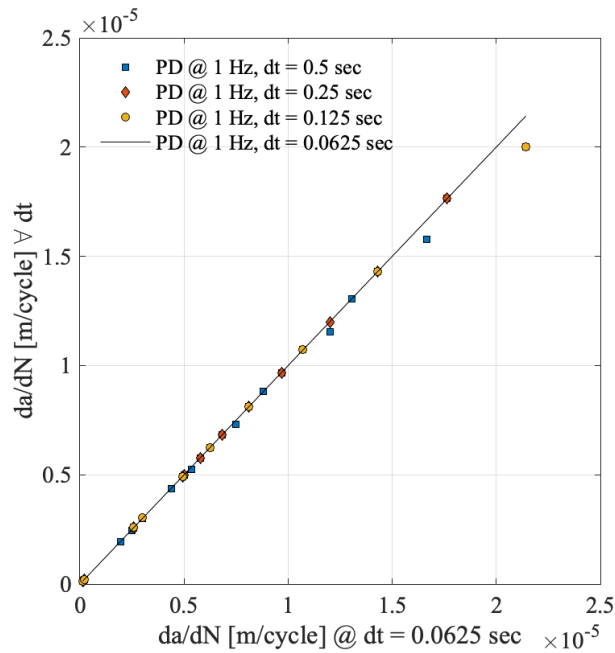
Figure 7.8 Comparison between four different time-step sizes.

Additionally, to optimise the simulation time, the displacements u (in x-direction) and v (in y-direction) are solved only for half of the period $T/2$ and the resultant displacements are mirrored for the other half of the period. This means that for a period of T, for example, with $dt = 0.0625\ sec$ shown in Figure 7.7b, forces $F_6 = F_{12}$ and displacements $u\ (F_6) = u(F_{12})$, $v\ (F_6) = v(F_{12})$. The resultant displacements are stored for each force within a period and called at each cycle. If damage occurs at any of the forces F_t at step dt within the period T, then the displacements are recalculated.

The simulations for evaluation of the influence of the time-step size on CFCG rates are performed for a cyclic load of $\Delta F = 3.15\ kN$ with a load ratio of $R = 0.1$ and loading frequency of 1 Hz. Figure 7.8 shows the results of the simulations where the model with the smallest time-step size of $dt = 0.0625\ sec$ is selected as a reference one (black line at the plot) and the other models with $dt = 0.5, 0.25$ and $0.125\ sec$ are compared with it. It can be noted that the differences in FCGR are almost unnoticeable, even for the $dt = 0.05\ sec$ when the simulations are performed under the load extremes of F_{max} and F_{min}. Due to this, $dt = 0.05\ sec$ is selected for further simulations in order to optimize the computational time and the simulations for the HE step are simulated in time domain under the loads of F_{max} and F_{min}.

7.6.4   PD hydrogen diffusion model

Figure 7.9 shows hydrogen coverage plots for loading of $\Delta F = 2.25\ kN$ and three frequencies of $f = 1, 5\ and\ 10\ Hz$ when fracture initiation occurs in the pre-cracked C(T) sample. The highest level of hydrogen concentration is at the crack tip, where the unit value of hydrogen coverage was initiated.

With the damage model introduced in Section 7.4 where the critical stretch of the bonds is degrading with the increased hydrogen concentration and also affected by the loading frequency, lower hydrogen diffusion time to initiate the fracture is necessary for a higher frequency of $f = 10\ Hz$.
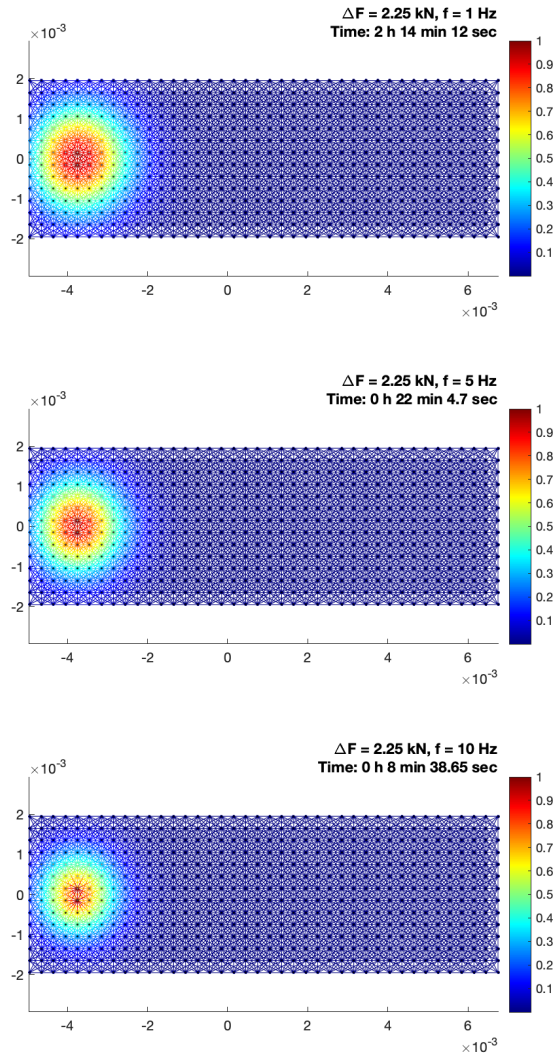
Figure 7.9 Hydrogen coverage field at the crack propagation initiation for loading frequencies of $f = 1, 5$ and $10\ Hz$.

7.7 PD CFCG predictions for a cast Ti6Al4V alloy

As discussed in Section 7.2 and Section 7.4, when $\Delta K > \Delta K_{SCC}$ an abrupt change in behaviour of $log(da/dN) - log(\Delta K)$ curve takes place with higher FCGR at lower frequencies. Such behaviour was noticed during the experiments performed on cast Ti6Al4V [274] in 3.5 wt.% NaCl solution where the results of FCGR showed frequency dependency. The experimental results indicated that the cyclic SCC occurred when $\Delta K > \Delta K_{SCC}$. The studies showed that at higher ΔK FCGR accelerates rapidly as ΔK_{SCC} is approached.

The current study predicts the CFCG rates under different frequencies by the developed numerical PD CFCG model as shown in Figure 7.4. The PD model set-up is described in Section 7.6.1 with a reference model (cast Ti6Al4V in the air) from Section 7.6.2.
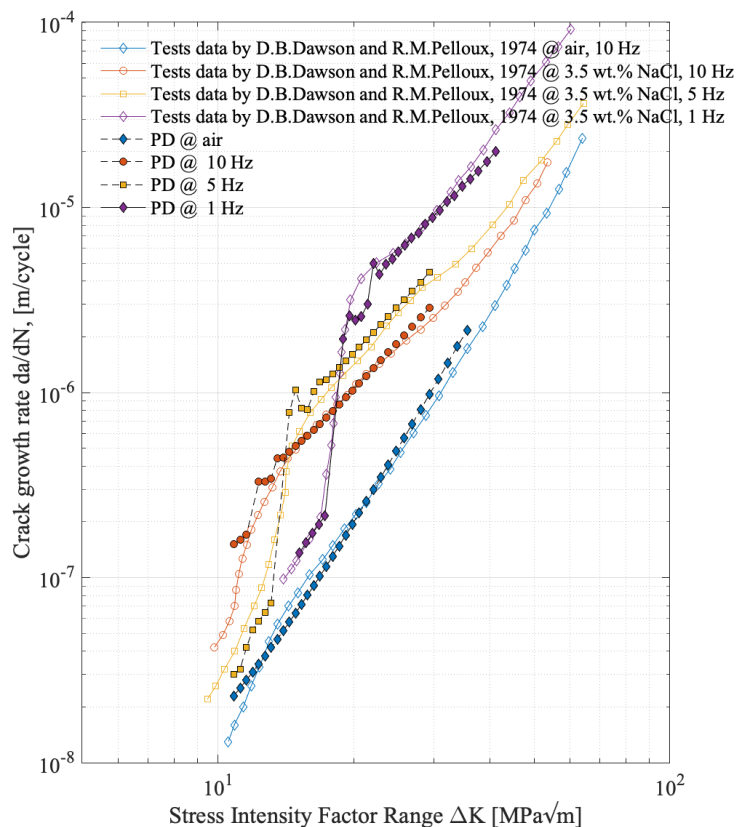
Figure 7.10 Effect of loading frequency on CFCG and crack growth curves comparison for a cast Ti6Al4V C(T)-samples between tests data [274] and PD CFCG model.

Figure 7.10 shows the comparison between the PD CFCG rates and test results by [274] concerning the effect of the loading frequency on CFCG rates. The results of the PD model showed good predictability of the effect of the frequency on CF behaviour of Ti6Al4V alloy. The application of three different frequencies showed three trends of corrosion-fatigue behaviour described in Figure 7.3 and that CFCG rates of Ti6Al4V alloy are frequency-dependent. It can be noticed from Figure 7.10 that low-frequency fatigue is more sensitive to the corrosive environment, showing the abrupt changes to FCGR with a higher FCGR when $\Delta K > \Delta K_{SCC}$.

The introduced HE model and integration of the HE model in the PD fatigue model showed the capability of the presented PD CFRG model to capture the main features of the complex interaction between the cycling loading, loading frequency and environment.

7.8 PD CFCG predictions for additively manufactured Ti6Al4V alloy

As discussed in Chapter 6, the difference between the cast/wrought and additively manufactured Ti6Al4V alloys is the anisotropy of additively manufactured alloys, for example, when the load is applied parallel or perpendicular to the built direction. The anisotropy is studied in Chapter 6, where the effect of the RS, defects and columnar grains on FCGR is analysed. Each factor in the structure contributes to reduced fatigue properties and decreases the fatigue life. The limited number of studies [253, 265] performed on additively manufactured Ti6Al4V alloy in the corrosive environment showed that hydrogen absorbs and diffuses in the structure and HE mechanism takes place. It is also concluded that the microstructure, like grain size and phase distribution, affects ΔK_{SCC} and the EBM built Ti6Al4V [265] has $\Delta K_{SCC} = 23\ MPa\sqrt{m}$ tested under the load frequency of $f = 0.5\ Hz$ and load rate of $R = 0$. Additionally, other studies concluded that the presence of stresses and temperature also determine the diffusion of hydrogen in the material. But, due to the lack of studies on CFCG of additively manufactured Ti6Al4V alloys and data related to the tested samples anisotropy, there are difficulties for a developed numerical model validation and some simplifications are performed.

As for the cast Ti6Al4V, it is assumed that the additively manufactured Ti6Al4V alloy is homogenous with the diffusion properties described in Section 7.3. The tests performed in the air on SLM [253] and EBM [265] Ti6Al4V alloys are considered as reference models in order to calibrate the PD FCG model parameters A_2 and m_2. After the performed calibration process, $A_2 = 550$, $m_2 = 3.0$ for SLM Ti6Al4V tested in the air, and $A_2 = 350$, $m_2 = 3.0$ for EBM Ti6Al4V tested in the air. The PD FCGR with the calibrated parameters are plotted against the test data in Figure 7.11, where a good match can be noticed.
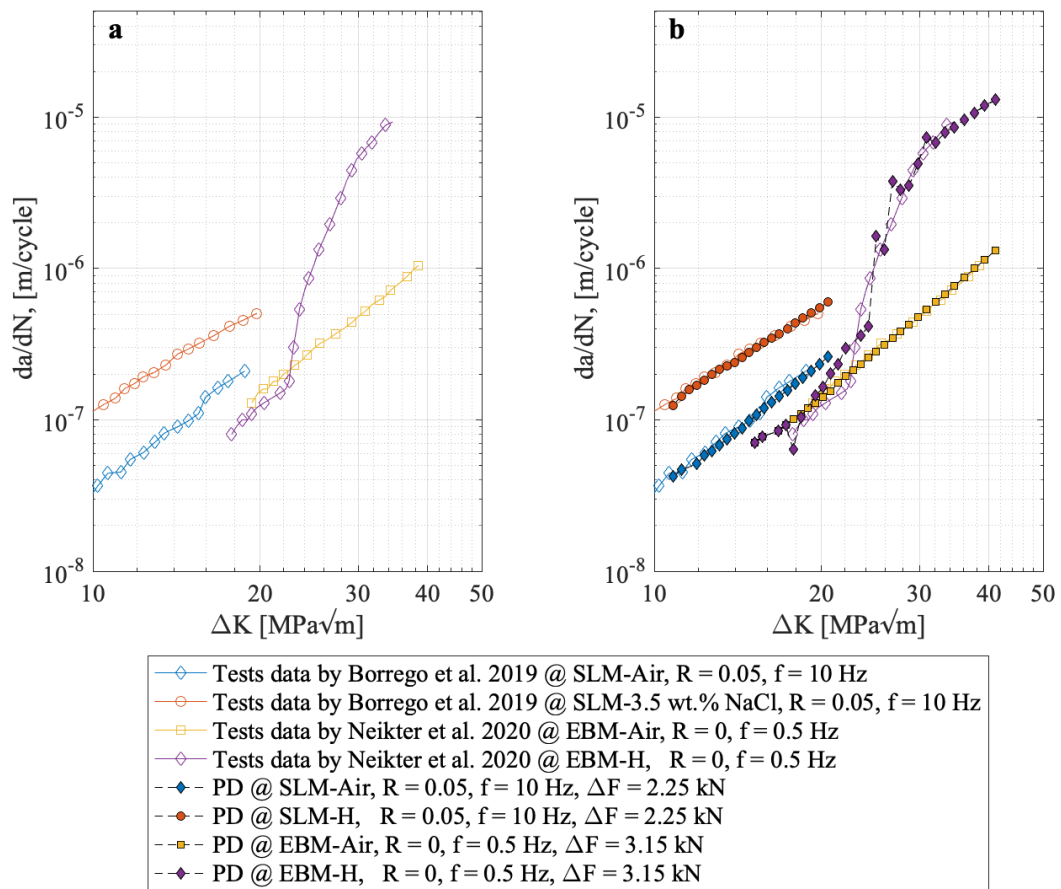
Figure 7.11 Crack growth curves comparison for a cast Ti6Al4V C(T)-samples between tests data [274] and PD CFCG model.

Utilising the proposed numerical model with the combined fatigue and hydrogen diffusion model, both structures (SLM Ti6Al4V and EBM Ti6Al4V) are solved with the HE mechanism taking place, as discussed in Section 7.4. The SLM Ti6Al4V C(T) samples are analysed under the load of $\Delta F = 2.25\ kN$, load frequency of $f = 10\ Hz$, load rate of $R = 0.05$, and the EBM Ti6Al4V C(T) are subjected to the cyclic load of $\Delta F = 3.15\ kN$, load frequency of $f = 0.5\ Hz$, load rate of $R = 0$

Figure 7.11 shows the comparison between the CFCG rates of numerical model and experiments [253, 265] concerning the relationship between the crack growth rate da/dN and SIF range ΔK. The numerical results are in a good agreement with the expected CFCG in the structure reported by experimental results.

For SLM and EBM Ti6Al4V alloys, tested in the air, the FCG rates followed the Paris law. Instead, the samples exposed to the environmental effects with the hydrogen diffusion ahead of the crack tip, the material experience HE mechanism and has faster crack propagation in the structure. The FCGR of EBM Ti6Al4V alloy rapidly increased at $\Delta K_{SCC} = 23\ MPa\sqrt{m}$ and the FCGR are higher compared to sample tested in the air.

The proposed PD CFCG model is capable of capturing the fatigue response of the additively manufactured Ti6Al4V alloys affected by a corrosive environment.

7.9   Gaps and future work

Further improvements to the current study can be made by introducing the different types of microstructures in the PD model, considering the crystal orientation and the diffusivity of hydrogen. Moreover, the current study has limitations to the sample discretisation due to the computational time, and a finer discretised model can be used to capture the hydrogen diffusion mechanism on a microscopic level. Lastly, the presented study is the starting point of CFCG numerical modelling by PD, and different types of materials with more detailed structures can be further investigated.

7.10   Summary

This Chapter presents a numerical PD framework for modelling the fatigue response of the metal affected by a corrosive environment. A numerical model combines mechanical and diffusion fields in order to capture the behaviour of the structure due to the applied cyclic loading and SCC phenomena. Considering the Ti6Al4V alloy for the study, a very common phenomenon in the titanium alloys subjected to SCC is HE, and numerical modelling is performed for adsorbed-hydrogen SCC.

Firstly, the proposed CFCG PD model is applied for the cast/wrought Ti6Al4V and validated with the experimental data available in the literature. As multiple studies indicated the effect of the loading frequency on the fatigue performance of the Ti6Al4V, the CFCG rates are analysed for three frequencies. The CFCG rates calculated by PD are in good agreement with experimental data. The combination of cycling loading and the corrosive environment in PD model is capable of capturing the complex fracture behaviour in Ti6Al4V observed in experiments.

Secondly, the proposed PD CFCG model is applied to additively manufactured Ti6Al4V. Due to the lack of data on material structure and the fatigue tests performed on the alloy subjected to the corrosive environment, the simplifications in the PD model are applied. The material is treated as homogenous, so the effects of the material anisotropy (microstructure and RS), as well as the porosities discussed in Chapter 6, are neglected. After the calibration of the PD parameters of the fatigue model for SLM and EBM Ti6Al4V alloys tested in the air, the PD CFCG model showed a good predictability of the material behaviour in the corrosive environment.

The results of this study have been published in [26].

8 CONCLUSIONS

8.1 Achievements against the objectives

This research is aimed to utilise the numerical tool, PD, to assess the fatigue and corrosion performance of 3D printed (additively manufactured) structures. With the challenges of the numerical tool development due to the anisotropy of the additively manufactured materials, the achievements of this research are the following:

- A PD model for investigating the dual role of holes and micro-crack arrays on toughening and degradation mechanisms in structures was created. The study showed the capability of PD to capture complex crack propagation paths, crack branching phenomena and the macro- and micro-cracks interaction problem with various cases of the micro-crack distribution and inclination angles. The PD simulations showed good agreement with analytical solutions, and the numerical results demonstrated the efficiency of the PD modelling of multiple crack interaction problems. This study was a starting point for modelling defects (porosities) in additively manufactured structures and analysis of the material with process-induced defects under fatigue loading.

- A PD model for the investigation of the porosity effects of the fatigue life was developed. The application of the PD model showed a capability of crack nucleation prediction for the titanium alloy samples under cycling loading. The predicted results showed good agreement with experimental data by comparing the stress-life (S-N) curves. The study presented a numerical approach to assessing the influence of the pore location and size on the fatigue life of Ti6Al4V alloys. The PD predictions indicated the critical pore characteristics and the applicability of the developed PD model on samples with low porosity for HCF loads.

- A PD model of fatigue crack propagation in additively manufactured structures was created. The study included the development of 1. A polycrystalline model with elongated grains, representing the microstructure of additively manufactured materials; 2. Porosity model and combined porosity and

polycrystalline model; 3. The model with the initial RS in the material by the employment of parabolic temperature profile. All the models were analysed under the cycling loading conditions, and the effect of all factors (microstructure, porosity, RS) on FCGR were investigated. The developed numerical models showed the capability of PD to predict the FCGR in additively manufactured structures, which are close to the experimental data available in the literature.

- A PD model of CF phenomena was developed for FCG problems by coupling the PD fatigue model and PD diffusion model (SCC). The newly developed PD model showed its capability of capturing the complex CF phenomena with results close to the experimental data.

8.2   Gaps and recommended future work

The materials are treated as elastic through all the presented studies with the assumption that no plastic deformations occur. In work on the materials like PMMA and concrete, the following assumptions did not affect the results of the studies with the numerical predictions very close to the experimental data. Concerning the fatigue crack nucleation studies in metals, plastic deformations occur in the structure due to the plastic slips in the grains. The following phase in the material could be analysed in-depth, and the numerical framework could be further extended by modelling the plastic deformations in the material with the development of micro-cracks in the crystallographic planes. The validation of the plastic deformation process is required.

Concerning the microstructures analysed in the presented studies, the grains are generated randomly in coarse numerical models. Instead, the parallel computing and the refinement models (for example, with a dual-horizon approach) could be used to have fine discretised models in order to reproduce and investigate the real microstructures. Additionally, the grain coefficients are selected randomly. Therefore, further investigation is necessary to calibrate the GB and GI coefficients to reproduce the real effect of the values on crack propagation problems.

Concerning implementing RS in the PD model, the simplified parabolic temperature profile is utilised. Further investigation could be performed on the possible profiles representing the RS in the structure with additional experimental validation.

Concerning the PD CF model, experimental validation is required for the diffusion model. Additionally, the SCC is modelled for the HE mechanism, but the numerical framework could be extended by modelling the re-passivation mechanisms and pit to crack transitions. Moreover, the PD model on fatigue corrosion problems could not be analysed thoroughly on additively manufactured materials, including the material microstructure, porosities, and RS, due to the lack of experimental data available in the literature. Therefore, experimental validation is required to perform an in-depth analysis of the crack growth in the additively manufactured materials subjected to environmental fatigue.

Finally, the studies on fatigue and CF of additively manufactured materials are performed on titanium alloys, and the studies could be extended on other types of metals subjected to the different loading conditions.

8.3   Research outputs

Karpenko, O., Oterkus, S., & Oterkus, E. (2020). An In-depth Investigation of Critical Stretch Based Failure Criterion in Ordinary State-based Peridynamics. *International Journal of Fracture.* https://doi.org/10.1007/s10704-020-00481-z

Karpenko, O., Oterkus, S., & Oterkus, E. (2020). Influence of Different Types of Small-Size Defects on Propagation of Macro-cracks in Brittle Materials. *Journal of Peridynamics and Nonlocal Modeling*, *2*(3), 289–316. https://doi.org/10.1007/s42102-020-00032-z

Karpenko, O., Oterkus, S., & Oterkus, E. (2021). Peridynamic Investigation of the Effect of Porosity on Fatigue Nucleation for Additively Manufactured Titanium Alloy Ti6Al4V. *Theoretical   and   Applied   Fracture   Mechanics*, 102925. https://doi.org/10.1016/j.tafmec.2021.102925

Karpenko, O., Oterkus, S., & Oterkus, E. (2021). Investigating the Influence of Residual Stresses on Fatigue Crack Growth for Additively Manufactured Titanium Alloy Ti6Al4V by using Peridynamics. *International Journal of Fatigue*, 155(October 2021), 106624. https://doi.org/10.1016/j.ijfatigue.2021.106624

Karpenko, O., Oterkus, S., & Oterkus, E. (2022). Peridynamic analysis to investigate the influence of microstructure and porosity on fatigue crack propagation in Additively Manufactured Ti6Al4V. *Engineering Fracture Mechanics*, 261(December 2021), 108212. https://doi.org/10.1016/j.engfracmech.2021.108212

Karpenko, O., Oterkus, S., & Oterkus, E. (2022). Titanium alloy corrosion fatigue crack growth rates prediction: Peridynamics based numerical approach. *International Journal of Fatigue*, *162* (April), 107023. https://doi.org/10.1016/j.ijfatigue.2022.107023

REFERENCES

1. Frazier, W. E. (2014). Metal additive manufacturing: A review. *Journal of Materials Engineering and Performance*, *23*(6), 1917–1928. https://doi.org/10.1007/s11665-014-0958-z

2. Murr, L. E., Martinez, E., Amato, K. N., Gaytan, S. M., Hernandez, J., Ramirez, D. A., … Wicker, R. B. (2012). Fabrication of metal and alloy components by additive manufacturing: Examples of 3D materials science. *Journal of Materials Research and Technology*, *1*(1), 42–54. https://doi.org/10.1016/S2238-7854(12)70009-1

3. Kruth, J.-P., Leu, M. C., & Nakagawa, T. (1998). Progress in Additive Manufacturing and Rapid Prototyping. *CIRP Annals*, *47*(2), 525–540. https://doi.org/10.1016/s0007-8506(07)63240-5

4. Zhai, Y., Lados, D. A., & Lagoy, J. L. (2014). Additive Manufacturing: Making imagination the major Limitation. *Jom*, *66*(5), 808–816. https://doi.org/10.1007/s11837-014-0886-2

5. Strickland, J. D. (2016). Applications of Additive Manufacturing in the marine industry. *PRADS 2016 - Proceedings of the 13th International Symposium on PRActical Design of Ships and Other Floating Structures*, (September). https://doi.org/10.13140/RG.2.2.29930.31685

6. Chandrasekaran, S., Hari, S., & Amirthalingam, M. (2020). Wire arc additive manufacturing of functionally graded material for marine risers. *Materials Science and Engineering: A*, *792*, 139530. https://doi.org/10.1016/j.msea.2020.139530

7. DebRoy, T., Wei, H. L., Zuback, J. S., Mukherjee, T., Elmer, J. W., Milewski, J. O., … Zhang, W. (2018). Additive manufacturing of metallic components – Process, structure and properties. *Progress in Materials Science*, *92*, 112–224. https://doi.org/10.1016/j.pmatsci.2017.10.001

8. Liu, S., & Shin, Y. C. (2019). Additive manufacturing of Ti6Al4V alloy: A review. *Materials and Design*, *164*, 107552. https://doi.org/10.1016/j.matdes.2018.107552

9. McAndrew, A. R., Alvarez Rosales, M., Colegrove, P. A., Hönnige, J. R., Ho, A., Fayolle, R., … Pinter, Z. (2018). Interpass rolling of Ti-6Al-4V wire + arc additively manufactured features for microstructural refinement. *Additive Manufacturing*, *21*(February), 340–349. https://doi.org/10.1016/j.addma.2018.03.006

10. Biswal, R., Zhang, X., Syed, A. K., Awd, M., Ding, J., Walther, F., & Williams, S. (2019). Criticality of porosity defects on the fatigue performance of wire + arc additive manufactured titanium alloy. *International Journal of Fatigue*, *122*(September 2018), 208–217. https://doi.org/10.1016/j.ijfatigue.2019.01.017

11. Tammas-Williams, S., Withers, P. J., Todd, I., & Prangnell, P. B. (2017). The Influence of Porosity on Fatigue Crack Initiation in Additively Manufactured Titanium Components. *Scientific Reports*, *7*(1), 1–13. https://doi.org/10.1038/s41598-017-06504-5

12. Wycisk, E., Solbach, A., Siddique, S., Herzog, D., Walther, F., & Emmelmann, C. (2014). Effects of defects in laser additive manufactured Ti-6Al-4V on fatigue properties. In *Physics Procedia* (Vol. 56, pp. 371–378). https://doi.org/10.1016/j.phpro.2014.08.120

13. Biswal, R., Syed, A. K., & Zhang, X. (2018). Assessment of the effect of isolated porosity defects on the fatigue performance of additive manufactured titanium alloy. *Additive Manufacturing*, *23*(March), 433–442. https://doi.org/10.1016/j.addma.2018.08.024

14. Seifi, M., Salem, A., Satko, D., Shaffer, J., & Lewandowski, J. J. (2017). Defect distribution and microstructure heterogeneity effects on fracture resistance and fatigue behavior of EBM Ti–6Al–4V. *International Journal of Fatigue*, *94*, 263–287. https://doi.org/10.1016/j.ijfatigue.2016.06.001

15. Kok, Y., Tan, X. P., Wang, P., Nai, M. L. S., Loh, N. H., Liu, E., & Tor, S. B. (2018). Anisotropy and heterogeneity of microstructure and mechanical properties in metal additive manufacturing: A critical review. *Materials & Design*, *139*, 565–586. https://doi.org/10.1016/j.matdes.2017.11.021

16. Xie, Y., Gao, M., Wang, F., Zhang, C., Hao, K., Wang, H., & Zeng, X. (2018). Anisotropy of fatigue crack growth in wire arc additive manufactured Ti-6Al-4V. *Materials Science and Engineering A*, *709*(October 2017), 265–269. https://doi.org/10.1016/j.msea.2017.10.064

17. Fatemi, A., Molaei, R., Sharifimehr, S., Phan, N., & Shamsaei, N. (2017). Multiaxial fatigue behavior of wrought and additive manufactured Ti-6Al-4V including surface finish effect. *International Journal of Fatigue*, *100*, 347–366. https://doi.org/10.1016/j.ijfatigue.2017.03.044

18. Liu, X., Sun, C., & Hong, Y. (2015). Effects of stress ratio on high-cycle and very-high-cycle fatigue behavior of a Ti-6Al-4V alloy. *Materials Science and Engineering A*, *622*, 228–235. https://doi.org/10.1016/j.msea.2014.09.115

19. Leuders, S., Thöne, M., Riemer, A., Niendorf, T., Tröster, T., Richard, H. A., & Maier, H. J. (2013). On the mechanical behaviour of titanium alloy TiAl6V4 manufactured by selective laser melting: Fatigue resistance and crack growth performance. *International Journal of Fatigue*, *48*, 300–307. https://doi.org/10.1016/j.ijfatigue.2012.11.011

20. Milella, P. . (2013). *Fatigue and Corrosion in Metals. Angewandte Chemie International Edition, 6(11), 951–952.*

21. Karpenko, O., Oterkus, S., & Oterkus, E. (2020). An In-depth Investigation of Critical Stretch Based Failure Criterion in Ordinary State-based Peridynamics. *International Journal of Fracture*. https://doi.org/10.1007/s10704-020-00481-z

22. Karpenko, O., Oterkus, S., & Oterkus, E. (2020). Influence of Different Types of Small-Size Defects on Propagation of Macro-cracks in Brittle Materials. *Journal of Peridynamics and Nonlocal Modeling*, *2*(3), 289–316. https://doi.org/10.1007/s42102-020-00032-z

23. Karpenko, O., Oterkus, S., & Oterkus, E. (2021). Peridynamic Investigation of the Effect of Porosity on Fatigue Nucleation for Additively Manufactured Titanium Alloy Ti6Al4V. *Theoretical and Applied Fracture Mechanics*, 102925. https://doi.org/10.1016/j.tafmec.2021.102925

24. Karpenko, O., Oterkus, S., & Oterkus, E. (2021). Investigating the Influence of Residual Stresses

on Fatigue Crack Growth for Additively Manufactured Titanium Alloy Ti6Al4V by using Peridynamics. *International Journal of Fatigue*, *155*(October 2021), 106624. https://doi.org/10.1016/j.ijfatigue.2021.106624

25. Karpenko, O., Oterkus, S., & Oterkus, E. (2022). Peridynamic analysis to investigate the influence of microstructure and porosity on fatigue crack propagation in Additively Manufactured Ti6Al4V. *Engineering Fracture Mechanics*, *261*(December 2021), 108212. https://doi.org/10.1016/j.engfracmech.2021.108212

26. Karpenko, O., Oterkus, S., & Oterkus, E. (2022). Titanium alloy corrosion fatigue crack growth rates prediction: Peridynamics based numerical approach. *International Journal of Fatigue*, *162*(April), 107023. https://doi.org/10.1016/j.ijfatigue.2022.107023

27. Irwin, G. R. (1957). Analysis of Stresses and Strains Near the End of a Crack Traversing a Plate. *Journal of Applied Mechanics*, *24*(September), 361–364. https://doi.org/no DOI

28. Cotterell, B. (1965). On brittle fracture paths. *International Journal of Fracture Mechanics*, *1*(2), 96–103. https://doi.org/10.1007/BF00186747

29. Bowden, F. P., Brunton, J. H., Field, J. E., & Heyes, A. D. (1967). Controlled fracture of brittle solids and interruption of electrical current. *Nature*, *216*(5110), 38–42. https://doi.org/10.1038/216038a0

30. Fineberg, J., Sharon, E., & Cohen, G. (2003). Crack front waves in dynamic fracture. *International Journal of Fracture*, *119*(3), 247–261. https://doi.org/10.1023/A:1023954211188

31. Ramulu, M., & Kobayashi, A. S. (1985). Mechanics of crack curving and branching - a dynamic fracture analysis. *International Journal of Fracture*, *27*(3–4), 187–201. https://doi.org/10.1007/BF00017967

32. Döll, W. (1975). Investigations of the crack branching energy. *International Journal of Fracture*, *11*(1), 184–186. https://doi.org/10.1007/BF00034729

33. Gorynin, I. V., Chechulin, B. B., Ushkov, S. S., & Belova, O. S. (1974). Brittleness and characteristics of the fracture of titanium alloys, (9), 37–40.

34. Charalambides, P. G., & McMeeking, R. M. (1987). Finite element method simulation of crack propagation in a brittle microcracking solid. *Mechanics of Materials*, *6*(1), 71–87. https://doi.org/10.1016/0167-6636(87)90023-8

35. Ortiz, M., & Pandolfi, A. (1999). Finite-deformation irreversible cohesive elements for three-dimensional crack-propagation analysis. *International Journal for Numerical Methods in Engineering*, *44*(9), 1267–1282. https://doi.org/10.1002/(SICI)1097-0207(19990330)44:9<1267::AID-NME486>3.0.CO;2-7

36. Hillerborg, A., Modeer, M., & Petersson, P. E. (2008). Analysis of crack formation and crack growth in concrete by means of fracture mechanics and finite elements. *American Concrete Institute, ACI Special Publication*, *SP-249*, 225–237.

37. Elices, M., Guinea, G. V., Gómez, J., & Planas, J. (2001). The cohesive zone model: Advantages,

limitations and challenges. *Engineering Fracture Mechanics*, *69*(2), 137–163. https://doi.org/10.1016/S0013-7944(01)00083-2

38. Fries, T. ., & Belytschko, T. (2010). The extended/generalized finite element method: An overview of the method and its applications. *International Journal for Numerical Methods in Engineering*, *84*(February), 253–304. https://doi.org/10.1002/nme

39. Belytschko, T., Liu, W. K., Moran, B., & Elkhodary, K. (2001). *Nonlinear finite elements for continua and structures*. *Choice Reviews Online* (Vol. 38). John wiley & sons. https://doi.org/10.5860/choice.38-3926

40. Menouillard, T., & Belytschko, T. (2010). Dynamic fracture with meshfree enriched XFEM. *Acta Mechanica*, *213*(1–2), 53–69. https://doi.org/10.1007/s00707-009-0275-z

41. Nicak, T., Mutz, A., Keim, E., & Meier, G. (2015). Application of XFEM to model crack initiation and propagation during a PTS event. *American Society of Mechanical Engineers, Pressure Vessels and Piping Division (Publication) PVP*, *6A-2015*, 1–11. https://doi.org/10.1115/PVP201545180

42. Mariani, S., & Perego, U. (2003). Extended finite element method for quasi-brittle fracture. *International Journal for Numerical Methods in Engineering*, *58*(1), 103–126. https://doi.org/10.1002/nme.761

43. Geniaut, S., & Galenne, E. (2012). A simple method for crack growth in mixed mode with X-FEM. *International Journal of Solids and Structures*, *49*(15–16), 2094–2106. https://doi.org/10.1016/j.ijsolstr.2012.04.015

44. Ren, X., & Guan, X. (2017). Three dimensional crack propagation through mesh-based explicit representation for arbitrarily shaped cracks using the extended finite element method. *Engineering Fracture Mechanics*, *177*, 218–238. https://doi.org/10.1016/j.engfracmech.2017.04.007

45. Zi, G., & Belytschko, T. (2003). New crack-tip elements for XFEM and applications to cohesive cracks. *International Journal for Numerical Methods in Engineering*, *57*(15), 2221–2240. https://doi.org/10.1002/nme.849

46. Zhou, F., Molinari, J. F., & Shioya, T. (2005). A rate-dependent cohesive model for simulating dynamic crack propagation in brittle materials. *Engineering Fracture Mechanics*, *72*(9), 1383–1410. https://doi.org/10.1016/j.engfracmech.2004.10.011

47. Ravi-Chandar, K., & Yang, B. (1997). On the role of microcracks in the dynamic fracture of brittle materials. *Journal of the Mechanics and Physics of Solids*, *45*(4), 535–563. https://doi.org/10.1016/S0022-5096(96)00096-8

48. Wawersik, W. R., & Fairhurst, C. (1970). A study of brittle rock fracture in laboratory compression experiments. *International Journal of Rock Mechanics and Mining Sciences and*, *7*(5), 561–575. https://doi.org/10.1016/0148-9062(70)90007-0

49. Bocca, P., Carpinteri, A., & Valente, S. (1991). Mixed mode fracture of concrete. *International*

Journal of Solids and Structures, *27*(9), 1139–1153. https://doi.org/10.1016/0020-7683(91)90115-V

50.   Malvar, L. J., & Warren, G. E. (1988). *Fracture energy for three-point-bend tests on single-edge-notched beams*. *Experimental Mechanics* (Vol. 28). California. https://doi.org/10.1007/BF02329022

51.   Arya, S. (1998). *Chloroquine resistance among malarial episodes in Saudi Arabia [1]*. *Annals of Saudi Medicine* (Vol. 18). https://doi.org/10.5144/0256-4947.1998.84

52.   Bleyer, J., Roux-Langlois, C., & Molinari, J. F. (2017). Dynamic crack propagation with a variational phase-field model: limiting speed, crack branching and velocity-toughening mechanisms. *International Journal of Fracture*, *204*(1), 79–100. https://doi.org/10.1007/s10704-016-0163-1

53.   Kachanov, M. (1986). On Crack - Microcrack interactions. *International Journal of Fracture*, *30*, 65–72.

54.   Brencich, A., & Carpinteri, A. (1998). Stress field interaction and strain energy distribution between a stationary main crack and its process zone. *Engineering Fracture Mechanics*, *59*(6), 797–814. https://doi.org/10.1016/S0013-7944(97)00158-6

55.   Nagaraja Rao, G. M., & Murthy, C. R. L. (2001). Dual role of microcracks: Toughening and degradation. *Canadian Geotechnical Journal*, *38*(2), 427–440. https://doi.org/10.1139/cgj-38-2-427

56.   Rubinstein, A. A. (1985). Macrocrack interaction with semi-infinite microcrack array. *International Journal of Fracture*, *27*(2), 113–119. https://doi.org/10.1007/BF00040390

57.   Rose, L. R. F. (1986). Microcrack interaction with a main crack. *International Journal of Fracture*, *31*(3), 233–242. https://doi.org/10.1007/BF00018929

58.   Petrova, V., Tamuzs, V., & Petrova, V. (2000). A survey of macro-microcrack interaction problems. *Applied Mechanics Reviews*, *53*(5), 117–146. https://doi.org/10.1115/1.3097344

59.   Tamuzs, V., Romalis, N., & Petrova, V. (1993). Influence of microcracks on thermal fracture of macrocrack. *Theoretical and Applied Fracture Mechanics*, *19*(3), 207–225. https://doi.org/10.1016/0167-8442(93)90022-4

60.   Milios, J., & Spathis, G. (1988). Dynamic interaction of a propagating crack with a hole boundary. *Acta Mechanica*, *72*(3–4), 283–295. https://doi.org/10.1007/BF01178314

61.   Theocaris, P. S., & Milios, J. (1981). Crack-arrest at a bimaterial interface. *International Journal of Solids and Structures*, *17*(2), 217–230. https://doi.org/10.1016/0020-7683(81)90077-9

62.   Theocaris, P. S., & Milios, J. (1981). Crack arrest modes of a transverse crack going through a longitudinal crack or a hole. *Journal of Engineering Materials and Technology, Transactions of the ASME*, *103*(2), 177–182. https://doi.org/10.1115/1.3224991

63.   Hu, K. X., Chandra, A., & Huang, Y. (1993). Multiple void-crack interaction. *International Journal of Solids and Structures*, *30*(11), 1473–1489. https://doi.org/10.1016/0020-

7683(93)90072-F

64.   Madenci, E., & Oterkus, E. (2014). *Peridynamic Theory and Its Applications*. Springer New York Heidelberg Dordrecht London. https://doi.org/DOI 10.1007/978-1-4614-8465-3

65.   Silling, S. A. (2000). Reformulation of elasticity theory for discontinuities and long-range forces. *Journal of the Mechanics and Physics of Solids*, *48*(1), 175–209. https://doi.org/10.1016/S0022-5096(99)00029-0

66.   Gagg, C. R., & Lewis, P. R. (2009). In-service fatigue failure of engineered products and structures - Case study review. *Engineering Failure Analysis*, *16*(6), 1775–1793. https://doi.org/10.1016/j.engfailanal.2008.08.008

67.   Wöhler, A. (1870). *Über die festigkeitsversuche mit eisen und stahl*. Ernst & Korn,.

68.   Nalla, R. K., Boyce, B. L., Campbell, J. P., Peters, J. O., & Ritchie, R. O. (2002). Influence of Microstructure on High-Cycle Fatigue of Ti-6Al-4V: Bimodal vs. Lamellar Structures. *Metallurgical and Materials Transactions A: Physical Metallurgy and Materials Science*, *33A*. https://doi.org/10.13140/RG.2.1.3668.1201

69.   Meng, L., Gao, J., Yue, J., Zhang, J., Zhao, X., & Zhang, D. (2020). Stress-based fatigue behavior of Ti–6Al–4V alloy with a discontinuous lamellar microstructure fabricated by thermomechanical powder consolidation. *Materials Science and Engineering A*, *798*(May), 140085. https://doi.org/10.1016/j.msea.2020.140085

70.   Lütjering, G. (1998). Influence of processing on microstructure and mechanical properties of (α + β) titanium alloys. *Materials Science and Engineering A*, *243*(1–2), 32–45. https://doi.org/10.1016/s0921-5093(97)00778-8

71.   Cao, Y., Zeng, F., Liu, B., Liu, Y., Lu, J., Gan, Z., & Tang, H. (2016). Characterization of fatigue properties of powder metallurgy titanium alloy. *Materials Science and Engineering A*, *654*, 418–425. https://doi.org/10.1016/j.msea.2015.12.058

72.   Sonntag, R., Reinders, J., Gibmeier, J., & Kretzer, J. P. (2015). Fatigue performance of medical Ti6Al4V alloy after mechanical surface treatments. *PLoS ONE*, *10*(3), 1–15. https://doi.org/10.1371/journal.pone.0121963

73.   HOBSON, P. D. (1982). the Formulation of a Crack Growth Equation for Short Cracks. *Fatigue & Fracture of Engineering Materials & Structures*, *5*(4), 323–327. https://doi.org/10.1111/j.1460-2695.1982.tb01241.x

74.   Chung, H. M., Chopra, O. K., Erck, R. A., Kassner, T. F., Michaud, W. F., Rulher, W. E., … Soppet, W. K. (1993). *Environmentally Assisted Cracking in Light Water Reactors Semiannual Report* (Vol. 31).

75.   Paris, P. C. (1964). The fracture mechanics approach to fatigue Fatigue. – An Interdisciplinary Approach (pp. 107–132). United States.

76.   Forman, R. G., Kearney, V. E., & Engle, R. M. (1967). Numerical analysis of crack propagation in cyclic-loaded structures. *Journal of Fluids Engineering, Transactions of the ASME*, *89*(3),

459–463. https://doi.org/10.1115/1.3609637

77. Klesnil, M., & Lukáš, P. (1972). Influence of strength and stress history on growth and stabilisation of fatigue cracks. *Engineering Fracture Mechanics*, *4*(1), 77–92. https://doi.org/10.1016/0013-7944(72)90078-1

78. Schijve, J. (1981). Defining the ratio. *Engineering Fracture Mechanics*, *14*, 461–465.

79. Weertman, J. (1966). Rate of growth of fatigue cracks calculated from the theory of infinitesimal dislocations distributed on a plane. *International Journal of Fracture Mechanics*, *2*(2), 460–467. https://doi.org/10.1007/BF00183823

80. ELBER W. (1971). the Significance of Fatigue Crack Closure. *ASTM Special Technical Publication*, (486), 230–242.

81. McEvily, A. J., & Minakawa, K. (1984). on the Role of Crack Closure in Fatigue Crack Growth. *ASTM STP*, (982), 763–768.

82. Bittencourt, T. N., Wawrzynek, P. A., Ingraffea, A. R., & Sousa, J. L. (1996). Quasi-automatic simulation of crack propagation for 2D lefm problems. *Engineering Fracture Mechanics*, *55*(2), 321–334. https://doi.org/10.1016/0013-7944(95)00247-2

83. Poursaeidi, E., & Bakhtiari, H. (2014). Fatigue crack growth simulation in a first stage of compressor blade. *Engineering Failure Analysis*, *45*, 314–325. https://doi.org/10.1016/j.engfailanal.2014.06.018

84. Schöllmann, M., Fulland, M., & Richard, H. A. (2003). Development of a new software for adaptive crack growth simulations in 3D structures. *Engineering Fracture Mechanics*, *70*(2), 249–268. https://doi.org/10.1016/S0013-7944(02)00028-0

85. Zerres, P., & Vormwald, M. (2012). Finite element based simulation of fatigue crack growth with a focus on elastic-plastic material behavior. *Computational Materials Science*, *57*, 73–79. https://doi.org/10.1016/j.commatsci.2012.01.018

86. Zargarian, A., Esfahanian, M., Kadkhodapour, J., & Ziaei-Rad, S. (2016). Numerical simulation of the fatigue behavior of additive manufactured titanium porous lattice structures. *Materials Science and Engineering C*, *60*, 339–347. https://doi.org/10.1016/j.msec.2015.11.054

87. Ince, A., & Glinka, G. (2016). Innovative computational modeling of multiaxial fatigue analysis for notched components. In *International Journal of Fatigue* (Vol. 82, pp. 134–145). https://doi.org/10.1016/j.ijfatigue.2015.03.019

88. Chakherlou, T. N., Shakouri, M., Akbari, A., & Aghdam, A. B. (2012). Effect of cold expansion and bolt clamping on fretting fatigue behavior of Al 2024-T3 in double shear lap joints. *Engineering Failure Analysis*, *25*, 29–41. https://doi.org/10.1016/j.engfailanal.2012.04.008

89. Silva, A. L. L., de Jesus, A. M. P., Xavier, J., Correia, J. A. F. O., & Fernandes, A. A. (2017). Combined analytical-numerical methodologies for the evaluation of mixed-mode (I + II) fatigue crack growth rates in structural steels. *Engineering Fracture Mechanics*, *185*, 124–138. https://doi.org/10.1016/j.engfracmech.2017.04.016

90. Hu, X. F., & Yao, W. A. (2013). A new enriched finite element for fatigue crack growth. *International Journal of Fatigue*, *48*, 247–256. https://doi.org/10.1016/j.ijfatigue.2012.11.003

91. Sih, G. C. (1991). *Mechanics of Fracture Initiation and Propagation. Mechanics of Fracture Initiation and Propagation*. Springer Netherlands. https://doi.org/10.1007/978-94-011-3734-8

92. Erdogan, F., & Sih, G. C. (1963). On the crack extension in plates under plane loading and transverse shear. *Journal of Fluids Engineering, Transactions of the ASME*, *85*(4), 519–525. https://doi.org/10.1115/1.3656897

93. Raju, I. S. (1987). Calculation of strain-energy release rates with higher order and singular finite elements. *Engineering Fracture Mechanics*, *28*(3), 251–274. https://doi.org/10.1016/0013-7944(87)90220-7

94. Nayroles, B., Touzot, G., & Villon, P. (1992). Generalizing the finite element method: Diffuse approximation and diffuse elements. *Computational Mechanics*, *10*(5), 307–318. https://doi.org/10.1007/BF00364252

95. Belytschko, T., Lu, Y. Y., & Gu, L. (1995). Crack propagation by element-free Galerkin methods. *Engineering Fracture Mechanics*, *51*(2), 295–315. https://doi.org/10.1016/0013-7944(94)00153-9

96. Belytschko, T., Lu, Y. Y., & Gu, L. (1994). Element-free galerkin methods, *37*(April 1994), 229–256.

97. Melenk, J. M., & Babuška, I. (1996). The partition of unity finite element method: Basic theory and applications. *Computer Methods in Applied Mechanics and Engineering*, *139*(1–4), 289–314. https://doi.org/10.1016/S0045-7825(96)01087-0

98. Oden, J. T., Duarte, C. A. M., & Zienkiewicz, O. C. (1998). A new cloud-based hp finite element method. *Computer Methods in Applied Mechanics and Engineering*, *153*(1–2), 117–126. https://doi.org/10.1016/S0045-7825(97)00039-X

99. Strouboulis, T., Babuška, I., & Copps, K. (2000). The design and analysis of the Generalized Finite Element Method. *Computer Methods in Applied Mechanics and Engineering*, *181*(1–3), 43–69. https://doi.org/10.1016/S0045-7825(99)00072-9

100. Moës, N., Dolbow, J., & Belytschko, T. (1999). A finite element method for crack growth without remeshing. *International Journal for Numerical Methods in Engineering*, *46*(1), 131–150. https://doi.org/10.1002/(SICI)1097-0207(19990910)46:1<131::AID-NME726>3.0.CO;2-J

101. Singh, I. V., Mishra, B. K., Bhattacharya, S., & Patil, R. U. (2012). The numerical simulation of fatigue crack growth using extended finite element method. *International Journal of Fatigue*, *36*(1), 109–119. https://doi.org/10.1016/j.ijfatigue.2011.08.010

102. Sukumar, N., Chopp, D. L., & Moran, B. (2003). Extended finite element method and fast marching method for three-dimensional fatigue crack propagation. *Engineering Fracture Mechanics*, *70*(1), 29–48. https://doi.org/10.1016/S0013-7944(02)00032-2

103. Wang, Z., Yu, T., Bui, T. Q., Trinh, N. A., Luong, N. T. H., Duc, N. D., & Doan, D. H. (2016).

Numerical modeling of 3-D inclusions and voids by a novel adaptive XFEM. *Advances in Engineering Software*, *102*, 105–122. https://doi.org/10.1016/j.advengsoft.2016.09.007

104. Yngvesson, M., & Nilsson, F. (1999). Fatigue crack growth of surface cracks under non-symmetric loading. *Engineering Fracture Mechanics*, *63*(4), 375–393. https://doi.org/10.1016/s0013-7944(99)00033-8

105. Barlow, K. W., & Chandra, R. (2005). Fatigue crack propagation simulation in an aircraft engine fan blade attachment. *International Journal of Fatigue*, *27*(10–12), 1661–1668. https://doi.org/10.1016/j.ijfatigue.2005.06.016

106. Spievak, L. E., Wawrzynek, P. A., Ingraffea, A. R., & Lewicki, D. G. (2001). Simulating fatigue crack growth in spiral bevel gears. *Engineering Fracture Mechanics*, *68*(1), 53–76. https://doi.org/10.1016/S0013-7944(00)00089-8

107. Sutradhar, A., Paulino, G. H., & Gray, L. J. (2008). Symmetric galerkin boundary element method. *Symmetric Galerkin Boundary Element Method*, 1–276. https://doi.org/10.1007/978-3-540-68772-6

108. Prasad, N. N. V., Aliabadi, M. H., & Rooke, D. P. (1996). The dual boundary element method for transient thermoelastic crack problems. *International Journal of Solids and Structures*, *33*(19), 2695–2718. https://doi.org/10.1016/0020-7683(95)00183-2

109. Hong, H. K., & Chen, J. T. (1988). Derivations of integral equations of elasticity. *Journal of Engineering Mechanics*, *114*(6), 1028–1044. https://doi.org/10.1061/(ASCE)0733-9399(1988)114:6(1028)

110. Cisilino, A. P., & Aliabadi, M. H. (2004). Dual boundary element assessment of three-dimensional fatigue crack growth. *Engineering Analysis with Boundary Elements*, *28*(9), 1157–1173. https://doi.org/10.1016/j.enganabound.2004.01.005

111. Blackburn, W. S. (1999). Three dimensional calculation of growth of cracks starting in parallel planes by boundary elements. *International Journal of Fatigue*, *21*(9), 933–939. https://doi.org/10.1016/S0142-1123(99)00079-1

112. Blackburn, W. S., Hall, W. S., & Rooke, D. P. (1995). Numerical simulation of the initiation and growth of new fatigue cracks following crack intersections. *International Journal of Fatigue*, *17*(6), 437–446. https://doi.org/10.1016/0142-1123(95)00022-L

113. Cisilino, A. P., & Aliabadi, M. H. (1997). Three-dimensional BEM analysis for fatigue crack growth in welded components. *International Journal of Pressure Vessels and Piping*, *70*(2), 135–144. https://doi.org/10.1016/S0308-0161(96)00031-2

114. Prasad, N. N. V., Aliabadi, M. H., & Rooke, D. P. (1996). Thermomechanical fatigue crack growth. *International Journal of Fatigue*, *18*(6), 349–361. https://doi.org/10.1016/0142-1123(96)00027-8

115. Dirgantara, T., & Aliabadi, M. H. (2002). Numerical simulation of fatigue crack growth in pressurized shells. *International Journal of Fatigue*, *24*(7), 725–738.

https://doi.org/10.1016/S0142-1123(01)00195-5

116. Bourell, D., Kruth, J. P., Leu, M., Levy, G., Rosen, D., Beese, A. M., & Clare, A. (2017). Materials for additive manufacturing. *CIRP Annals - Manufacturing Technology*, *66*(2), 659–681. https://doi.org/10.1016/j.cirp.2017.05.009

117. Herzog, D., Seyda, V., Wycisk, E., & Emmelmann, C. (2016). Additive manufacturing of metals. *Acta Materialia*, *117*, 371–392. https://doi.org/10.1016/j.actamat.2016.07.019

118. Dutta, B., & Froes, F. H. (Sam). (2017). *The Additive Manufacturing (AM) of titanium alloys*. *Metal Powder Report* (Vol. 72). Elsevier Inc. https://doi.org/10.1016/j.mprp.2016.12.062

119. Lampman, S. A. S. M. (1990). Wrought titanium and titanium alloys. In *Metal handbook 2* (pp. 592–633).

120. Martina, F., Colegrove, P. A., Williams, S. W., & Meyer, J. (2015). Microstructure of Interpass Rolled Wire + Arc Additive Manufacturing Ti-6Al-4V Components. *Metallurgical and Materials Transactions A: Physical Metallurgy and Materials Science*, *46*(12), 6103–6118. https://doi.org/10.1007/s11661-015-3172-1

121. Wysocki, B., Maj, P., Sitek, R., Buhagiar, J., Kurzydłowski, K. J., & Święszkowski, W. (2017). Laser and electron beam additive manufacturing methods of fabricating titanium bone implants. *Applied Sciences (Switzerland)*, *7*(7), 1–20. https://doi.org/10.3390/app7070657

122. Taminger, K. M., & Hafley, R. A. (2004). Electron Beam Freeform Fabrication for Cost Effective Near-Net Shape Manufacturing. *Nato Unclassified*, 19.

123. Greitemeier, D., Palm, F., Syassen, F., & Melz, T. (2017). Fatigue performance of additive manufactured TiAl6V4 using electron and laser beam melting. *International Journal of Fatigue*, *94*, 211–217. https://doi.org/10.1016/j.ijfatigue.2016.05.001

124. Spierings, A. B., Starr, T. L., & Wegener, K. (2013). Fatigue performance of additive manufactured metallic parts. *Rapid Prototyping Journal*, *19*(2), 88–94. https://doi.org/10.1108/13552541311302932

125. Thijs, L., Verhaeghe, F., Craeghs, T., Humbeeck, J. Van, & Kruth, J. P. (2010). A study of the microstructural evolution during selective laser melting of Ti-6Al-4V. *Acta Materialia*, *58*(9), 3303–3312. https://doi.org/10.1016/j.actamat.2010.02.004

126. Mukherjee, T., Zuback, J. S., De, A., & Debroy, T. (2016). Printability of alloys for additive manufacturing. *Scientific Reports*, *6*(1), 19717. https://doi.org/10.1038/srep19717

127. Khosravani, M. R., Berto, F., Ayatollahi, M. R., & Reinicke, T. (2020). Fracture behavior of additively manufactured components: A review. *Theoretical and Applied Fracture Mechanics*, *109*(July), 102763. https://doi.org/10.1016/j.tafmec.2020.102763

128. Lewandowski, J. J., & Seifi, M. (2016). Metal Additive Manufacturing: A Review of Mechanical Properties. *Annual Review of Materials Research*, *46*, 151–186. https://doi.org/10.1146/annurev-matsci-070115-032024

129. Martina, F., Roy, M. J., Szost, B. A., Terzi, S., Colegrove, P. A., Williams, S. W., … Hofmann,

M. (2016). Residual stress of as-deposited and rolled wire+arc additive manufacturing Ti–6Al–4V components. *Materials Science and Technology (United Kingdom)*, *32*(14), 1439–1448. https://doi.org/10.1080/02670836.2016.1142704

130. Kasperovich, G., & Hausmann, J. (2015). Improvement of fatigue resistance and ductility of TiAl6V4 processed by selective laser melting. *Journal of Materials Processing Technology*, *220*, 202–214. https://doi.org/10.1016/j.jmatprotec.2015.01.025

131. Wycisk, E., Siddique, S., Herzog, D., Walther, F., & Emmelmann, C. (2015). Fatigue performance of laser additive manufactured Ti–6Al–4V in very high cycle fatigue regime up to 10 9 cycles. *Frontiers in Materials*, *2*(December), 2–9. https://doi.org/10.3389/fmats.2015.00072

132. Günther, J., Krewerth, D., Lippmann, T., Leuders, S., Tröster, T., Weidner, A., … Niendorf, T. (2017). Fatigue life of additively manufactured Ti–6Al–4V in the very high cycle fatigue regime. *International Journal of Fatigue*, *94*, 236–245. https://doi.org/10.1016/j.ijfatigue.2016.05.018

133. Baufeld, B., Brandl, E., & Van Der Biest, O. (2011). Wire based additive layer manufacturing: Comparison of microstructure and mechanical properties of Ti-6Al-4V components fabricated by laser-beam deposition and shaped metal deposition. *Journal of Materials Processing Technology*, *211*(6), 1146–1158. https://doi.org/10.1016/j.jmatprotec.2011.01.018

134. Liu, Q. C., Elambasseril, J., Sun, S. J., Leary, M., Brandt, M., & Sharp, P. K. (2014). The effect of manufacturing defects on the fatigue behaviour of Ti-6Al-4V specimens fabricated using selective laser melting. *Advanced Materials Research*, *891–892*, 1519–1524. https://doi.org/10.4028/www.scientific.net/AMR.891-892.1519

135. Brandl, E., Heckenberger, U., Holzinger, V., & Buchbinder, D. (2012). Additive manufactured AlSi10Mg samples using Selective Laser Melting (SLM): Microstructure, high cycle fatigue, and fracture behavior. *Materials and Design*, *34*, 159–169. https://doi.org/10.1016/j.matdes.2011.07.067

136. Kobryn, P. A., Moore, E. H., & Semiatin, S. L. (2000). Effect of laser power and traverse speed on microstructure, porosity, and build height in laser-deposited Ti-6Al-4V. *Scripta Materialia*, *43*(4), 299–305. https://doi.org/10.1016/S1359-6462(00)00408-5

137. Brown, S. D., Biddulph, R. B., & Wilcox, P. D. (1964). A Strength–Porosity Relation Involving Different Pore Geometry and Orientation. *Journal of the American Ceramic Society*, *47*(7), 320–322. https://doi.org/10.1111/j.1151-2916.1964.tb12993.x

138. Boccaccini, A. R., Ondracek, G., Mazilu, P., & Windelberq, D. (1993). On the effective young's modulus of elasticity for porous materials: Microstructure modelling and comparison between calculated and experimental values. *Boccaccini, A. R., & Ondracek, G. (1993). On the Effective Young's Modulus of Elasticity for Porous Materials: Microstructure Modelling and Comparison Between Calculated and Experimental Values. 4.*, *4*(2), 119–128. https://doi.org/10.1515/JMBM.1993.4.2.119

139. Paul, B. (1962). The Elastic Moduli of Heterogeneous Materials.

140. Hashin, Z. (1960). *The elastic moduli of heterogeneous materials. Journal of Applied Mechanics, Transactions ASME* (Vol. 29). https://doi.org/10.1115/1.3636446

141. Knudsen, F. P. (1959). Dependence of Mechanical Strength of Brittle Polycrystalline Specimens on Porosity and Grain Size. *Journal of the American Ceramic Society*, *42*(8), 376–387. https://doi.org/10.1111/j.1151-2916.1959.tb13596.x

142. Nielsen, L. F. (1990). Strength and Stiffness of Porous Materials. *Journal of the American Ceramic Society*, *73*(9), 2684–2689. https://doi.org/10.1111/j.1151-2916.1990.tb06746.x

143. Phani, K. K., & Niyogi, S. K. (1987). Young's modulus of porous brittle solids. *Journal of Materials Science*, *22*(1), 257–263. https://doi.org/10.1007/BF01160581

144. Pabst, W., & Gregorová, E. (2004). New relation for the porosity dependence of the effective tensile modulus of brittle materials. *Journal of Materials Science*, *39*(10), 3501–3503. https://doi.org/10.1023/B:JMSC.0000026961.12735.2a

145. Kováčik, J. (2006). Correlation between Poisson's ratio and porosity in porous materials. *Journal of Materials Science*, *41*(4), 1247–1249. https://doi.org/10.1007/s10853-005-4237-0

146. El Haddad, M. H., Topper, T. H., & Smith, K. . (1978). Prediction of non propagating cracks. *Engineering Fracture Mechanics*, *11*, 573–584.

147. Murakami, Y. (1991). Effects of small defects and nonmetallic inclusions on the fatigue strength of metals. *Mechanical and corrosion properties. Series A, Key engineering materials*, *51–52*(2), 37–42. https://doi.org/10.4028/www.scientific.net/kem.51-52.37

148. Beretta, S., & Romano, S. (2017). A comparison of fatigue strength sensitivity to defects for materials manufactured by AM or traditional processes. *International Journal of Fatigue*, *94*, 178–191. https://doi.org/10.1016/j.ijfatigue.2016.06.020

149. Sheridan, L., Scott-Emuakpor, O. E., George, T., & Gockel, J. E. (2018). Relating porosity to fatigue failure in additively manufactured alloy 718. *Materials Science and Engineering A*, *727*(March), 170–176. https://doi.org/10.1016/j.msea.2018.04.075

150. Siddique, S., Imran, M., Rauer, M., Kaloudis, M., Wycisk, E., Emmelmann, C., & Walther, F. (2015). Computed tomography for characterization of fatigue performance of selective laser melted parts. *Materials and Design*, *83*, 661–669. https://doi.org/10.1016/j.matdes.2015.06.063

151. Gammon, L. M., Briggs, R. D., Packard, J. M., Batson, K. W., Boyer, R., & Domby, C. W. (2004). Metallography and Microstructures of Titanium and Its Alloys. *Materials Park, OH: ASM International, 2004.*, *9*, 899–917. https://doi.org/10.1361/asmhba0003779

152. Pederson, R. (2002). Microstructure and Phase Transformation of Ti-6Al-4V, 27–30.

153. Åkerfeldt, P., Pederson, R., & Antti, M. L. (2016). A fractographic study exploring the relationship between the low cycle fatigue and metallurgical properties of laser metal wire deposited Ti-6Al-4V. *International Journal of Fatigue*, *87*, 245–256. https://doi.org/10.1016/j.ijfatigue.2016.02.011

154. Brandl, E., Palm, F., Michailov, V., Viehweger, B., & Leyens, C. (2011). Mechanical properties of additive manufactured titanium (Ti-6Al-4V) blocks deposited by a solid-state laser and wire. *Materials and Design*, *32*(10), 4665–4675. https://doi.org/10.1016/j.matdes.2011.06.062

155. Ivasishin, O. M., & Markovsky, P. E. (1996). Enhancing the mechanical properties of titanium alloys with rapid heat treatment. *Jom*, *48*(7), 48–52. https://doi.org/10.1007/BF03222998

156. Baufeld, B., Biest, O. Van Der, & Dillien, S. (2010). Texture and crystal orientation in Ti-6Al-4V builds fabricated by shaped metal deposition. *Metallurgical and Materials Transactions A: Physical Metallurgy and Materials Science*, *41*(8), 1917–1927. https://doi.org/10.1007/s11661-010-0255-x

157. Simonelli, M., Tse, Y. Y., & Tuck, C. (2014). Effect of the build orientation on the mechanical properties and fracture modes of SLM Ti-6Al-4V. *Materials Science and Engineering A*, *616*, 1–11. https://doi.org/10.1016/j.msea.2014.07.086

158. Morita, T., Tsuda, C., Sakai, H., & Higuchi, N. (2017). Fundamental properties of Ti-6Al-4V alloy produced by selective laser melting method. *Materials Transactions*, *58*(10), 1397–1403. https://doi.org/10.2320/matertrans.M2017103

159. Van Hooreweder, B., Moens, D., Boonen, R., Kruth, J. P., & Sas, P. (2012). Analysis of fracture toughness and crack propagation of Ti6Al4V produced by selective laser melting. *Advanced Engineering Materials*, *14*(1–2), 92–97. https://doi.org/10.1002/adem.201100233

160. Riemer, A., Leuders, S., Thöne, M., Richard, H. A., Tröster, T., & Niendorf, T. (2014). On the fatigue crack growth behavior in 316L stainless steel manufactured by selective laser melting. *Engineering Fracture Mechanics*, *120*, 15–25. https://doi.org/10.1016/j.engfracmech.2014.03.008

161. Vrancken, B., Cain, V., Knutsen, R., & Van Humbeeck, J. (2014). Residual stress via the contour method in compact tension specimens produced via selective laser melting. *Scripta Materialia*, *87*, 29–32. https://doi.org/10.1016/j.scriptamat.2014.05.016

162. Rangaswamy, P., Griffith, M. L., Prime, M. B., Holden, T. M., Rogge, R. B., Edwards, J. M., & Sebring, R. J. (2005). Residual stresses in LENS® components using neutron diffraction and contour method. *Materials Science and Engineering A*, *399*(1–2), 72–83. https://doi.org/10.1016/j.msea.2005.02.019

163. Syed, A. K., Ahmad, B., Guo, H., Machry, T., Eatock, D., Meyer, J., … Zhang, X. (2019). An experimental study of residual stress and direction-dependence of fatigue crack growth behaviour in as-built and stress-relieved selective-laser-melted Ti6Al4V. *Materials Science and Engineering A*, *755*(February), 246–257. https://doi.org/10.1016/j.msea.2019.04.023

164. ASTM E647−13. (2014). Standard Test Method for Measurement of Fatigue Crack Growth Rates. *American Society for Testing and Materials*, *03*, 1–50. https://doi.org/10.1520/E0647-13A.2

165. Mukherjee, T., Zhang, W., & DebRoy, T. (2017). An improved prediction of residual stresses

and distortion in additive manufacturing. *Computational Materials Science*, *126*, 360–372. https://doi.org/10.1016/j.commatsci.2016.10.003

166. Mercelis, P., & Kruth, J. P. (2006). Residual stresses in selective laser sintering and selective laser melting. *Rapid Prototyping Journal*, *12*(5), 254–265. https://doi.org/10.1108/13552540610707013

167. Wang, Z., Denlinger, E., Michaleris, P., Stoica, A. D., Ma, D., & Beese, A. M. (2017). Residual stress mapping in Inconel 625 fabricated through additive manufacturing: Method for neutron diffraction measurements to validate thermomechanical model predictions. *Materials and Design*, *113*, 169–177. https://doi.org/10.1016/j.matdes.2016.10.003

168. Mughal, M. P., Fawad, H., Mufti, R. A., & Siddique, M. (2005). Deformation modelling in layered manufacturing of metallic parts using gas metal arc welding: Effect of process parameters. *Modelling and Simulation in Materials Science and Engineering*, *13*(7), 1187–1204. https://doi.org/10.1088/0965-0393/13/7/013

169. Alimardani, M., Toyserkani, E., & Huissoon, J. P. (2007). A 3D dynamic numerical approach for temperature and thermal stress distributions in multilayer laser solid freeform fabrication process. *Optics and Lasers in Engineering*, *45*(12), 1115–1130. https://doi.org/10.1016/j.optlaseng.2007.06.010

170. Parry, L., Ashcroft, I. A., & Wildman, R. D. (2016). Understanding the effect of laser scan strategy on residual stress in selective laser melting through thermo-mechanical simulation. *Additive Manufacturing*, *12*, 1–15. https://doi.org/10.1016/j.addma.2016.05.014

171. Baragetti, S. (2014). Notch corrosion fatigue behavior of Ti-6Al-4V. *Materials*, *7*(6), 4349–4366. https://doi.org/10.3390/ma7064349

172. Smith, H. R., Piper, D. E., & Downey, F. K. (1967). A sudy of stress-corrosion cracking by wedge-force loading. *Engineering Fracture Mechanics*, (878), 123–128.

173. McEvily, A., & Wei, R. (1972). Fracture mechanics and corrosion fatigue. *Corrosion fatigue: chemistry, mechanics and microstructure NACE-2*.

174. Baboian, R., Schully, J., & Gangloff, R. (2009). Chapter 26—Environmental Cracking-Corrosion Fatigue. *Corrosion Tests and Standards: Application and Interpretation—Second Edition*, 302-302–20. https://doi.org/10.1520/mnl11032m

175. Wei, R. P., & Landes, J. D. (1969). Correlation between sustained-load and fatigue crack growth in high-strength steels. *Mater Res Stand*.

176. Wei, R. P., & Gao, M. (1983). Reconsideration of the superposition model for environmentally assisted fatigue crack growth. *Scripta Metallurgica*, *17*, 959–962.

177. Austen, I. M., & McIntyre, P. (1979). Corrosion fatigue of high-strength steel in low-pressure hydrogen gas. *Metal Science*, *13*(7), 420–428. https://doi.org/10.1179/msc.1979.13.7.420

178. Ramsamooj, D. V., & Shugar, T. A. (2001). Modeling of corrosion fatigue in metals in an aggressive environment. *International Journal of Fatigue*, *23*(SUPPL. 1), 301–309.

https://doi.org/10.1016/s0142-1123(01)00139-6

179. Kang, D. H., Lee, J. K., & Kim, T. W. (2011). Corrosion fatigue crack propagation of high-strength steel HSB800 in a seawater environment. *Procedia Engineering*, *10*, 1170–1175. https://doi.org/10.1016/j.proeng.2011.04.195

180. Wang, R. (2008). A fracture model of corrosion fatigue crack propagation of aluminum alloys based on the material elements fracture ahead of a crack tip. *International Journal of Fatigue*, *30*(8), 1376–1386. https://doi.org/10.1016/j.ijfatigue.2007.10.007

181. Weng, L., Zhang, J., Kalnaus, S., Feng, M., & Jiang, Y. (2013). Corrosion fatigue crack growth of AISI 4340 steel. *International Journal of Fatigue*, *48*, 156–164. https://doi.org/10.1016/j.ijfatigue.2012.10.015

182. Silling, S. A., Epton, M., Weckner, O., Xu, J., & Askari, E. (2007). *Peridynamic states and constitutive modeling*. *Journal of Elasticity* (Vol. 88). https://doi.org/10.1007/s10659-007-9125-1

183. Silling, S. A., & Askari, E. (2005). A meshfree method based on the peridynamic model of solid mechanics. *Computers and Structures*, *83*(17–18), 1526–1535. https://doi.org/10.1016/j.compstruc.2004.11.026

184. Silling, S. A., Weckner, O., Askari, E., & Bobaru, F. (2010). Crack nucleation in a peridynamic solid. *International Journal of Fracture*, *162*(1–2), 219–227. https://doi.org/10.1007/s10704-010-9447-z

185. Huang, D., Lu, G., & Qiao, P. (2015). An improved peridynamic approach for quasi-static elastic deformation and brittle fracture analysis. *International Journal of Mechanical Sciences*, *94–95*, 111–122. https://doi.org/10.1016/j.ijmecsci.2015.02.018

186. Ha, Y. D., & Bobaru, F. (2011). Characteristics of dynamic brittle fracture captured with peridynamics. *Engineering Fracture Mechanics*, *78*(6), 1156–1168. https://doi.org/10.1016/j.engfracmech.2010.11.020

187. Bobaru, F., & Hu, W. (2012). The meaning, selection, and use of the peridynamic horizon and its relation to crack branching in brittle materials. *International Journal of Fracture*, *176*(2), 215–222. https://doi.org/10.1007/s10704-012-9725-z

188. Basoglu, M. F., Zerin, Z., Kefal, A., & Oterkus, E. (2019). A computational model of peridynamic theory for deflecting behavior of crack propagation with micro-cracks. *Computational Materials Science*, *162*(November 2018), 33–46. https://doi.org/10.1016/j.commatsci.2019.02.032

189. Vazic, B., Wang, H., Diyaroglu, C., Oterkus, S., & Oterkus, E. (2017). Dynamic propagation of a macrocrack interacting with parallel small cracks. *AIMS Materials Science*, *4*(1), 118–136. https://doi.org/10.3934/matersci.2017.1.118

190. Kilic, B., & Madenci, E. (2009). Structural stability and failure analysis using peridynamic theory. *International Journal of Non-Linear Mechanics*, *44*(8), 845–854.

https://doi.org/10.1016/j.ijnonlinmec.2009.05.007

191. Foster, J. T., Silling, S. A., & Chen, W. W. (2010). Viscoplasticity using peridynamics. *International Journal for Numerical Methods in Engineering*, *81*, 1242–1258. https://doi.org/10.1002/nme

192. Silling, S., & Askari, A. (2014). *Peridynamic model for fatigue cracks*. Retrieved from http://docs.lib.purdue.edu/ses2014/mss/cfm/22/%0Ahttps://www.osti.gov/scitech/biblio/11602 89-peridynamic-model-fatigue-cracking

193. Zhang, G., Le, Q., Loghin, A., Subramaniyan, A., & Bobaru, F. (2016). Validation of a peridynamic model for fatigue cracking. *Engineering Fracture Mechanics*, *162*, 76–94. https://doi.org/10.1016/j.engfracmech.2016.05.008

194. Hu, Y. L., & Madenci, E. (2017). Peridynamics for fatigue life and residual strength prediction of composite laminates. *Composite Structures*, *160*, 169–184. https://doi.org/10.1016/j.compstruct.2016.10.010

195. Kilic, B., & Madenci, E. (2010). An adaptive dynamic relaxation method for quasi-static simulations using the peridynamic theory. *Theoretical and Applied Fracture Mechanics*, *53*(3), 194–204. https://doi.org/10.1016/j.tafmec.2010.08.001

196. Oterkus, S., Madenci, E., & Agwai, A. (2014). Peridynamic thermal diffusion. *Journal of Computational Physics*, *265*, 71–96. https://doi.org/10.1016/j.jcp.2014.01.027

197. Gao, Y., & Oterkus, S. (2020). Fluid-elastic structure interaction simulation by using ordinary state-based peridynamics and peridynamic differential operator. *Engineering Analysis with Boundary Elements*, *121*(August), 126–142. https://doi.org/10.1016/j.enganabound.2020.09.012

198. Chen, Z., & Bobaru, F. (2015). Peridynamic modeling of pitting corrosion damage. *Journal of the Mechanics and Physics of Solids*, *78*, 352–381. https://doi.org/10.1016/j.jmps.2015.02.015

199. Bobaru, F., & Ha, Y. D. (2011). Adaptive refinement and multiscale modeling in 2D peridynamics. *International Journal for Multiscale Computational Engineering*, *9*(6), 635–659. https://doi.org/10.1615/IntJMultCompEng.2011002793

200. Silling, S. A., & Bobaru, F. (2005). Peridynamic modeling of membranes and fibers. *International Journal of Non-Linear Mechanics*, *40*(2–3), 395–409. https://doi.org/10.1016/j.ijnonlinmec.2004.08.004

201. Dyyaroglu, C. (2016). *Peridynamics and its applications in marine structures*. University of Strathclyde.

202. Van der Vorst, H. A. (1992). Bi-CGSTAB: A Fast and Smoothly Converging Variant of Bi-CG for the Solution of Nonsymmetric Linear Systems. *SIAM Journal on scientific and Statistical Computing*, *13*(2), 631–644. https://doi.org/https://doi.org/10.1137/0913035

203. Suzuki, S., & Sakaue, K. (2004). Measurement of Crack Opening Displacement and Energy Release Rate of Rapidly Bifurcating Cracks by High-Speed Holographic Microscopy. *The*

Abstracts of ATEM : International Conference on Advanced Technology in Experimental Mechanics : Asian Conference on Experimental Mechanics, *2003*(0), 23. https://doi.org/10.1299/jsmeatem.2003.23

204. Yang, R. S., Ding, C. X., Yang, L. Y., Xu, P., & Chen, C. (2018). Hole Defects Affect the Dynamic Fracture Behavior of Nearby Running Cracks. *Shock and Vibration*, *2018*. https://doi.org/10.1155/2018/5894356

205. Guz', A. N. (1983). Mechanics of the brittle failure of materials with initial stress. *Soviet Applied Mechanics*, *19*(4), 293–308. https://doi.org/10.1007/BF00884855

206. Cottrell, A. (1978). Theory of brittle fracture in steel and similar metals. *Trans. Metallurgical Society*, *212*, 192. Retrieved from http://garfield.library.upenn.edu/classics1979/A1979HZ20900001.pdf

207. Jayatilaka, A. D. S., & Trustrum, K. (1977). Statistical approach to brittle fracture. *Journal of Materials Science*, *12*(7), 1426–1430. https://doi.org/10.1007/BF00540858

208. Deighton, M. (1976). *Fracture of Brittle Solids*. *Physics Bulletin* (Vol. 27). Cambridge University Press. https://doi.org/10.1088/0031-9112/27/5/044

209. Freund, L. B. (1998). Dynamic fracture mechanics. In *Dynamic Fracture Mechanics* (pp. 1–366). Cambridge University Press. https://doi.org/10.1142/6139

210. Yoffe, E. H. (1951). LXXV. The moving griffith crack. *The London, Edinburgh, and Dublin Philosophical Magazine and Journal of Science*, *42*(330), 739–750. https://doi.org/10.1080/14786445108561302

211. Abraham, F., Brodbeck, R., Rafey, A., & Rudge, W. E. (1994). Instability of fracture—a computer-simulation investigation. *Physical Review Letters*, *73*(2), 272–275.

212. Sharon, E., Gross, S. P., & Fineberg, J. (1995). Local crack branching as a mechanism for instability in dynamic fracture. *Physical Review Letters*, *74*(25), 5096–5099. https://doi.org/10.1103/PhysRevLett.74.5096

213. Fineberg, J., Gross, S. P., Marder, M., & Swinney, H. L. (1999). Fast Cracks. *Science*, *284*(5418), 1233d – 1233. https://doi.org/10.1126/science.284.5418.1233d

214. Ravi-Chandar, K., & Knauss, W. G. (1984). An experimental investigation into dynamic fracture: IV. On the interaction of stress waves with propagating cracks. *International Journal of Fracture*, *26*(3), 189–200. https://doi.org/10.1007/BF01140627

215. Ravi-Chandar, K., & Knauss, W. G. (1984). An experimental investigation into dynamic fracture: II. Microstructural aspects. *International Journal of Fracture*, *26*(1), 65–80. https://doi.org/10.1007/BF01152313

216. Hull, D. (1970). Effect of crazes on the propagation of cracks in polystyrene. *Journal of Materials Science*, *5*(4), 357–363. https://doi.org/10.1007/BF02397790

217. Kalthoff, J. F. (1986). The Shadow Optical Method of Caustics. In *Photoelasticity* (pp. 109–120). Vienna: Springer. https://doi.org/10.1007/978-4-431-68039-0_14

218. Madenci, E., & Oterkus, S. (2016). Ordinary state-based peridynamics for plastic deformation according to von Mises yield criteria with isotropic hardening. *Journal of the Mechanics and Physics of Solids*, *86*, 192–219. https://doi.org/10.1016/j.jmps.2015.09.016

219. Sundaram, B. M., & Tippur, H. V. (2018). Dynamic fracture of soda-lime glass: A full-field optical investigation of crack initiation, propagation and branching. *Journal of the Mechanics and Physics of Solids*, *120*, 132–153. https://doi.org/10.1016/j.jmps.2018.04.010

220. Bobaru, F., & Zhang, G. (2015). Why do cracks branch? A peridynamic investigation of dynamic brittle fracture. *International Journal of Fracture*, *196*(1–2), 59–98. https://doi.org/10.1007/s10704-015-0056-8

221. Ha, Y. D., & Bobaru, F. (2010). Studies of dynamic crack propagation and crack branching with peridynamics. *International Journal of Fracture*, *162*(1–2), 229–244. https://doi.org/10.1007/s10704-010-9442-4

222. Chen, Y. Z. (1993). Interaction between cracks and rigid lines in an infinite plate. *Acta Mechanica*, *101*(1–4), 15–29. https://doi.org/10.1007/BF01175594

223. Kachanov, M. (1994). Elastic solids with many cracks and related problems. In *Advances in Applied Mechanics* (pp. 259–445).

224. Gong, S. X., & Horii, H. (1989). General solution to the problem of microcracks near the tip of a main crack. *Journal of the Mechanics and Physics of Solids*, *37*(1), 27–46. https://doi.org/10.1016/0022-5096(87)90003-2

225. Romalis, N. B., & Tamuzh, V. P. (1984). Propagation of a main crack in a body with distributed microcracks. In *Mechanics of Composite Materials* (Vol. 20, pp. 35–43). https://doi.org/10.1007/BF00611573

226. Chandar, K. R., & Knauss, W. G. (1982). Dynamic crack-tip stresses under stress wave loading -A comparison of theory and experiment. *International Journal of Fracture*, *20*(3), 209–222. https://doi.org/10.1007/BF01140336

227. Zhao, X., Li, S., Zhang, M., Liu, Y., Sercombe, T. B., Wang, S., … Murr, L. E. (2016). Comparison of the microstructures and mechanical properties of Ti-6Al-4V fabricated by selective laser melting and electron beam melting. *Materials and Design*, *95*, 21–31. https://doi.org/10.1016/j.matdes.2015.12.135

228. Oterkus, E., Guven, I., & Madenci, E. (2010). Fatigue failure model with peridynamic theory. In *2010 12th IEEE Intersociety Conference on Thermal and Thermomechanical Phenomena in Electronic Systems*. IEEE. https://doi.org/10.1109/itherm.2010.5501273

229. Zhang, J., Wang, X., Paddea, S., & Zhang, X. (2016). Fatigue crack propagation behaviour in wire+arc additive manufactured Ti-6Al-4V: Effects of microstructure and residual stress. *Materials and Design*, *90*, 551–561. https://doi.org/10.1016/j.matdes.2015.10.141

230. Bobaru, F., Yang, M., Frota Alves, L., Silling, S. A., Askari, E., & Xu, J. (2008). Convergence, adaptive refinement, and scaling in 1D peridynamics. *International Journal for Numerical*

Methods in Engineering, (August). https://doi.org/10.1002/nme

231. Spriggs, R. M. (1961). Expression for Effect of Porosity on Elastic Modulus of Polycrystalline Refractory Materials, Particularly Aluminum Oxide. *Journal of the American Ceramic Society*, *44*(12), 628–629. https://doi.org/10.1111/j.1151-2916.1961.tb11671.x

232. Zhu, K., Li, C., Zhu, Z., & Liu, C. S. (2007). Measurement of the dynamic Young's modulus of porous titanium and Ti6Al4V. *Journal of Materials Science*, *42*(17), 7348–7353. https://doi.org/10.1007/s10853-007-1532-y

233. Titanium Alloys - Ti6Al4V Grade 5 properties. (n.d.). Retrieved from https://www.azom.com/properties.aspx?ArticleID=1547

234. Chen, Z., Niazi, S., & Bobaru, F. (2019). A peridynamic model for brittle damage and fracture in porous materials. *International Journal of Rock Mechanics and Mining Sciences*, *122*(October 2018), 104059. https://doi.org/10.1016/j.ijrmms.2019.104059

235. Wu, X. (2018). On Tanaka-Mura's fatigue crack nucleation model and validation. *Fatigue and Fracture of Engineering Materials and Structures*, *41*(4), 894–899. https://doi.org/10.1111/ffe.12736

236. Duckworth, W. E., & Ineson, E. (1963). The effects of externally introduced alumina particles on the fatigue life of En24 steel. *Iron Steel Inst*, *77*, 87–103.

237. Kung, C. Y., & Fine, M. E. (1979). Fatigue crack initiation and microcrack growth in 2024-T4 and 2124-T4 Aluminium Alloys. *Metallurgical Transactions A*, *10A*, 603–610. https://doi.org/10.1111/j.1460-2695.2006.01088.x

238. Murakami, Y., & Miller, K. J. (2005). What is fatigue damage? a view point from the observation of low cycle fatigue process. *International Journal of Fatigue*, *27*(8), 991–1005. https://doi.org/10.1016/j.ijfatigue.2004.10.009

239. Carlton, H. D., Haboub, A., Gallegos, G. F., Parkinson, D. Y., & MacDowell, A. A. (2016). Damage evolution and failure mechanisms in additively manufactured stainless steel. *Materials Science and Engineering A*, *651*, 406–414. https://doi.org/10.1016/j.msea.2015.10.073

240. Murakami, Y., & Endo, M. (1994). Effects of defects, inclusions and inhomogeneities on fatigue strength. *International Journal of Fatigue*, *16*(3), 163–182. https://doi.org/10.1016/0142-1123(94)90001-9

241. Kitagawa, H., Takahashi, S. (1976). Application of fracture mechanics to very small cracks or the cracks in early stage. In *Proc. of 2nd ICM, Cleveland* (pp. 627–631).

242. Fomin, F., Horstmann, M., Huber, N., & Kashaev, N. (2018). Probabilistic fatigue-life assessment model for laser-welded Ti-6Al-4V butt joints in the high-cycle fatigue regime. *International Journal of Fatigue*, *116*(March), 22–35. https://doi.org/10.1016/j.ijfatigue.2018.06.012

243. Askari, E., Bobaru, F., Lehoucq, R. B., Parks, M. L., Silling, S. A., & Weckner, O. (2008). Peridynamics for multiscale materials modeling. *Journal of Physics: Conference Series*, *125*.

https://doi.org/10.1088/1742-6596/125/1/012078

244.   Jafarzadeh, S., Chen, Z., & Bobaru, F. (2018). Peridynamic Modeling of Intergranular Corrosion Damage. *Journal of The Electrochemical Society*, *165*(7), C362–C374. https://doi.org/10.1149/2.0821807jes

245.   Xudong, Q. (2013). *Effect of rolling on fatigue crack growth rate of wire and arc additive manufacture (WAAM) processed titanium*.

246.   Coules, H. E., Smith, D. J., Orrock, P. J., Abburi Venkata, K., & Pirling, T. (2016). A Combined Experimental and Modelling Approach to Elastic–Plastic Crack Driving Force Calculation in the Presence of Residual Stresses. *Experimental Mechanics*, *56*(8), 1313–1325. https://doi.org/10.1007/s11340-016-0171-0

247.   ELBER W. (1970). Fatigue Crack Closure Under Cyclic Tension. *Engineering Fracture Mechanics*, *2*(1), 37–44. https://doi.org/10.1016/0013-7944(70)90028-7

248.   Pasta, S., & Reynolds, A. P. (2008). Residual stress effects on fatigue crack growth in a Ti-6Al-4V friction stir weld. *Fatigue and Fracture of Engineering Materials and Structures*, *31*(7), 569–580. https://doi.org/10.1111/j.1460-2695.2008.01258.x

249.   De Meo, D., Diyaroglu, C., Zhu, N., Oterkus, E., & Siddiq, M. A. (2016). Modelling of stress-corrosion cracking by using peridynamics. *International Journal of Hydrogen Energy*, *41*(15), 6593–6609. https://doi.org/10.1016/j.ijhydene.2016.02.154

250.   Palin-Luc, T., Pérez-Mora, R., Bathias, C., Domínguez, G., Paris, P. C., & Arana, J. L. (2010). Fatigue crack initiation and growth on a steel in the very high cycle regime with sea water corrosion. *Engineering Fracture Mechanics*, *77*(11), 1953–1962. https://doi.org/10.1016/j.engfracmech.2010.02.015

251.   Shipilov, S. A. (1998). Corrosion Fatigue Crack Growth Behavior of Titanium Alloys in Aqueous Solutions. *Corrosion*, *54*(1), 29–39. https://doi.org/10.5006/1.3284825

252.   Jesus, J. S., Borrego, L. P., Ferreira, J. A. M., Costa, J. D., & Capela, C. (2020). Fatigue crack growth under corrosive environments of Ti-6Al-4V specimens produced by SLM. *Engineering Failure Analysis*, *118*(July), 104852. https://doi.org/10.1016/j.engfailanal.2020.104852

253.   Borrego, L. P., De Jesus, J., Ferreira, J. A. M., Costa, J. D., & Capela, C. (2019). Environmental effect on the fatigue crack propagation of AM TiAl6V4 alloy specimens. *Procedia Structural Integrity*, *17*, 562–567. https://doi.org/10.1016/j.prostr.2019.08.075

254.   Baragetti, S. (2013). Corrosion fatigue behaviour of Ti-6Al-4V in methanol environment. *Surface and Interface Analysis*, *45*(10), 1654–1658. https://doi.org/10.1002/sia.5203

255.   Donahue, J. R., Lass, A. B., & Burns, J. T. (2017). The interaction of corrosion fatigue and stress-corrosion cracking in a precipitation-hardened martensitic stainless steel. *npj Materials Degradation*, *1*(1). https://doi.org/10.1038/s41529-017-0013-2

256.   Nelson, H. G. (1976). A film-rupture model of hydrogen-induced, slow crack growth in acicular alpha-beta titanium. *Metallurgical Transactions A*, *7*(4), 621–627.

https://doi.org/10.1007/BF02646469

257. Largitte, L., & Pasquier, R. (2016). A review of the kinetics adsorption models and their application to the adsorption of lead by an activated carbon. *Chemical Engineering Research and Design*, *109*, 495–504. https://doi.org/10.1016/j.cherd.2016.02.006

258. Alvarez, A. M., Robertson, I. M., & Birnbaum, H. K. (2004). Hydrogen embrittlement of a metastable β-titanium alloy. *Acta Materialia*, *52*(14), 4161–4175. https://doi.org/10.1016/j.actamat.2004.05.030

259. Tal-Gutelmacher, E., & Eliezer, D. (2005). The hydrogen embrittlement of titanium-based alloys. *Jom*, *57*(9), 46–49. https://doi.org/10.1007/s11837-005-0115-0

260. Young, G. A., & Scully, J. R. (1994). Hydrogen Embrittlement of Solution Heat-Treated and Aged β-Titanium Alloys Ti-15% V-3% Cr-3% Al-3% Sn and Ti-15% Mo-3% Nb-3% Al. *Corrosion*, *50*(12), 919–933. https://doi.org/10.5006/1.3293483

261. Beachem, C. D. (1972). A new model for hydrogen-assisted cracking (hydrogen "embrittlement"). *Metallurgical Transactions*, *3*(2), 441–455. https://doi.org/10.1007/BF02642048

262. Christ, H.-J., Senemmar, A., Decker, M., & Prubner, K. (2003). Effect of hydrogen on mechanical properties of β-titanium alloys, *28*, 453–465.

263. Dai, N., Zhang, L. C., Zhang, J., Zhang, X., Ni, Q., Chen, Y., … Yang, C. (2016). Distinction in corrosion resistance of selective laser melted Ti-6Al-4V alloy on different planes. *Corrosion Science*, *111*, 703–710. https://doi.org/10.1016/j.corsci.2016.06.009

264. Yang, J., Yang, H., Yu, H., Wang, Z., & Zeng, X. (2017). Corrosion Behavior of Additive Manufactured Ti-6Al-4V Alloy in NaCl Solution. *Metallurgical and Materials Transactions A: Physical Metallurgy and Materials Science*, *48*(7), 3583–3593. https://doi.org/10.1007/s11661-017-4087-9

265. Neikter, M., Colliander, M., de Andrade Schwerz, C., Hansson, T., Åkerfeldt, P., Pederson, R., & Antti, M. L. (2020). Fatigue crack growth of electron beam melted TI-6AL-4V in high-pressure hydrogen. *Materials*, *13*(6). https://doi.org/10.3390/ma13061287

266. Rimoli, J. J. (2009). A Computational Model for Intergranular Stress Corrosion Cracking Thesis by, *2009*, 127.

267. Fisher, J. C. (1951). Calculation of diffusion penetration curves for surface and grain boundary diffusion. *Journal of Applied Physics*, *22*(1), 74–77. https://doi.org/10.1063/1.1699825

268. Neikter, M. (2019). *Microstructure and hydrogen embrittlement of additively manufactured Ti-6Al-4V*.

269. Hardie, D., & Ouyang, S. (1999). Effect of hydrogen and strain rate upon the ductility of mill-annealed Ti6A14V. *Corrosion Science*, *41*(1), 155–177. https://doi.org/10.1016/S0010-938X(98)00109-7

270. Hondros, E. D., & Seah, M. P. (1977). Theory of Grain Boundary Segregation in Terms of

Surface Adsorption Analogues. *Metall Trans A*, *8 A*(9), 1363–1371. https://doi.org/10.1007/BF02642850

271. Zaccariotto, M., Mudric, T., Tomasi, D., Shojaei, A., & Galvanetto, U. (2018). Coupling of FEM meshes with Peridynamic grids. *Computer Methods in Applied Mechanics and Engineering*, *330*, 471–497. https://doi.org/10.1016/j.cma.2017.11.011

272. Baragetti, S., & Villa, F. (2015). Corrosion fatigue of high-strength titanium alloys under different stress gradients. *Jom*, *67*(5), 1154–1161. https://doi.org/10.1007/s11837-015-1360-5

273. Jaske, C. E., Payer, J. H., & Balint, V. S. (1981). Corrosion Fatigue of Metals in Marine Environments. *MCIC Report (Metals and Ceramics Information Center)*, (July).

274. Dawson, D. B., & Pelloux, R. M. (1974). Corrosion Fatigue Crack Growth of Titanium Alloys in Aqueous Environments. *Metall Trans*, *5*(3), 723–731. https://doi.org/10.1007/BF02644669